Neutralino Dark Matter, where Particle Physics meets Cosmology

CANDIDATE:

Stefano Profumo

SUPERVISORS:

Prof. Serguey T. Petcov

Dott. Piero Ullio

Yet from these flames
No light, but rather darkness visible

J. Milton

Il faut regarder dans le noir, avec insolence.

M. Yourcenar

Contents

Preface

The present thesis work is based on the following papers, here listed in chronological order, as appeared on the preprint arXiv:

- S. Profumo,
"*Neutralino dark matter, b - tau Yukawa unification and non-universal sfermion masses*",
Phys. Rev. D **68** (2003) 015006 [arXiv:hep-ph/0304071]

- S. Profumo,
"*Extended coannihilations from non universal sfermion masses*",
arXiv:hep-ph/0305040, published in the *Proceedings of the XXXVIIIth Rencontres de Moriond on ElectroWeak Interactions and Unified Theories, March 15th to 22nd, 2003*

- S. Profumo,
"*Neutralino relic density in supersymmetric GUTs with no-scale boundary conditions above the unification scale*",
JHEP **0306** (2003) 052 [arXiv:hep-ph/0306119]

- S. Profumo and P. Ullio,
"*SUSY dark matter and quintessence*",
JCAP **0311** (2003) 006 [arXiv:hep-ph/0309220]

- A. Masiero, S. Profumo, S. K. Vempati and C. E. Yaguna,
"*Lepton flavor violation, neutralino dark matter and the reach of the LHC*",
JHEP **0403** (2004) 046 [arXiv:hep-ph/0401138]

- S. Profumo and C. E. Yaguna,
"*Gluino annihilations and neutralino dark matter*",
Phys. Rev. D **69** (2004) 115009 [arXiv:hep-ph/0402208]

- S. Profumo and P. Ullio,
"*Neutralino relic density enhancement in non-standard cosmologies*",
arXiv:astro-ph/0404390, published in the *Proceedings of the XXXIXth Rencontres de Moriond on Exploring the Universe, Contents and Structures of the Universe, March 28th to April 4th, 2004*

- S. Profumo and P. Ullio,
"*The role of antimatter searches in the hunt for supersymmetric dark matter*",
JCAP **0406** (2004) 011 [arXiv:hep-ph/0406018]

- S. Profumo and C. E. Yaguna,
"*A statistical analysis of supersymmetric dark matter in the general MSSM after WMAP*",
arXiv:hep-ph/0407036, submitted to Physical Review D

During his PhD, the Candidate also worked on other research topics, namely on reduced models of lattice gauge theories and the lattice formulation of noncommutative field theories, and on charged lepton flavor violating processes in minimal supersymmetric extensions of the standard model. These complementary research activities have lead to the following research articles, which will not be discussed in what follows:

- S. Profumo,
"*Noncommutative principal chiral models*",
JHEP **0210** (2002) 035 [arXiv:hep-th/0111285]

- S. Profumo and E. Vicari,
"*Twisted Eguchi-Kawai reduced chiral models*",
JHEP **0205** (2002) 014 [arXiv:hep-th/0203155]

- F. Bazzocchi, M. Cirafici, C. Maccaferri and S. Profumo,
"*Matrix models of noncommutative (2d+1) lattice gauge theories*",
arXiv:hep-th/0211060, to be published in the International Journal of Modern Physics A

- S. T. Petcov, S. Profumo, Y. Takanishi and C. E. Yaguna,
"*Charged lepton flavor violating decays: Leading logarithmic approximation versus full RG results*",
Nucl. Phys. B **676** (2004) 453 [arXiv:hep-ph/0306195]

- S. Profumo and C. E. Yaguna,
"*Non-universal gaugino masses and the fate of mu $\to$ e gamma*",
Nucl. Phys. B **681** (2004) 247 [arXiv:hep-ph/0307225]

Chapter 1

Introduction

One of the greatest puzzles of our present understanding of the Universe is the nature of *Dark Matter*. The issue is two-fold: on the one hand, a number of astrophysical and cosmological observations, which will be shortly reviewed in Chapter 2, indicates that *most of the matter contained in the Universe is dark and non-baryonic*; on the other hand, the Standard Model of Particle Physics, though remarkably successful and tested with astonishing precision, does not contain any suitable candidate for Dark Matter. The *macro-cosmo* indicates that most of what the Universe is made of is different from what *we* are made of; on the other hand, our understanding of the *micro-cosmo* is unable, as it stands in its minimal, and successful, formulation, to give us a clue about the *nature* of this mysterious fundamental component.

As a strong indication of *physics beyond the Standard Model*, the Dark Matter problem needs to be addressed not only from the original astrophysical point of view, but also as a dramatically concrete urgency to extend the current standard theory of Elementary Particles. Though it is well known that the Standard Model is an *effective*, and not a *fundamental* theory, any attempt to go beyond it must necessarily confront the conceptual lack of giving an answer to the Dark Matter problem. Remarkably, the most widely investigated Dark Matter scenarios stem from theories which consistently face, at once, the problem of extending the Standard Model (for instance addressing the *hierarchy problem*, or the *strong CP problem*) and of providing a suitable Dark Matter particle candidate.

Among these theoretical attempts, perhaps the most appealing, from various points of view, and for sure the most widely investigated, involves supersymmetric extensions to the Standard Model. Although supersymmetry (SUSY) has been introduced in the realm of the extensions of the Standard Model without any reference to Dark Matter, it soon became clear that in its minimal formulation it could provide a natural and suitable Dark Matter particle candidate, the lightest among the supersymmetric partners of the Standard Model particles. Many theoretical arguments have been put forward as motivations for a "low energy" realization of SUSY (*i.e.* at energy scales not far from the electroweak symmetry breaking scale): SUSY provides an elegant solution to the hierarchy problem and a mechanism for radiative electro-weak symmetry breaking; it yields the unification of gauge couplings; it predicted a heavy top quark and indicated a correct value for $\sin^2\theta_W$ long before experimental programs managed to perform the actual measurements; moreover, consistently with the latest Standard Model global fits from LEP, it implies a light Higgs boson. Last but not least, on purely theoretical grounds, it has been realized that SUSY is an essential ingredient of any attempt to unify gravity with the other Standard Model interactions.

The minimal supersymmetric extension of the Standard Model (MSSM) is a very elegant theory, whose only shortcoming is to feature an embarrassingly large number of unknown parameters (Chapter 3). In this respect, the situation is pretty similar to that of the Standard Model itself, which also contains a wealth of parameters that could have been fixed only

through the experiment. The MSSM, in its general setup, is in fact again an *effective field theory*, possibly with the relevant virtue of being theoretically consistent up to energies well above those where the Standard Model is expected to reliably describe the fundamental particle physics processes. Nevertheless, and thanks to this apparent freedom in the low energy realizations of SUSY, a wealth of high energy setups, ranging from Grand Unified Theories (GUTs) and supergravity to various string-inspired or brane world-inspired scenarios, have been put forward. An unmistakable value added to these frameworks is that the number of free parameters is constrained to a reasonably restricted set, at some high energy scale. On the other hand, one must always be aware that resorting to a particular high energy setup means introducing some kind of *theoretical bias* in the low energy phenomenology, and, therefore, eventually translates into a possible loss of generality.

Excitingly enough, at the dawn of the CERN Large Hadron Collider (LHC) era, particle physics experiments are going to probe an energy range where some kind of physics beyond the Standard Model is expected to show up. In this respect, the investigation of what is largely considered to be the most intriguing Standard Model extension is, in itself, an important point. A further strong motivation to the scrutiny of the phenomenology of SUSY is moreover provided by the extensive experimental program, which began in the early Eighties, facing the problem of the detection of Dark Matter particles. Standing as the best motivated particle candidate for Dark Matter, the lightest SUSY particle is of course in pole position in the realm of the predictions of dark matter detection rates and of the quest for the experimental routes toward the discovery of the yet mysterious, though ubiquitous, dark particle. Given a supersymmetric setup, one has the actual possibility of addressing at once the perspectives of detecting the resulting Dark Matter particle at direct detection experiments, and of assessing which signals the same setup would give at completely orthogonal experiments, like at the LHC or at indirect detection experiments, which may range from antimatter searches to gamma rays surveys, to the detection of neutrinos produced by pair annihilations in the center of the Sun. When encompassed with theories accounting for the discovery of neutrino masses, and therefore of lepton flavor violation, SUSY theories also predict charged lepton flavor violating processes at rates which could be observable at next generation experimental facilities. It is therefore certainly not surprising that the issue of *complementarity* between SUSY search strategies is nowadays a hot topic in particle physics phenomenology.

The aim of the present thesis work is to *provide concrete instances of phenomenological analysis of Dark Matter physics within supersymmetric theories.* The first issue one must face while addressing the plausibility of a given Dark Matter particle candidate is to assess whether or not the latter gives the correct cosmological abundance, as needed from observations (Chapter 4). In this respect, a wide theoretical and computational effort has been produced in recent years, and a sophisticated machinery has been built in order to estimate the relic density of a given species. It has been realized that often the relic abundance of neutralinos (the SUSY Dark matter candidate to which we will restrict here our attention) critically depends on the occurrence of a quasi-degenerate SUSY particle, which can *co-annihilate* with it. Different high energy principles can generate a low energy spectrum with various coannihilating partners, significantly affecting the low energy phenomenology. We will carry out a detailed analysis of all possible coannihilating partners, and in particular of the gluino, the SUSY counterpart of the gluon, which we showed to be the most effective coannihilating partner in the MSSM. In one of the most studied setups, minimal Supergravity (mSUGRA), the presence of a coannihilating partner, which the theory mostly restricts to be either the lightest stau or the lightest stop, is often mandatory to achieve a suppression of the relic density such as to be compatible with the cold dark matter abundance. We will show as a concrete instance, that a minimal deviation, motivated by GUT arguments, from the mSUGRA framework may give rise to unusual coannihilating partners, namely the

superpartners of the tau neutrino or of the lightest bottom quark. Another case in which the neutralino relic abundance may undergo remarkable suppressions is when a resonant annihilation channel is open.

An intriguing issue in the computation of the thermal relic abundance of species is the interplay between particle physics and cosmology. A given particle *freezes-out* from the thermal bath of the Early Universe when the interaction rate of particle annihilations becomes smaller than the expansion rate of the Universe. This process is determined by both fundamental physics and cosmology. A modification of the thermal history of the Universe may therefore drastically affect the final relic abundance of a species. This topic has recently become of great actuality, in view of the fact that the energy density budget of the Universe has been found to feature a large fraction of an unknown form of *Dark Energy*. The latter may simply be the effect of the presence of a cosmological constant term, but alternative explanations have been put forward. We therefore addressed the issue of the stability of relic density computations when the role of Dark Energy is played by a *dynamical scalar field*, which has been generally dubbed as *Quintessence*. We show in Sec. 4.3 that the neutralino relic abundance can be *increased* by the presence of this dynamical cosmological component, and that, as a by-product, models with a low thermal relic abundance in the standard cosmological scenario may well make up the whole of the required cold dark matter content of the Universe. As a further consequence, large annihilation rates, responsible for the late freeze-out, and hence for the low "standard" relic abundance, may give rise to spectacular detection signals in those channels which depend on neutralino annihilation (like antimatter or gamma rays production).

We will then turn to the question of the detection of a given SUSY Dark Matter particle candidate. In view of the fact that the MSSM is a hardly manageable theory in its full generality, one must resort to one out of the following two complementary approaches:

1. Take a particular search strategy and investigate it, focusing on either benchmark supersymmetric scenarios or on a statistical sample of viable MSSM realizations, or

2. Assume a specific high energy framework, possibly with a restricted number of parameters, and study the various low energy phenomenological implications.

We will take the first approach in Chapter 5, where we will discuss, and compare, various Dark Matter search strategies, resorting both to three benchmark scenarios featuring large annihilation rates, and to a large random scan of the MSSM parameter space, which will allow us to draw general, though statistical, conclusions on the different search perspectives. Particular emphasis will be given to neutralino searches through antimatter detection, in view of the imminent launch of space-based experiments which will greatly improve our knowledge of cosmic antiprotons and positron fluxes.

Chapter 6 takes, instead, the second approach, and provides some instances of SUSY Dark Matter phenomenology in specific high energy setups. In particular, we will introduce supersymmetric Grand Unified Theories (GUTs), which provide a well-motivated benchmark of top-down *modus operandi* in SUSY phenomenology. We treat in Sec. 6.1 the issue of third generation partial (b-τ) Yukawa coupling unification, showing in particular the constraints stemming from this GUT motivated requirement on the supergravity soft breaking parameters. As concrete realizations of GUTs, we then refer to a set of truly "minimal" theories, namely the so-called *no-scale models* (Sec. 6.2), where the scalar sector of the theory is radiatively generated through GUT interactions between some high energy scale and the scale of Grand Unification. The overall number of parameters is limited to two, and further constraints are provided by the already introduced GUT unification of the bottom and tau Yukawa couplings. The viable parameter space is shown to be highly restricted, rendering

the theory particularly predictive; details on future accelerator and dark matter detection perspectives are also discussed. Finally, we give in Sec. 6.3 an example of a GUT inspired supergravity framework, where the radiative effects of a see-saw mechanism generating neutrino masses and mixing are taken into account. We show that charged lepton flavor violating processes may occur at remarkably large rates, and, for a given SUSY parameter space choice, may be competitive with both Dark Matter searches and with SUSY searches at the CERN LHC.

Lastly, Chapter 7 gives an overview of perspectives for supersymmetric Dark Matter search strategies in the next years, and concludes.

Chapter 2

The Dark Universe

The aim of the present chapter is to provide an overview of the observational evidences that converge towards a picture of our Universe mainly consisting in a non-baryonic and non-luminous matter component (what is usually dubbed as *Dark Matter*, DM), plunged into a gravitationally non-clustering form of energy featuring a negative pressure, named *Dark Energy*. The first striking point is that within this frame, ordinary matter we deal with in our everyday life turns out to be nothing but a *subdominant fraction* of the overall energy density of the Universe. Moreover, and not less remarkably, observational evidences pointing to this overall picture are increasingly *accurate*, leading people to talk about a *precision era* in cosmological measurements; moreover, and to an impressive extent, available observational indications are *orthogonal to each other*, and ranging over a widespread class of scales, from the smallest Galaxies to the whole of the cosmological dynamics of the Universe. In this short review chapter we will try to collect this striking set of evidences as a motivation for particle physics investigations in the field, although we will only mention those candidates which will be of relevance for the following discussion. The vast plethora of more or less exotic DM candidates has been reviewed in several works (an incomplete list includes *e.g.* [1–4]).

Despite most of our information about the Universe comes from electromagnetic radiation at different wavelengths, the history of astronomical discoveries of objects whose presence can only be inferred from the resulting gravitational effects on luminous matter is longstanding. For instance, in 1846 this method led to the discovery of Neptune from unexplained residuals in the motion of Uranus. In a similar way, in 1933 Zwicky pointed out that the very existence of the Coma cluster of galaxies would be impossible unless its dynamics was dominated by some kind of Dark Matter. It took however a few decades to realize that most of the Dark Matter differs drastically from ordinary baryonic matter, and even longer to pin down a quantitative statement about the actual amount of this exotic form of matter.

The only realistic model for cosmology, and the one which has become more and more soundly established by recent observations, is the Big Bang model [5]: the Universe has been, and still is, expanding from a primordial dense and hot phase, which existed around 13.7 billion years ago [6]. The observational cornerstones of the Big Bang theory – the expansion of the Universe, the fossil record of light elements synthesized during the first few minutes, and the existence of a relic thermal radiation field, the cosmic microwave background (CMB) – are more solid than ever, particularly after the recent results of the first year Wilkinson Microwave Anisotropy Probe (WMAP) data [6]. The determination of cosmological parameters made possible by the combination of these latest data on CMB anisotropies, of Lyman-α forest data and of Supernovae Ia surveys is of extraordinary accuracy, when compared with previous estimates. What is however most striking about these measurements is the apparent concordance of sets of very different observational pieces of evidences towards a minimal model, commonly dubbed ΛCDM or *concordance* model. The observed structure of Galaxies

and clusters of Galaxies, their motions, the anisotropies of the CMB, the abundance of light elements, the large scale structure and the theory of structure formation all, to a satisfactory extent, nicely fit into this relatively simple single model. This does not mean of course that there are no marginal frictions between the ΛCDM predictions and some astronomical or cosmological observations, and that the model is, in itself, theoretically complete and exhaustive: nevertheless it constitutes a sound framework, to which, unless differently specified, we will hereafter refer.

2.1 Astrophysical evidences

Perhaps the cleanest observational evidence for a non-luminous component in the Universe stems from the rotation curves deduced from the observation of stars and cold hydrogen HI clouds traveling on circular orbits around Galaxies of the type we live in, *i.e.* spiral galaxies. Stars in a spiral galaxy are mainly contained in a thin disk characterized by an exponential surface brightness profile

$$I(R) \sim e^{-R/R_d}, \tag{2.1}$$

where R is the galactocentric distance and $R_d \simeq 2-4$ kpc is the disk scale length. The circular velocity $v_c(R)$ of a given object at a distance R from the galactic center, in a cylindrically symmetric system with a gravitational potential $\phi(R,z)$ will then be given by

$$\frac{v_c^2(R)}{R} = \left(\frac{\partial\phi}{\partial R}\right)_{z=0}. \tag{2.2}$$

Since color and luminosity gradients in spiral disks are generally modest, the disk mass-to-light ratio[1] is approximately constant, and the disk surface density profile will have the same functional dependence as in Eq. (2.1). This, in turns, implies that the circular velocity profile determined by the luminous component of a spiral galaxy has the following analytical behavior, in terms of modified Bessel functions, [7]:

$$v_c(R) \sim R\left[I_0\left(\frac{R}{2R_d}\right)K_0\left(\frac{R}{2R_d}\right) - I_1\left(\frac{R}{2R_d}\right)K_1\left(\frac{R}{2R_d}\right)\right]^{1/2}, \tag{2.4}$$

which can be approximated, for evident purposes of clarity, as follows

$$v_c(R) \sim \begin{cases} R\,, & R < R_d \\ R^{-1/2}\,, & R > 3\,R_d\,. \end{cases} \tag{2.5}$$

On the other hand, observations show that all rotation curves show the same qualitative behavior: a linear rise in the inner region until a maximum around $R \simeq 2R_d$ beyond which they stay flat out to the last measured point, *i.e.*

$$v_c(R) \sim \begin{cases} R\,, & R < R_d \\ \text{constant}\,, & R > 3\,R_d\,. \end{cases} \tag{2.6}$$

This clearly indicates that the agreement is good in the inner region of the galaxies ($R < R_d$), but that at larger galactocentric distances ($R > 3R_d$), where the disagreement is dramatic, Dark Matter dominates the matter budget of spiral galaxies, see Fig. 2.1. Remarkably, this turns out to be a universal property of spiral Galaxies [8,9].

[1]The mass-to-light ratio of an object of total mass M and optical luminosity L in a given band (here taken to be the blue band) is defined in solar units as

$$\Upsilon \equiv \frac{M/M_\odot}{L/L_\odot} \tag{2.3}$$

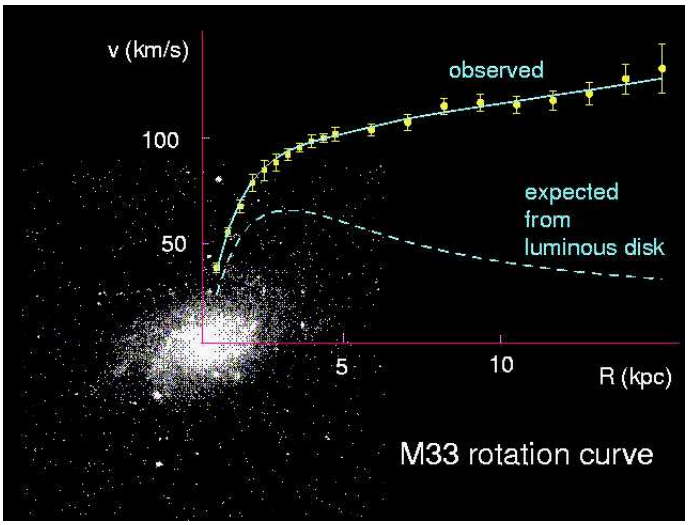

Figure 2.1: *Observed rotation curve of the nearby spiral galaxy M33, superimposed on its optical image (Fig. from Ref. [2]).*

Optical methods allow one to conclude that in spiral galaxies, the optical region $R < R_{\rm opt} \simeq 4R_d$ contains roughly the same amount of luminous and dark matter. Radio observations of HI clouds, which extend out to twice the optical radius, point at a growing amount of Dark Matter in outer galactic regions. A very neat example is provided by the spiral Galaxy $NGC3198$, where it has been determined that

$$M_{\rm dark}(R < 10R_d) \simeq 17M_{\rm lum}, \tag{2.7}$$

with $M_{\rm lum}$ denoting the luminous mass. At even larger distances, different tracers must be used, namely satellite galaxies. The investigation of the gravitational field of the primary galaxy through the dynamical behavior of the satellites leads one to conclude that, in most spiral galaxies [9, 10],

$$M_{\rm dark} > 30M_{\rm lum}. \tag{2.8}$$

The technique of rotation curves cannot be applied to galaxies with different morphologies, as in the case of elliptical galaxies, where the star motion is highly chaotic. In this case a dynamical analysis of stellar motion must be applied, resorting to an Euler equation relating the kinetic pressure of a given stellar population and the overall gravitational field. This method relies however on strong assumptions on various observables, and only recently these kinds of Dark Matter determinations in ellipticals have been confirmed through strong gravitational lensing techniques [11], leading to the conclusion [12] that also the optical region of ellipticals contains equal amounts of luminous and Dark Matter[2]. On the other hand, bright elliptical galaxies, containing a sizable amount of ionized gases outside the optical region, allow for a more quantitative determination of the Dark Matter amount through the study of X-ray emissions [13]. It has been estimated that bright elliptical galaxies are totally dominated by Dark Matter,

$$M_{\rm dark} \simeq 45M_{\rm lum}. \tag{2.9}$$

At the scale of galaxy clusters, the determination of the dark to luminous matter proceeds through either a dynamical technique, relying on the virial theorem, or through the gravitational distortion of background galaxies images (strong and weak lensing, according to

[2]However, contrary to the case of spirals, several exceptions to this statement have been found for elliptical Galaxies.

whether one deals with multiple or single images). The first strategy is based on the fact that any isolated self-gravitating system reaches an equilibrium state in which gravity is balanced by kinetic pressure, *i.e.*

$$2K + U = 0, \tag{2.10}$$

where K and U respectively stand for the kinetic energy and the potential energy in the cluster. Both these quantities can be expressed as functions of the mean effective radius and of the mean squared velocity, which, under suitable isotropicity assumptions, allow a determination of the overall mass of a cluster. A separate analysis of the hot gas content of galaxy clusters, as well as strong and weak gravitational lensing results, confirm that the Dark Matter content of so-called regular clusters lies in between what found for spirals and for ellipticals, Eq. (2.8) and (2.9).

2.2 Cosmological evidences

One of the crucial tests of the standard Big Bang theory is provided by the theory of the synthesis of light elements. Since the Universe monotonically cools during its expansion, atomic nuclei form when the energy of the background thermal bath becomes comparable to the nuclear binding energy. Apart from the input nuclear cross sections, the theory contains only a single parameter, namely the baryon-to-photon ratio η. Once this information is provided, one is then allowed to make quantitative predictions, with well defined uncertainties, on the abundances of the light elements, D, ^{3}He, ^{4}He and ^{7}Li. A comparison between the predicted and observed light elements abundances unambiguously fixes the baryon contribution to the Universe critical energy density, $\Omega_B h^2$, where the constant h is related to the Hubble constant by $h = H_0/100\,\mathrm{km,\ s^{-1}Mpc^{-1}}$, and we define, for a species i

$$\Omega_i \equiv \frac{\rho_i}{\rho_c}, \quad \rho_c = \frac{3H^2}{8\pi G_N} \simeq 1.9 \cdot 10^{-38} h^2 \ \mathrm{kg \cdot m^{-3}}. \tag{2.11}$$

The agreement is achieved, at the 95% C.L., in the range [14]

$$0.018 < \Omega_B h^2 < 0.023. \tag{2.12}$$

An independent estimate of $\Omega_B h^2$, remarkably consistent with the range of Eq. (2.12), arises moreover from the features of high-redshift Lyman-α forest absorption lines of neutral hydrogen observed in the spectra of background quasars [15]. The piece of information stemming from the determination of the overall baryonic matter content of the Universe may be used to quantify the amount of *non-baryonic* Dark Matter, once the total amount of matter has been determined. The methods outlined in the previous section, in fact, only provide evidences of the presence of a large amount of *non-luminous matter*, and give only marginal indications of the baryonic fraction of the matter in the Universe.

A basic piece of information on the value of cosmological parameters comes from the interplay of data from the Cosmic Microwave Background (CMB) and from the analysis of Type-Ia Supernovae. The detection of CMB has been a major confirmation of the standard Big Bang theory: when the photons temperature becomes comparable to the atomic binding energy, atoms come into existence, and matter becomes neutral and decouples from radiation (*recombination*), which then freely streams in the expanding Universe. The relic radiation hence gives a snapshot of the Universe at recombination, $t_{\mathrm{rec}} \simeq 3 \cdot 10^5$ years after the Big Bang. The CMB, once the effects of the proper motion of the Sun are accounted for, has been measured to be a highly isotropic black body radiation with a temperature $T_0 \simeq 2.726\ K$. Anisotropies corresponding to temperature fluctuations $\Delta T/T \sim 10^{-5}$ have been discovered

in 1992 by the COBE mission [16]. The latest data on the CMB temperature fluctuations have been recently delivered by the WMAP Collaboration [6], which also gave statistical estimates of the cosmological parameters with unprecedented accuracy.

The physics of the CMB reflects the acoustic oscillations of the matter-radiation fluid at the time of recombination, driven by the interplay of *gravity* and *radiation pressure*. A statistical treatment of the harmonic analysis of the temperature anisotropies,

$$\frac{\Delta T}{T}(\theta,\phi) = \sum_{l=0}^{\infty} \sum_{m=-l}^{l} a_{lm} Y_{lm}(\theta,\phi), \tag{2.13}$$

where Y_{lm} denote the spherical harmonics, provides the coefficients c_l of the variance of a_{lm}, defined as

$$c_l \equiv \langle |a_{lm}|^2 \rangle = \frac{1}{2l+1} \sum_{m=-l}^{l} |a_{lm}|^2. \tag{2.14}$$

The *CMB power spectrum*, *i.e.* the quantity $l(l+2)c_l/2\pi$, as a function of l, reflects the above mentioned acoustic oscillations in terms of acoustic peaks, whose location and height provide the information on the geometry and composition of the Universe. Namely, the position of the first acoustic peak is controlled by the angle θ_1 under which we see today the size ot the sound horizon. Being an angle, θ_1 is very sensitive to the geometry of the Universe, that is to say to $\Omega_{\rm tot}$, with the recent result that [6]

$$\Omega_{\rm tot} = 1.02 \pm 0.02, \tag{2.15}$$

pointing at a *flat Universe*, as predicted by inflation. On the other hand, it turns out that the relative height of the first and second acoustic peak entails a determination[3] of Ω_B, which gives [6]

$$\Omega_B h^2 = 0.024 \pm 0.001, \tag{2.16}$$

in remarkable agreement with the predictions from Big Bang Nucleosynthesis, Eq. (2.12).

On purely theoretical grounds, the energy budget of a flat Universe is the sum of the contributions from matter (Ω_M), radiation (Ω_R)and vacuum energy (cosmological constant, Ω_Λ). Today, $\Omega_M \gg \Omega_R$, thus one can safely write, after the CMB result of Eq. (2.15),

$$1 = \Omega_M + \Omega_\Lambda. \tag{2.17}$$

Clearly, one needs a further handle on the relative contribution from the two terms appearing in Eq. (2.17) for solving the degeneracy in the $(\Omega_M, \Omega_\Lambda)$ plane. It was long ago that Hubble realized that one could get information on the geometry of the Universe observing *standard candles*, *i.e.* astronomical objects of known absolute luminosity, located at cosmological distances. The measurement of the apparent luminosity (the radiative flux) of a source yields its distance D, once the absolute luminosity is known. The distance D depends in a known way on the cosmological parameters Ω_M and Ω_Λ, as a function of the redshift z of the object, defined as

$$1 + z = \frac{\lambda_{\rm emit}}{\lambda_{\rm obs}}, \tag{2.18}$$

where λ denotes the emitted and observed wavelength associated with a specific spectral line. In practice, a given $(\Omega_M, \Omega_\Lambda)$ pair yields a curve in the plane of apparent luminosity versus redshift (the *Hubble diagram*). Both apparent luminosity and redshift can be measured for a

[3]Notice that the results we report refer to the overall best fit statistical analysis carried out by the WMAP Collaboration [6], and not only to a determination based on the ratio of the heights of the first and second acoustic peak.

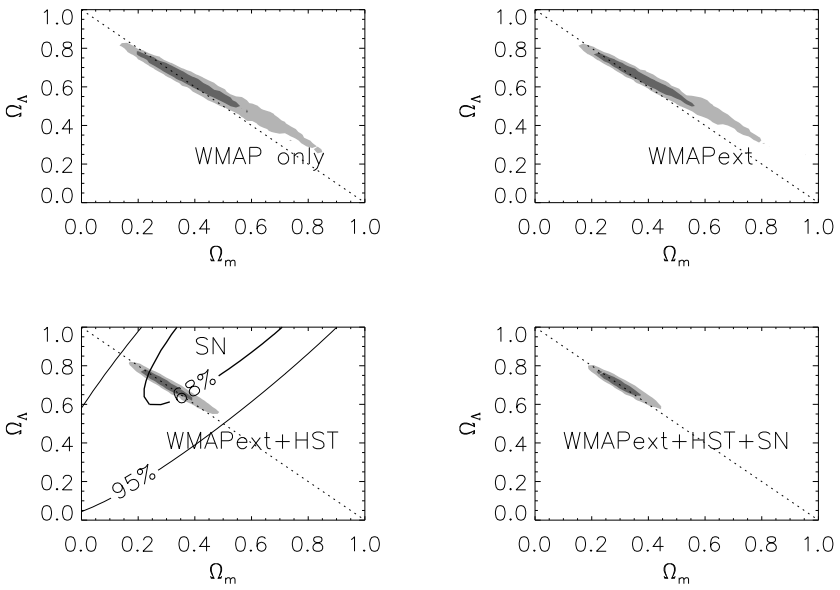

Figure 2.2: *Constraints on the geometry of the universe in the $\Omega_m - \Omega_\Lambda$ plane from the CMB anistropies as measured by the WMAP satellite. The figure shows the two dimensional likelihood surfaces for various combinations of data: (upper left) WMAP data only; (upper right) WMAP data + (CBI, ACBAR) (WMAPext); (lower left) WMAPext + HST Key Project (supernovae data [17, 18] are shown but not used in the likelihood in this part of the panel); (lower right) WMAPext + HST Key Project + supernovae. + supernovae. (Figure from Ref. [6])*

given sample of a standard candle species: it turns out that a very favorable case is that of distant Type-Ia supernovae. A best fit to the data gives [18]

$$\Omega_\Lambda \simeq 1.33\Omega_M + 0.33. \tag{2.19}$$

Given our previous estimate of $\Omega_{\rm tot}$, Eq. 2.15, this equation implies that *the Universe contains a large fraction of Dark Energy*, giving rise to the large Ω_Λ contribution. The term Dark Energy labels a generic fluid contributing to the Universe energy density featuring negative pressure, and which does not cluster gravitationally, at least up to the galactic clusters scales. The most renowned candidate is the *cosmological constant* Λ, which, as well known, poses severe conceptual problems (fine tuning, coincidence). Alternative explanations, such a a dynamical scalar field (*Quintessence*) have also been pursued: we will describe in some details a particular quintessential model in Sec. 4.3, but a detailed survey of Dark Energy models lies beyond the scopes of the present work.

Fig. 2.2 collects the results from the WMAP analysis of CMB data alone (upper plots) and the implications of the combination of supernovae and CMB data (lower plots) on the $(\Omega_M, \Omega_\Lambda)$ plane. Notice that in the lower plots, the iso confidence level contours have been determined taking into account also the results on the determination of the Hubble constant from the Hubble Space Telescope (HST) Key Project [19]. The determination of the cosmological parameters carried out by the WMAP collaboration [6] takes however into account also data on large scale structure, which we discuss in the next section.

2.3 Large scale structure

The structure of the matter distribution at large scales provides a further independent argument in favour of a non-baryonic matter component in the Universe. Moreover, the theory of structure formation provides an indication on the nature of Dark Matter from its kinetic budget at the time of matter-radiation equality (*i.e.*, the time when the radiation energy density equals the matter energy density, corresponding to a certain temperature T_m). Under the hypothesis of adiabatic perturbations, as predicted by inflation, the amplitude of density perturbations $\delta\rho/\rho$ is proportional to the anisotropies $\delta T/T \sim \delta$ produced in the CMB, according to the relation [14, 20]

$$\delta\rho/\rho \sim \delta(1 + z_{\rm rec}) \tag{2.20}$$

where $1 + z_{\rm rec} \sim 10^3$ is the redshift at the time of recombination. Since $\delta \sim 10^{-5}$, the resulting $\delta\rho/\rho$ would be too small to argue that growth has entered the nonlinear regime, needed to explain the large value (10^5) of $\delta\rho/\rho$ in galaxies. In the presence of Dark Matter, the linear growth of perturbations continues after radiation-matter equality, driving $\delta\rho_{\rm DM}/\rho_{\rm DM}$ to values larger than 1 after recombination. Baryons, although still bound to the radiation until decoupling, see the deep potential wells formed by Dark Matter perturbations. They therefore start to gravitationally collapse, thus circumventing the slow linear growth regime, and providing seeds of the correct size for the observed structures to form.

Noticeably, the formation of structures markedly depends on the nature of the Dark Matter particles at the time of matter-radiation equality, thus providing a first clue of the deep relation between astrophysics and elementary particles theory. Dark Matter particles which are relativistic at T_m, like neutrinos or other particles with masses $m_\chi < 100$ eV, are dubbed *Hot Dark Matter* (HDM). If, instead, the Dark Matter particles move at non-relativistic velocities at the time structures start to form, one speaks of *Cold Dark Matter* (CDM).

In the HDM scenario, particles free-stream out of galaxy-sized overdense regions, so that only very large structures can form early. Structures then form top-down by the fragmentation of large objects ("pancakes") into smaller. This pattern is nowadays strongly disfavored in view of observations of the distribution of galaxies at very high redshift, but a HDM component even at a 10% level cannot be ruled out. In CDM scenarios, instead, structures typically form hierarchically, with small clumps merging into larger ones, thus forming galaxy halos and successively larger structures. A further possibility is an intermediate case, warm Dark Matter, which could be made up of keV scale neutral particles. In this case, the inverse of the mass scale of the particle defines a lenght scale of structure formation, below which early structures are suppressed. Although from the particle physics and structure formation point of view this possibility is not particularly favoured, it still remains a viable option.

In what follows we will only concentrate on a purely Cold Dark Matter scenario: one should bear in mind that this setup encounters some kind of frictions with observations. To mention a few open problems, CDM overproduces substructures at the sub-galactic level, and numerical simulations generically indicate a highly cuspy profile towards the galactic center, much steeper than what is actually observed. A number of caveats to these problems, related for instance to the reliability of numerical simulations [21], to models of self-interacting Dark Matter [22] or of interactions with a long-lived charged particle, heavier than the CDM particle [23], as well as extensions of the standard ΛCDM model [24], are currently under investigation.

A crucial quantity in the theory of large scale structure is the linear matter power spectrum $P(k)$, defined as the Fourier transform of the two-point function of density fluctuations in the linear regime. $P(k)$ is constrained by large scale structures data [25] on wavelengths which only partially overlap those probed by CMB data, and which extend to larger wavenumbers

(smaller scales). Moreover, a complementary piece of information comes from observations of the Lyman-α forest, which probe the linear matter power spectrum at redshifts of 2-3, and are sensitive to small lenght scales, inaccessible to CMB experiments. The joint likelihood analysis of cosmological parameters performed by the WMAP collaboration took into account an extended set of CMB data, including those collected by the WMAP satellite and other CMB data sets studying smaller scales (CBI, ACBAR), as well as astronomical measurements of the power spectrum from the 2dF Galaxy Redshift Survey [25] and from the Lyman-α forest [26,27]. The main results of interest here read

$$\Omega_B h^2 = 0.024 \pm 0.0009 \quad \text{and} \quad \Omega_M h^2 = 0.135^{+0.008}_{-0.009}, \tag{2.21}$$

yielding a *Cold Dark Matter abundance preferred range*, at the $2-\sigma$ level, of

$$0.095 < \Omega_{\rm CDM} < 0.129. \tag{2.22}$$

This range will be the reference estimate for the Dark Matter abundance in the Universe which will be used throughout this thesis.

2.4 The Dark Matter problem

In view of the overwhelming evidence for a dominating non-baryonic matter component, a urgent issue regards the particle physics nature of the Dark Matter elementary constituent. As a first remark, let us mention the possibility that some of the evidences for Dark Matter may in principle be ascribed to a modification of the gravitational interactions outside the scales which have been directly probed by experiments (essentially within the Solar System range). Though it is in principle possible to find phenomenological modifications to gravity in order to accomodate some of the mentioned evidences for Dark Matter into a standard baryonic matter scenario (for instance galaxy rotational curves), the lack of fully consistent theory alternative to general relativity, and the wide range of scales over which evidences for Dark Matter are spread, makes it hard to envisage this scenario.

A suitable particle physics candidate for Dark Matter χ should fulfill a list of requirements, dictated by cosmology, astrophysical observations and Dark Matter detection experiments:

1. The cosmological abundance of the species χ must lie in the range dictated by Eq. (2.22), *i.e.* $\Omega_\chi h^2 \simeq 0.11$;

2. The particle must not be a baryon;

3. The species χ must be electrically and color neutral; strong and electromagnetically interacting particles would become bound with normal matter forming anomalously heavy isotopes. Very strong upper limits exist on the abundances, relative to hydrogen, of nuclear isotopes, [28]

$$n/n_H \lesssim 10^{-15} \div 10^{-29} \quad \text{for} \quad 1 \text{ GeV} \lesssim m_\chi \lesssim 1 \text{ TeV}. \tag{2.23}$$

   Since a strongly interacting stable relic is expected to have an abundance $n/n_H \lesssim 10^{-10}$, with a higher abundance for charged particles, we conclude that a good DM candidate must be, over a wide mass range, at most *weakly interacting* with matter.

This set of requirements entails that the only plausible Dark Matter candidate *within the Standard Model* is the neutrino, which, at least, features the "undisputed virtue to exist" [2]. However, combining the well-known estimate of the neutrino relic abundance

$$\Omega_\nu h^2 = \sum_{i=1}^{3} \frac{m_i}{93 \text{ eV}} \tag{2.24}$$

with upper limits on the neutrino masses from tritium β-decay,

$$m_\nu < 2.05 \text{ eV} \quad (95\% \text{ C.L.}) \tag{2.25}$$

shows that neutrinos may at best be a subdominant Dark Matter component. Moreover, combined CMB and large scale structure data further restrict the possible amount of Hot Dark Matter composed by neutrinos all the way down to

$$\Omega_\nu h^2 < 0.0067. \tag{2.26}$$

The bottom line is therefore that *the existence of Dark Matter requires physics beyond the Standard Model.* We will not enter here into the blooming garden of more or less exotic particle Dark Matter candidates; we simply state that the minimal supersymmetric extension of the Standard Model is perhaps the best motivated particle physics framework beyond the SM, and provides an ideal candidate for Cold Dark Matter, the lightest neutralino, to whom the remainder of this thesis is devoted.

Chapter 3

The supersymmetric extension of the Standard Model

The Standard Model (SM) of particle physics is a remarkably successful effective theory, whose predictions have been verified (with the possible caveat of the Higgs boson discovery) to a very high degree of precision at all past accelerator experiments, and particularly at the electron-positron collider LEP II at CERN. Any field theory which aims to play the role of an extension of it must then first of all *reproduce* the correct and accurate SM predictions, and encompass, therefore, the observed SM particles and field content, as well as its gauge group structure. Moreover, new physics contributions and corrections to SM precision measurements must naturally be compatible with experimental results. Finally, novel predictions of any extension of the SM, like, in the case of supersymmetric theories with conserved R parity (see below), the relic abundance of the lightest species, must be consistent with available astrophysical data.

The minimal supersymmetric extension of the standard model (MSSM) is the supersymmetric theory, with $\mathcal{N} = 1$ supersymmetry (SUSY) generators, constructed in order to account, with the *minimal possible field content*, for all the SM fields, as well as for the most general set of soft SUSY breaking (SSB) terms which do not explicitly violate lepton and baryon numbers. Since SUSY is a broken symmetry at low energies, the SSB lagrangian, on which we will detail in what follows, constitutes a complete parameterization, in terms of all the possible regularizable operators, of the still unknown mechanism of SUSY breaking.

Being a symmetry relating bosons and fermions, the MSSM *doubles* the quantum field degrees of freedom of the SM, attributing bosonic and fermionic (super-)partners to fermionic and bosonic SM fields. Anomaly cancellation and the superpotential Yukawa structure force, moreover, the introduction of a second Higgs doublet, instead of the single one appearing in the SM.

We will not review here the general construction of the MSSM, referring the reader to some of the existing excellent reviews on the topic (see *e.g.* [29–32]); we will instead concentrate on:

1. the *structure* which defines the MSSM, *i.e.* its *particle content*, its *superpotential* and its *SSB lagrangian*: these three pieces of information fully determine the MSSM parameter space;

2. the neutralino sector, which will be widely investigated in what follows as regards its phenomenological implications.

Sec. 3.2 deals with the numerous constraints on the phenomenology of SUSY models coming from both direct sparticle and Higgs searches at accelerators such as LEP or Tevatron,

Normal particles/fields		Supersymmetric partners			
		Interaction eigenstates		Mass eigenstates	
Symbol	Name	Symbol	Name	Symbol	Name
$q = d, c, b, u, s, t$	quark	$\tilde{q}_L$, $\tilde{q}_R$	squark	$\tilde{q}_1$, $\tilde{q}_2$	squark
$l = e, \mu, \tau$	lepton	$\tilde{l}_L$, $\tilde{l}_R$	slepton	$\tilde{l}_1$, $\tilde{l}_2$	slepton
$\nu = \nu_e, \nu_\mu, \nu_\tau$	neutrino	$\tilde{\nu}$	sneutrino	$\tilde{\nu}$	sneutrino
g	gluon	$\tilde{g}$	gluino	$\tilde{g}$	gluino
$W^\pm$	W-boson	$\tilde{W}^\pm$	wino	$\tilde{\chi}^\pm_{1,2}$	chargino
H^-	Higgs boson	$\tilde{H}_1^-$	higgsino		
H^+	Higgs boson	$\tilde{H}_2^+$	higgsino		
B	B-field	$\tilde{B}$	bino	$\tilde{\chi}^0_{1,2,3,4}$	neutralino
W^3	W^3-field	$\tilde{W}^3$	wino		
H_1^0	Higgs boson	$\tilde{H}_1^0$	higgsino		
H_2^0	Higgs boson	$\tilde{H}_2^0$	higgsino		
H_3^0	Higgs boson				

Table 3.1: *The 'normal' particles and their superpartners in the MSSM, adapted from Ref. [33].*

and from SUSY contributions to rare quark decays (such as $b \to s\gamma$) or to the muon anomalous magnetic moment δa_μ. When considering a given SUSY setup, one must naturally be consistent with all the bounds we review here. The last part of the chapter, Sec. 3.3 focuses on two different and complementary approaches to the investigation of the SUSY parameter space, a top-down and a bottom-up attitude. Concerning the latter, we provide details on a phenomenological scan of the SUSY parameter space in Sec. 3.3.1

3.1 Structure of the MSSM

It is beyond the scopes of the present introduction to describe the superfield formalism, which will be used to write down the superpotential and the soft breaking lagrangian of the MSSM. The reader is again referred to [29–32] for details.

As stated above, the field content of the MSSM consists of the superfields associated with each field of the SM, plus an additional Higgs doublet. The fermionic superpartners fields are named after their bosonic counterpart plus a suffix *-ino*: the superpartners of the gauge bosons W^i, B and g will be called *winos* $\widetilde{W}^i$, *bino* $\widetilde{B}$ and *gluino* $\widetilde{g}$, while those of the Higgs bosons $H^i_{1,2}$ will be indicated as *higgsinos* $\widetilde{H}^i_{1,2}$. After electroweak symmetry breaking, the listed fermionic states with the same quantum numbers *mix*, and the resulting mass eigenstates are called *neutralinos*, if possessing zero electric charge, and *charginos*, if featuring a non vanishing electric charge. Scalar counterparts of the fermions get instead the prefix *s-*. We list in Tab. 3.1 the particle content of the MSSM, including both the interaction and mass eigenstates.

The Lagrangian of theories with $\mathcal{N} = 1$ SUSY in four dimensions is fully singled out once three functions of the superfield matter content are specified: (i) the gauge kinetic function f, (ii) the Kähler potential K, and (iii) the superpotential W. Low energy effective theories, like the MSSM, are defined to feature canonical kinetic terms, and renormalizable couplings only. In this respect, general recipes exist to build the SUSY Lagrangian, and the only part which need to be explicitly detailed is the superpotential W [34].

As regards the MSSM, the superpotential can be written, as a function of the superfields corresponding to $SU(2)$ singlet and doublet leptons ($\hat{\mathbf{e}}$, $\hat{\mathbf{l}}$), quarks ($\hat{\mathbf{q}}$, $\hat{\mathbf{u}}$, $\hat{\mathbf{d}}$) and to the two up and down type Higgses ($\hat{H}_{1,2}$), as

$$W = \epsilon_{ij}\left(-\hat{\mathbf{e}}^*_R \mathbf{Y}_E \hat{\mathbf{l}}^i_L \hat{H}^j_1 - \hat{\mathbf{d}}^*_R \mathbf{Y}_D \hat{\mathbf{q}}^i_L \hat{H}^j_1 + \hat{\mathbf{u}}^*_R \mathbf{Y}_U \hat{\mathbf{q}}^i_L \hat{H}^j_2 - \mu \hat{H}^i_1 \hat{H}^j_2\right), \tag{3.1}$$

where i and j are $SU(2)$ indexes and Y are the Yukawa coupling 3×3 matrices in flavor space (generation indexes have been omitted). Additional renormalizable superpotential terms, which violate lepton L or baryon B number, are in principle allowed by gauge invariance. Combinations of such couplings, which would lead to rapid proton decay, must be somehow suppressed. A common assumption is to impose a discrete symmetry, dubbed R or matter parity, acting as a multiplicative quantum number defined as

$$R \equiv (-1)^{3B+L+2s}, \tag{3.2}$$

where s denotes the spin of the particle. SM particles feature $R = 1$, while their superpartners (sparticles) $R = -1$. R parity conservation leads to the superpotential of Eq. (3.1), and, as a welcome byproduct, to the stability of the *lightest supersymmetric particle* (LSP), since sparticles can only decay into an odd number of sparticles. In this thesis we will always assume R parity conservation (see *e.g.* Ref. [35] for a recent review on R particle violating SUSY models phenomenology).

SUSY must be a broken symmetry, since exact SUSY would dictate that every superpartner is degenerate in mass with its SM partner, a possibility which is decisively ruled out by negative experimental searches. Not surprisingly, the mechanism of SUSY breaking is not yet understood (much like the EW symmetry breaking was the last thing to be understood in the SM, assuming it is!). SUSY may be *explicitly broken*, avoiding to spoil its attractive field theoretical features, provided the breaking is *soft*, *i.e.* it includes all possible renormalizable terms which do not introduce quadratic divergences to any order in perturbation theory. The most general MSSM soft breaking lagrangian reads [34]

$$\begin{aligned}
\mathcal{L}_{\text{soft}} \;=\; & \epsilon_{ij}\Big(\tilde{\mathbf{e}}^*_R \mathbf{A}_E \mathbf{Y}_E \tilde{\mathbf{l}}^i_L H^j_1 + \tilde{\mathbf{d}}^*_R \mathbf{A}_D \mathbf{Y}_D \tilde{\mathbf{q}}^i_L H^j_1 - \tilde{\mathbf{u}}^*_R \mathbf{A}_U \mathbf{Y}_U \tilde{\mathbf{q}}^i_L H^j_2 + \text{h.c.}\Big) \\
& -\epsilon_{ij}\Big(B\mu H^i_1 H^j_2 + \text{h.c.}\Big) \\
& + H^{i*}_1 m^2_1 H^i_1 + H^{i*}_2 m^2_2 H^i_2 + \tilde{\mathbf{q}}^{i*}_L \mathbf{M}^2_Q \tilde{\mathbf{q}}^i_L + \tilde{\mathbf{u}}^*_R \mathbf{M}^2_U \tilde{\mathbf{u}}_R + \tilde{\mathbf{d}}^*_R \mathbf{M}^2_D \tilde{\mathbf{d}}_R \\
& + \tilde{\mathbf{l}}^{i*}_L \mathbf{M}^2_L \tilde{\mathbf{l}}^i_L + \tilde{\mathbf{e}}^*_R \mathbf{M}^2_E \tilde{\mathbf{e}}_R \\
& + \frac{1}{2} M_1 \tilde{B}\tilde{B} + \frac{1}{2} M_2 \left(\tilde{W}^3 \tilde{W}^3 + 2\tilde{W}^+ \tilde{W}^-\right) + \frac{1}{2} M_3 \tilde{g}\tilde{g}.
\end{aligned} \tag{3.3}$$

The first line corresponds to *soft trilinear scalar interactions*, the second to *soft bilinear scalar interactions*, the third and fourth lines to *scalar mass-squares* and the last to *gaugino soft breaking masses*.

The SUSY spectrum can be deduced through a standard procedure from the various particles mass matrices originating from the superposition of all the contributions appearing in the Lagrangian terms which have been collected above. In the context of Dark Matter studies, crucial phenomenological features stem in particular from the *composition* of neutralinos in terms of their interaction eigenstates, which we therefore shortly review here for the benefit of clarity. Neutralinos are defined as the mass eigenstates of the superposition of the fermionic partners of the gauge and Higgs bosons. In the basis $(\tilde{B}, \tilde{W}_3, \tilde{H}^0_1, \tilde{H}^0_2)$, the mass matrix is given by

$$\mathcal{M}_{\tilde{\chi}^0} = \begin{pmatrix} M_1 & 0 & -\frac{g' v_1}{\sqrt{2}} & +\frac{g' v_2}{\sqrt{2}} \\ 0 & M_2 & +\frac{g v_1}{\sqrt{2}} & -\frac{g v_2}{\sqrt{2}} \\ -\frac{g' v_1}{\sqrt{2}} & +\frac{g v_1}{\sqrt{2}} & 0 & -\mu \\ +\frac{g' v_2}{\sqrt{2}} & -\frac{g v_2}{\sqrt{2}} & -\mu & 0 \end{pmatrix}, \tag{3.4}$$

where $v_{1,2}$ are the vacuum expectation values of the $H_{1,2}$ Higgs doublets. Additional contributions to the tree level mass matrix of Eq. (3.4) originate from loop corrections, the most

important entries being those in positions (3,3) and (4,4) in the matrix (3.4) [33]. The neutralino mass matrix can be diagonalized, providing the mass eigenstates, the four neutralinos, which can be expressed as

$$\tilde{\chi}_i^0 = N_{i1}\tilde{B} + N_{i2}\tilde{W}^3 + N_{i3}\tilde{H}_1^0 + N_{i4}\tilde{H}_2^0. \tag{3.5}$$

The lightest neutralino, $\tilde{\chi}_1^0$, that will be indicated as *the* neutralino, χ, is a suitable candidate particle for Dark Matter provided it is also the lightest sparticle in the low energy SUSY spectrum (as it is the case in large portions of the parameter space of the most studied models, like those we mentioned above).

We define *bino fraction* of the lightest neutralino the quantity $|N_{11}|$, *wino fraction* the quantity $|N_{12}|$, and finally *higgsino fraction* the quantity $\sqrt{|N_{13}|^2 + |N_{14}|^2}$.

The mass matrix for the charged Higgs and gauge boson superpartners

$$\mathcal{M}_{\tilde{\chi}^\pm} = \begin{pmatrix} M_2 & gv_2 \\ gv_1 & \mu \end{pmatrix}, \tag{3.6}$$

provides, instead, the chargino composition and mass spectrum. If the lightest neutralino is wino-like, *i.e.* if it has a dominant wino fraction, it is also approximately degenerate in mass with the lightest chargino; analogously, if it is higgsino-like, there will be a quasi-degeneracy both with the next-to-lightest neutralino and with the lightest chargino. This spectral feature yields important consequences at both the level of relic abundance computations (see Sec. 4) and at the level of SUSY searches at future accelerators (see *e.g.* [36, 37]).

3.2 Particle physics constraints on SUSY models

The search for SUSY has since long been one of the scientific purposes of many accelerator experiments. There are essentially two ways for looking at SUSY at particle colliders: on the one hand, one can directly search for SUSY particles production, the main limitation being the energy reach of colliders; on the other hand, SUSY often non-negligibly contributes to rare processes, and a significant deviation of the rates from the SM predictions may be interpreted as a clue towards the occurrence of SUSY loop effects. In the first category, moreover, also enters the search for the lightest CP even neutral Higgs, whose mass can be determined given a certain SUSY model. This yet unseen particle, in fact, phenomenologically behaves, over most of SUSY parameter space, quite similarly to the SM Higgs. Negative searches for the SM Higgs can thus be rephrased as a constraint on SUSY models predicting a light Higgs boson.

We briefly collect here the existing accelerator constraints on SUSY phenomenology.

- *Invisible Z width*

  If SUSY particles $\tilde{P}$ are lighter than half the mass of the Z boson, the latter can invisibly decay into them with a non-zero branching fraction. Of course, there is a substantial background to these events, namely $Z \to \nu\bar{\nu}$ decays, but still the analysis of LEP2 finds that a decay width of $\Gamma_{Z\to\tilde{P}\tilde{P}} < 4.2$ MeV is required. This bound excludes, for instance, sneutrinos with masses above 43 GeV.

- *New Charged Particles*

  LEP2 has put very stringent bounds on charged particles lighter than about 100 GeV. In e^+e^- colliders, in fact, cross sections for the direct pair production of charged particles are quite large, allowing for limits to be placed at, or slightly below, half the center-of-mass energy of the collision. At LEP2, which reached a center-of-mass energy of

209 GeV, chargino were constrained to have a mass larger than 103 GeV, while for charged sleptons the bounds obtained were respectively $m_{\tilde{e}} > 99$ GeV, $m_{\tilde{\mu}} > 96$ GeV, and $m_{\tilde{\tau}} > 87$ GeV. If the LSP is only slightly more massive than one of the mentioned charged particles, however, these limits may be substantially lowered. Limits from charged sleptons may be indirectly used to bound the mass of sneutrinos, when the $SU(2)$ symmetry between the SSB masses of sneutrinos and left-handed sleptons is used. This entails, in particular, a limit on the sneutrino mass of $m_{\tilde{\nu}} > 85$ GeV. Moreover, if one assumes particular relations among the SSB entering the neutralino mass matrix, the limit on the chargino mass can also be translated into a limit on the lightest neutralino mass. Namely, assuming the so called GUT relation between the SSB gaugino masses M_1 and M_2, one obtains $m_\chi \gtrsim 50$ GeV.

- *New Colored Particles*

  Hadron colliders, such as the Tevatron, can place the strongest limits on colored particles, like squarks and gluinos. Such particles should undergo a series of cascade decays, and mass limits can be put searching for jets and missing energy signatures. The negative search results are often shown as exclusion contours in the squarks-gluino mass plane. Notice however that the spectrum of particles lighter than the colored ones is critical in placing limits on the masses of the latter. The limits we use for these particles are reported in Tab. 3.3.

- *Higgs Searches*

  In SUSY models, the Higgs mass is increased from its tree level value (below m_Z) by loop processes involving superparticles, most importantly top squarks. Current bounds on the lightest Higgs mass, therefore, constrain the masses of top squarks and other superparticles. Furthermore, predictions exist that if SUSY features a mass spectrum below 1 TeV, the Higgs mass should be less than 130 GeV, not very far from the current limits from LEP2, $m_h > 114.1$ GeV. The SM Higgs boson mass limit can be reliably used at low values of $\tan\beta$, while at larger values, or if the mixing α in the SUSY Higgs sector is large, less stringent bounds should be applied.

- $b \to s\gamma$

  Within SUSY models with minimal flavor violation the decay $b \to s\gamma$ proceeds through the $\tilde{t}\tilde{W}$ and tH^+ loops, in addition to the SM contribution from the tW loop. The branching fraction $BF(b \to s\gamma)$ has been measured by the BELLE, ALEPH, and CLEO collaborations. A weighted averaging of these measurements of $B \to X_s\gamma$ decays at CLEO and BELLE leads to bounds on the branching ratio $b \to s\gamma$. The mentioned constraint is particularly strong if the mentioned SUSY contributions positively interfere, and if the value of $\tan\beta$ is large.

- $B_s \to \mu^+\mu^-$

  The branching fraction $B_s \to \mu^+\mu^-$ is quite small in the SM ($\simeq 3.5 \times 10^{-9}$) Though the contribution from SUSY to this rare decay scales as $\tan^6\beta$, and thus may become quite large for models with large values of $\tan\beta$, current sensitivity does not constrain significantly the SUSY parameter space. In run I, Tevatron found a value for this rare decay which is compatible with the SM expectation. The sensitivity of run II is however expected to be considerably larger, and therefore this rare process may soon become more competitive as a constraint on SUSY models.

- *Anomalous magnetic moment of the muon* δa_μ

The deviation δa_μ of the muon anomalous magnetic moment a_μ from its predicted value in the Standard Model can be interpreted as arising from SUSY contributions, δa_μ^{SUSY}, mainly given by neutralino-smuon and chargino-muon sneutrino loops. The BNL E821 experiment recently delivered a high precision measurement (0.7 ppm) of $a_\mu^{\rm exp} = 11659203(8) \times 10^{-10}$. The theoretical computation of the SM prediction is however still plagued by the problem of estimating the hadronic vacuum polarization contribution. In particular, there is a persisting discrepancy between the calculations based on the τ decay data and those based on low-energy e^+e^- data. Recent evaluations [38, 39] give the following range for the deviation of the SM value of a_μ from the experimental one:

$$a_\mu^{exp} - a_\mu^{SM} = (35.6 \pm 11.7) \times 10^{-10} \quad (e^+ e^-) \tag{3.7}$$

$$a_\mu^{exp} - a_\mu^{SM} = (10.4 \pm 10.7) \times 10^{-10} \quad (\tau \text{ decay}) \tag{3.8}$$

A very low SUSY particle spectrum may be easily ruled out, even while resorting to a conservative approach to the interpretation of the above mentioned results; nevertheless, SM theoretical uncertainties and the entangled experimental situation recommend that caution must be used in drawing severe constraints from SUSY corrections to this quantity.

- *Electroweak Precision Measurements*

  Various limits on the scale of new physics have been derived from the impressively accurate electroweak (EW) measurements performed at LEP2, Tevatron and other experiments. Though dramatically important for other theories beyond the standard model, the strongest constraint from EW precision measurements on SUSY phenomenology, namely the value of the ρ parameter, is always found to be weaker than the other bounds mentioned above.

We discuss in sec. 3.3.1 the *statistical relevance* of the mentioned constraints on the general MSSM parameter space. We just quote here that the strongest requirements are those from direct particle searches and from the $b \to s\gamma$ decays, while the others (like δa_μ) only marginally constrain the parameter space. We also provide an analysis of the *predictions* for m_h, $b \to s\gamma$ and δa_μ within all viable SUSY models we considered in the MSSM parameter space scan we resorted to.

3.3 The SUSY parameter space: "chance and necessity"

After global rephasing of the fields, the most general MSSM lagrangian contains 124 entries to be determined by the experiment, including the SM parameters. It is rather easy to figure out the difficulties related to tackling a theory which features such a large number of physical variables, which, in principle, are allowed to take values on extremely wide ranges, compatibly with the available constraints reviewed in the preceding Section. One is, *de facto*, left with two possible, and not rarely complementary, kinds of attitudes:

- **Top-down Approach** (*necessity*): a first possibility is to make a sufficient number of assumptions on the parameter space, typically motivated by a theoretical framework, or by particular physical scenarios (most often regarding the SUSY breaking mechanism), and to end up with a reduced set of parameters; the latter may be defined either at some high energy scale, where enhanced symmetries are supposed to exactly hold, or at the low energy scale, being it that of SUSY particles masses or that of the electroweak symmetry breaking.

- **Bottom-Up Approach** (*chance*): on the other hand, a second plausible procedure is to single out the parameters which physically affect the phenomenology one wants to study, and try to scan over the largest possible set of models, in order to explore the most complete range of experimental outcomes compatible with the theory. An appealing possibility, relying on a naturalness argument, is to resort to a statistically based survey, where one tries to figure out which is the most "natural" result for a given experiment assessing its statistical relevance on a random scan of the viable space of parameters. To be as model independent as possible, in this second approach the parameters ought to be defined at a low energy scale, in order to avoid uncertainties related to the Renormalization Group evolution of the involved quantities.

Along the top-down approach, in the remainder of this thesis work we will often make reference to specific high energy frameworks, namely *minimal supergravity* (mSUGRA) [40, 41] and the *minimal anomaly mediated SUSY breaking scenario* (AMSB) [42–45], which, for the sake of clarity, we briefly review here.

In mSUGRA, the boundary conditions at the grand unification scale ($M_{\rm GUT}$) are defined requiring gauge coupling unification and a gaugino soft breaking unified mass equal to $M_{1/2}$ at $M_{\rm GUT}$, as well as the universality of sfermions and Higgs mass terms, all set to a common value m_0, again set at $M_{\rm GUT}$, *i.e.*

$$m_1 = m_2 = m_0 \qquad \mathbf{M}_Q^2 = \mathbf{M}_U^2 = \mathbf{M}_D^2 = \mathbf{M}_L^2 = \mathbf{M}_E^2 = m_0^2\mathbf{I}. \tag{3.9}$$

Finally, universality of trilinear couplings is also assumed at the unification scale,

$$\mathbf{A}_E = \mathbf{A}_U = \mathbf{A}_D = A_0\mathbf{I}. \tag{3.10}$$

Requiring proper electroweak radiative symmetry breaking, and indicating with $\tan\beta$ the ratio of the up and down type Higgs vevs, one is then left with a theory defined by a set of four parameters and one sign,

$$\tan\beta,\ M_{1/2},\ m_0,\ A_0,\ \mathrm{sign}\mu. \tag{3.11}$$

The low energy phenomenology is then dictated by the resulting SSB terms as derived through RG running down at the electroweak scale, or at some low energy scale $M_{\rm SUSY}$. One of the consequences of the assumed gaugino universality at the GUT scale, is that $M_2 \sim 0.4\ M_1 \sim M_{1/2}$, *i.e.* the mSUGRA ligthest neutrlaino cannot be wino-like.

The AMSB scenario is motivated by the possible dominance of SUSY breaking contributions originating in the super-Weyl anomaly, which are always present when SUSY is broken [43]. When the SUSY breaking and the visible sector reside on different branes, sufficiently separated in a higher dimensional space, gravity contributions can in fact be strongly suppressed [42]. In this case, the resulting soft parameters are *UV insensitive*, and can be expressed in terms of low energy entries, such as the Yukawa and gauge couplings and the gravitino mass, $m_{3/2}$. For instance, the gaugino spectrum is given by

$$M_i = \frac{\beta_{g_i}}{g_i} m_{3/2}, \tag{3.12}$$

where β_{g_i} indicate the beta functions of the g_i coupling, $i = 1, 2, 3$. This yields a specific relationship in the low energy gaugino mass spectrum, namely

$$M_1 : M_2 : M_3 = 2.8 : 1 : 7.1, \tag{3.13}$$

which reverse the mSUGRA hierarchy between the bino and wino soft breaking masses. A further universal scalar mass m_0 is postulated to cure tachyonic sfermions, and radiative electroweak symmetry breaking is required, thus yielding an overall parameter space consisting of the following set

$$\tan\beta,\ m_{3/2},\ m_0,\ \mathrm{sign}\mu. \tag{3.14}$$

In the remainder of this thesis we will discuss various aspects of the phenomenology of the AMSB scenario (see also [44, 45] for early studies on this topic).

Regarding the bottom-up attitude, we review here the general MSSM parameter space scan we carried out in Ref. [46], to which we will often refer in the following analysis of SUSY Dark Matter properties (see in particular Sec. 5).

3.3.1 A phenomenological scan of the MSSM parameter space

Many of the parameters of the soft breaking lagrangian $\mathcal{L}_{soft}$ of Eq. (3.3) are severely constrained because they would imply FCNC or CP violating effects at a rate which is already ruled out by the experiments. For simplicity, we will assume, as usually done in the literature, that all soft parameters are real, so that supersymmetry breaking does not introduce new sources of CP violation. To suppress potentially dangerous FCNC, we will set to zero all off-diagonal elements in the sfermions masses, and assume that the first and second generation of squarks are degenerate (for a recent discussion see [47]). Squarks masses therefore have the form

$$m^2_{\tilde{Q}} = \begin{pmatrix} m_q^2 & & \\ & m_q^2 & \\ & & m^2_{Q3} \end{pmatrix},\ m^2_{\tilde{u}} = \begin{pmatrix} m_q^2 & & \\ & m_q^2 & \\ & & m^2_{u3} \end{pmatrix},\ m^2_{\tilde{d}} = \begin{pmatrix} m_q^2 & & \\ & m_q^2 & \\ & & m^2_{d3} \end{pmatrix}, \tag{3.15}$$

with m_q^2, m^2_{Q3}, m^2_{u3} and m^2_{d3} arbitrary numbers. Slepton masses, on the other hand, contain three independent entries each.

The trilinear couplings A_t, A_b, A_τ and A_μ are allowed to have both signs. All other trilinear couplings are neglected[1]. Gaugino masses are independent of one another, and negative values for M_2 are also considered. The remaining low energy parameters we take into account are $\tan\beta$, μ and m_A, the mass of the pseudo-scalar Higgs boson.

We scan the resulting 20-dimensional parameter space using a *uniform probability distribution*. $\tan\beta$ takes values between 2 and 50, whereas all mass parameters are generated in the interval $(50\,\mathrm{GeV}, 5\,\mathrm{TeV})$ possibly with both signs, according to Table 3.2. From this set of low energy parameters, one can determine the mass spectra and mixing matrices of the superparticles.

Once the full particle spectrum has been determined, the resulting model must be consistent with the particle physics constraints we outlined in Sec. 3.2, and must give rise to a relic particle abundance compatible with astrophysical observations. We applied the following phenomenological constraints:

- *The spectrum:* The presence of non-zero trilinear couplings could give rise to tachyonic sfermions, so the first consistency requirement we ask is to exclude all such unphysical models.

- *Neutralino LSP:* In the MSSM the lightest supersymmetric particle is stable and therefore must be an electrically neutral and not strongly interacting particle [28]. Since the sneutrino, in the MSSM, has been shown not to be a suitable Dark Matter candidate [48], the only possibility we are left with is the lightest neutralino. We therefore also require the LSP to be the lightest neutralino.

[1] We include A_μ for its relevance in the computation of $(g-2)_\mu$.

Name	# of parameters	Symbol	Range
Gluino and Bino Masses	2	M_1,M_3	(50 GeV, 5 TeV)
Wino Mass	1	M_2	$\pm$ (50 GeV, 5 TeV)
Left-handed slepton masses	3	$m_{\tilde{l}_i}$	(50 GeV, 5 TeV)
Right-handed slepton masses	3	$m_{\tilde{e}_i}$	(50 GeV, 5 TeV)
1st and 2nd family squark masses	1	m_q	(50 GeV, 5 TeV)
3rd family squark masses	3	$m_{\tilde{u}_3}$,$m_{\tilde{d}_3}$,$m_{\tilde{Q}_3}$	(50 GeV, 5 TeV)
Third family trilinear couplings	3	A_t, A_b, A_τ	($-$5 TeV, 5 TeV)
Pseudo-scalar Higgs boson mass	1	m_A	(50 GeV, 5 TeV)
Muon trilinear coupling	1	A_μ	($-$5 TeV, 5 TeV)
μ	1	μ	$\pm$(50 GeV, 5 TeV)
$\tan\beta$	1	$\tan\beta$	(2, 50)
Total	20		

Table 3.2: List of the MSSM parameters taken into account in our scan, and their allowed range of variation.

- $b \to s\gamma$: We require
$$2 \times 10^{-4} \leq BR(b \to s\gamma) \leq 4.6 \times 10^{-4}. \tag{3.16}$$
The calculation of $BR(b \to s\gamma)$ is carried out with the latest release of the `micrOMEGAs` package [49], which includes an improved NLO and the charged Higgs contributions as well as a beyond-to-leading-order treatment of large $\tan\beta$ effects.

- *Direct Accelerator Searches*: We also take into account the limits derived from the unsuccessful searches for supersymmetric particles and the Higgs boson. In Table 3.3 we detail on the mass limits we impose on each SUSY particle.

Name	Mass Limit (GeV)
Charginos	103.5
sneutrinos	43.0
charged sleptons	95.0
sbottoms	91.0
stops	86.4
other squarks	100.0
gluino	195.0
Higgs boson	114.0
Pseudoscalar Higgs boson	85.0

Table 3.3: Mass limits

- *Relic density*: Finally, we require that the neutralino relic density lies below the WMAP $2-\sigma$ upper bound [6],
$$\Omega_{DM}h^2 \leq 0.13. \tag{3.17}$$
The WMAP lower bound ($\Omega_{DM}h^2 \geq 0.09$) is not imposed since it may well be that neutralinos are only a subdominant Dark Matter component.

We *quantify* the effectiveness of the different constraints mentioned above in Fig. 3.1. A given color for a given requirement correspond to a successive reduction of the considered

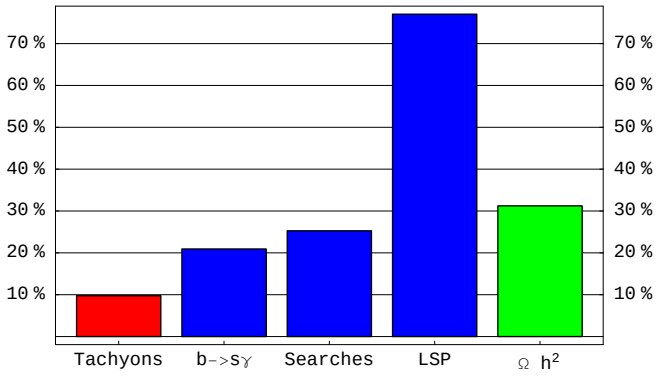

Figure 3.1: *Effectiveness of the different constraints imposed on supersymmetric models.*

sample, in a tree structure. The red column refers to the relative effectiveness over the whole sample, the blue columns to those models *surviving* the red constraint, and the green one to those surviving the blue one. We see that 10% of all models contain a tachyon; of the remaining models, 20% are ruled out by the $b \to s\gamma$ constraint, 25% are excluded by direct searches and almost 80% contain a LSP different from a neutralino. Finally, 30% of the models which are not excluded by any of the previous tests give rise to a neutralino relic abundance larger than the WMAP upper bound. The surviving models will be called *viable*, and are the only ones we considered in the statistical analysis of Dark Matter detection methods. Our sample consists, overall, of 10^5 viable models.

Chapter 4

The dawn of the Darkness: Neutralino relic abundance

The present chapter is devoted to various aspects of the computation of the neutralino Dark Matter relic abundance, from the general theory to the particularly relevant case of the so-called *coannihilation processes* (Sec. 4.1). We give two detailed and motivated examples of the latter phenomenon in Sec. 4.1.1 and 4.1.2. The case of resonant neutralino annihilation is briefly discussed in Sec. 4.2. The last section is finally devoted to the case where a non-standard cosmology dramatically affects the neutralino relic abundance; motivated by the recent observational evidences (see Sec. 2), we will namely focus on *Quintessential* cosmologies, where a homogeneous dynamical scalar field ϕ plays, today, the role of the apparently mandatory Dark Energy component (Sec. 4.3).

A stable (or sufficiently long lived) weakly interacting massive particle (WIMP), produced in the Early Universe, yields, today, a relic abundance fixed by the details of the dynamics of the expansion of the Universe and of the interaction (and therefore annihilation) rates of the particle itself. The equilibrium number density reads

$$n_\chi^{\rm eq} = \frac{g}{(2\pi)^3}\int f(\mathbf{p}){\rm d}^3\mathbf{p}, \tag{4.1}$$

where

$$f(\mathbf{p}) = \frac{1}{e^{E/T}\pm 1}, \qquad E \equiv \sqrt{\mathbf{p}^2+m_\chi^2} \tag{4.2}$$

are the familiar Fermi-Dirac (+) and Bose-Einstein (-) distributions, and g are the WIMP internal degrees of freedom (*i.e.* the number of helicity states). The equilibrium distribution (4.1) is maintained by annihilation processes of χ's into lighter particles l, $\chi\chi \to l\bar{l}$, and vice versa, $l\bar{l} \to \chi\chi$. Shortly after T drops below m_χ the number density of χ's exponentially drops, and the corresponding annihilation rate $\Gamma = \langle\sigma_A v\rangle n_\chi$, where $\langle\sigma_A v\rangle$ is the thermally averaged total annihilation cross section of χ into lighter particles times the relative velocity v, drops below the expansion rate, $\Gamma \lesssim H$. At this point, the χ's cease to annihilate, fall out of equilibrium, and a relic cosmological abundance remains.

The quantitative detailed description of this process relies on the Boltzmann equation, which provides the time evolution of the number density $n_\chi(t)$ of WIMPs,

$$\frac{{\rm d}n_\chi}{{\rm d}t} + 3Hn_\chi = -\langle\sigma_A v\rangle[(n_\chi)^2 - (n_\chi^{\rm eq})^2], \tag{4.3}$$

where

$$H = \frac{1}{a}\frac{{\rm d}a}{{\rm d}t} \tag{4.4}$$

is the Hubble expansion rate, and a is the scale factor of the Universe. The various terms appearing in the equation are easily traced back: the second term on the left hand side accounts for the expansion of the Universe: in absence of annihilation processes (*i.e.* when the right hand side of the equation vanishes), $n_\chi \propto a^{-3}$, diluting as the Universe expands. The right hand side, which vanishes at thermal equilibrium (*i.e.* when $n_\chi = n_\chi^{\rm eq}$), accounts for particle depletion and creation, respectively scaling as the squared of the actual and equilibrium number densities. Once solved Eq. (4.3), the value of the contribution of χ to the critical energy density of the Universe ρ_c, indicated by the quantity $\Omega_\chi \equiv \rho_\chi/\rho_c$, is simply given by

$$\Omega_\chi = m_\chi n_\chi/\rho_c, \quad \rho_c \equiv \frac{3H^2}{8\pi G_N} \tag{4.5}$$

An approximate, quasi analytical approach to Eq. (4.3) consists in expanding $\sigma_A v$ in powers of the squared relative velocity v^2, namely

$$\sigma_A v = a + bv^2 + \cdots . \tag{4.6}$$

The first coefficient comes from s-wave annihilations, while the second from both s and p waves. In most cases, the first two coefficients allow for a fair estimate of the relic abundance, with the approximate expression

$$\Omega_\chi h^2 = 2.82 \times 10^8 \times Y_\infty \ (m_\chi/\text{GeV}), \tag{4.7}$$

where

$$Y_\infty^{-1} = 0.264 g_*^{1/2} M_{\rm Pl} m_\chi \left(a/x_f + 3(b - a/4)/x_f^2\right), \tag{4.8}$$

where $M_{\rm Pl} = 1.22 \times 10^{19}$ GeV indicates the Planck mass, while the quantity g_* represents the number of effective degrees of freedom at the freeze-out temperature $T_f = m_\chi/x_f$, self consistently determined from the equation

$$x_f = \ln[0.0764 M_{\rm Pl}(a + 6b/x_f)c(c+2)m_\chi/(g_* x_f)^{1/2}]. \tag{4.9}$$

The constant $c \simeq 1/2$ is a number chosen with the criterion of optimum agreement with numerical solutions to Eq. (4.3). Important exceptions to the range of applicability of the outlined procedure [1, 50, 51] include:

1. *final state thresholds* (*i.e.* kinematically forbidden channels at $T = 0$ which become relevant at finite temperatures),

2. *coannihilation processes* (*i.e.* cases where there exists a particle slightly heavier than χ which freezes-out at the same epoch when χ decouples), and

3. *resonances* in the annihilation cross section (*i.e.* when the WIMP mass is half the mass of a particle exchanged in an s-channel).

While case 1. only requires a systematic appropriate treatment of final temperature corrections, and relatively marginally affect the final WIMP relic abundance, cases 2. and 3. critically depend on the particle spectrum, and therefore on the parameter space, of a given SUSY model, and may yield substantial variations, even of orders of magnitude, to the naively computed value of Ω_χ. For this reason we devote the following two subsections to a deeper analysis of the latter two cases.

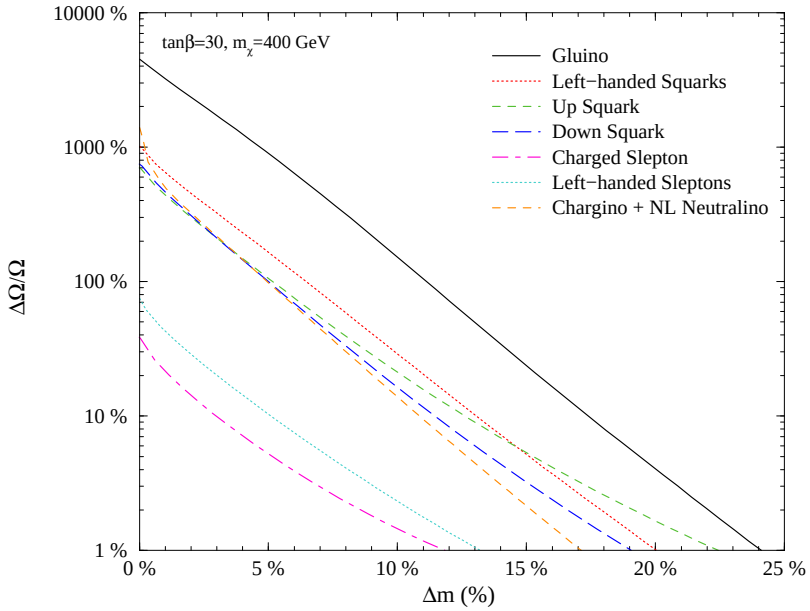

Figure 4.1: *Effectiveness of bino coannihilations in the MSSM: a plot of $\Delta\Omega/\Omega$ as a function of the mass splitting between a bino-line neutralino and all possible coannihilating partners in the MSSM.*

4.1 Coannihilation processes

The thermal history of a generic supersymmetric particle $\widetilde{P}$ heavier than the lightest one, χ, proceeds through initial steps which are analogous to those described above: when its number density begins to exponentially fall when departing from thermal equilibrium, as $T \lesssim m_{\widetilde{P}}$, the species freezes out from the thermal bath, in which both χ and the other lighter particles l are still in equilibrium. Since $\widetilde{P}$ is unstable, it will suddenly decay[1] into χ and l particles. The number density of χ's will however not get affected by these decay, as long as χ is still in thermal equilibrium: $\chi\chi \leftrightarrow l\bar{l}$ processes will in fact efficiently erase any such contributions to n_χ.

A different situation occurs if, say, N particles lie *sufficiently* close, in mass, to the LSP mass (to be quantitative, in most cases this means within at most 50% of the LSP mass, to have non-negligible effects on the neutralino relic abundance). In this case, the freeze-out processes of the N heavier particles $\widetilde{P}_i$ overlaps that of χ. Provided the particle physics model predicts the existence of processes which *couple* the $\widetilde{P}_i$ and χ number densities, the latter must be tracked together. This amounts to replacing, in Eq. (4.3),

$$n_\chi = n_\chi + \sum_{i=1}^{N} n_{\widetilde{P}_i}, \quad n_\chi^{\rm eq} = n_\chi^{\rm eq} + \sum_{i=1}^{N} n_{\widetilde{P}_i}^{\rm eq} \tag{4.10}$$

$$\langle \sigma_A v \rangle = \sum_{i,j} \langle \sigma_{i,j} v \rangle \frac{n_i^{\rm eq}}{n^{eq}} \frac{n_j^{\rm eq}}{n^{eq}} \tag{4.11}$$

where the double sum in Eq. (4.11) runs over all possible annihilation and coannihilation processes. The precise prescription on how to perform the sum in Eq. (4.10) can be found for

[1] Possible exceptions, where heavier SUSY particle lifetimes are not negligible with respect to the time scales of the freeze-out processes in the Early Universe, are given by setups where the LSP is a gravitino or few cases of very high degeneracy of the next-to-LSP with the LSP, which we will not however consider here.

instance in Ref. [52]. Suffices it to say that coannihilation processes may have in general two effects: if the annihilation cross section of coannihilating partners, or the coannihilation cross section, is larger than the annihilation cross section of χ's, the χ freeze-out will be driven by the number density entering the process with the largest cross section. The efficiency of coannihilations with a species $\widetilde{P}$ will however always be exponentially controlled by the ratio

$$\exp[-\Delta_m/T_f], \quad \Delta_m = \frac{m_{\widetilde{P}} - m_\chi}{m_\chi} \tag{4.12}$$

which dictates the amount of $\widetilde{P}$ particles which survive up to the χ freeze-out. On the other hand, as we will explicitly show in Sec. 4.1.2, the occurrence of a coannihilating partner with a less efficient annihilation than that of the other involved species will increase the final relic abundance, in that it will only introduce extra degrees of freedom over which the overall (co-)annihilation cross section of Eq. (4.10) is summed.

The importance of *co-annihilations* was first recognized in the seminal papers of Ref. [50, 51, 53]. Many dedicated studies have since then analyzed the impact of considering various coannihilating partners. In particular, within the framework of mSUGRA, the NLSP is found to be, in the low m_0 region, the lightest stau [52, 54–56]. In the so-called focus point region of mSUGRA, instead, a non-trivial higgsino fraction may give rise to chargino and next-to-lightest neutralino coannihilation processes, see *e.g.* [52, 57–59]. Again within mSUGRA, at large scalar trilinear couplings, it may well be that the next-to-LSP is the stop, whose coannihilations were considered in [52, 60, 61]. Minimal deviations from the assumed universality of scalar SSB terms have been shown to lead to other viable coannihilating partners: for instance, lowering the scalar SSB mass of particles belonging to the **5** representation of $SU(5)$ (namely the $SU(2)$ lepton doublet and down-type singlet, $\tilde{\mathbf{l}}$ and $\tilde{\mathbf{d}}$ in the notation of Eq. (3.3)) gives rise to coannihilations with the lightest bottom squark and with the tau sneutrino [62, 63]. Relaxing the assumption of universality at the high energy (grand unification) scale in the Higgs sector may also give rise to sneutrino and other coannihilating partners which are not present in the mSUGRA [64, 65]. Finally, in a recent analysis it has been shown that the strongest coannihilation processes in the MSSM are those with the *gluino*, and that the maximal bino mass is reached precisely in the gluino coannihilation tail [66].

The quantitative effect of including coannihilations in the computation of the relic density of neutralinos has been carried out for particular coannihilating partners, see *e.g.* Ref. [52]. The importance of coannihilations for the neutralino relic abundance computation is easily understood: if the lightest neutralino is wino or higgsino like, then the chargino mass matrix structure dictates the occurrence of a quasi degenerate chargino, and therefore of chargino coannihilations; if, on the other hand, the lightest neutralino is bino-like, then its relic abundance is typically found to be, for masses $m_\chi \gtrsim 100$ GeV, such that $\Omega_\chi \gg \Omega_{\rm CDM}$. Binos then *require* relic density suppression mechanisms, among which a possibility is precisely provided by the occurrence of a coannihilating partner.

In [66] we analyzed the relevant case of *bino* coannihilations with all possible partners, assuming, within an effective low energy MSSM, that all relevant SSB masses are three times larger than the bino mass m_1, except for the particular coannihilating partner mass, which was taken to be close to m_1. The relevant parameter we used was the relative splitting between the bino mass and the mass of the coannihilating particle $m_{\widetilde{P}}$, $\Delta m \equiv (m_{\widetilde{P}} - m_1)/m_1$. The results are mostly independent of both the absolute size of m_1 and of the details of the spectrum of the other SUSY particles. Moreover, the dependence on $\tan\beta$ was found to be not critical.

We show in Fig. 4.1 the relative difference in relic density without and with coannihilations

[52]

$$\frac{\Delta\Omega}{\Omega} \equiv \frac{\Omega_\chi^{\text{no coann}} - \Omega_\chi^{\text{coann}}}{\Omega_\chi^{\text{coann}}}. \tag{4.13}$$

The lower limit on $\Delta\Omega/\Omega$ has been set to 1%, since this is the typical numerical accuracy of the numerical packages we employed to carry out the computations [52, 67]. The plot was taken at a neutralino mass $m_\chi = 400$ GeV and at $\tan\beta = 30$.

From the plot we clearly deduce that gluino coannihilations are the strongest possible bino coannihilation processes in the MSSM, as it might be expected considering the strong gluino-gluino annihilation cross section and the number of final SM states, much larger than that of squarks. Binos can also annihilate with a quasi degenerate wino without altering the bino purity (the same does not hold true for the higgsino, *i.e.* in case $m_1 \simeq \mu$, due to the neutralino mass matrix structure of Eq. (3.4)), and therefore undergo chargino and next-to-lightest neutralino coannihilations. These processes are found to be of the same order of magnitude of those involving up and down squarks (or two of them at the same time). Much more suppressed are, instead, slepton coannihilations.

The statistical analysis of Ref. [46], which was carried out on the scan of the general MSSM parameter space outlined in Sec. 3.3.1, showed some important results for bino-like Dark Matter, which give a snapshot of the importance of coannihilations in a generic SUSY Dark Matter setup. We found in particular that:

1. Among the binos compatible with the *upper* WMAP bound, 91% have at least one coannihilating partner

2. Binos which produce a relic density *within* the WMAP range have a coannihilating partner in 86% of considered cases.

3. The largest bino mass compatible with the WMAP bound, and such that coannihilations are not present, is around 160 GeV.

The next two Sections are devoted to the analysis of two particular setups where different coannihilating partners affect the model parameter space allowed by the requirement of a sufficiently low relic abundance. In Sec. 4.1.1 we consider a minimal deviation from mSUGRA universality in the scalar fermion sector, motivated by $SU(5)$ Grand Unification [62]; in Sec. 4.1.2 we outline and analyze in detail scenarios where coannihilations with gluinos, which we showed above to be the strongest possible coannihilating sparticles, take place [66].

4.1.1 Extended coannihilations in a next-to-minimal mSUGRA scenario with sfermions non-universality

We will analyze here the phenomenology of a class of GUT-inspired mSUGRA models, characterized by the relaxation of the hypothesis of *universality* in the sector of the fermions scalar superpartners (see Sec. 3.1) and by partial (b-τ) Yukawa coupling Unification (YU) at the scale of Grand Unification. These models are motivated by a minimal $SU(5)$ SUSY GUT theory in which the scale of grand unification M_{GUT} lies below the scale M_X where universality is assumed [68] (we will discuss in greater detail the issue SUSY GUTs and their phenomenological consequences in Sec. 6). The $SU(5)$ RG running between M_X and M_{GUT} induces a non-universality in the whole scalar sector (the gaugino sector universality is instead not spoiled by the grand unification running [68]). As regards the sfermions, the multiplet structure of the assumed GUT theory, which collects the particle content into the $\overline{\mathbf{5}}$ (down-type quark $SU(2)$ singlet and lepton doublet) and the **10** (up-type quark and lepton singlets and quark doublet) representations of $SU(5)$, implies for this model the following parameterization for the SSB masses at M_{GUT}:

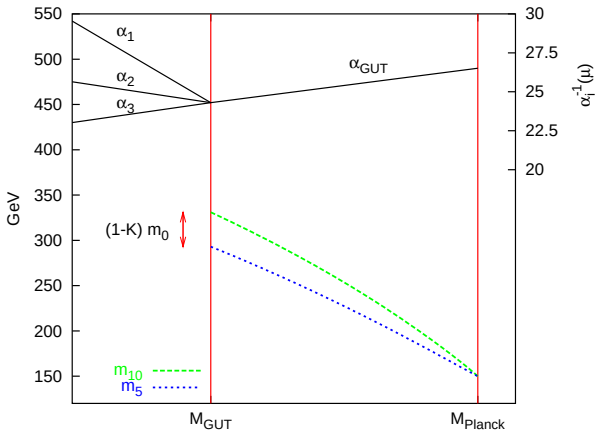

Figure 4.2: *The evolution of the coupling constants and of the SSB masses of the* $\overline{\mathbf{5}}$ *and* $\mathbf{10}$ $SU(5)$ *multiplets for a* $SU(5)$ *SUSY GUT theory with* M_{GUT} *smaller than the scale where scalar universality is assumed (here* $M_{\rm Planck}$*).*

$$m_Q^2 = m_U^2 = m_E^2 \equiv m_{\mathbf{10}}^2 \equiv m_0^2 \tag{4.14}$$

$$m_L^2 = m_D^2 \equiv m_{\overline{\mathbf{5}}}^2 = K^2 m_{\mathbf{10}}^2 \tag{4.15}$$

In Fig. 4.2 we sketch a typical pattern for the running of $m_{\mathbf{10}}^2$ and $m_{\overline{\mathbf{5}}}^2$, compared above with the coupling constants running. Although the full GUT theory would also imply a large non-universality in the Higgs sector and $K \gtrsim 0.7$, we will resort here to a simplification of the model, and let $m_{H_{1,2}}^2 = m_0^2$ in order to concentrate only on the implications of minimal non-universal sfermion masses (mNUSM). We also vary K between 0 and 1 (the latter value reproducing the fully universal case). We therefore generically expect a *lighter spectrum*, with respect to the universal case, for the sparticles belonging to the $\overline{\mathbf{5}}$ representation for $K < 1$.

On top of sfermion non-universality, we also inherit from the original $SU(5)$ SUSY GUT the prediction of b-τ YU. We impose *exact YU* at M_{GUT}, and fix the common Yukawa coupling $h_b = h_\tau(M_{GUT})$ in order to get the right value for $m_\tau(M_Z)$, after including running effects and the SUSY thresholds corrections at $M_{SUSY} \equiv \sqrt{m_{\tilde{t}_1} m_{\tilde{t}_2}}$. The output is $m_b(M_Z)$, which is then required to lie within the properly evolved experimental range [69].

In the context of b-τ YU, the SUSY corrections to the mass of the b quark constrain the allowed $\tan\beta$ range as well as the sign of μ. In fact, the sign of these corrections is given by the sign of μ, and is proportional to $\tan\beta$; since the tree level value of m_b, fixed by the common b-τ Yukawa coupling determined by m_τ, is typically higher than the upper experimental bound on m_b, the corrections are required to be *negative* (hence $\mu < 0$) and *large* (hence large $\tan\beta$). In mNUSM models [62], the adopted top-down YU excludes $\mu > 0$ and forces, in the $\mu < 0$ case, $31 < \tan\beta < 45$ (see Sec. 6.1).

The large values of the Yukawa couplings of the third generation fermions, owing to RG running, yield lighter superpartners than the ones of the other two generations. Beside the widely discussed case of the stau [52, 54–56], in presence of non-universal sfermion boundary conditions, the role of NLSP can be played by both the sbottom and the tau sneutrino [62]. In order to quantify this statement, we plot in Fig. 4.3 the masses of the two sparticles at various values of m_0 as functions of the parameter K. The features shown in Fig. 4.3 are traced back to the generic form of the approximate solutions to the RG equations at the electroweak scale, which can be parameterized as

$$m_{\tilde{\nu},\tilde{b}} \simeq m_0 \sqrt{a_{\tilde{\nu},\tilde{b}} + b_{\tilde{\nu},\tilde{b}} K^2}, \tag{4.16}$$

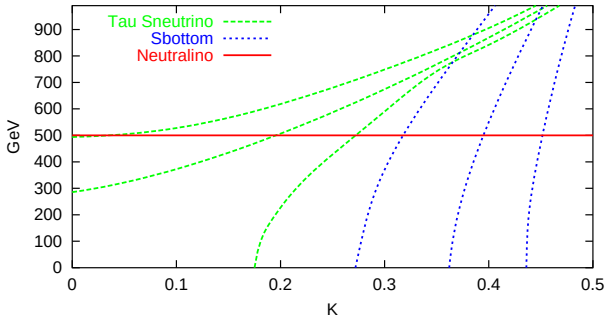

Figure 4.3: *The sbottom and sneutrino mass spectrum at* $M_{1/2} = 1.1$ TeV, $\tan\beta = 38.0$ *and* $A_0 = 0$, *for several values of* m_0, *as functions of the non-universality parameter* K. *For the tau sneutrino, from left to right,* $m_0 = 1350,\ 1650,\ 1950$ *GeV, while, for the sbottom,* $m_0 = 2850,\ 3300,\ 3750$ *GeV.*

where a and b are, to a good approximation, functions of the ratio $(m_0/M_{1/2})$ and of $\tan\beta$, and weakly depend on the trilinear coupling A_0 [62]. In all cases we notice that for a given value of m_0 there exists a corresponding range for K where the sbottom or the tau sneutrino are quasi-degenerate with the neutralino (whose mass roughly depends only on $M_{1/2}$ and is therefore insensitive to K). The mass isolevel curves plotted in Fig. 4.4 highlight the plausible coannihilation regions produced by the particle spectrum of NUSM models. The shape of Fig. 4.4 is qualitatively unchanged by the variation of any SUSY parameter, slowly moving to the right when increasing $\tan\beta$ [62].

Minimal NUSM produces a new coannihilation branch at $K < 0.5$ (see Fig. 4.4), where the coannihilating NLSP is the tau sneutrino in the range $1.5 \lesssim (m_0/M_{1/2}) \lesssim 3$, while it is the lightest sbottom for $(m_0/M_{1/2}) \gtrsim 3$. We study in Fig. 4.5 the new extended sfermion coannihilations at $A_0 = 0$ and at an intermediate value of $\tan\beta = 38$. Frame (a) refers to the tau sneutrino NLSP, at $K = 0.1$, while frame (b) to the sbottom, at $K = 0.35$. We parameterize the remaining variables of the model, m_0 and $M_{1/2}$, through $m_{\tilde{\chi}}$ and $\Delta_{NLSP} \equiv \dfrac{m_{NLSP} - m_{\tilde{\chi}}}{m_{\tilde{\chi}}}$: via RG running, in fact, $(m_0, M_{1/2})$ uniquely determines $(m_{\tilde{\chi}}, \Delta_{NLSP})$, and vice-versa. The NLSP mass range where $\Omega_{\tilde{\chi}} \lesssim 0.13$, at a fixed given $m_{\tilde{\chi}}$, is as large as allowed by the efficiency of the coannihilation processes. We clearly notice that sbottom-neutralino coannihilations (frame (b)), which involve strong interaction processes, suppress the relic density much more effectively than in the $\tilde{\chi}$-$\tilde{\nu}_\tau$-$\tilde{\tau}$ case (frame (a)). We also find that

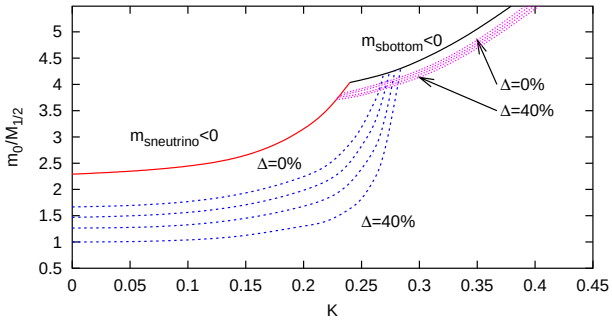

Figure 4.4: *Mass isolevel curves for the tau sneutrino and for the sbottom in the* $(K, m_0/M_{1/2})$ *plane. The solid red and black lines indicate respectively* $m_{\tilde{\nu}_\tau} = 0$ *and* $m_{\tilde{b}} = 0$. *The splitting between the isolevel curves is 10% of the neutralino mass* $m_{\tilde{\chi}} \simeq 500$ GeV; $\tan\beta = 38.0$, $A_0 = 0$, $\mu < 0$.

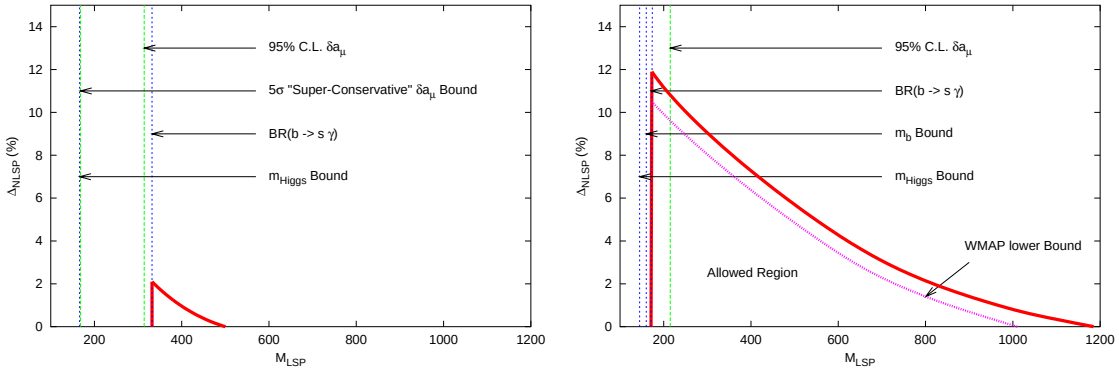

Figure 4.5: *The cosmologically and phenomenologically allowed regions in the* $(m_{\tilde{\chi}}, \Delta_{NLSP})$ *plane at* $\tan\beta = 38.0$*, at* $K = 0.1$ *(a) and* $K = 0.35$ *(b).*

$\tilde{\chi}$-$\tilde{b}$ and $\tilde{b}$-$\tilde{b}$ (co-)annihilations evolve, through strong interactions, into few final SM states (respectively g-b and g-g or b-$\bar{b}$) and largely dominate over $\tilde{\chi}$-$\tilde{\chi}$ annihilations, while triple $\tilde{\chi}$-$\tilde{\nu}_\tau$-$\tilde{\tau}$ coannihilations present a wider and more complex pattern of final states (see Ref. [62]). In the left part of the figures we show the bounds dictated by the 95% C.L. exclusion regions of various accelerator constraints. Scanning the values of $\tan\beta$ we find that, for $\tan\beta \gtrsim 45$ and $\tan\beta \lesssim 31$, the cosmologically allowed region squeezes until no points simultaneously fulfill b-τ YU and the accelerator constraints.

As far as the coannihilation channels are concerned, the case of the sbottom is characterized by a rather simple pattern, clearly dominated by strong interaction processes. We find that when sbottom masses are quasi-degenerate with the neutralino mass, the neutralino pair annihilation rate is very low (less than few percent). The dominant channels concern instead neutralino-sbottom coannihilations into gluon-b quark (up to 10%) and sbottom-sbottom annihilations into a couple of b quarks (up to 15%) or into a couple of gluons (up to 80%).

When the coannihilating partner is the tau sneutrino, the coannihilation pattern is instead by far more complicated. We show in Fig. 4.6 a typical situation for the (percent) contributions of the possible coannihilating initial sparticles, and a detail of the most relevant final states, taken at $m_\chi \simeq m_{\widetilde{\nu_\tau}}$ and $\tan\beta = 38$. This pattern is however rather dependent on the $\tan\beta$ value and on the relative mass splitting.

4.1.2 Gluino coannihilations

We showed that the gluino is the strongest possible coannihilating partner of the lightest neutralino in the MSSM. In Ref. [66] we studied in detail the possibility of neutralino coannhilations with gluinos, and provided some examples of theoretical frameworks where such processes become either plausible or ubiquitious.

The low-energy condition for having gluino coannihilation processes is that $m_\chi \simeq m_3 \equiv m_{\tilde{g}}$. Since it is a strongly interacting particle, we expect in particular gluino-gluino annihilations to be greatly effective in reducing the LSP relic abundance. In view of what we outlined above, if the LSP is to be the *main Dark Matter component*, this scenario will be of particular interest in case the lightest neutralino is *bino-like*: gluino coannihilations will then provide, depending on the bino-gluino mass splitting, the required relic density suppression mechanism to obtain the correct Dark Matter thermal relic abundance. In particular, due to the very large gluino-gluino annihilation cross section, and to the presence of coannihilation

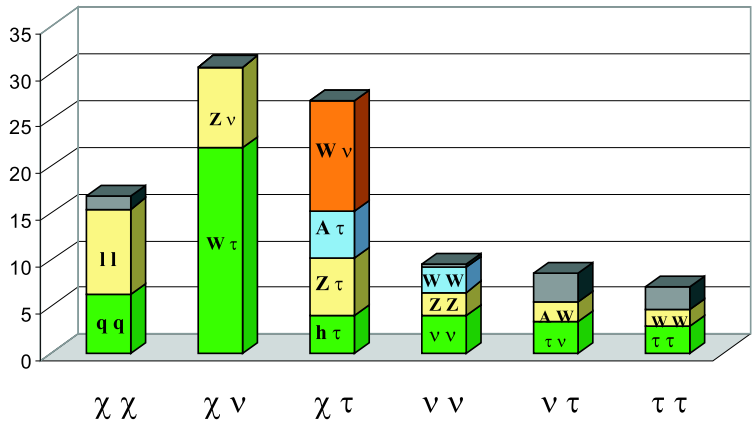

Figure 4.6: *A typical pattern of the relative contribution of coannihilation processes in the tau sneutrino coannihilation region. The plot refers to the case* $\tan\beta = 38$, $A_0 = 0$ *and* $m_\chi \simeq m_{\widetilde{\nu_\tau}}$. *The upper gray part of the columns represents other contributing channels.*

processes which couple neutralino and gluino freeze-out processes, the net effect of neutralino relic abundance suppression is mainly driven by the gluino effective annihilation cross section, even for relatively large gluino-neutralino mass splittings. We emphasize that this feature is peculiar of the Gluino Coannihilation scenario, since for any other coannihilating partner and for sufficinetly large mass splittings, the coannihilation amplitude dominates over the coannihilating partner pair annihilations. In case the lightest neutralino is higgsino or wino-like, gluino coannihilations will only be helpful at very large masses ($m_\chi \sim 1 \div 2$ TeV). We will show that, though featuring larger annihilation cross sections, the resulting relic abundance of winos and higgsinos which coannihilate with a quasi degenerate gluino is *larger* than that of coannihilating binos, due to the presence of additional effective degrees of freedom brought by charginos and by the next-to-lightest neutralino in the case of higgsinos. This is therefore a case where *additional coannihilating partners actually increase the final neutralino relic abundance.*

In the conventional mSUGRA model, gaugino masses at low energies (m_i) are proportional to the corresponding $\alpha_i \equiv g_i^2/(4\pi)$, obeying

$$m_3 : m_2 : m_1 \sim \alpha_3 : \alpha_2 : \alpha_1 \sim 6 : 2 : 1 \ . \tag{4.17}$$

This relation is a consequence of the *assumed* gaugino mass universality at high energies ($M_i = M_{1/2}$ at $M_{\rm GUT}$) and, if valid, implies that the gluino is the heaviest gaugino. However, there are plenty of well motivated models which do not satisfy Eq. (4.17) (see, for instance, [70]). In particular, we are interested in low energy realizations of the MSSM with gluino-neutralino quasi-degeneracy and, therefore, with gluinos lighter than what expected from Eq. (4.17). The high energy setup and some phenomenological implications of such models, as well as those of related scenarios with a gluino LSP, have been considered previously in the literature [71–74].

One of the mentioned setups is the so-called O-II superstring inspired model, in the limit in which SUSY breaking is dominated by the universal size modulus. Gaugino masses, which are determined by the standard RGE coefficients and by the Green-Schwartz parameter, arise at one-loop and, in the preferred range of the model, typically yield either a (heavy) gluino LSP, or neutralino-gluino quasi-degeneracy [71].

Another example emerges in the context of Gauge Meditated SUSY Breaking (GMSB). In some GUT models, as a result of the doublet-triplet splitting mechanism and due to the

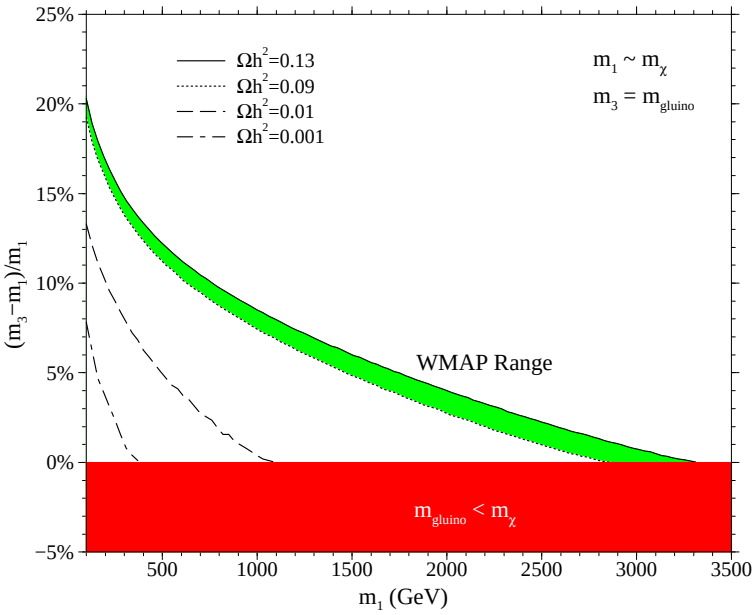

Figure 4.7: *The area shaded in green shows the parameter space, in the* $(m_1, (m_3 - m_1)/m_1)$ *plane, compatible with the WMAP estimate of the cold Dark Matter content of the Universe. The red shaded region at negative values of* $(m_3 - m_1)/m_1$ *is not allowed because the neutralino is no longer the LSP: a heavy gluino LSP is ruled out by anomalously heavy isotopes searches [28].*

mixing between the Higgs and the messengers, gluino masses are suppressed [72]. Notice that in this model a smooth change in the parameter B, the ratio of the doublets and triplets masses, easily leads from a gluino LSP to a neutralino-gluino quasi degeneracy.

It is known that bino-like neutralinos tend to produce a relic abundance well above the WMAP preferred range, whereas wino- and higgsino-like neutralinos have the opposite behavior. Hence, relic density suppression mechanisms, such as gluino coannihilations, are particularly interesting for the case of bino-like neutralinos and we will devote most of this analysis to that situation.

The Gluino Coannihilation (GC) model we consider here is defined as any realization of the MSSM satisfying the conditions

$$m_\chi \lesssim m_3 \ll m_{\rm susy}, \tag{4.18}$$

where m_χ and m_3 are respectively the neutralino and the gluino masses at low energy, and $m_{\rm susy}$ stands for any other SUSY particle masses.

Let us mention that in previous studies gluino-photino processes were considered within *low gaugino mass models* [75, 76]. There, however, the coannihilating partner was *not* the gluino, but rather the R^0 gluon-gluino hadronic bound state. Furthermore, since gaugino masses were radiatively induced in the absence of dimension-3 SUSY breaking operators, the mass range of the models was limited to the few GeV's region [76]. Therefore, the whole phenomenological setup was largely different from the one we describe here.

In what follows we will study the parameter space of the GC Model using as parameters m_χ and the ratio $\dfrac{m_3 - m_\chi}{m_\chi}$, arbitrarily setting $m_{\rm susy} = a \cdot m_\chi$, with the numerical factor $a > 1$, in order to single out the specific features of gluino coannihilations. For definiteness we fixed all the (flavor diagonal) scalar soft breaking masses $m_{\tilde{s}} = a \cdot m_\chi$, with $a = 3$. Let us remark that any other free parameter of the MSSM, like the sign of μ, $\tan\beta$, the scalar

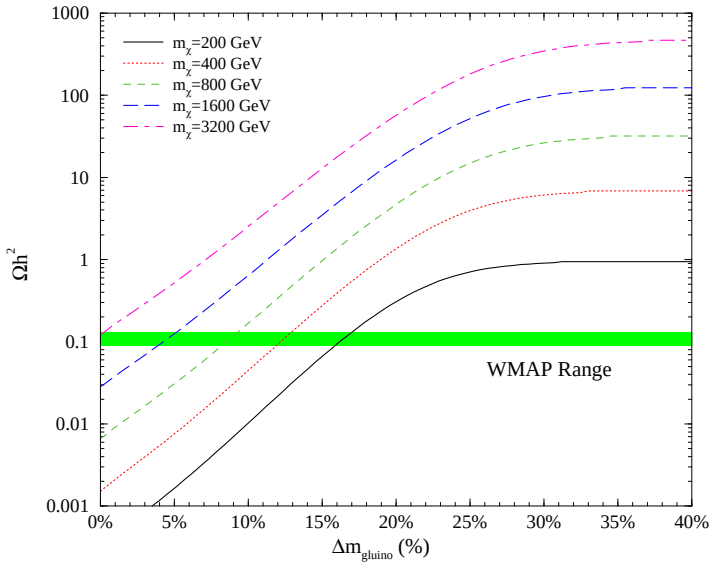

Figure 4.8: *The relic density as a function of the mass splitting between the neutralino and the gluino for different values of the neutralino mass. The WMAP range is shown as a green band.*

trilinear couplings A_i and possible phases are largely irrelevant to the following analysis: in this respect we fixed $\mu > 0$, $\tan\beta = 30$ (when not specified otherwise), $A_i = 0$, and any imaginary phase to zero.

The numerical study is performed through the most recent versions of the packages `micrOMEGAs` [67] and `DarkSUSY` [77], as respectively pertains the relic density computations and the Dark Matter detection rates[2]. We do not include here the perturbative cross sections for gluino-gluino and neutralino-gluino processes, which can be found elsewhere in the literature (see *e.g.* [73]). Changing the parameter a slightly affects the computation of the relic density, since it varies the masses of the SUSY particles exchanged in the tree-level (co-)annihilation processes, but it leaves our analysis and our conclusions absolutely unchanged.

In Fig. 4.7 we show, in the $\left(m_1,\ \dfrac{m_3 - m_1}{m_1}\right)$ plane, the parameter space of the GC scenario for a bino-like neutralino ($m_1 \approx m_\chi$). The region shaded in green corresponds to a value of the relic density compatible with the WMAP result $\Omega_{\rm CDM}h^2 = 0.1126^{+0.0161}_{-0.0181}$ [6]. Below the green strip the relic density is over-suppressed. We show in this region isolevel curves corresponding to $\Omega h^2 = 0.01\,, 0.001$.

As expected, along the allowed region, the larger the neutralino mass, the smaller the mass splitting which ensures the needed relic density suppression. Notice that the neutralino, which is bino-like, can be as heavy as $m_\chi \sim 3.3$ TeV without entering in conflict with the constraint on the relic abundance. We recall that in mSUGRA models the upper bound on the mass of a bino-like neutralino is found to be $m_\chi \lesssim 600$ GeV [78]. Let us mention that for all parameter space points we considered, direct SUSY particle searches and indirect accelerator limits on rare processes put weaker bounds than that coming from cosmology.

Fig. 4.8 shows the relic density as a function of the mass splitting between a (bino-like) neutralino and the gluino $\Delta m_{\tilde g} \equiv (m_{\tilde g} - m_\chi)/m_\chi$ for different values of the neutralino mass. As $\Delta m_{\tilde g}$ increases, $\Omega_\chi h^2$ approaches its asymptotic value in the absence of coannihilations. In particular, a neutralino with a mass $m_\chi = 200$ GeV requires a gluino with a mass splitting

[2]The current version of `DarkSUSY` does not include processes with the gluino in the initial state [77], but this does not affect the Dark Matter detection rates computations, for which the package is used here.

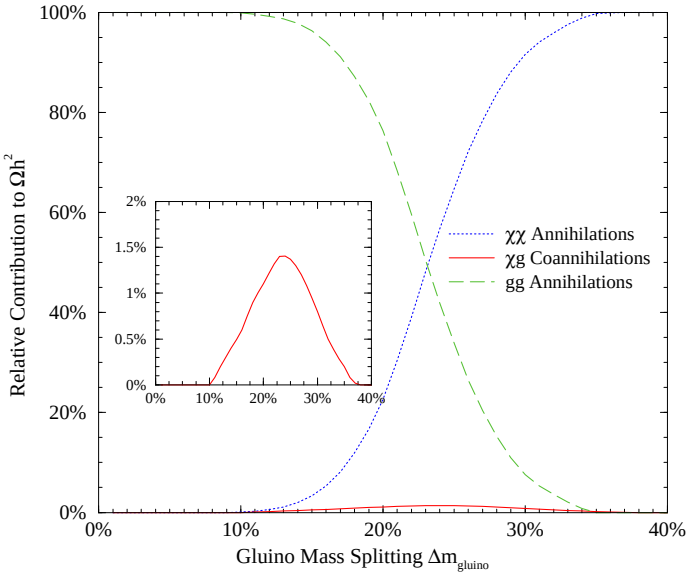

Figure 4.9: *Relative contributions to the relic density of $\chi\chi$ annihilations, $\chi\tilde{g}$ coannihilations and $\tilde{g}\tilde{g}$ annihilations as a function of the mass splitting between the gluino and a bino-like neutralino.*

of about 16% ($m_{\tilde{g}} \approx 232$ GeV) in order to obtain a relic density within the WMAP range. If the neutralino mass is $m_\chi = 1600$ GeV, the required splitting falls to about 5% ($m_{\tilde{g}} \approx 1680$ GeV). Finally, a 3 TeV neutralino needs a nearly complete gluino degeneracy in order to fulfill the upper bound on the relic abundance, as also emerging from Fig. 4.7.

When the gluino is quasi-degenerate with the neutralino there are three sets of processes that contribute to the evaluation of the neutralino relic density: *a*) The usual neutralino-neutralino ($\chi\chi$) annihilations. *b*) The neutralino-gluino ($\chi\tilde{g}$) coannihilations. *c*) The gluino-gluino ($\tilde{g}\,\tilde{g}$) annihilations. In Fig. 4.9 we show the relative contribution of these three channels to the effective cross section which determines Ωh^2 as a function of the gluino mass splitting $\Delta m_{\tilde{g}}$ in the case of a *bino-like* lightest neutralino[3]. The rest of the spectrum is taken to be decoupled ($a = 3$). As seen in Fig. 4.9, the $\tilde{g}\,\tilde{g}$ process dominates at small mass differences, whereas the $\chi\chi$ process dominates at larger ones. The transition between these two regimes takes place at $\Delta m_{\tilde{g}} \approx 23\%$. Remarkably, the $\chi\tilde{g}$ coannihilations play only a minor role and never contribute for more than 1.5%, as shown in the blown up region. This fact is a very peculiar feature of gluino coannihilations. For all other possible coannihilating partners in the MSSM there is always a region, at moderate mass splittings ($\Delta m \approx$ 10-20%), where coannihilations (in the strict sense) are the dominant processes.

Table 4.1 shows the different final states of $\chi\tilde{g}$ coannihilations and of $\tilde{g}\,\tilde{g}$ annihilations, as well as their relative importance. $\chi\tilde{g}$ coannihilations are $\tan\beta$-dependent, and are investigated for $\tan\beta = 50$ in (*a*) and $\tan\beta = 5$ in (*b*). Notice that the $t\bar{t}$ channel, due to the large top Yukawa coupling, always gives the largest contribution. The $b\bar{b}$ channel, on the other hand, is very sensitive to the value of $\tan\beta$, approaching the $t\bar{t}$ contribution at large $\tan\beta$. As expected, the results for the first and second generations are identical. Let us stress that, in view of the gluino-gluino dominance shown in Fig. 4.9, the inclusion of quark Yukawa couplings is largely irrelevant in the present scenario.

Since $\tilde{g}\,\tilde{g}$ annihilations are driven by strong interactions, they do not depend on $\tan\beta$.

[3]The situation is similar for winos and higgsinos, though the transition from gluino annihilations to neutralino annihilations dominance in the effective cross section takes place at a smaller gluino mass splitting, since the neutralino annihilation cross section is larger.

$\chi\,\widetilde{g}$	$t\bar{t}$	37.8%
	$b\bar{b}$	31.2%
	$u\bar{u}$	11.1%
	$c\bar{c}$	11.1%
	$d\bar{d}$	4.4%
	$s\bar{s}$	4.4%
		100%

(a)

$\chi\,\widetilde{g}$	$t\bar{t}$	48.5%
	$u\bar{u}$	17.2%
	$c\bar{c}$	17.2%
	$b\bar{b}$	5.7%
	$s\bar{s}$	5.7%
	$d\bar{d}$	5.7%
		100%

(b)

$\widetilde{g}\,\widetilde{g}$	gg	59.8%
	$u\bar{u}$	6.7%
	$c\bar{c}$	6.7%
	$t\bar{t}$	6.7%
	$b\bar{b}$	6.7%
	$d\bar{d}$	6.7%
	$s\bar{s}$	6.7%
		100%

(c)

Table 4.1: *(a) Final states for the coannihilation process* $\chi\widetilde{g}$ *at* large $\tan\beta = 50$. *(b) Final states for the coannihilation process* $\chi\widetilde{g}$ *at* low $\tan\beta = 5$. *(c) Final states for the annihilation process* $\widetilde{g}\,\widetilde{g}$.

In (*c*), the possible final states for the $\widetilde{g}\,\widetilde{g}$ annihilations are shown. Notice that the purely gluonic *g*-*g* final state gives the lion's share of the effective annihilation cross section. The other final states are quark-antiquark pairs, and all of them give the same contribution.

The fact that the annihilation cross section of a gluino is by far larger than that of a neutralino holds true not only if the neutralino is bino-like, but also if it is wino- or higgsino-like. In this respect, we now turn to the comparison of the relic abundance of higgsinos, winos and binos which coannihilate with gluinos. We focus on the fully degenerate mass case ($m_\chi = m_{\tilde{g}}$) for clarity. We plot in Fig. 4.10 the relic abundances for the cases of bino, wino and higgsino-gluino coannihilations. We also plot the relic density of a gluino LSP, $\Omega_{\tilde{g}}h^2$. All other relevant SUSY masses are set to 5 times the LSP mass (this maximizes the gluino cross section, suppressing the negatively interfering t and u channel squark exchanges), and $\tan\beta$ is set to 30, though, clearly, the gluino cross section does not depend on it.

Due to the gluino dominance in the effective cross section, the relic abundance of binos turns out to be the most suppressed one, as shown in Fig. 4.10. This depends on a suppression factor originating from the effective degrees of freedom which enter in the number density computation, and which depend in their turn on the dominant gauge component of the lightest neutralino, due to the neutralino and chargino mass matrix structure. We emphasize that the following discussion relies on the results found in the previous section, namely on the dominance of gluino annihilation processes over coannihilations in a wide range of mass splittings, and on the presence of inter-conversion processes between the two species, which is mandatory to enable gluino annihilations to drive the neutralino relic abundance to low values affecting the neutralino freeze-out effective (co-)annihilation cross section.

The computation of the degrees of freedom suppression factor goes like this: the LSP relic density scales as the inverse of the thermally averaged effective (co-)annihilation cross section

$$\Omega_\chi h^2 \propto \langle\sigma_{\rm eff}\, v\rangle^{-1}. \tag{4.19}$$

In its turn,

$$\langle\sigma_{\rm eff}\, v\rangle(T) = \frac{A(T)}{n_{\rm eq}^2(T)}, \tag{4.20}$$

where A is the annihilation rate per unit volume at a given temperature, and $n_{\rm eq}$ is the equilibrium number density, which follows a Maxwell-Boltzmann distribution to a very good approximation [52],

$$n_{\rm eq} = \frac{T}{2\pi^2}\sum_i g_i m_i^2 K_2\left(\frac{m_i}{T}\right). \tag{4.21}$$

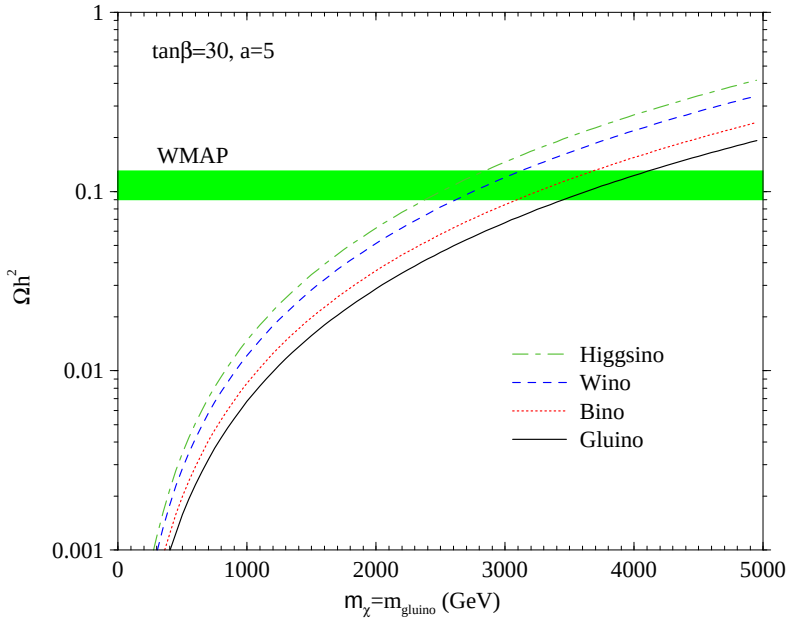

Figure 4.10: *The relic abundance of higgsinos, winos and binos purely degenerate in mass with the gluino. The rest of the spectrum is set to be 5 times larger than the lightest neutralino mass, and* $\tan\beta = 30$. *We also depict the relic density of a gluino LSP, and the cold Dark Matter range favored by WMAP. The relic abundance of the neutralino is driven by that of the gluino, modulo an overall factor which depends on the effective degrees of freedom carried by the neutralino (see the text).*

Since

$$A_{\widetilde{g}\widetilde{g}} \gg A_{\widetilde{g}\chi},\ A_{\chi\chi} \tag{4.22}$$

we will simply have that

$$\frac{\Omega_\chi}{\Omega_{\widetilde{g}}} = \left(\frac{n_{\rm eq}^{\chi-\widetilde{g}}}{n_{\rm eq}^{\widetilde{g}-\widetilde{g}}}\right)^2 = \left(\frac{g_{\widetilde{g}}+g_\chi}{g_{\widetilde{g}}}\right)^2. \tag{4.23}$$

In the case of the bino, since $g_{\widetilde{g}} = 16$ and $g_\chi = 2$ one gets a net increase factor equal to 1.27.

The stated result is easily generalized to the case of other coannihilating partners $\widetilde{P}_i$ beside the gluino, again featuring an annihilation cross section much smaller than that of the gluino, and explains why further coannihilating partners actually *rise* the final relic density:

$$\Omega_\chi h^2 = \Omega_{\widetilde{g}} h^2 \left(\frac{g_{\widetilde{g}}+g_\chi+\sum_i g_{\widetilde{P}_i}}{g_{\widetilde{g}}}\right)^2. \tag{4.24}$$

For instance, in the case of the higgsino one has 6 additional degrees of freedom from the next-to-lightest neutralino and from the lightest chargino, while in that of the wino there are 4 further chargino degrees of freedom. This translates into a relic density which is respectively 2.25 and 1.89 times larger than that of a pure gluino. Remarkably, the numerical results nicely agree with the stated predictions (see Fig. 4.10).

We emphasize that in the present computations we neglected non-perturbative effects in the gluino-gluino scattering cross section [72, 73, 79]: the evaluation of the effects of multiple gluon exchanges between interacting gluinos has in fact been shown to be highly model-dependent [73]. We must however warn the reader that the mentioned non-perturbative effects could *enhance* the gluino annihilation cross section by even orders of magnitude, and

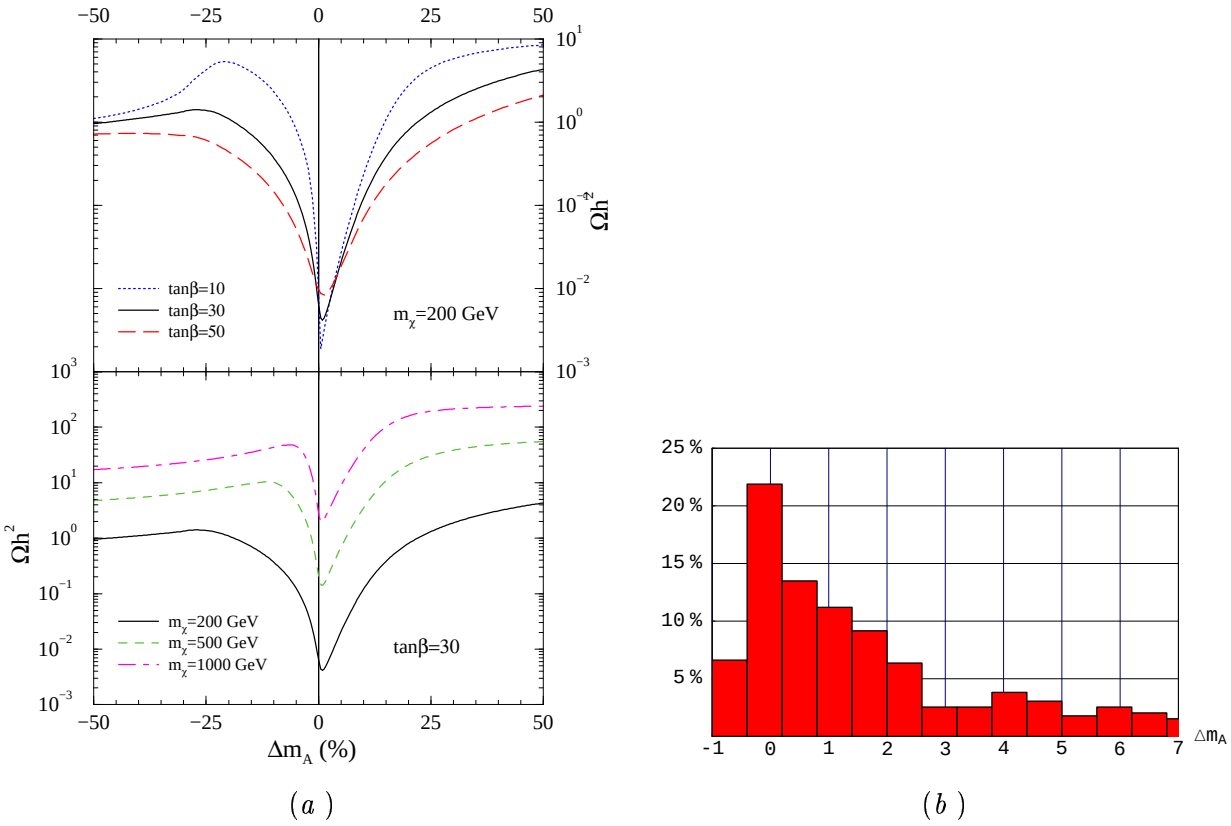

(*a*) (*b*)

Figure 4.11: *The relic density in the presence of a resonant annihilation cross section, as a function of* Δm_A*, for different values of* $\tan\beta$ *and different neutralino masses* (*a*)*. In* (*b*) *we display an histogram of* Δm_A *for all viable models with a bino-like neutralino and* Ωh^2 *in the WMAP range.*

that therefore the relic density may be *much smaller* than what we show. In this respect, our results must be effectively regarded as conservative *upper bounds* on the final gluino relic density (and therefore on the coannihilating neutralino relic abundance as well). The same applies for the comparison of the efficiency of coannihilation effects we carry out in the next section, as well as for the determination of an upper bound on the neutralino mass: when taken into account, non-perturbative contributions may considerably enlarge the cosmologically allowed mass ranges.

4.2 Resonances

The computation of the relic density of a thermally produced particle χ needs particular care when the mass of χ lies close to half the mass of another particle P in which χ can annihilate through an s-channel P exchange. The propagator of the s-channel diagram features in this case a resonant behavior. This is precisely what occurs, for instance, in the MSSM for the heavy CP-odd A and CP-even H Higgs bosons, as well as for the SM-like light CP-even Higgs, at very low χ masses. The calculation of the thermally averaged cross section for the resonant $\chi\chi$ annihilation requires in particular a thermally averaged treatment [80], see *e.g.* Ref. [81].

The effects of a heavy Higgs resonance on the annihilation rate of neutralinos depend on three inputs: first, the mass splitting between the annihilating particle χ and half the mass

of the resonantly exchanged particle A, which we quantify through the parameter

$$\Delta m_A \equiv \frac{m_A - 2 \cdot m_\chi}{2 \cdot m_\chi}; \tag{4.25}$$

second, the total decay width of the resonance Γ_A and third its mass m_A [81]. Finally, the ratio of the naïvely computed cross section to the correct one depends on the relevant $\chi\chi A$ couplings and on the couplings of the resonance to the final particle states. For recent studies dedicated to the effects of resonant annihilation cross sections see [82, 83].

We show in Fig. 4.11 the overall non-trivial combination of the effects of these input parameters. In the upper panel we show the dependence of the neutralino relic density $\Omega_\chi h^2$ on Δm_A at fixed $m_\chi = 200$ GeV for three different values of $\tan\beta$, while in the lower panel we fix $\tan\beta = 30$ and analyze three different m_χ, namely 200, 500 and 1000 GeV. The plot clearly highlights the effect of the resonance around $\Delta m_A = 0$, and in particular the results of the *thermal averaging*: in fact, the maximal effects are at *positive* $\Delta m_A \approx 1\%$, since particles with mass $m_\chi \lesssim m_A/2$ have in general larger thermal energy contributions than those with $m_\chi \gtrsim m_A/2$.

In the upper panel we see the effect of a broader resonance (the width of m_A grows with $\tan\beta$) on the relic density: for larger $\tan\beta = 50$ resonance effects are operative for a larger Δm_A range. In the lower panel, instead, it is shown how larger masses reduce the effectiveness of resonances, shrinking the relevant Δm_A range.

Resonances have drastic consequences on the cosmological constraints on the MSSM parameter space, mainly when the $\chi\chi$ annihilation cross section is relatively low, as it is the case for a bino-like LSP. The plot on the right illustrates the overall statistical effects of the A pole resonance, showing the fraction of binos in a given bin of Δm_A for the parameter space scan of Ref. [46] (for details see Sec. 3.3.1). We clearly see that the privileged values are those around $\Delta m_A = 0$, as expected.

4.3 Relic density enhancement in non-standard cosmologies: the case of Quintessence

As we outlined above, like in any process involving a departure from thermal equilibrium, the freeze-out of neutralinos implicates a particle interaction rate Γ falling below the expansion rate of the Universe H. Γ and its scaling with temperature are fully defined once the particle physics setup has been specified; what, instead, about H and its thermal scaling? The freeze-out of WIMPs is predicted to take place at a temperature T_f in the range of a few GeV or above: much earlier, in the history of the Universe, than any of the processes which can be directly tested through cosmological observations. The common approach, which reflects that which has been adopted in the present thesis up to now, is to extrapolate the expasion rate as a function of the temperature $a(T)$ of the Universe we derive from tests of the standard big bang nucleosynthesis (BBN), at a temperature of about 1 MeV, backward to the WIMP freeze-out temperature, assuming a radiation dominated Universe. Models where the role of dark energy is played by a dynamical scalar field (*Quintessence*), or scenarios where extra energy density components are present at the time of neutralino freeze-out, may yield significant modifications in the relic abundance of neutralinos [84]. This in turns translates into the intriguing possibility that SUSY models with large neutralino annihilation cross sections, and hence with copious Dark Matter detection rates, give rise to the required amount of cold Dark Matter.

In the present section we will mainly focus on the attractive case of a *quintessential* enhancement of the neutralino relic abundance, motivated by the observational evidence for

a *dark energy* component in the Universe. In a recent analysis, Salati [85] pointed out that predictions for the WIMP relic abundance are significantly different if one supposes that the freeze-out happens during a period of Quintessence domination, as it can be the case if the Quintessence field undergoes a phase of "kination". The underlining idea is rather simple: if on top of the radiation energy density a Quintessence contribution is added, the Universe is forced into having a faster expansion. A larger H implies that the matching between annihilation rate and expansion rate takes place at a higher temperature, hence the WIMP equilibrium number density freezes in at a larger value, giving a net increase in the final WIMP relic abundance (even a modest increase in T_f induces large effects, because the freeze-out of WIMPs happens when WIMPs are non-relativistic and their equilibrium number density is along the exponentially suppressed Maxwell-Boltzmann tail).

We examine here this mechanism in detail: we implement a realistic prototype for Quintessence into the density evolution equation describing the decoupling of a WIMP Dark Matter species, and solve such equation numerically with the state of the art technique as developed in the `DarkSUSY` package [52,77,86]. We are then in the position of giving some general criteria to quantify the quintessential enhancement of relic densities, and of illustrating what classes of models are more sensitive to such an effect. We present results for a few sample cases of neutralino Dark Matter candidates in the context of the minimal supersymmetric extension of the SM (MSSM). In particular we discuss at length the case of higgsinos and winos, which are usually disregarded as Dark Matter candidates, as their thermal relic abundance is typically exceedingly small in the standard cosmological scenario.

4.3.1 Quintessential modifications to the standard cosmological scenario

We consider a Friedmann-Robertson-Walker universe including, in addition to the usual radiation and matter terms, a Quintessence component, which we sketch as a single spatially homogeneous scalar field ϕ with a potential $V(\phi)$. The energy density and pressure associated to this component are, respectively:

$$\rho_\phi = \frac{1}{2}\left(\frac{d\phi}{dt}\right)^2 + V(\phi) \ , \qquad p_\phi = \frac{1}{2}\left(\frac{d\phi}{dt}\right)^2 - V(\phi) \ . \tag{4.26}$$

By formally writing the equation of state for ϕ, $p_\phi = w\rho_\phi$, we see that w can vary between $+1$ and -1, going from the regime in which the kinetic term is much larger than the potential term ("kination" phase [87,88]) to the opposite case when the field is frozen into one configuration and just behaves as a cosmological constant term.

To trace the Hubble expansion rate H as a function of the temperature T, we need to solve the Friedmann equation (we assume a spatially flat Universe):

$$H^2(T) = \frac{1}{3M_{\rm Pl}^2}\left[\rho_{\rm rad}(T) + \rho_m(T) + \rho_\phi(T)\right] \ , \tag{4.27}$$

coupled to the equation of motion for ϕ:

$$\frac{d^2\phi}{dt^2} + 3H\frac{d\phi}{dt} + \frac{dV}{d\phi} = 0 \ . \tag{4.28}$$

In Eq. (4.27) above, $M_{\rm Pl} \equiv 1/\sqrt{8\pi G}$ is the reduced Plank mass, while $\rho_{\rm rad}$ and ρ_m are, respectively, the energy density in radiation and in matter. To find $\rho_m(T)$ we simply scale its current value with the appropriate equation of state; for $\rho_{\rm rad}(T)$ the analogous procedure, often implemented in Quintessence studies, is not accurate enough for our purpose. We write instead $\rho_r(T)$ as:

$$\rho_{\rm rad}(T) = \frac{\pi^2}{30} g_{\rm eff}(T)\, T^4 \tag{4.29}$$

and compute $g_{\rm eff}(T)$, the effective degrees of freedom coefficient, summing the contributions from all particles in the context at hand (*i.e.*, in the supersymmetric extension to the SM we consider below, we find $g_{\rm eff}(T)$ for each of the mass spectrum we generate, including both standard model particles and the supersymmetric partners; details on how to compute $g_{\rm eff}(T)$ are given, *e.g.*, in Ref. [89]).

$\rho_\phi(T)$ and $H(T)$ can be derived once we specify the initial conditions and the potential $V(\phi)$. The set of initial conditions we resort to is not the most generic in a context of quintessential cosmology, as we wish to restrict ourselves to solutions in which ρ_ϕ is initially larger than $\rho_{\rm rad}$, and then is red-shifted away more rapidly than the radiation component (this happens in the *kination* phase) so that the radiation domination epoch can start before the time of BBN. This corresponds, *e.g.*, to the reheating scenario suggested in Ref. [90] and, more generically, in models that try to generate, through the same mechanism, the current inflationary period and a period of inflation in the early Universe (see, *e.g.*, the quintessential inflationary models of Ref. [91]). As regards the potential, we choose to work with the exponential form [92]:

$$V(\phi) = M_P^4 \exp\left(-\lambda\phi/M_P\right) \ , \tag{4.30}$$

one of the simplest examples of potential which can lead to an attractor solution, self-tuning the contribution of ϕ to the energy density to the "background" contributions, *i.e.*, in our case, radiation plus matter. We will select regions in the parameter space in which the attractor is reached, so that we deal with a Quintessence model playing a main dynamical rôle in the recent past; actually the simple form for the potential we picked is not going to give the behavior of ρ_ϕ observed today (the solution converges to the same equation of state as the largest background component), however slight modifications to it can introduce the right scaling, see, *e.g.*, Ref. [93, 94]. On the other hand, we checked in a few test cases that this slight reshuffling of the potential can be introduced without varying significantly the dynamics of the field in the early Universe[4]; we can therefore safely ignore details in the late time behavior of the field. The exponential form itself is not critical for the results we will present; however, in order to have a viable prototype for Quintessence, one should restrict to setups which allow to reach tracking after going through a kination phase, a feature which is not shared by all potentials which do admit an attractor solution; further examples of such setups are given in Ref. [95].

The possibility of having a kination regime with the exponential potential introduced above was examined in detail by Ferreira and Joyce in Ref. [88]; we closely follow their analysis here, choosing, in particular, the same set of initial conditions. In terms of H_i, the expansion rate at the end of inflation, we fix:

$$V(\phi_{\rm init}) = 3M_P^2 H_i^2 \ , \quad \left.\frac{d\phi}{dt}\right|_{\phi_{\rm init}} = 0 \ , \quad \text{and} \quad \rho_r(T_{\rm init}) = 10^{-3} H_i^4 \ ; \tag{4.31}$$

the energy scale for H_i can be in the range $[10^8,10^{16}]$ GeV [88]. For any given choice of the two parameters in our model, *i.e.* the parameter λ in the exponential potential and H_i, the system of differential equations (4.27) and (4.28) can be easily solved numerically. A few sample cases (see also Ref. [88]) are shown in Fig. 4.12 where we plot the energy density components as a function of the Universe scale factor a. Solid lines refer to the sum of the matter and radiation component (with an ankle at the value when the former, scaling as a^{-3}, takes over the latter, which scales instead as a^{-4}); Quintessence energy density components (scaling as a^{-6} in the initial kination phase) are also shown. An increase in H_i shifts the initial conditions to a higher temperature and, at the same time, lowers the initial ratio

[4]We explicitly worked out the cases of the hyperbolic cosine [94] and of the so-called AS potential, *i.e.* an exponential potential with a power-law prefactor [93].

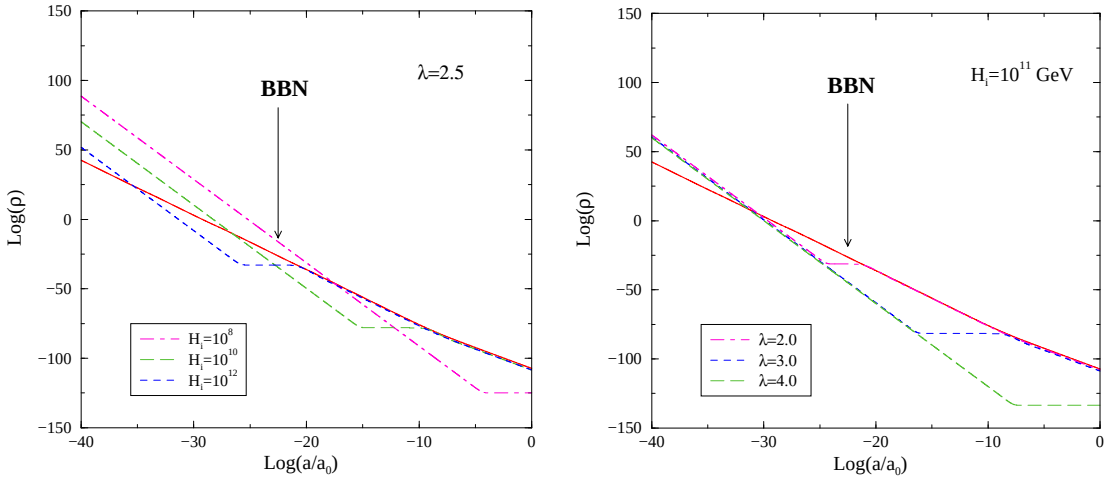

Figure 4.12: *Sample cases of Cosmologies with a Quintessence field in a kination phase dominating the total energy density in the early Universe. The solid lines refer to the sum of the radiation and matter energy density components, the other curves to the Quintessence contributions. We considered the case of an exponential potential and show here the effect of varying the two parameters in our setup: In the left panel three sample values for the expansion rate at the end of inflation H_i are chosen, in the right panel the parameter λ in the exponential potential is varied.*

$\rho_\phi/\rho_{\rm rad} \propto H_i^{-2}$: the effect is obviously to anticipate the radiation dominated phase and the tracking phase. An increase in λ makes the potential steeper, henceforth the kination phase to last longer; from the point of view of the early time behavior, there is just a slight decrease of the normalization of ρ_ϕ in the kination phase due to a quicker transition from the initial condition (with ϕ at rest) into the fast rolling phase (for this specific potential the normalization of ρ_ϕ at tracking scales instead as $1/\lambda^2$ [88], but, as already mentioned, we can neglect here the details in the late time behavior of ρ_ϕ).

In Fig. 4.13 we show the region of the parameter space H_i versus λ which is compatible with the limits from BBN. The latter are often reported in terms of bounds on the extra relativistic degrees of freedom $\Delta N_{\rm eff}$ at BBN, which may be translated in an upper bound on the fraction $\Omega_\phi \equiv \rho_\phi/\rho_r \lesssim 0.1$ for $\Delta N_{\rm eff} \simeq 1.0$. In the dark shaded region the Quintessence field produces a contribution to the energy density at 1 MeV which exceeds the stated constraint. In the lower part of the figure this happens because the ϕ field is still in the kination phase, and exceeds the bound $\Omega_\phi \lesssim 0.1$ at the time of BBN; in the upper-left part, instead, the field is already in the attractor solution at 1 MeV, and again violates the BBN bound. The light shaded region indicates, on the other hand, the cases in which the ratio between ρ_ϕ and the background components gets overly damped, so that tracking does not take place before the present epoch (*overshooting solutions*); both this cases are disregarded in the present work.

4.3.2 Quintessence and neutralino Dark Matter

Rephrasing the density evolution equation of Eq. (4.3) in terms of $Y = n/s$, where s is the entropy density, as a function of the ratio between the particle mass and the temperature, $x = m/T$, one gets the equation

$$\frac{dY}{dx} = \frac{\langle \sigma_{\rm eff} v \rangle}{3H} \frac{ds}{dx} \left(Y^2 - Y_{\rm eq}^2 \right) \ , \tag{4.32}$$

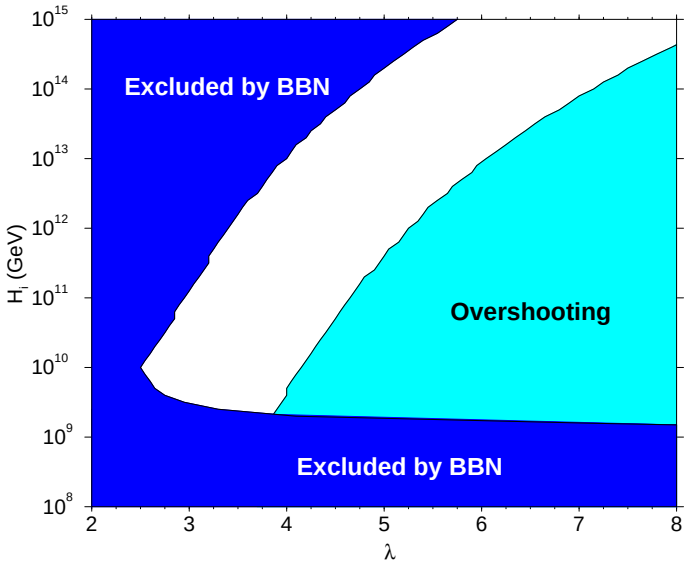

Figure 4.13: *Region of the parameter space H_i versus λ which is excluded by the limits from standard big bang nucleosynthesis. Also indicated is the region where the ratio Quintessence energy density to background energy density gets exceedingly small and tracking does not take place before the present epoch.*

which can be recast as

$$\frac{x}{Y_{\rm eq}}\frac{dY}{dx} = \frac{\Gamma}{H}\frac{x}{3s}\frac{ds}{dx}\left(\frac{Y^2}{Y_{\rm eq}^2}-1\right) \simeq -\frac{\Gamma}{H}\left(\frac{Y^2}{Y_{\rm eq}^2}-1\right), \tag{4.33}$$

where the rôles of the annihilation rate $\Gamma \equiv n_{\rm eq}\langle\sigma_{\rm eff}v\rangle$ and of the expansion rate H become more transparent: when $\Gamma/H \gg 1$, thermal equilibrium holds, that is $Y \simeq Y_{\rm eq}$, while in the opposite regime $Y_{\rm eq} \ll Y$. As a rule-of-thumb, the freeze-out occurs when the ratio $\Gamma/H \sim 1$. An increase in $\langle\sigma_{\rm eff}v\rangle$ yields a decrease in the freeze-out temperature. On the other hand, as already mentioned, and first noticed by Salati [85], if we increase H adding an extra component on top of the radiation component, such as in the quintessential scenario outlined in the previous section, the freeze-out takes place at larger temperatures, and the thermal relic density can be sharply *enhanced*. Even a modest shift in T_f has a dramatic effect, with the increase in the relic density of typical Dark Matter candidates which can be of several orders of magnitude: this is due to the fact that the thermal equilibrium number density scales *exponentially* with the temperature, *i.e.* $n_{\rm eq} \propto (mT)^{3/2}\exp(-m/T)$.

To better quantify the enhancement, rather than introducing a simplified toy-model and deriving an approximate solution to Boltzmann equation as done in Ref. [85], we interface the expansion rate of the Universe H we have derived in the Quintessence scheme described in Sec. 2 into the accurate numerical solution of Boltzmann equation included in the `DarkSUSY` software package [52, 77, 86]. For any given set of initial conditions in the early Universe, and for any particle physics setup with given mass spectrum and particle couplings, we have then a tool to compute WIMP relic abundances with an accuracy of the order of 1%, *i.e.* at the precision level of upcoming measurements of Ω_m.

We choose as indicator of the enhancement produced by a quintessential cosmology onto the neutralino relic density the quantity

$$\Delta\Omega \equiv \frac{\Omega_Q - \Omega}{\Omega}, \tag{4.34}$$

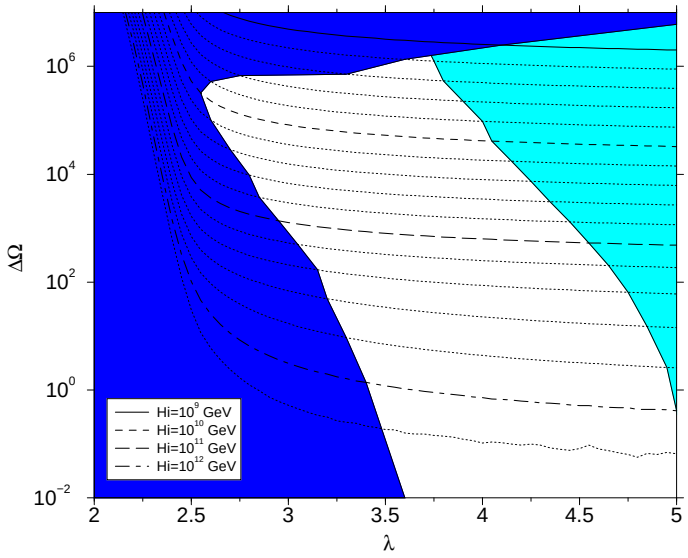

Figure 4.14: *Allowed region and iso-H_i curves in the (λ, $\Delta\Omega$) plane. The dark blue region does not fulfill BBN constraints, while in the light blue zone no tracking takes place before nowadays cosmological times (*overshooting*). We show with bold lines the curves with the same $H_i = 10^9$, 10^{10}, 10^{11} and 10^{12}. Also shown, in dotted lines, curves at equal* logarithmic spacing *from those in bold lines,* i.e. *at around 1.58, 2.51, 3.98 and 6.31 times the upper bold line H_i.*

Ωh^2 being the neutralino relic density in a cosmology *without* Quintessence (standard case), and $\Omega_Q h^2$ that *with* Quintessence. In Fig. 4.14 we show a first example of how large an enhancement we can obtain in our Quintessence setup. In the (λ, $\Delta\Omega$) plane, we plot curves at fixed Hubble rate at the end of inflation H_i; in this figure we have focussed on a specific neutralino Dark Matter candidate, selecting the point in the *bulk* region of minimal supergravity defined by the supersymmetric parameters (see Eq. (3.11)) $M_{1/2} = 2300$ GeV, $m_0 = 3000$ GeV, $\tan\beta = 45$, $A_0 = 0$ and $\mu > 0$. With such choice we avoid, for the moment, coannihilation regions or resonances, and consider the case of a heavy (bino-like) neutralino ($m_\chi \approx 1$ TeV), for which the enhancement effects are maximized: as we will discuss in detail below, the heavier the freezing-out particle, the larger the Quintessence-to-radiation ratio at freeze-out and therefore the larger $\Delta\Omega$. The shadings in the figure reproduce those of Fig. 4.13: dark blue corresponds to a scenario ruled out by BBN constraints, while light blue indicates overshooting (*i.e.* tracking is not achieved at current cosmological times). The largest enhancement allowed is of the order of 10^6 and it is about the largest enhancement we can get with a WIMP of mass smaller than 1 TeV. Moreover, we see that the minimum variations we are sensitive to, namely enhancements of the order of 1%, occur for H_i slightly above 10^{12}. This is the limit around which, in the process of decoupling of a WIMP with mass below 1 TeV, we are not sensitive to the presence of a kination phase any longer.

As a last remark on Fig. 4.14, we comment on the shape of the iso-H_i curves at low λ: the abrupt raise in $\Delta\Omega$ is due to the fact that tracking takes place, at low λ, as soon as $\rho_\phi \simeq \rho_{\rm rad}$, without an overshooting period where $\rho_\phi \ll \rho_{\rm rad}$. This of course yields a large quintessential contribution to H at all time scales relevant to neutralino freeze-out, contrary to the case where an overshooting ($\rho_\phi \ll \rho_{\rm rad}$) takes place. However, these sudden rises in $\Delta\Omega$ happen in the region excluded by BBN constraints, as the tracking phase cannot appear before BBN. Rejecting these cases, we find, as expected, that all large enhacements take place for models in which the field ϕ is in a kination phase, $\rho_\phi \propto a^{-6}$. It appears then natural, rather than searching for a parametrization of $\Delta\Omega$ as a function of λ and H_i, to introduce the relative

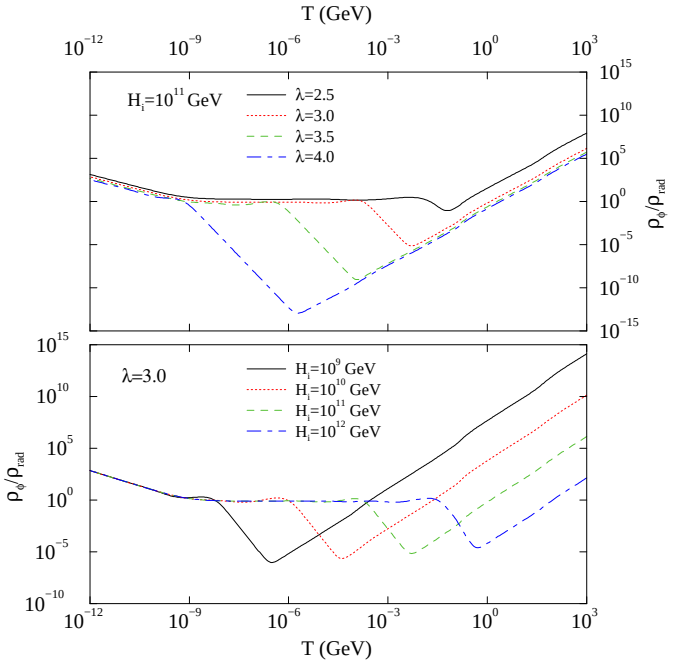

Figure 4.15: *Ratio of the Quintessence energy density to the radiation energy density as a function of temperature, for a few sample choices of the paramters λ and H_i.*

normalization of ρ_ϕ and $\rho_{\rm rad}$ at a given temperature as the single relevant parameter. We do not have the freedom to choose such temperature as low as, say, the BBN scale $T \simeq 1$ MeV, as it is not unusual for the field ϕ to be, at this temperature, in its transient phase between kination and tracking (this is true even for our Quintessence model in which the transient is always very sharp, with ϕ behaving like a cosmological constant; more generic models allow for softer and more complicated transients). This is implicit in Fig. 4.12 and illustrated more directly in Fig. 4.15, where the ratio $\rho_\phi/\rho_{\rm rad}$ is plotted versus the temperature for a few sample choices of the parameters λ and H_i: in the kination phase this ratio scales nearly as T^2 (behaviour of all curves for the largest temperatures display) but this is not necesseraly true at 1 MeV.

In order to quantify the amount of Quintessence relevant for the neutralino relic density enhancement, we choose to resort to the parameter:

$$\xi_\phi \equiv \frac{\rho_\phi}{\rho_{\rm rad}}\left(T_f^{\rm NQ}\right) \tag{4.35}$$

where we defined $T_{\rm f.o.}^{\rm NQ}$ as the temperature of neutralino freeze-out in absence of Quintessence (we use here the convention that the freeze-out temperature is the temperature at which the abundance of the relic species is 50% larger than the equilibrium value, as computed from the full numerical solution of the density evolution equation). Avoiding the reference to a single cosmological temperature, the parameter ξ_ϕ entails a nearly model-independent estimate of the relevant amount of Quintessence. In order to have a rough estimate of this effect, we can consider the s-wave expansion of Eq. (4.7), obtaining

$$\Omega = \frac{\rho_\chi(T_0)}{\rho_c} = \frac{m_\chi n(T_0)}{\rho_c} \simeq \frac{m_\chi n_{\rm eq}(T_f)\ s(T_0)}{\rho_c\ s(T_f)} \simeq \frac{m_\chi\ s(T_0)}{\rho_c\ s(T_f)}\frac{H(T_f)}{\langle\sigma_{\rm eff}v\rangle}, \tag{4.36}$$

where in the third step we introduced the approximation that $Y(T_0) \simeq Y_{\rm eq}(T_f)$, while in the last step we assumed that the freeze-out temperature is *defined* by the relation $\Gamma(T_f) = H(T_f)$.

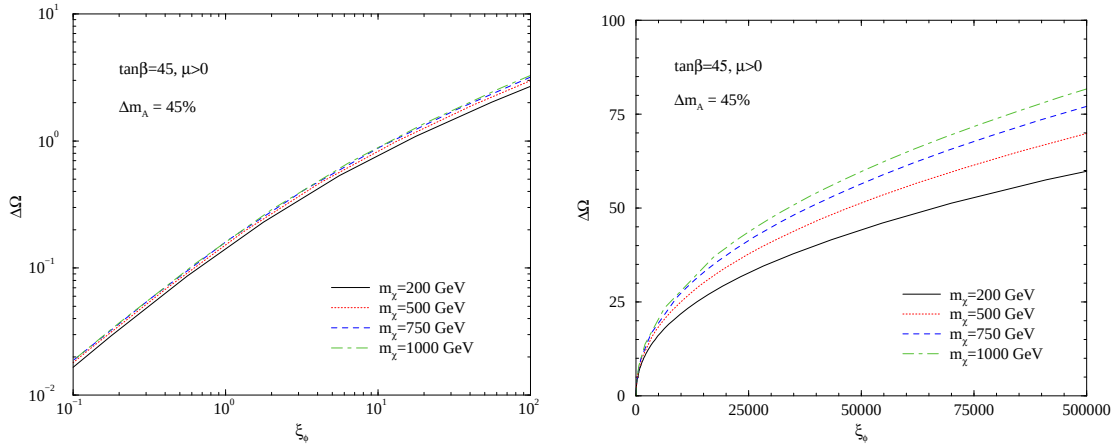

Figure 4.16: *The relic density enhancement $\Delta\Omega$ as a function of the Quintessence-to-radiation ratio at neutralino freeze-out ξ_ϕ for four SUSY models with neutralino masses equal to 200, 500, 750 and 1000 GeV. In all cases, $\tan\beta = 45$, $\mu > 0$ and $A_0 = 0$. The parameters m_0 and $M_{1/2}$ are tuned in order to obtain the desired neutralino mass and a mass splitting $\Delta m_A = (2m_\chi - m_A)/(2m_\chi) = 45\%$.*

In the context of a quintessential cosmology, the expansion rate gets an additional factor given by:

$$H^{\rm NQ}(T_f^{\rm NQ}) \to H^{\rm NQ}(T_f^{\rm Q})\sqrt{1+\frac{\rho_\phi}{\rho_{\rm rad}}(T_f^{\rm Q})} \simeq H^{\rm NQ}(T_f^{\rm Q})\sqrt{1+\xi_\phi\frac{(T_f^{\rm Q})^2}{(T_f^{\rm NQ})^2}}, \qquad (4.37)$$

where the last approximate equality holds under the simplifying hypothesis that $\rho_\phi \propto a^{-6}$. Since the actual shift in the freeze-out temperature should not be dramatic, *i.e.* $T_f^{\rm Q} \approx T_f^{\rm NQ}$, we expect the relic abundance enhancement to be roughly driven by the factor $\sqrt{1+\xi_\phi}$.

4.3.3 Quintessential enhancement and the SUSY parameter space

As already alluded, the phenomenon of quintessential enhancement of the neutralino relic density should depend not only on the particular quintessential setup, but also on the details of the choice of the supersymmetric Dark Matter candidate. In particular, we will show here that there is a dependence (1) on the lightest neutralino mass, since this sets the overall energy scale at which neutralinos freeze-out, (2) on the details of the composition of the lightest neutralino in terms of its bino, wino and higgsino fractions, and (3) on the supersymmetric mass spectrum, especially if it entails coannihilation processes or resonances.

We focus first on the rôle of the neutralino mass. In the left panel of Fig. 4.16 we plot $\Delta\Omega$ versus ξ_ϕ, the ratio of the Quintessence energy density to the radiation energy density computed at the freeze-out temperature, for four neutralinos in the bulk region of the minimal supergravity model and with masses $m_\chi = 200,\ 500,\ 750$ and 1000 GeV. The supersymmetric parameters have been chosen in order to exclude coannihilations or resonance effects, and the neutralinos are always almost completely bino-like. As regards the cosmological setup, we fixed $\lambda = 3.5$, and let H_i vary in order to span over ξ_ϕ. As already mentioned, larger masses yield larger enhancements for a given Quintessence setup; we can deduce however from the figure that, to a good approximation, for relatively low quintessential fractions, the quantity ξ_ϕ fixes $\Delta\Omega$. In particular we find that a 10% enhancement in the relic abundance is obtained if at $T_{\rm f.o.}^{\rm NQ}$ the Quintessence energy density is about 60% of the radiation energy density, and that a 100% effect is generated by $\xi_\phi \simeq 12$. As the amount of Quintessence grows, the spread

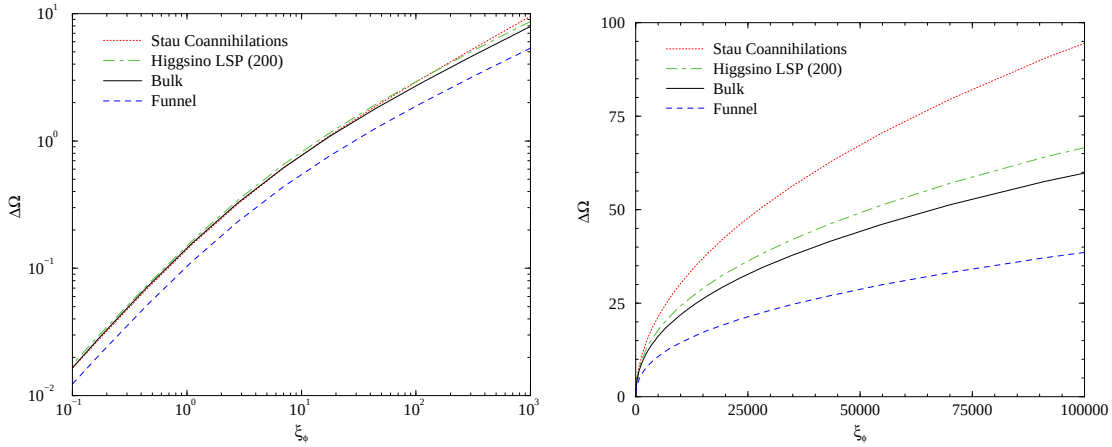

Figure 4.17: *The quintessential enhancement of the neutralino relic density for the four* benchmark *models of Tab. 4.2 as a function of ξ_ϕ, respectively at large ξ_ϕ in a linear scale (*left*) and at small ξ_ϕ in a logarithmic scale (*right*).*

in enhancements for different masses, and at a fixed ξ_ϕ, starts to increase, as shown in the right panel of Fig. 4.16; $\Delta\Omega$ lies in the range 60 to 80 for the largest value of the ratio we display, $\xi_\phi = 10^5$. This reminds us that the freeze-out is not a sudden process characterized by a single energy scale, and if an accurate estimate of the relic abundance is needed, a careful numerical solution to the Boltzmann equation has to be implemented.

In order to study the dependence of the quintessential enhancement on the particular structure of the lightest neutralino, we focus on four *benchmark points*, chosen *ad hoc* to have the same freeze-out temperature in absence of Quintessence $T_f^{\rm NQ} \simeq 9.35$ GeV. We report the details of the four benchmark models under scrutiny in Tab. 4.2. The model with the label *bulk* is characterized by a mass splitting with the A Higgs boson $\Delta m_A \equiv (2m_\chi - m_a)/(2m_\chi) \simeq 45\%$ and with the NLSP, which is the lightest stau, of $\Delta m_{\tilde\tau_1} \equiv (m_{\tilde\tau_1} - m_\chi)/m_\chi \simeq 85\%$. The model is therefore outside both the resonance and the stau-coannihilation regions. The model in the *stau coannihilation* region achieves nearly complete mass degeneracy between the neutralino and the lightest stau, $\Delta m_{\tilde\tau_1} \simeq 0$, while the model in the *funnel* region has $\Delta m_A \simeq 0$. Finally, the model representative of the *higgsino* Dark Matter case is picked in the representation **200** and has a higgsino fraction larger than 95%.

We analyze in Fig. 4.17 the quintessential relic density enhancement generated in the four benchmark cases as a function of the Quintessence-to-radiation ratio at the neutralino freeze-out temperature without Quintessence (ξ_ϕ). We let ξ_ϕ vary from zero up to 10^5, highlighting the large and small ξ_ϕ regimes in the left and right panels respectively. We find that the region of parameter space where the enhancement is more effective is the coannihilation

	m_0	$M_{1/2}$	$\tan\beta$	μ	m_χ	Ωh^2	Wino fract.	Higgsino fract.
Bulk	500	500	45.0	> 0	204	0.582	$< 1\%$	$< 0.01\%$
Stau Coan.	327	590	45.0	> 0	241	0.022	$< 1\%$	$< 0.01\%$
Funnel	408	592	45.0	< 0	243	0.005	$< 1\%$	$< 0.01\%$
Higgsino	800	323	45.0	> 0	250	0.009	4%	95.5%

Table 4.2: *The four* Benchmark models *representing different possible scenarios for the lightest neutralino. The scalar trilinear coupling is set to $A_0 = 0$ in all cases, and the neutralino freeze-out temperature in absence of Quintessence is, again for all four scenarios, fixed at $T_f^{\rm NQ} \simeq 9.35$ GeV.*

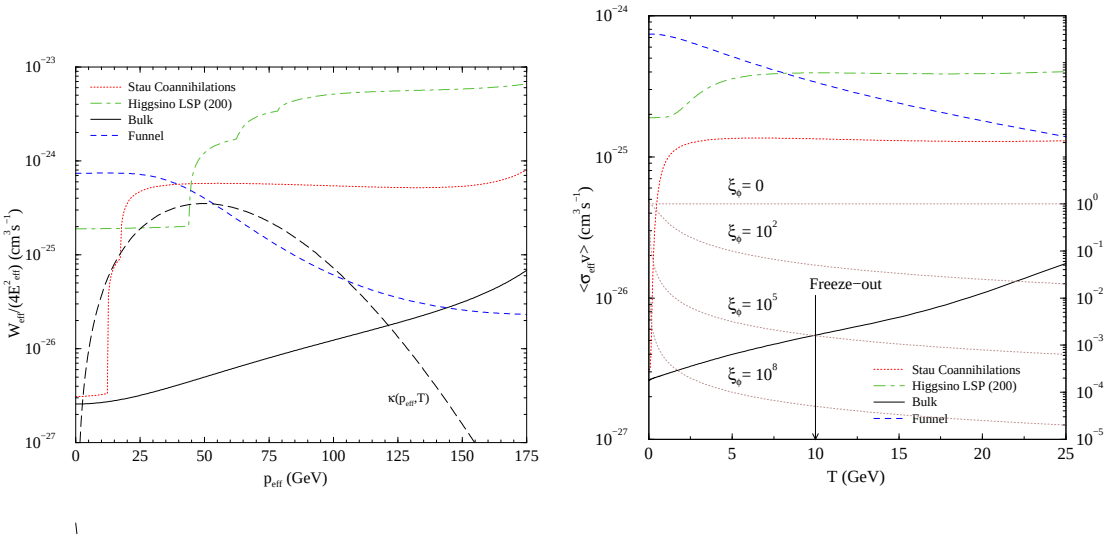

Figure 4.18: *(*Left *): The effective annihilation cross section $W_{\rm eff}/(4E^2_{\rm eff})$ as a function of $p_{\rm eff}$ for the four benchmark models of Tab. 1. The dashed line indicates the thermal weight factor $\kappa(p_{\rm eff}, T)$ at the freeze-out temperature $T^{\rm NQ}_{\rm f.o.}$.* (Right)*: The thermally averaged effective cross section $\langle\sigma_{\rm eff} v\rangle$ as a function of the temperature for the four benchmark models. The brown dotted lines represent the suppression factor $\left(\sqrt{1+\xi_\phi \frac{T^2}{T_f^2}}\right)^{-1}$ due to a quintessential component whose amount at freeze-out is given by ξ_ϕ; the corresponding reference scale is shown on the right-hand side of the figure.*

strip. Between the coannihilation and the bulk regions, we find the intermediate case of the higgsino LSP: this is expected actually, since coannihilations phenomena take place there as well, though on top of neutralino pair-annihilation processes which are by far more efficient than in the bino-like case. Finally, the weakest quintessential enhancement is found in the funnel region.

With the purpose of understanding the peculiar pattern emerging from Fig. 4.17, we consider the effective thermally averaged annihilation cross section $\langle\sigma_{\rm eff} v\rangle$, which we rewrite in the following form [52]:

$$\langle\sigma_{\rm eff} v\rangle = \int_0^\infty {\rm d}p_{\rm eff} \frac{W_{\rm eff}(p_{\rm eff})}{4E^2_{\rm eff}} \kappa(p_{\rm eff}, T), \tag{4.38}$$

where $p_{\rm eff}$ and $E_{\rm eff} = \sqrt{p^2_{\rm eff} + m^2_\chi}$ are respectively the three-momentum and energy for a pair of lightest neutralinos in their center of mass frame. $W_{\rm eff}$ is the effective annihilation rate per unit volume and unit time; in case coannihilation processes are present, it can be written as a weighted sum over all annihilation and coannihilation processes [53]:

$$W_{\rm eff} = \sum_{ij} \frac{4p^2_{ij}}{p_{11}} \frac{g_i g_j}{g_1^2} \sqrt{s}\ \sigma_{ij}. \tag{4.39}$$

Here g_i is the number of internal degrees of freedom for the particle i, p_{ij} the common magnitude of the three-momentum in the center of mass frame for the process involving particles i and j, σ_{ij} the relative cross section, while the index 1 refers to the LSP (*i.e.* $W_{\rm eff}$ correctly reduces to the light neutralino pair-annihilation rate W_{11} if no coannihilations are present). Finally, Eq. (4.38) defines the function $\kappa(p_{\rm eff}, T)$, which contains the temperature dependence in the Maxwell-Boltzmann approximation.

We plot the resulting $W_{\rm eff}/(4E^2_{\rm eff})$ for the four benchmark models of Tab. 4.2 in the left panel of Fig. 4.18. When a coannihilation channel becomes kinematically allowed, the

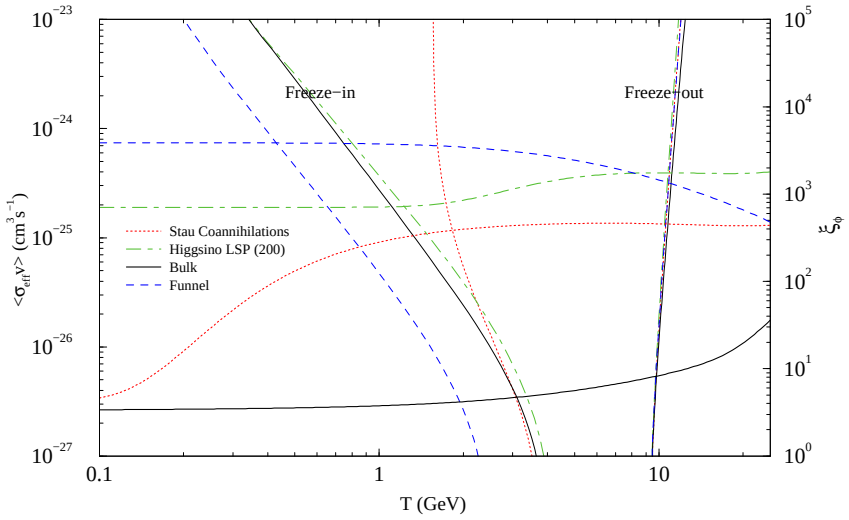

Figure 4.19: *A comparison between the thermally averaged cross section* $\langle\sigma_{\rm eff}v\rangle$ *as a function of the temperature, compared with the temperatures of* freeze-out T_f *(nearly vertical lines on the right) and of* freeze-in $T_{\rm f.i.}$ *(left lying lines). The first one is defined as the temperature when the neutralino number density becomes 50% larger than the equilibrium number density [52], while* $T_{\rm f.i.}$ *is the temperature corresponding to the moment when the number density normalized to the entropy density gets 50% larger than its* asymptotic *value,* i.e. Y_0*, which gives the nowadays relic density.*

effective cross section abruptly rises, as evident from both the case of the stau coannihilations and that of the higgsino LSP. In this last case, also notice how the cross section at low $p_{\rm eff}$ is larger than in the bulk, or stau coannihilations, case. The figure also shows the typical bell shape of the function κ, which exponentially suppresses the large $p_{\rm eff}$ tails of $W_{\rm eff}$ upon integration over $p_{\rm eff}$. As T is reduced, the peak of the corresponding κ function is shifted towards lower $p_{\rm eff}$ values. In the right panel of Fig. 4.18 we plot the result of the integration over $p_{\rm eff}$, obtaining the corresponding curves as functions of T for the various cases. The shape of the resulting curves comes not as a surprise: a decreasing function of $p_{\rm eff}$ (*e.g.* the case of the funnel) gives rise to a *decreasing* function of T, and *vice-versa*.

The temperature evolution of $\langle\sigma_{\rm eff}v\rangle$ critically enters the thermal history of neutralinos, which, we remind the reader, proceeds from higher to lower temperatures, *i.e.* from right to left in Fig. 4.18. At very large temperatures, the number density of relic species closely follows the equilibrium number density. Afterwards two steps can be identified. First, the number density n starts to become *larger* than the equilibrium number density $n_{\rm eq}$, the stage commonly called *freeze-out*. This step takes place when the quantity $\Gamma \equiv n\langle\sigma_{\rm eff}v\rangle$ becomes comparable to the expansion rate of the universe $H(T)$. (We recall that we did not define the freeze-out temperature T_f from the relation $\Gamma = H$, but rather as the temperature when the neutralino number density becomes 50% larger than the equilibrium number density, *i.e.* $n = 1.5 n_{\rm eq}$ [52]). Then, a second step goes on, where (co-)annihilations of neutralinos further reduce the number-to-entropy density Y towards its asymptotic value Y_0, with an efficiency which depends on the relevant scattering cross sections at temperatures below the freeze-out. For definiteness, we label as *freeze-in* temperature $T_{\rm f.i.}$ the temperature at which $Y = 1.5\ Y_0$.

In our discussion we have considered so far just the first step, *i.e.* the increase in T_f set by the shift $H^{\rm NQ} \to H^{\rm NQ}\sqrt{1+\rho_\phi/\rho_{\rm rad}}$. To explain the pattern emerging from Fig. 4.18, we need however to consider also the second effect mentioned above. The evolution of Y after the freeze-out temperature is described by the Boltzmann equation (4.32) with $Y_{\rm eq} = 0$. Once

the equation is exactly integrated, one obtains:

$$\frac{1}{Y_0} = \frac{1}{Y_f} + \int_{T_0}^{T_f} \mathrm{d}T \frac{\langle \sigma_{\rm eff} v \rangle}{H} \frac{1}{3} \frac{ds}{dT}. \tag{4.40}$$

In presence of Quintessence, the integrand in the right-hand side gets the suppression factor, which similarly to step 1 has the form

$$\frac{1}{H^{\rm NQ}(T)} \to \frac{1}{H^{\rm NQ}(T)} \frac{1}{\sqrt{1+\rho_\phi/\rho_{\rm rad}(T)}} \simeq \frac{1}{H^{\rm NQ}(T)} \frac{1}{\sqrt{1+\xi_\phi T^2/T_f^2}}. \tag{4.41}$$

Clearly, the longer the post-freeze-out annihilations last, the larger the suppression of the relic abundance is. The convolution between $\langle \sigma_{\rm eff} v \rangle$ and the suppression factor of Eq. (4.41) sets the shift in the temperature range where neutralino annihilations are effective, down to the *freeze-in* temperature. The four benchmark models present very different low temperatures behaviors of $\langle \sigma_{\rm eff} v \rangle$: in the case of the funnel, $\langle \sigma_{\rm eff} v \rangle$ *increases* at lower temperatures, hence we expect a sharp shift of $T_{\rm f.i.}$ to lower values when ξ_ϕ increases; on the other hand, in the case of stau coannihilations, $\langle \sigma_{\rm eff} v \rangle$ rapidly drops to low values at low temperatures, therefore the freeze-in takes place earlier, at higher temperatures. The higgsino LSP and the bulk cases are intermediate, and quite similar to each other. The emerging picture is clarified in Fig. 4.19, which summarizes the two effects we discussed: we depict both the freeze-out and the freeze-in temperatures as functions of ξ_ϕ, which is shown on the vertical scale of the right-hand side of the plot, and the thermally averaged cross sections in the four cases under inspection. While the (slight) hierarchy in the freeze-out temperature depends on the cross sections at temperatures larger than that of freeze-out, the above mentioned convolution dictates the shape of the freeze-in curves. The pattern emerging from the superposition of the two mentioned effects is the one we found in Fig. 4.17.

Since both the freeze-in and freeze-out temperatures depend on the same factor, which scales with ξ_ϕ as $\approx \sqrt{1+\xi_\phi T^2/T_f^2}$, we expect to be able to give a rough rule-of-thumb estimate of the quintessential enhancement effects for a given ξ_ϕ. We do not, however, expect a rigorous scaling as the two intervening effects act on different temperature ranges. The approximate scaling we propose tries to keep track of both the correct limit as $\xi_\phi \to 0$ and the would-be behavior at large ξ_ϕ:

$$\Omega^Q/\Omega \approx (1 + a \cdot \xi_\phi)^b, \quad b \simeq 0.5 \tag{4.42}$$

We find that the actual enhancement in the full numerical computation reproduces, at *large* ξ_ϕ, our simple ansatz, although with a less steep increase: a best fit procedure gives in fact $0.4 \lesssim b \lesssim 0.5$. Moreover, the interplay between the shifts in the freeze-out and freeze-in temperatures (see Fig. 4.19), non-trivially dictates the value of the a parameter. From the overall fit to the benchmark model data we obtain $0.1 \lesssim a \lesssim 0.2$. Though the accuracy of resorting to such an approximate formula is necessarily low, Eq. (4.42) gives the correct order of magnitude of the quintessential enhancement, and may be of relevance in some cases. For instance, if one deals with a cold Dark Matter model giving rise to extremely low relic densities, and embeds it in a quintessential cosmological scenario, the formula given in Eq. (4.42) may reveal the order-of-magnitude amount of Quintessence at freeze-out which the given model would need in order to get the correct relic density today.

4.3.4 Light higgsinos and winos as Dark Matter candidates

When the lightest neutralino is dominated by its higgsino or wino component, the corresponding relic abundance is typically *smaller* than the estimated non-baryonic matter content of

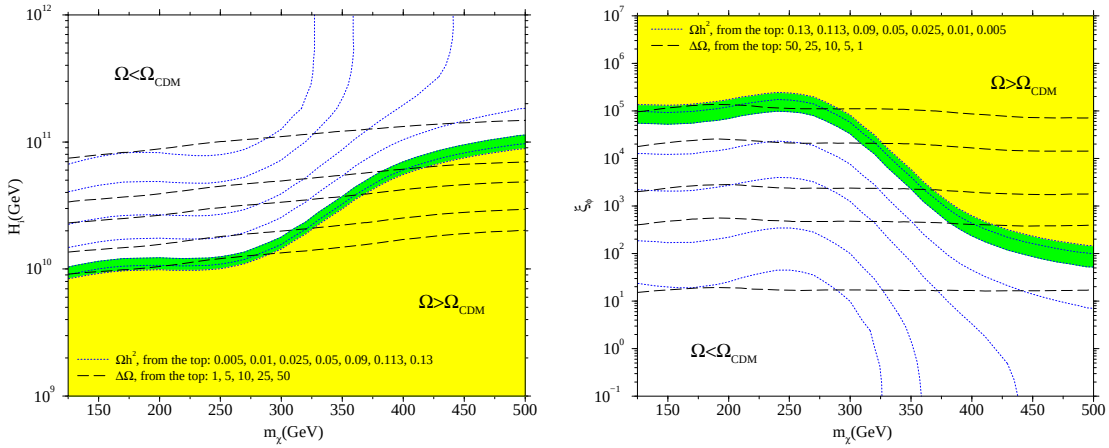

Figure 4.20: *(*Left *): The* $(m_\chi,\ H_i)$ *plane for the case of the representation* **200***, with SUSY parameters* $\tan\beta = 45$, $A_0 = 0$, $\mu > 0$, $m_0 = 500$ GeV *and fixing* $\lambda = 3.5$. *The yellow shaded region has* $\Omega_\chi h^2 > 0.13$, *while in the green-shaded strip* $0.09 < \Omega_\chi h^2 < 0.13$. *(*Right *): The* $(m_\chi,\ \xi_\phi)$ *plane at the same values of the SUSY parameters as before. In both panels, the blue dotted lines correspond to points at fixed* $\Omega h^2 = 0.005,\ 0.01,\ 0.025,\ 0.05,\ 0.09,\ 0.113,\ 0.13$, *while the black dashed lines to points at fixed enhancements* $\Delta\Omega = 1,\ 5,\ 10,\ 25,\ 50$.

the Universe. This is first due to the direct annihilation rate of higgsino-like or wino-like LSPs, which is by far larger than that of a bino-like LSP (see *e.g.* the left panel of Fig. 4.18). In fact, not only the couplings involving, for instance, a wino are larger than those involving a bino, since $g_2 > g_1$, but also the number of final states in which winos or higgsinos can annihilate is larger. As an example, winos can annihilate into a couple of weak bosons without any intermediate scalar superpartners, whereas binos cannot. Furthermore, the mass spectrum of a wino-like LSP always yields an approximate mass degeneracy with the lightest chargino, as does a higgsino-like LSP, which is in its turn also very close in mass to the next-to-lightest neutralino. This means that coannihilations between the LSP and the lightest chargino, as well as, in the case of the higgsino, with the neutralino $\widetilde{\chi}_2$, further reduce the relic abundance *in the whole parameter space*. This mass degeneracy with the chargino also bears a rather strong lower bound on the neutralino mass through direct accelerator searches. As a result, in the absence of relic density enhancement processes[5], wino or higgsino LSPs are not adequate to be the main Dark Matter component.

In the present framework of quintessential cosmologies, the enhancement resulting from the shift towards larger values of the freeze-out temperature of cold relics may naturally render wino or higgsino LSPs attractive Dark Matter candidates. In order to elucidate this point, we will discuss two particular cases: mSUGRA with non-universal gaugino masses generated by a gauge kinetic function belonging to the **200** representation of the symmetric product of two $SU(5)$ adjoints, where the LSP is mostly higgsino-like, and the minimal Anomaly Mediated SUSY Breaking (mAMSB), where the LSP is typically almost completely a wino. We show that (1) the relic abundance naturally falls into the preferred cosmological range for a suitable choice of the quintessential parameters and (2) that the needed *fine tuning* in the cosmological parameters is reasonably low, and comparable with that of the supersymmetric parameters.

We study the requirements on the cosmological sector needed to achieve a neutralino relic density compatible with the current estimates of the Dark Matter content of the Universe.

[5] Among these, we mention non-thermal neutralino production through direct or indirect decays of gravitinos or moduli fields [96].

In particular, we consider a sample case in which we fix $\tan\beta = 45$, $A_0 = 0$, $\mu > 0$ and $m_0 = 500$ GeV, and let $M_{1/2}$ vary within the range allowed by EWSB. Changing the value of m_0 does not lead to remarkable changes in the results: we only find that at lower values $m_0 < 500$ GeV and at low $M_{1/2}$ the A-funnel condition $2\ m_\chi \simeq m_A$ approximately holds, while at larger values of m_0 the $M_{1/2}$ range is more and more reduced by the requirement of successful EWSB. In order to have a wider range of neutralino masses, we resort to a large value of $\tan\beta$.

We report our results in Fig. 4.20, where rather than $M_{1/2}$ we consider the neutralino mass m_χ as the last SUSY parameter which fully fixes our model setup: the mass range displayed is dictated by the fulfillment of phenomenological bounds and of successful radiative EWSB. The Quintessence contribution to the expansion rate of the Universe is defined by fixing the parameter $\lambda = 3.5$ in the exponential potential of Eq. (4.30) and by varying the initial condition on H_i. In the left panel we show the parameter H_i, while in the right panel we plot a more model independent result by trading H_i for the Quintessence-to-radiation ratio at neutralino freeze-out ξ_ϕ. The region shaded in yellow bears an excessive relic density enhancement, giving rise to $\Omega_\chi h^2 > 0.13$, while the green shaded strip has $0.09 < \Omega_\chi h^2 < 0.13$, and thus approximately reproduces the 2-σ range for $\Omega_{\rm CDM} h^2$. In the figures we also plot some isolevel curves both for Ωh^2 (blue dotted lines) and for $\Delta\Omega$ (black dashed lines). At large H_i, *i.e.* when Quintessence is dominant only at very early times, the iso-Ω curves tend to become vertical lines, in the region where $\Delta\Omega \ll 1$. As expected, we find that the quintessential enhancement, quantified by $\Delta\Omega$, is, to a good approximation, fixed by ξ_ϕ, as emerging from the (m_χ, ξ_ϕ) plane, where the lines are almost horizontal. The peculiar behavior of the iso-Ω curves as functions of m_χ is due to the fact that, increasing m_χ, the higgsino fraction of the lightest neutralino grows, thus partly compensating (at $m_\chi \lesssim 250$ GeV) the effect of a larger mass on the relic density. When the neutralino starts to be largely higgsino-dominated ($m_\chi \gtrsim 250$ GeV), Ωh^2 monotonously grows with the neutralino mass. We highlight that at the left sides of the figures, *i.e.* at low m_χ, the required enhancement is $\Delta\Omega \approx 50$, which means that the neutralino relic density in the absence of Quintessence is two orders of magnitude below $\Omega_{\rm CDM}$. Actually, in the absence of Quintessence, the neutralino relic density, at the smallest value for m_χ is found to be $\Omega h^2 \simeq 0.002$. We checked that the **200** model yields, at any $\tan\beta$, a neutralino relic density lying at least a factor 2 below $\Omega_{\rm CDM}$, and in the specific case $\tan\beta = 45.0$, $\Omega_\chi h^2 < 0.03$: therefore, in this context, a relic density enhancement mechanism is mandatory.

We already mentioned the case of the minimal anomaly mediated SUSY breaking (mAMSB) model. Since at the weak scale $M_1/M_2 \sim 3.2$, the LSP of mAMSB models is dominantly a *wino*, with a purity typically larger than 99%. The lightest chargino is thus quasi degenerate with the LSP, and the total cross section of neutralino pair annihilation is very large [44]. The pattern for the quantity $W_{\rm eff}$ is therefore rather similar to that of the higgsino LSP case, a part from the absence of the coannihilations with the next-to-lightest neutralino, and therefore of the second bump visible in the left panel of Fig. 4.18. As far as the quintessential enhancement is concerned, we find, as expected, that the enhancement pattern for wino-like neutralinos is very close to that in the higgsino case.

We study in Fig. 4.21 the quintessential relic density enhancement needed to obtain cosmologically viable neutralino relic densities in the wino LSP mAMSB scenario. We focus on a sample case at $m_0 = 1$ TeV, $\tan\beta = 5$, $\mu > 0$ and $m_{3/2}$ ranging from 32 to 192 TeV. As in the previous higgsino case, we plot the neutralino mass range allowed by accelerator searches (lower bound) and by successful EWSB (upper bound). Again we shade the cosmologically preferred region in green, while the yellow shaded parts yield an overproduction of neutralinos. We plot the $(m_\chi,\ H_i)$ plane in the left part of the figure, while $(m_\chi,\ \xi_\phi)$ is in the right panel. We also show the curves corresponding to particular values of the resulting relic

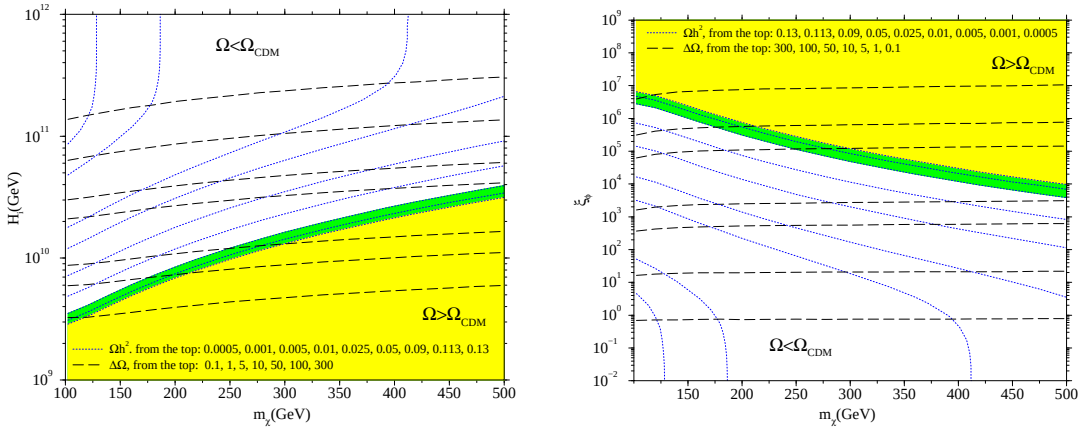

Figure 4.21: *(*Left *): The* $(m_\chi,\ H_i)$ *plane for the case of the anomaly mediated SUSY breaking, at* $\tan\beta = 50$*,* $\mu > 0$ *and* $m_0 = 1$ TeV*. The yellow shaded region has* $\Omega_\chi h^2 > 0.13$*, while in the green-shaded strip* $0.09 < \Omega_\chi h^2 < 0.13$*. (*Right *): The* $(m_\chi,\ \xi_\phi)$ *plane at the same values of the SUSY parameters as before. In both panels, the blue dotted lines correspond to points at fixed* $\Omega h^2 = 0.0005,\ 0.001,\ 0.005,\ 0.01,\ 0.025,\ 0.05,\ 0.09,\ 0.113,\ 0.13$*, while the black dashed lines to points at fixed enhancements* $\Delta\Omega = 0.1,\ 1,\ 5,\ 10,\ 25,\ 50$*.*

density (blue dotted lines) and of the quintessential enhancement (black dashed lines). As emerging from the comparison between Fig. 4.20 and Fig. 4.21, in the present mAMSB case, the needed enhancement factors are *larger* than in the higgsino LSP case, since wino pair annihilations have a larger cross section with respect to the higgsinos. In mAMSB scenarios, the wino-purity does not critically depend on the neutralino mass, thus the iso-Ω curves are remarkably smooth. The relic density, in its turn, is a growing function of m_χ, and therefore the quintessential enhancement needed to drive the resulting neutralino relic abundance to the cosmologically preferred range decreases with increasing neutralino masses. We remark that in the present case the neutralino relic density in the absence of Quintessence is always very low, being $\Omega h^2 \simeq 0.0003$ in correspondence to the lowest neutralino masses. In fact, in the case shown in Fig. 4.21, the needed enhancement factor can be as large as $\Delta\Omega \approx 300$.

4.3.5 Alternative cosmological relic density enhancement scenarios

Other cosmological scenarios, where $H(T)$ is significantly larger than in the ΛCDM model at neutralino decoupling, range from scalar-tensor [6] theories [97, 98] to homogeneous but anisotropic cosmologies [98]: in this latter framework, for the simplest case of Bianchi-I type space-times, where the metric reads

$$\mathrm{d}s^2 = -\mathrm{d}t^2 + R_1^2(t)(\mathrm{d}x_1)^2 + R_2^2(t)(\mathrm{d}x_2)^2 + R_3^2(t)(\mathrm{d}x_3)^2, \tag{4.43}$$

an effective shear energy density, scaling as $\rho_s \sim a^{-6}$, rapidly falls off, but may well dominate at $T_{\mathrm{f.o.}}$. The initial size of the shear component, which can be quantified through the temperature T_s at which $\rho_s = \rho_r$, dictates the value of the parameter ξ, which again faithfully parameterizes the thermal relic abundance enhancement (Fig. 4.22).

Since most indirect detection rates depend on the neutralino self-annihilation rate at zero temperature, one naturally expects that models with a low relic abundance (and therefore with a large neutralino annihilation rate) will give conspicuous detection signals. This in fact

[6] In the case of scalar-tensor theories it has been found that re-annihilations of neutralinos may however reduce the expected size of the relic abundance enhancement [97]

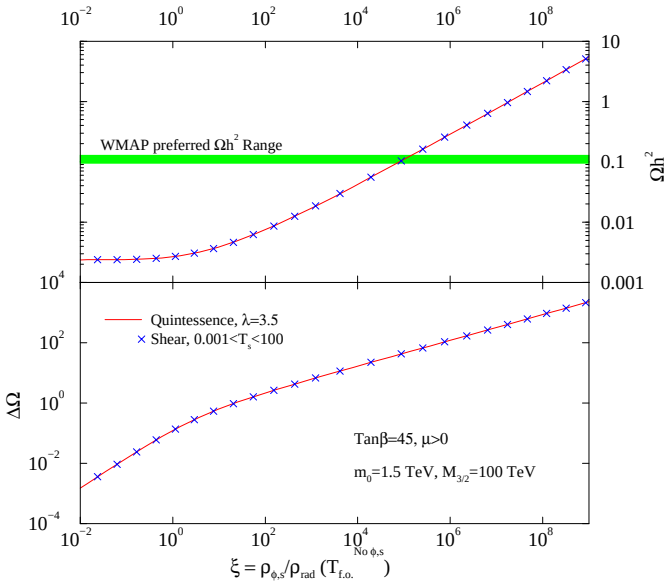

Figure 4.22: *The relic abundance $\Omega_\chi h^2$ and the relative enhancement $\Delta\Omega_\chi$ for the mAMSB model at $\tan\beta = 45$, $\mu > 0$, $m_0 = 1.5$ TeV and $m_{3/2} = 100$ TeV as a function of the energy density ratio of non-standard over standard components at the temperature of neutralino freeze-out (ξ). The red lines correspond to quintessential models with an exponent $\lambda = 3.5$, while blue crosses represent models with primordial anisotropies of various initial size.*

turns out to be the case, particularly for indirect neutralino detection through antimatter searches (see Sec. 5.4). Within the context of cosmological enhancement of neutralino relic abundance, low relic density models may therefore account for the whole Dark Matter content of the Universe, and give spectacular detection rates at future detection experiments. We will give a thorough and detailed discussion of this point in Sec. 5.

Chapter 5

Supersymmetric Dark Matter detection

Provided the Dark Matter content of the Universe, and in particular of our Galaxy, is made up of neutralinos, the latter may in principle be detected. This fascinating chapter of physics lying at the interface of astrophysics and theoretical and experimental particle physics is relatively young, and in the recent years has undergone a major effort of investigation. Here, we will concentrate here only on neutralino detection, though we mention that a vast program of Dark Matter detection for alternative candidates, *e.g.* the axions, is also operative or in a deployment phase.

The detection of Dark Matter particles essentially proceeds through two different strategies. On the one hand, one can hope to *directly* detect the scattering of Dark Matter particles off ordinary matter, by measuring the energy release in detectors (*Direct Dark Matter Detection*). This technique will be reviewed, together with a short snapshot of the current and future experimental programs, in Sec. 5.1. On the other hand, one can look for indirect signals, searching for annihilation products of neutralino pairs which possess features allowing for a discrimination from background sources (*Indirect Dark Matter Detection*). Within this second category, the largest experimental efforts concentrate on the detection of the muon flux originating from charged current interactions of neutrinos produced in neutralino pair annihilations in the center of the Earth or of the Sun (Sec. 5.2). Other indirect detection strategies, which may be particularly promising within given scenarios, include the detection of antimatter (or gamma rays) from neutralino annihilations in the Galactic halo (Sec. 5.4).

Given a particle physics model, it is naturally of the utmost importance to understand which is the most promising detection strategy. This issue not only depends on the details of the supersymmetric scenario, but also on the experimental setup and on the features of the Dark Matter distribution in our Galaxy. We address this question in Sec. 5.5, where we resort both to a set of benchmark theoretical models and to the mentioned MSSM parameter space scan (see Sec. 3.3).

5.1 Direct Dark Matter detection

Although detection techniques involving *inelastic scattering* of neutralinos off nuclei were proposed in the past [99, 100], it was soon realized that the most promising direct detection strategy, both from the point of view of event rates and of signal to background ratios, involves elastic interactions. The physical processes occurring in the direct detection of neutralinos through elastic scattering are schematically sketched in Fig. 5.1: a neutralino scatters off a target nucleus and releases a certain amount of energy, which is measured

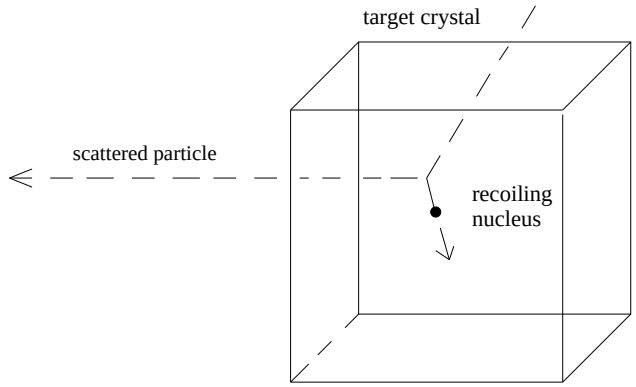

Figure 5.1: *Schematic representation of the elastic scattering of a Dark Matter particle with an atomic nucleus in a detector, from Ref. [3].*

through the ionization produced by collisions with electrons. An updated overview of various experimental setups may be found *e.g.* in Ref. [3].

Elastic scattering proceeds through *spin independent* and *spin dependent* interactions, the latter contributing only in materials featuring a non-zero nuclear spin. Once computed the elementary particles processes, involving quarks and gluons, one must translate the result in terms of interactions with nucleons and finally with nuclei. The relevant effective Lagrangian is given by [3]

$$\mathcal{L}_{\text{eff}} = \sum_{i,q} \alpha^q_{2i} \bar{\chi}\gamma^\mu\gamma^5\chi\bar{q}_i\gamma_\mu q_i + \alpha^q_{3i}\bar{\chi}\chi\bar{q}_i q_i. \tag{5.1}$$

The Lagrangian is to be summed over the quark generations, and the subscript i refers to up- ($i = 1$) and down- ($i = 2$) type quarks. The couplings $\alpha_{2,3}$ can be found *e.g.* in Ref. [101].

The *scalar* neutralino-(A, Z) nucleus scattering cross section, as a function of the hadronic matrix elements $f^{(p,n)}_{Tq,TG}$, is given by

$$\sigma^{\text{SI}}_{\chi N} = \frac{4M_r^2}{\pi}\left(Zf_p + (A-Z)f_n\right)^2, \tag{5.2}$$

where M_r stands for the reduced mass of the nucleus-neutralino system, and

$$\frac{f_{p,n}}{m_{p,n}} = \sum_{q=u,d,s} f^{(p,n)}_{Tq}\frac{\alpha^q_3}{m_q} + \frac{2}{27}f^{(p,n)}_{TG}\sum_{q=c,b,t}\frac{\alpha^q_3}{m_q}. \tag{5.3}$$

Since the f_p and the f_n are basically equal, one can safely write

$$\sigma^{\text{SI}}_{\chi N} \simeq \frac{4M_r^2}{\pi}A^2 f_p^2, \tag{5.4}$$

i.e. the spin-independent scattering adds coherently, giving rise to a cross section proportional to the squared of the atomic weight A. On the other hand, the axial-vector spin-dependent interaction is incoherent. This is the main reason why the current and projected experimental sensitivity of spin-independent searches is by far more promising than that of spin-dependent, as we will further discuss in what follows. We therefore give here a closer look to the structure of scalar neutralino-nucleon interactions.

The scalar interaction channels between quarks and neutralinos are given by the two diagrams collected in Fig. 5.2, involving either a CP-even Higgses t-channel exchange or a scalar quark s-channel exchange. In a typical SUSY setup, the largest contributions to

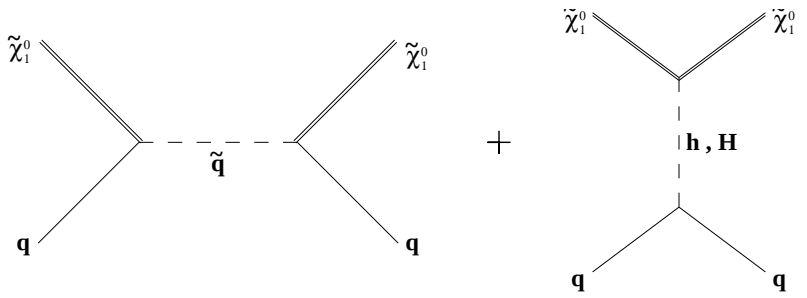

Figure 5.2: *The Feynman diagrams contributing to the direct spin-independent neutralino detection, from [3].*

the effective coupling stems from the Higgses exchange channels. In most cases a good approximation to the neutralino-proton scattering cross section is given by

$$\sigma_{\chi-p} \simeq \frac{1}{4\pi}\left(\frac{gg' f_{Ts}^{(p)} m_p^2}{m_W \cos\beta}\right)^2 \times \left(N_{11}N_{14}\sin\alpha\cos\alpha\left(\frac{1}{m_h^2}-\frac{1}{m_H^2}\right)+N_{11}N_{13}\left(\frac{\sin^2\alpha}{m_h^2}-\frac{\cos^2\alpha}{m_H^2}\right)\right)^2 \tag{5.5}$$

Clearly, the scattering cross section for direct detection greatly depends on many details of the SUSY particle spectrum. The most sensitive dependence, as apparent from Eq. (5.5), relies on the Higgs sector (particularly on the Higgs mixing parameter α and on the heavy Higgses mass scale) and on the relative bino-higgsino content of the lightest neutralino, through the parameters N_{1i}. Cancellations may take place among the dominating amplitudes, in particular if a sufficiently large value of $\tan\beta$ occurs with opposite signs for M_2 and μ [101], while the largest possible values for $\sigma_{\chi-p}$ are achieved for mixed bino-higgsino states with a sufficiently low heavy Higgs sector.

To make the results as model-independent as possible, we plot in Fig. 5.3 the results of the parameter space scan of the general MSSM performed in Ref. [46] (see Sec. 3.3.1 for details). We plot, for reference and guidelines, the current exclusion limit from the Edelweiss experiment [102]; the future experimental reach is instead simulated for the Xenon-1 Ton experiment (or similar facilities) [103]. The right panel shows the results for the spin-dependent neutralino-proton scattering cross section, where we took the exclusion results of the combined available data from Ref. [104], and the prospected reach from Ref. [105]. The results we report are restricted to those SUSY models where the thermal relic abundance lies *within the preferred WMAP range*. The color/symbol code for the scatter plot is as follows: black circles refer to bino-like neutralinos, red squares to higgsino-like and blue diamonds to wino-like.

We notice that models lying in the very upper part of the scatter plot feature either bino or higgsino dominant components; as evident from the figure, spin-dependent searches always feature an experimental sensitivity which is unable to probe any viable SUSY model in our scan.

In order to analyze the statistical properties of neutralino dark matter, we resort to a statistical analysis of *visibility ratios*, *i.e.* signal-to-sensitivity ratios, which allow a transparent comparison between different methods and between current and projected sensitivities. Fig. 5.4 collects the statistical analysis of our results for *spin-independent searches*. The histograms to the left show the cumulative results for all models, while those to the right refer

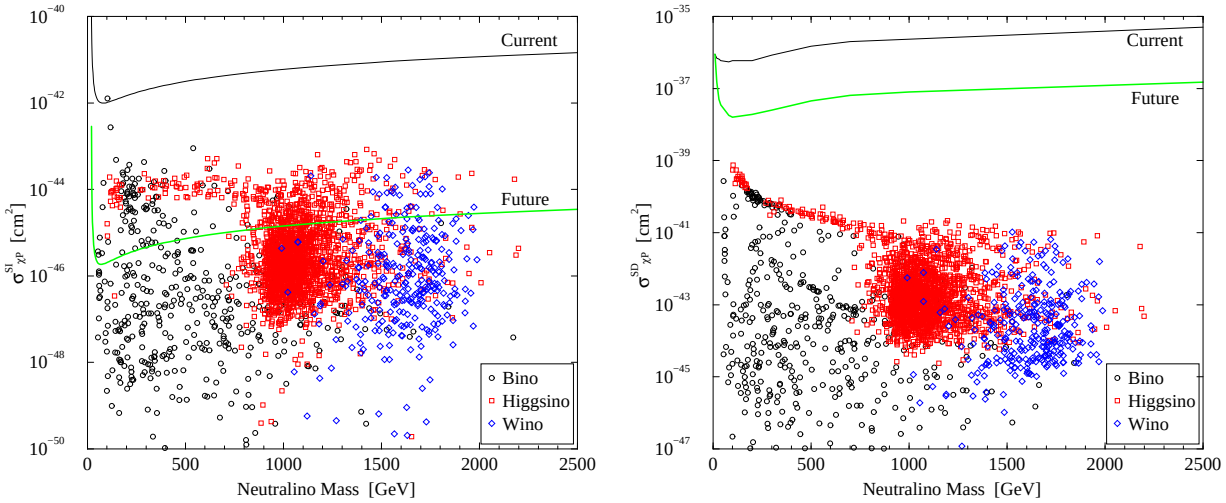

Figure 5.3: *A scatter plot of the Spin Independent (a) and Spin Dependent (b) neutralino-proton scattering cross sections for models whose relic density lies* within the WMAP range. *Black circles represent models in which the lightest neutralino is predominantly a Bino, red squares represent Higgsinos and Blue diamonds Winos. The black lines indicate the current exclusion limits [102], while the green lines the projected exclusion limits at future experiments [103].*

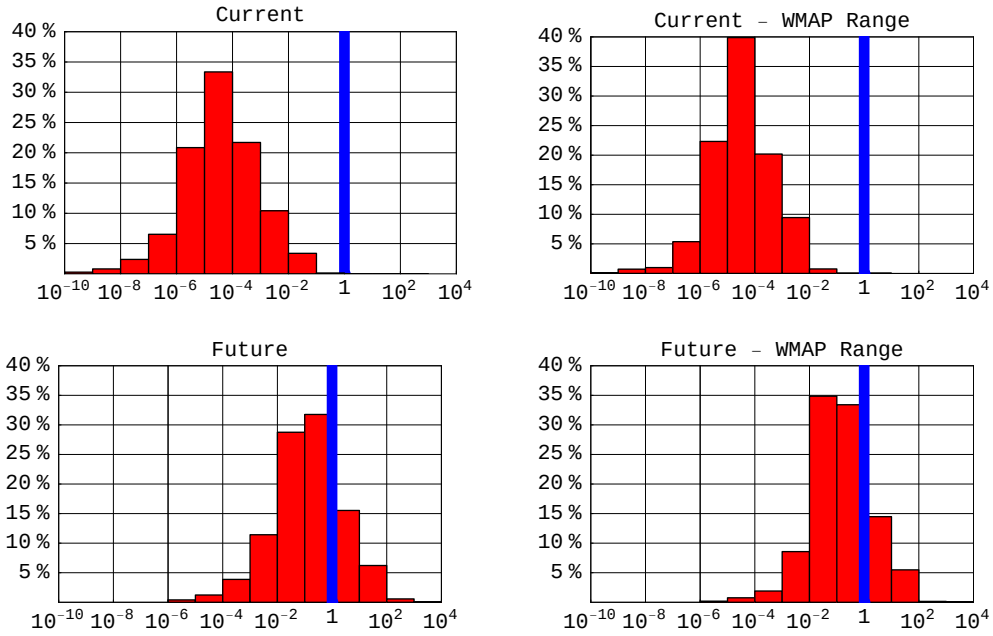

Figure 5.4: *A statistical analysis of the Visibility Ratio (signal-to-sensitivity) for the* Spin Independent neutralino-proton cross section *for all models with a sufficiently low relic abundance (plots to the left) and for models with a relic abundance in the WMAP range (plots to the right). The two upper plots refer to the current exclusion limits, as in Fig. 5.3 (a), black line, while the two lower plots to the future exclusion limits, Fig. 5.3 (a), green line.*

to models within the WMAP range (hence those shown in the scatter plots of Fig. 5.3). The two upper histograms refer to the current limits (those indicated with black lines in Fig. 5.3),

and the two lower ones to the future exclusion limits (green lines in Fig. 5.3). The vertical blue lines indicate the visibility threshold: models lying to the right of the blue line are *above* current or future sensitivities, those to the left currently give no (or will not give, at future experimental facilities) detectable signals. While a negligible fraction of the models lie above the current exclusion limits, approximately 20% of the models (in the WMAP range or with lower relic abundances) will be accessible to Xenon 1-ton [103], or to similar detection experiments. We notice that the current exclusion limits from spin-independent searches are still far from probing a significant portion of the general MSSM parameter space; on the other hand, future experiments will be able to probe 20% of the viable models. The scatter plots also show the mass clustering of pure higgsinos and of winos around, respectively, 1 TeV and 1.6 TeV: the dependence of the neutralino-proton scattering cross section on the details of the SUSY spectrum, particularly concerning the Higgs sector (the sign of the μ parameter and the masses of the CP-even h and H neutral Higgses), and to a less extent the squark sector, yield a scatter in $\sigma^{\rm SI}_{\chi {\rm P}}$ which can well be as large as *four orders of magnitude*.

5.2 Neutrino flux from neutralino annihilations

The density of neutralinos in the Galactic Dark Matter halo is not large enough to give a measurable flux of secondary neutrinos, with the possible exception of a large overdensity in the very poorly known central part of our Galaxy [106]. Quantitative predictions, and an experimentally detectable flux of neutrinos, can instead be traced from neutralino annihilations in the center of the Sun or of the Earth. Neutralinos from the Galactic halo may in fact get trapped into these astrophysical bodies, and begin to sink into the center, where the density enhancement produces annihilations into SM particles, among which are neutrinos, the only particles that may later be detected. In particular, the muon neutrinos are useful for indirect detection of neutralino annihilation processes, since muons have quite a long range in a suitable detector medium, like ice or water. Specifically, they can be detected through their Cherenkov radiation after being produced at or near the detector through the action of a charged current weak interaction of the generic type

$$\nu_\mu + A \to \mu + X. \tag{5.6}$$

Detection of neutralino annihilations into neutrinos is often regarded as one of the more promising indirect detection techniques, and will be subject to extensive experimental investigations at upcoming large neutrino telescopes, like AMANDA and Icecube [107, 108]. The advantage of this detection method, which is common to the case of gamma rays too (contrary, instead, to antimatter searches), is that neutrinos do not interact in the outer space, and therefore the direction from which they arrive points at the location where they were produced. A high-energy neutrino signal in the direction of the center of the Sun or of the Earth is therefore an excellent experimental signature, which may stand up against what is the main limitation of the technique itself, namely the neutrino background generated by cosmic-ray interactions in the Earth's atmosphere.

Quantitatively, the neutrino flux from neutralino annihilations depends on the one hand on the particle physics setup, *i.e.* on the details of the decay chain of a neutralino of a given mass and composition; on the other hand, a crucial role is played by the capture versus annihilation balance in the core of the celestial bodies and on the physics of the propagation of the relevant SM decay products. The differential neutrino flux is given by

$$\frac{{\rm d}N_\nu}{{\rm d}E_\nu} = \frac{\Gamma_A}{4\pi D^2} \sum_f B^f_\chi \frac{{\rm d}N^f_\nu}{{\rm d}E_\nu}, \tag{5.7}$$

where Γ_A is the annihilation rate, D is the distance of the detector from the source (central region of the Earth or of the Sun), f is the neutralino pair annihilation final state (heavy quark-antiquark pairs, $\tau^+\tau^-$ pairs, and gauge, Higgs bosons and gauge-Higgs bosons pairs), and B_χ^f are branching ratios into the final state, the latter giving rise to the energy distribution of neutrinos $\mathrm{d}N_\nu^f/\mathrm{d}E_\nu$. The computation of these spectra has been performed through Monte Carlo simulations [33, 109].

The neutrino-induced muon flux is usually detected looking at upward-going muons from the direction of the Sun and the Earth, since there is always a huge background of downward-going muons generated by cosmic ray interactions with the atmosphere. The differential flux of muons at the detector is given by the general formula

$$\frac{\mathrm{d}N_\mu}{\mathrm{d}E_\mu} = \int_{E_m u^{\mathrm{th}}}^{\infty} \mathrm{d}E_\nu \int_0^\infty \mathrm{d}\lambda \int_{E_\mu}^{E_\nu} \mathrm{d}E'_\mu \; P(E_\mu, E'_\mu; \lambda) \frac{\mathrm{d}\sigma_\nu(E_\nu, E'_\mu)}{\mathrm{d}E'_\mu} \frac{\mathrm{dN}_\nu}{\mathrm{d}E_\nu}, \tag{5.8}$$

where λ is the muon range in the medium (ice or water for the large detectors in the ocean or at the South Pole, or rock which surrounds the smaller underground detectors), $\mathrm{d}\sigma_\nu(E_\nu, E'_\mu)/\mathrm{d}E'_\mu$ is the weak interaction cross section for the production of a muon of energy E'_μ from a parent neutrino of energy E_ν, and $P(E_\mu, E'_\mu; \lambda)$ is the probability for a muon of initial energy E'_μ to have a final energy E_μ after passing a path length λ inside the given detector medium. Finally, E_μ^{th} is the detector threshold energy, which varies from 1 GeV for "small" neutrino telescopes, to tens of GeV for detectors of Km^2 size. Since the integrand of the preceding equation is more weighted over high energies (both because σ_ν approximately linearly rises with the energy, and because the average muon energy grows with E_ν), the final states providing a hard neutrino spectrum (like heavy quarks or leptons and gauge bosons) are those typically giving the largest contribution.

The final ingredient is the computation of Γ_A, the annihilation rate of neutralinos. To this extent, one must follow in detail the rate of change of the neutralino number N_χ in the center of the given celestial body, governed by the equation

$$\frac{\mathrm{d}N_\chi}{\mathrm{d}t} = C_C - C_A N_\chi^2, \tag{5.9}$$

where C_C is the capture rate and C_A is related to the annihilation rate $\Gamma_A = \frac{1}{2} C_A N_\chi^2$. The solution to the Eq. (5.9) in terms of the annihilation rate reads

$$\Gamma_A = \frac{C_C}{2} \tanh^2 \left(\frac{t}{\tau} \right), \tag{5.10}$$

where $\tau = 1/\sqrt{C_C C_A}$ is the equilibration time-scale. Provided $\tau \ll 10^9$ y, equilibrium is a good approximation, the annihilation rate is at his maximum, and it is fully determined by the capture rate.

A crucial and difficult quantity to compute is the capture rate C_C, which depends on the details of the interactions of neutralinos and nuclei inside the Sun or the Earth: form factors and other poorly known quantities often significantly affect the computations. In particular, since the Earth is mainly composed by nuclei with zero spin, while the Sun is dominated by hydrogen, the capture rates in the two celestial bodies will be dominated respectively by the spin independent (Earth) and spin dependent (Sun) rates. A good approximation for the capture rate inside the Sun is given by the relation [1]

$$\frac{C_\odot^{\mathrm{sd}}}{1.3 \cdot 10^{23} \mathrm{s}^{-1}} = \left(\frac{\rho_\chi}{0.3\,\mathrm{GeV\ \ cm}^{-3}} \right) \left(\frac{100\ \mathrm{GeV}}{m_\chi} \right) \left(\frac{\sigma_{p\chi}^{\mathrm{sd}}}{10^{-40} \mathrm{cm}^2} \right) \left(\frac{270\ \mathrm{km/s}}{\bar{v}} \right), \tag{5.11}$$

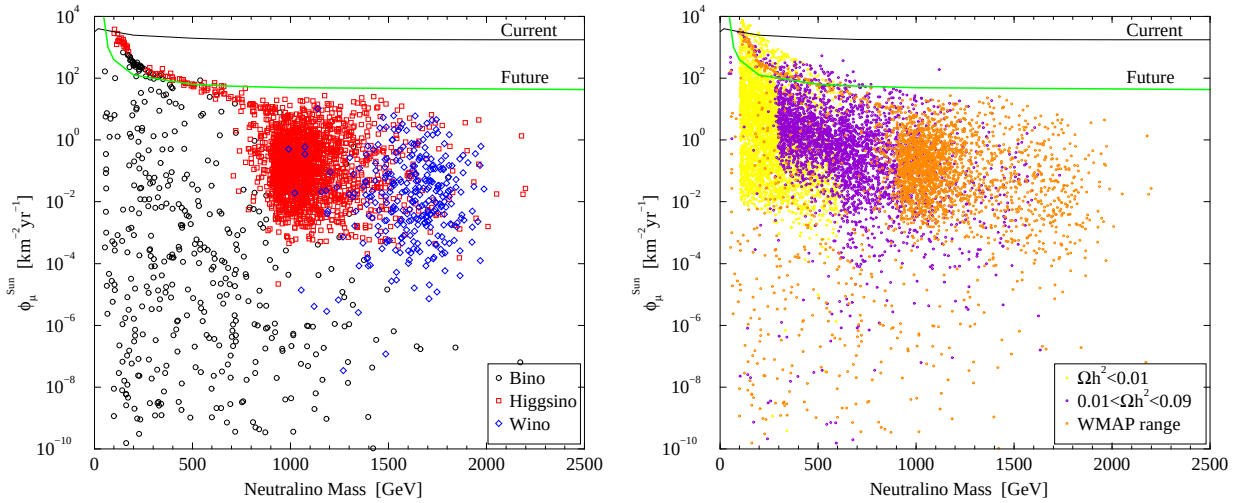

(a) (b)

Figure 5.5: *Scatter plots of the expected muon flux at neutrino telescopes from neutralino annihilations in the center of the Sun, above a 1 GeV threshold. Models in (a) have relic abundances in the WMAP range, and are grouped according to the bino, higgsino and wino content of the lightest neutralino. In (b) we show instead a selection of all models grouped by relic abundance. We also show, respectively with a black and a green line, current and future experimental sensitivity limits.*

where $\sigma_{p\chi}^{\rm sd}$ is the cross section for neutralino-proton elastic scattering via the axial-vector interaction, $\bar{v}$ is the Dark Matter velocity dispersion, and ρ_χ is the local Dark Matter mass density.

A crucial quantity in the actual computation of the muon flux induced by the neutrinos produced by neutralino annihilations is, as stated before, the balance between the capture rate and the annihilation rate: if this is an equilibrium process, then the signal is at his maximum; otherwise large suppressions may occur. The equilibrium time scale inside the Sun is in most cases very small compared to that in the Earth. Depending on the SUSY model, equilibrium may not be reached in the Sun, and it very rarely occurs in the case of the Earth. As a result, in most cases the flux of muon neutrinos from the Earth is far below current and future sensitivities; for this reason, we do not show here any result concerning this detection channel.

In Fig. 5.5 we show that the flux from the Sun may be large enough to be detectable at future experiments (we will use here the future sensitivity prospects for the Icecube experiment [108]). A few models are even already excluded by current SuperKamiokande data [110]. It goes without saying that models with a larger annihilation cross section give larger rates: this point is clarified in the right panel of Fig. 5.5, where we include also low relic density models. Interestingly, we find that, in any case, *DM searches at neutrino telescopes will not probe neutralino masses larger than about 750* GeV. Notice that the overall gross features for spin-dependent rates and for the muon flux from the Sun are rather similar to each other: this does not come as a surprise, since the capture rate into the Sun, mainly composed of nuclei with spin different from zero, depends in fact on the spin-dependent neutralino-nucleon cross section.

The suitable neutralino candidate whose relic abundance lies within the WMAP range, and which will be detectable at neutrino telescopes, is a composite bino-higgsino state with a large enough spin-dependent cross section, and a mass below half a TeV. Models with larger neutralino masses (as pure Higgsinos and Winos with relic abundances within the WMAP

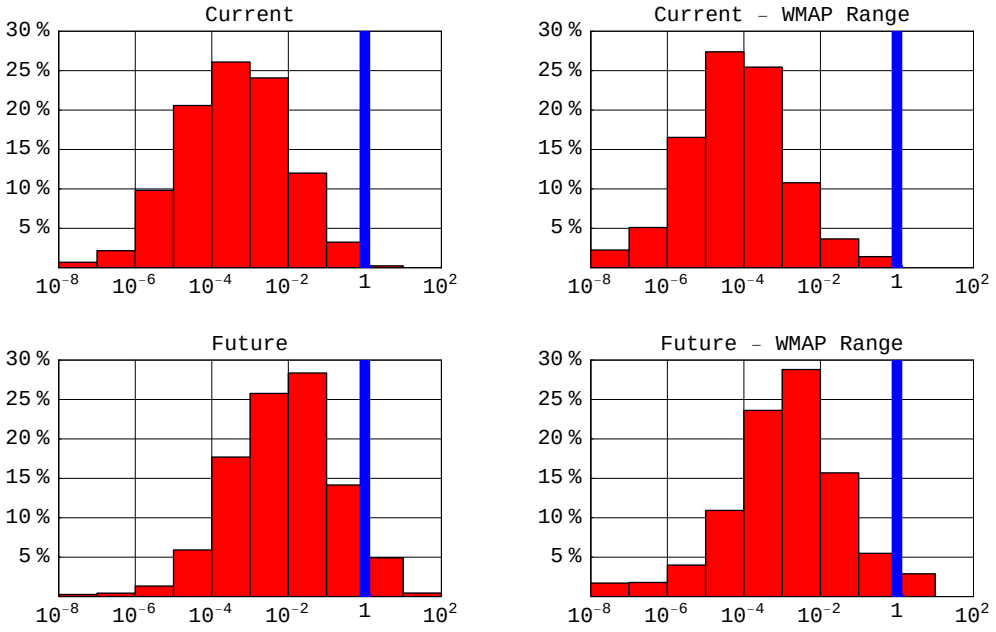

Figure 5.6: *A statistical analysis of the Visibility Ratio (signal-to-sensitivity) for the* Muon flux from the Sun at Neutrino Telescopes *for all models with a sufficiently low relic abundance (plots to the left) and for models with a relic abundance in the WMAP range (plots to the right). The two upper plots refer to the current exclusion limits, as in Fig. 5.5 (a), black lines, while the two lower plots to the future exclusion limits, Fig. 5.5, green lines.*

range) will not be probed at future experiments.

The statistical summary of our scan is shown in the histograms of Fig. 5.6. Once again, current experiments only probe a marginal fraction of the models, particularly if the neutralino relic abundance lies into the WMAP preferred range (histograms to the right). To summarize, we find that future experiments will be able to probe from 3 to 5% of all the viable models.

5.3 Correlating direct searches and neutralino induced muon fluxes

In this section we analyze the correlation between neutralino direct searches and indirect searches at neutrino telescopes. In particular, in Fig. 5.7 we correlate, , spin-dependent neutralino-proton rates with the muon flux from the Sun, and the scalar neutralino-proton cross section with the rate of muons from the Earth (mainly composed by spinless nuclei). As guidelines, we also include current and future sensitivities, at a putative neutralino mass of 1 TeV: models above (or at the right of) the horizontal (vertical) lines will be, or currently are, above projected, or current, sensitivity. The same color code as that of Fig. 5.3 has been used, although we include here models with low relic abundances too.

As a first remark, we point out the well known complementarity between direct and indirect searches: models which are not testable at spin-dependent searches could be accessible at indirect searches in the muon-from-the-Sun channel, and, vice-versa, models with too low muon flux from the Earth may well be above the visibility threshold at direct spin-independent searches.

The correlation between indirect searches at neutrino telescopes and direct detection experiments is clearly visible, though some comments are in order. First, binos always tend to have a smaller muon flux, than higgsinos or winos at the same neutralino-nucleon cross section. This fact is due to the pair annihilation rate, which is typically more suppressed in the case of binos than for winos or higgsinos; the sufficiently low relic abundance of binos has been shown to occur in most cases thanks to *coannihilation processes*, which are however not present for pair annihilations in the potential wells of the Sun or of the Earth. Secondly, the correlation between $\phi_\mu^{\rm Earth}$ and $\sigma_{\chi \rm P}^{SI}$, though clearly present, is scattered over at least four orders of magnitude in $\phi_\mu^{\rm Earth}$ at a given $\sigma_{\chi \rm P}^{SI}$, for each neutralino type. Various factors contribute to this spread: the mentioned effect due to the pair annihilation rate, the details of the annihilation-capture interplay, and possible enhancements due to kinematic effects for particular values of the neutralino mass.

We recall that, if equilibrium is reached, both $\phi_\mu^{\rm Earth}$ and $\sigma_{\chi \rm P}^{SI}$ scale as the squared of the nucleon matrix element of the effective Lagrangian for the scalar neutralino-nucleus interaction $|\langle \mathcal{L}_{\rm sc} \rangle|^2$, while if it is not then [111, 112]

$$\phi_\mu^{\rm Earth} \propto |\langle \mathcal{L}_{\rm sc} \rangle|^4 \langle \sigma_{\rm ann} v \rangle_0 , \tag{5.12}$$

$\langle \sigma_{\rm ann} v \rangle_0$ being the neutralino annihilation rate times the relative velocity in the zero velocity limit. In the case of the $\phi_\mu^{\rm Sun}$ - $\sigma_{\chi \rm P}^{SD}$ correlation, we notice that large fluxes, corresponding to cases where annihilation and capture are in equilibrium, tend to have an extremely strong correlation. The latter is lost when the signal is weaker, once again because equilibrium is not reached, and the dependence on $\langle \sigma_{\rm ann} v \rangle_0$ again enters into the game. In particular, this is the case for binos, where the effects of coannihilations with a large variety of partners can drastically lower the actual neutralino annihilation rate with respect to what expected from

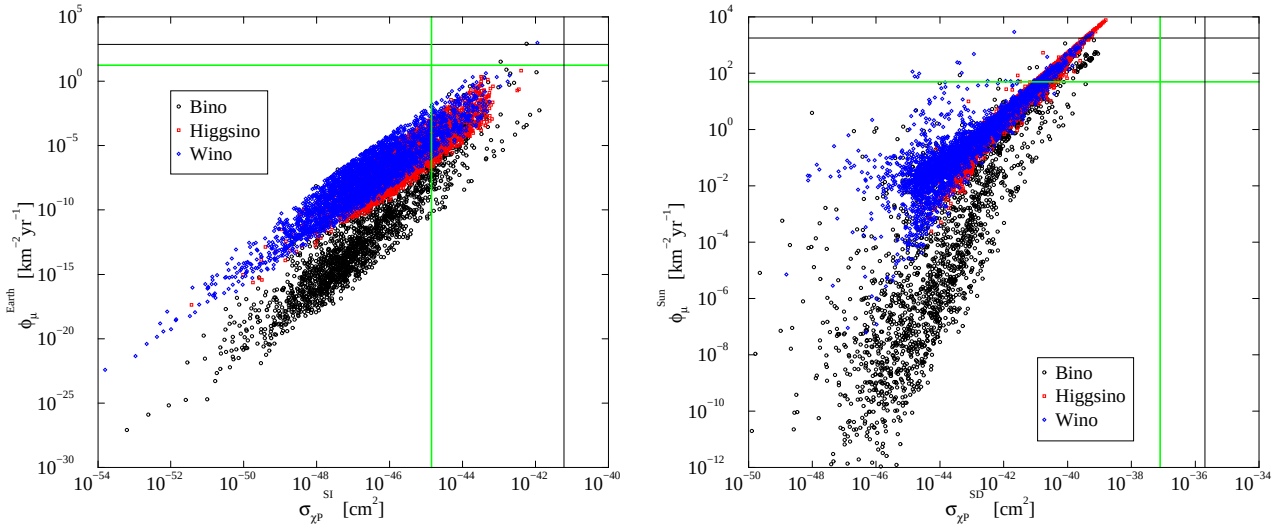

(*a*) (*b*)

Figure 5.7: *The correlation between the muon flux from the Earth and the Spin Independent neutralino-proton scattering cross section (a) and the correlation between the muon flux from the Sun and the Spin Dependent neutralino-proton scattering cross section (b). We show here a reduced sample of all the models considered (including models with relic density below the WMAP range). Black circles represent models in which the lightest neutralino is predominantly a Bino, red squares represent Higgsinos and Blue diamonds Winos. As guidelines, we also include green and black lines representing future and current sensitivities at a neutralino mass of 1000 GeV.*

cosmological abundance arguments: a coannihilating bino can in fact produce a sufficiently reduced relic abundance though featuring a large $\langle \sigma_{\rm ann} v \rangle_0$.

5.4 Antimatter searches

Pair annihilation is the mechanism which sets the thermal relic abundance of WIMPs; although the density of WIMPs in Dark Matter halos today is much smaller than in the early Universe environment, there is still a finite probability for WIMPs in the Galactic halo to annihilate in pairs. In these annihilations the same amount of matter and antimatter is produced; while the matter component is likely to be very subdominant compared to standard astrophysical sources, there seems to be no standard primary source of antimatter, with the bulk of the (scarce) antimatter component in cosmic rays likely being of secondary origin, *i.e.* generated in the interaction of primary cosmic rays (mainly protons) with the interstellar medium (mainly hydrogen and helium). The goal of indirect Dark Matter searches performed through antimatter surveys is then to identify the WIMP-induced antimatter fluxes through their peculiar spectral features, or at least to exclude those Dark Matter candidates which would overproduce antimatter compared to the relatively low background term.

Since the first proposals to search for the exotic antimatter components in cosmic rays due to Dark Matter WIMP pair annihilations [113, 114], calculations of the expected fluxes have been performed with an increasing degree of sophistication. In recent estimates, see, *e.g.*, refs. [115–119], refinements have regarded both the modeling of source functions and the description of the propagation of charged cosmic rays in the Galaxy.

Source functions are proportional to the number of WIMP pairs which may potentially annihilate anywhere in the Galaxy; postulating that Dark Matter is smoothly distributed in the Galactic halo, the number density of pairs can be expressed in terms of the Dark Matter density profile as $1/2\,(\rho_\chi(\vec{x})/m_\chi)^2$. Even in this limit, further extrapolations are needed, since unfortunately $\rho_\chi(\vec{x})$ is poorly constrained by available dynamical data on the Galaxy. In the present section, we will mainly focus on a Dark Matter halo described by the so-called Burkert profile [120]:

$$\rho_B(r) = \frac{\rho_B^0}{(1 + r/a)\,(1 + (r/a)^2)}\ ; \tag{5.13}$$

it is a profile with a large core radius, that has been tested against a large sample of rotation curves of spiral galaxies [121]. Such a choice is somehow conservative: results from N-body simulation of hierarchical structures in CDM cosmologies find in fact singular halo profiles. In an extreme model of baryon infall [122], with very large angular momentum transfer between the baryonic and the dark components, a Burkert-type profile may replace the CDM cuspy halo after the gas has been settling in the inner portion of a galaxy to form its luminous components.

Scenarios of baryon infall in which the CDM cusp is preserved are feasible as well, and we will discuss one such possibility in Sec. 5.5.2, where we will also discuss the implications of switching from one halo model to another for neutralino Dark Matter detection with different strategies. We make a sample choice of the free parameters in Eq. (5.13), fixing the length scale parameter $a = 11.7$ kpc and the local halo density $\rho_B(r_0) = 0.34$ GeV cm^{-3}, according to available dynamical constraints.

Once the source functions are fully specified, the next step is to model the *propagation* of charged cosmic rays through the Galactic magnetic fields. We consider here an effective two-dimensional diffusion model in the steady state approximation. In this propagation model we do not explicitly include reacceleration effects, but mimic them through a diffusion coefficient,

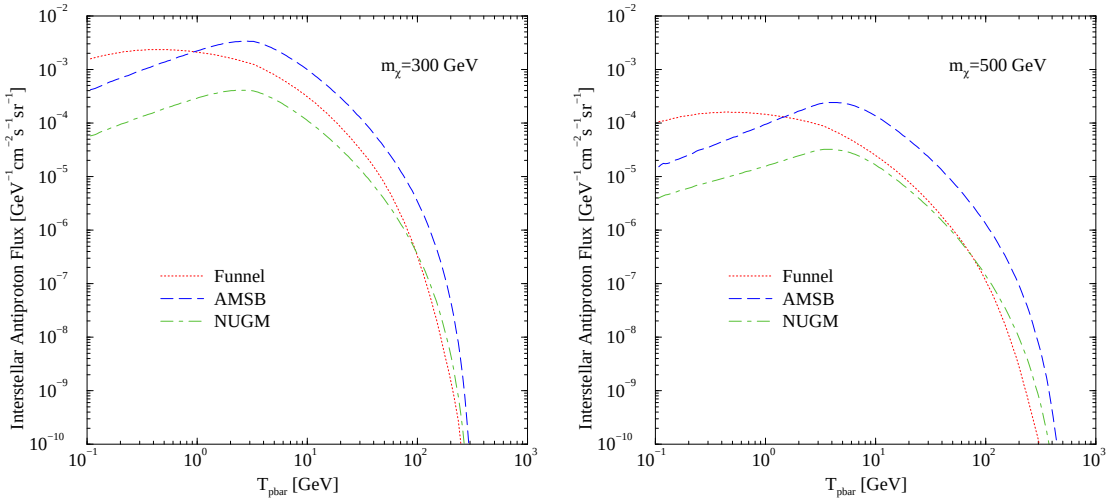

Figure 5.8: *The interstellar antiprotons flux, as a function of the antiprotons kinetic energy* $T_{\rm pbar}$*, for two values of the neutralino mass, respectively* $m_\chi = 300$ *GeV (left) and* $m_\chi = 500$ *GeV (right), for the three SUSY models of Tab. 5.1.*

D, which takes the form of a broken power law in rigidity, R,

$$\begin{aligned} D &= D_0\,(R/R_0)^{0.6} \qquad \text{if} \quad R \geq R_0 \\ D &= D_0 \qquad\qquad\quad \text{if} \quad R < R_0\,. \end{aligned} \tag{5.14}$$

This form has been used in a number of studies on the propagation of cosmic rays; *e.g.*, in Ref. [123], using the `Galprop` [124] propagation code, it has been shown that it gives a fair estimate of ratios of primary to secondary cosmic ray nuclei, for a suitable choice of the free parameters in the model. Here, we implement this same setup, *i.e.* take Eq. (5.14) with $D_0 = 2.5 \times 10^{28}$ cm^2 s^{-1} and $R_0 = 4$ GV, in a cylindrical diffusion region of radius equal to 30 kpc and half height equal to 4 kpc, plus a galactic wind term. For antiprotons and antideuterons, this setup is interfaced to the semi-analytic diffusive-convective propagation model described in Ref. [116], which do not allow for an energy loss term (particles are removed whenever they scatter off the interstellar medium). For positrons we exploit the results in Ref. [117], where a propagation model with a term accounting for positron energy losses (the dominant terms accounting for inverse Compton scattering on starlight and on the cosmic microwave background) was solved analytically; such model has been recently improved and extended to allow for the implementation of a diffusion coefficient in the form of Eq. (5.14) and to keep a full two-dimensional structure (the corresponding code is included in the latest release of the `DarkSUSY` package).

The final step needed to compare our results with measurements is to include a proper treatment of *solar modulation effects* on the propagation of cosmic rays through the solar system up to the Earth location. To sketch this effect, we implement the one parameter model based on the analytical force-field approximation by Gleeson & Axford [125] for a spherically symmetric model. The solar modulation parameter, sometimes dubbed Fisk parameter Φ_F [126], is assumed to be charge-sign independent for simplicity, and can therefore be taken for all species to be equal to the corresponding parameter as determined for proton cosmic-ray flux. The latter has been measured with some accuracy over the full 11-year solar cycle.

From the particle physics point of view, antimatter fluxes from neutralino annihilations

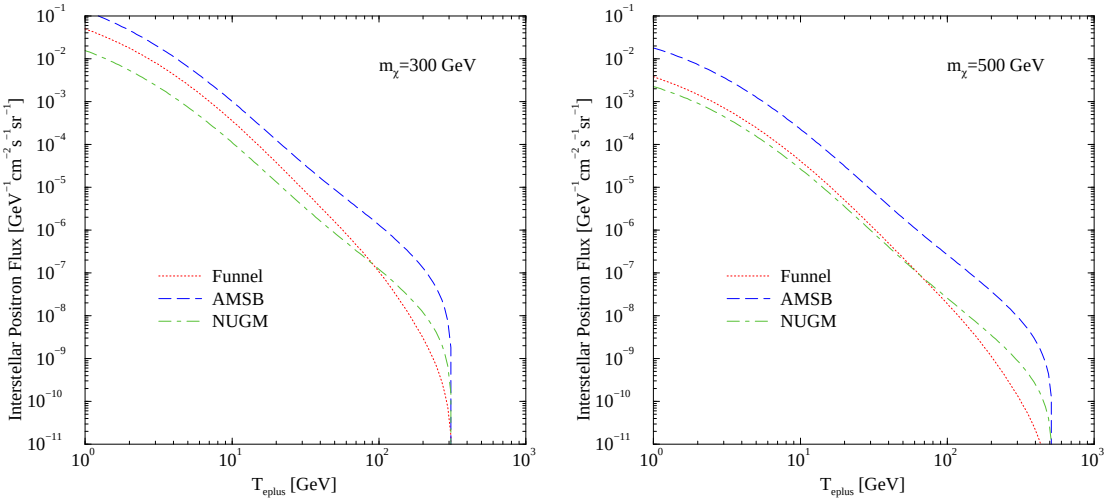

Figure 5.9: *The interstellar positrons flux, as a function of the positrons kinetic energy* $T_{\rm eplus}$*, for two values of the neutralino mass, respectively* $m_\chi = 300$ *GeV (left) and* $m_\chi = 500$ *GeV (right), for the three SUSY models of Tab. 5.1.*

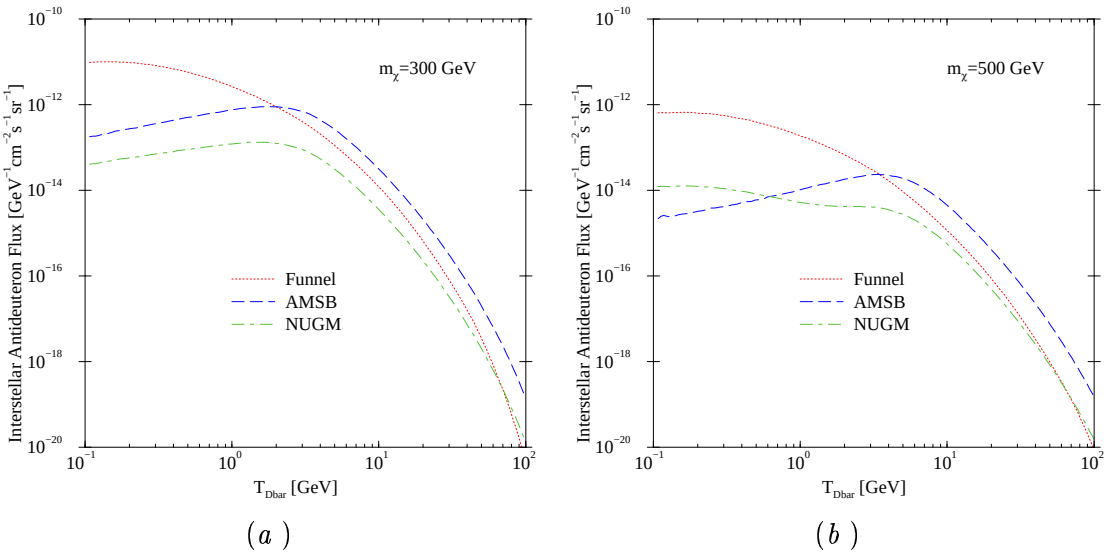

Figure 5.10: *The interstellar antideuterons flux, as a function of the antideuterons kinetic energy* $T_{\rm Dbar}$*, for two values of the neutralino mass, respectively* $m_\chi = 300$ *GeV (left) and* $m_\chi = 500$ *GeV (right), for the three SUSY models of Tab. 5.1.*

depend on the one hand on the number density of neutralinos in the galactic halo (and therefore, for a given CDM halo profile, on the inverse of the neutralino squared mass), and on the other hand on the specific features of the annihilation processes, in terms of the overall interaction rate and of the standard model final products. In figures 5.8, 5.9 and 5.10 we show the interstellar fluxes of antiprotons, positrons and antideuterons for a few selected models within three benchmark scenarios, which we will study and describe in some detail in Sec. 5.5.1, which feature respectively a resonantly annihilating bino (**Funnel** model) a wino (**AMSB** model) and a higgsino (**NUGM** model) lightest neutralino [127]. In the left and right panels of each of the figures we compare (kinetic) energy spectra for the given antimatter

species at different neutralino masses, respectively 300 GeV (left) and 500 GeV (right). The $1/m_\chi^2$ suppression effect due to the neutralino number density dilution at growing masses is everywhere evident. The spectral features of the antimatter fluxes critically depend on the decay channels of the annihilating neutralinos. In the case of the **Funnel** model (but the same holds for a typical bino within a mSUGRA like scenario), the largely dominating decay channels are $b\bar{b}$ (around 90%) and $\tau^+\tau^-$ (around 10%): this particular pattern is due to the fact that the value of $\tan\beta$ which has been chosen is particularly large, so that decays into up-type fermions (charm or top) are very suppressed with respect to those into down-types. The resulting antimatter from hadronization of b quarks as well as τ decay products yield typically *soft* antimatter particles: as emerging from the figures, at the lowest energies of interest, binos in the **Funnel** model always give larger fluxes than higgsinos and winos.

The energy spectrum in the **AMSB** model, where the lightest neutralino is a highly pure wino, reflects that of the dominating decay channel, namely W^+W^-, whose branching ratio is always above 98%. As regards hadronic antimatter (antiprotons and antideuterons), annihilating winos tend to give rise, from hadronization of W decay products, to a peak in the antimatter particle energy around a few GeV. The precise location of the peak non-trivially depends on the details of the antiproton and antineutron production, though its location in energy *increases* at larger masses (see Fig. 5.8 and 5.10). In the positron channel, a clean peak is located at $E_{e^+} \simeq m_\chi/2$: the origin of this very neat feature is the prompt decay $W^+ \to e^+ \nu_e$, where, since the annihilating neutralinos are non-relativistic, the energy of the decaying W is close to m_χ.

Turning to the case of higgsinos (in the **NUGM** model we fixed the higgsino content 99.8%, see Sec. 5.5.1), the spectral features of antiprotons and positrons neatly reproduce those of winos, though at lower fluxes (the suppression being motivated both by a smaller effective annihilation cross section and by a suppression factor in the couplings of higgsinos to the W bosons). Noticeably, the antideuteron flux is instead larger than that of winos at energies below the GeV. This spectral feature is motivated by the fact that higgsinos decay with $\sim 50\%$ probability into W^+W^-, and with $\sim 45\%$ probability into Z^0Z^0: while antiprotons and positrons production from Z^0 decays is very similar to that from W decays, the creation of low energy antineutrons from Z^0Z^0 is remarkably enhanced, thus giving rise to the mentioned peak in the antideuteron low-energy flux.

5.4.1 Constraining SUSY models through antimatter searches

Once the Dark Matter halo and the cosmic rays propagation and secondary flux have been set, it will be possible to rule out a given SUSY model confronting the obtained estimates with available data. The simplest and neatest way is simply to resort to a χ^2 analysis, as we will show below. Assessing the reach of next generation space-based experiments is instead a less trivial task, since it involves some further assumptions both on the detectors' sensitivity and on the statistical biases. In the present section we will discuss a novel approach to the determination of the experimental sensitivity on SUSY models at future antimatter search experiments, and present our results in full details in next section.

Fig. 5.11 shows the spectral features, after solar modulation for a given step along the solar activity cycle, of primary antiparticles and of the background, comparing the total expected signals to the data on antiprotons and positrons taken during the corresponding modulation phase. The figure refers to a common neutralino mass of 300 GeV. As regards the secondary antimatter fluxes, which play here the role of backgrounds, our estimates are produced running the `Galprop` [124] code in the configuration for the propagation parameters we have adopted for the signals. We remark that for both species, the computed backgrounds provide by themselves excellent fits of the data: we obtain, for background only, a reduced χ^2

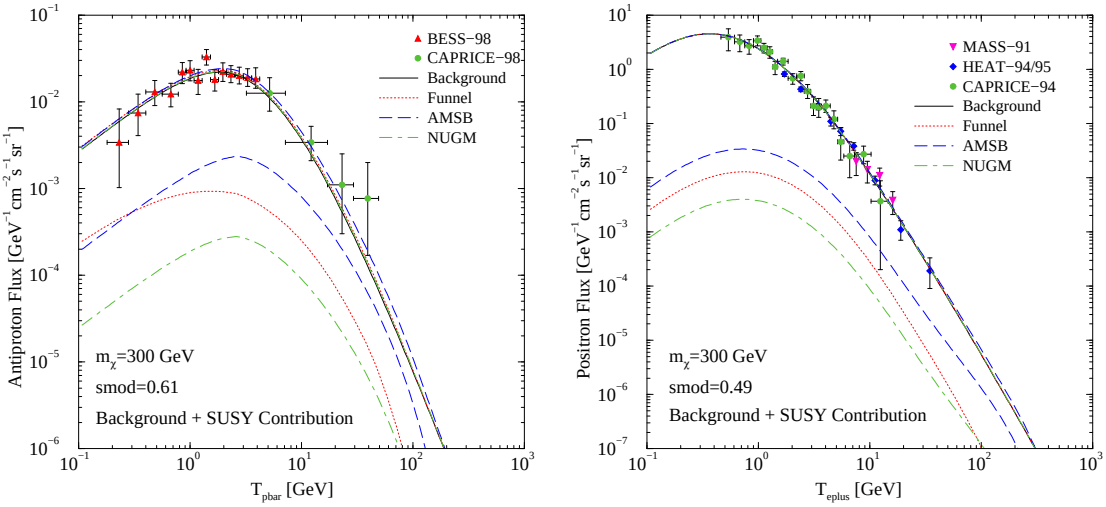

Figure 5.11: *(a): The solar-modulated antiprotons flux, as a function of the antiprotons kinetic energy* $T_{\rm pbar}$. *The black line corresponds to the calculated background, while the three colored thick lines to the total signal for the three SUSY models at a mass* $m_\chi = 300$ *GeV. The thin lines correspond to the SUSY contributions alone. The data from BESS-98 [128] and CAPRICE-98 [129] are also shown. (b) The solar-modulated positrons flux, as a function of the positrons kinetic energy* $T_{\rm eplus}$. *The black line corresponds to the calculated background, while the three colored thick lines to the total signal for the three SUSY models at a mass* $m_\chi = 300$ *GeV. The thin lines correspond to the SUSY contributions alone. We also plot the positron data from MASS-91 [130], HEAT-94/95 [131] and CAPRICE-98 [132].*

equal to 0.82 for antiprotons and to 0.95 for positrons. A primary flux will then be *excluded* as long as it gives rise to a statistically unacceptable χ^2, no longer compatible with currently available data. At a given neutralino mass, the signal-to-background ratio for antiprotons, after solar modulation, is much more promising than that for positrons, with the possible exception of the case of large energies, around the $m_\chi/2$ peak in the positron spectrum, which lies however far above the currently sampled energies.

New generation space-based experiments for antimatter searches PAMELA [133] and AMS [134] will tremendously enhance the resolution and accuracy of positron and antiproton spectra measurements, as compared to existing balloon borne results. With the purpose of assessing discrimination capabilities of future experimental facilities, we will sketch here the possibility of disentangling an exotic component out of a standard secondary background. To this extent, we will implement a statistical χ^2 analysis to compare the case of a pure background measurement with that of the occurrence of a signal.

The relevant experimental parameters entering the estimate are given by:

- The *geometrical factor* of the experimental facility, *i.e.* its effective area, A;
- The time of data acquisition T;
- The energy coverage of the experiment, with the relative definition of the energy bins, *i.e.* their number $n_{\rm b}$ and the size $(\Delta E)_i$ of each of them.

We will declare that a given SUSY model is going to be *discriminable* at a certain future experiment, and at given X% confidence level, if the χ^2 induced by the SUSY model is larger than the $(\chi^2)^{X\%}_{n_{\rm b}}$ corresponding to $n_{\rm b}$ degrees of freedom. Letting $N_i^P = N_i^S + N_i^B$ be

the number of projected events in a given bin i, the sum of the number of signal plus the background events, and N_i^O be the number of observed events, with a standard deviation $\Delta_{N_i^O}$, the χ^2 is defined as

$$\chi^2 = \sum_{i=1}^{n_b} \frac{\left(N_i^P - N_i^O\right)^2}{\left(\Delta_{N_i^O}\right)^2}, \quad N_i^P = N_i^S + N_i^B. \tag{5.15}$$

We will suppose that the standard deviation has a Gaussian distribution, *i.e.*

$$\Delta_{N_i^O} \simeq \sqrt{N_i^O}. \tag{5.16}$$

We are interested in finding the limiting cases, *i.e.* those cases for which an eventual signal is a small component compared to the background. Therefore, we will make the assumption that:

$$N_i^S \ll N_i^B\,, \quad \text{or} \quad N_i^O \simeq N_i^B\,. \tag{5.17}$$

Eq. (5.15) will then read

$$\chi^2 = \sum_{i=1}^{n_b} \frac{\left(N_i^S\right)^2}{\left(\sqrt{N_i^B}\right)^2} \tag{5.18}$$

Now, since the number of events in an energy bin ΔE is given, as a function of the flux of particles ϕ, by

$$N = (\Delta E) \cdot \phi \cdot A \cdot T, \tag{5.19}$$

and indicating with ϕ_s and ϕ_b the signal and background fluxes respectively, Eq. (5.18) will read

$$\chi^2 = \sum_{i=1}^{n_b} \frac{\left(\phi_s^i\right)^2}{\phi_b} \cdot (\Delta E)_i \cdot A \cdot T. \tag{5.20}$$

The quantity in Eq. 5.20 is what will be used to asses the future sensitivity at antimatter experiments. We will declare that a model is *within discrimination capabilities* of a given future experiment at X% confidence level if it satisfies the relation

$$\chi^2 \;>\; (\chi^2)_{n_b}^{X\%}. \tag{5.21}$$

We focus, for definiteness, on the case of the PAMELA detector, and compute the reduced χ^2 for an effective area of 24.5 cm^{2}sr, an exposure time of 3 years, and resorting to a trial energy binning as sketched in Ref. [135][1]. The results we will show in the next section, to be compared against other detection techniques, are in the limit of known background, *i.e.* in the (optimistic) scenario in which degeneracies in the parameters used to model the propagation of charged cosmic rays in the Galaxy are resolved, say, by precision measurements of ratios of secondaries to primaries for several light cosmic-ray nuclei; in this context, we model the background according to the same estimates already implemented above.

[1]The data binning is not going to be homogeneous, since the fluxes have a peak at a few GeV energy. For definiteness, we divided the total logarithmic energy interval scanned by Pamela into three parts and estimated the respective number of bins from Fig. 7 of Ref. [135].

5.5 Comparing different search strategies

The issue of the *comparison* between different search strategies, and of the complementarity among them, has since long been the subject of various investigations (see *e.g.* [111, 112]). A necessary step in order to carry out a sensible assessment of the potential of various detection methods is to assume consistent Dark Matter halo profiles, and to compute the various quantities with the resulting Dark Matter velocity and density distributions. We describe in Sec. 5.5.2 the procedure we will follow here.

Moreover, in order to directly confront detection experiments often scarcely homogeneous among each other, one must resort to suitable quantities which allow cross comparisons. To this extent, we adopt *Visibility Ratios*, *i.e.* signal-to-sensitivity ratios, as in the preceding sections for direct detection and for muon fluxes, as well as for antideuteron fluxes. For the more subtle case of antiprotons and positrons searches we will resort to the parameterization of the future experiments detection capability described in the preceding section; an alternative, though less accurate, estimate of the latter will be also used for statistical purposes in Sec. 5.5.3

As regards the particle physics setup, in the present work we resort to two different attitudes: in Sec. 5.5.1 we introduce three *benchmark models*, motivated by high energy principles, and representing three cases of neutralino compositions; the models we resort to feature large annihilation rates, and therefore a low relic abundance in the standard thermal scenario. On the other hand, in Sec. 5.5.3 we keep on with the low energy random parameter space scan within the general MSSM, following the procedure described in Sec. 3.3.1, allowing and discussing both low relic density models and models whose relic abundance falls within the WMAP range.

5.5.1 Direct and indirect Dark Matter searches in benchmark low relic density models

We focus here on three minimal SUSY frameworks with the lightest neutralino being respectively bino, wino and higgsino like, each of them in large purity configurations. All models are soundly motivated from the high energy physics setup point of view. The neutralino mass ranges within values allowed by all accelerator direct and indirect bounds.

Binos: the **Funnel** model. We consider the mSUGRA scenario, and select models within the funnel region, along a section of the $m_{1/2}$-m_0 parameter space in which the lightest neutralino mass *exactly matches* the resonance condition with the CP-odd Higgs boson mass, *i.e.* $2 \cdot m_\chi = m_A$. In mSUGRA, the tree level value of m_A is fixed by $\tan\beta$ and by the sign of μ through EWSB Conditions; taking into account that we need the lightest neutralino to be the LSP, the resonance is realized only at $\tan\beta \gtrsim 35$ in case $\mathrm{sgn}\mu < 0$, or at $\tan\beta \gtrsim 50$ if $\mathrm{sgn}\mu > 0$. Since for $\mu < 0$ and large $\tan\beta$ the SUSY contributions to $BR(b \to s\gamma)$ are large, and rule out models up to fairly heavy neutralinos, we consider an example with positive μ, $\tan\beta = 55$ and trilinear coupling $A_0 = 0$ (the latter is fixed for definiteness, as it does not play much of a role). In this configuration the resonance curve starts at a minimum value of $m_{1/2}$ (and therefore m_χ) below which the lightest stau is lighter than the lightest neutralino[2], and ends at at maximum $m_{1/2}$ corresponding to the model with neutralino relic abundance exceeding the CDM upper limit. The bino purity of these models is anywhere significantly large, always above 99.6% (see Tab. 5.2). We will hereafter indicate this set of configurations as the **Funnel** model.

[2]In this low mass region, stau coannihilation effects are also present, and are taken into account in the computation of the relic abundance; however, they are not relevant in the context of Dark Matter searches.

Model	$M_{1/2}$, $m_{3/2}$, M_3	$\tan\beta$	sgn(μ)	Defining Condition
Funnel	$700 \div 1450$	55	> 0	$2\, m_\chi \simeq m_A$
AMSB	$23 \div 231$	50	> 0	$m_0 = 1500$ GeV
NUGM	$879 \div 1096$	50	> 0	$M_1/M_3 = 10$, $M_2/M_3 = 2$, $\widetilde{H} = 99.8\%$

Table 5.1: *The three SUSY models under consideration. Models* **Funnel** *and* **NUGM** *have mSUGRA-like boundary conditions at the high energy scale, while model* **AMSB** *features minimal Anomaly Mediated SUSY Breaking. $M_{1/2}$ indicates the value (in GeV) of the common gaugino mass at the grand unification scale $M_{\rm GUT}$ in model* **Funnel** *(second column); in model* **AMSB** *the neutralino mass is driven instead by the value $m_{3/2}$ of the gravitino mass (in TeV, second column); finally, model* **NUGM** *(*non-universal gaugino masses*) has the gaugino non-universality pattern of the* **200** *representation of the symmetric product of two $SU(5)$ adjoints, and the high energy parameter we use is the gluino mass M_3 (in GeV, second column). For each model, the value of the common scalar SUSY breaking mass m_0 is dictated by the* Defining Condition*, which is indicated in the last column of the Table. The scalar trilinear coupling is set to $A_0 = 0$ for all models.*

Model	Bino fraction	Wino fraction	Higgsino fraction
Funnel	$> 99.6\%$	$< 0.05\%$	$< 0.5\%$
AMSB	$< 0.02\%$	$> 98\%$ for $m_\chi > 100$ GeV	$< 2\%$ for $m_\chi > 100$ GeV
NUGM	$< 0.01\%$	$< 0.2\%$	99.8%

Table 5.2: *The lightest neutralino composition for the three SUSY models of Tab 5.1, in terms of the bino, wino and higgsino fractions.*

Winos: the **AMSB** model. In the so-called minimal Anomaly Mediated SUSY Breaking (mAMSB) scenario [42–45] the gaugino masses are proportional, through the gravitino mass $m_{3/2}$, to the beta functions of the $SU(3)$, $SU(2)$ and $U(1)$ gauge groups; this drastically affects the soft breaking gaugino mass hierarchies at low energies, as compared to a supergravity and grand-unification inspired scenario: the lightest neutralino is in fact always *wino*-like, with a remarkably large purity. This feature induces a nice property of the mAMSB scenario, *i.e.* the homogeneity of observables over its parameter space: except for accidental cancellations, the relic abundance and the rates for indirect detection are sensitive to the value of the LSP mass, but have a rather mild dependence on other specific features of the low energy structure of the theory. We decided to resort to rather large values both for the common scalar mass parameter $m_0 = 1500$ GeV, and for $\tan\beta = 50$. The sign of μ was assumed to be positive. The range of the gravitino mass (and therefore of the lightest neutralino) is bounded from below by the null-results of chargino searches at LEP [136][3], and from above by the fact that one enters in the region where EWSB can no longer be fulfilled, giving raise to an unphysical Higgs sector. We label the configuration defined by this choice of parameters, which is summarized in Tab. 5.1, as **AMSB** model; details on the composition of the lightest neutralino are given in Tab. 5.2.

Higgsinos: the **NUGM** model. The assumption that gaugino masses unify at the GUT scale $M_{\rm GUT}$ may be relaxed in a number of ways. In the context of supergravity, non-vanishing gaugino masses are generated through the SUSY breaking vev of the auxiliary component of the lowest-order, non-renormalizable term in the gauge kinetic function. In order to preserve gauge invariance, the SUSY breaking vevs must lie in a representation belonging to the symmetric product of two adjoints of the underlying unified gauge group. In the case of

[3] In the case of mAMSB, the LEP bound on the chargino mass is somewhat weakened due to the very small splitting between the lightest neutralino and the lightest chargino. We will nonetheless restrict to values larger than 100 GeV.

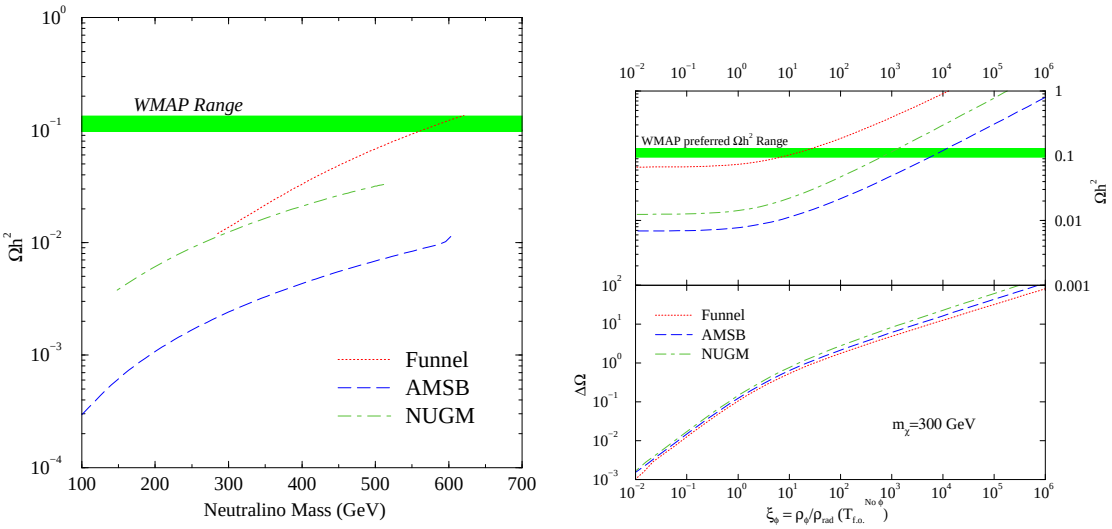

(*a*) (*b*)

Figure 5.12: *In the figure to the left we show as a function of the neutralino mass, the neutralino relic abundance, for the three models described in the text (see Tab. 5.1), respectively featuring a resonantly annihilating bino (***Funnel***), a wino (***AMSB***) and a higgsino (***NUGM***) lightest neutralino, in the standard cosmological scenario. The green band indicates the preferred WMAP range [6]. The right panel shows instead the relic density enhancement within the quintessential scenario of Ref. [88],* i.e. *with an exponential potential, with the exponent* $\lambda = 3.5$*, for the three benchmark models. The upper part shows the relic abundance, while the lower part the relative enhancement* $\Delta\Omega = (\Omega_Q - \Omega)/\Omega$*, both as a function of the parameter* ξ_ϕ*, the ratio of the quintessential to radiation energy densities at the neutralino freeze-out temperature computed in absence of Quintessence.*

$SU(5)$ GUTs, one has

$$(\mathbf{24} \times \mathbf{24})_{\text{symm}} = \mathbf{1} \oplus \mathbf{24} \oplus \mathbf{75} \oplus \mathbf{200}. \tag{5.22}$$

Universal gaugino masses are generated *only* if the SUSY breaking field lies in the singlet representation **1**. In all other cases, particular ratios between gaugino masses will hold at the GUT scale [137, 138]. In particular, two of the four representations yield a *higgsino-like* LSP, namely the **75** and the **200**. We focus here on the **200**, because in the case of the **75** successful EWSB forces the parameter space to rather narrow regions, and to low values of $\tan\beta$ [70]. The parameter space in the corresponding minimal scenario is analogous to the mSUGRA case, with a gaugino mass parameter, which we take to be the gluino mass M_3, and a common scalar mass parameter m_0 (plus again $\tan\beta$, A_0 and $\text{sgn}(\mu)$). Since we want to study the case of a pure higgsino, we solve the parameter space degeneracy by requiring a fixed higgsino content of the lightest neutralino, $\widetilde{H} = 99.8\%$. This specific value has been chosen in order to maximize the neutralino mass range. m_χ turns out to decrease at growing m_0, along the iso-higgsino content lines; analogously to our previous choices, we fix $\tan\beta = 50$, $A_0 = 0$ and $\text{sgn}\mu > 0$, and let m_0 vary from 0 to the largest value compatible with EWSB, achieving a rather wide neutralino mass range. Details on the model are provided in the bottom line of Tab. 5.1; this configuration will be indicated from now on as **NUGM** (non-universal gaugino mass) model.

For all the three benchmarks scenarios introduced above, soft breaking parameters, gauge and Yukawa couplings are evolved down to the weak scale with the ISASUGRA RGE code as given in version 7.67 of the ISAJET software package [139]. Weak scale spectra are interfaced into the `DarkSUSY` code [77], which is then used for the computations of the relic density and of direct and indirect detection rates. Regarding, in particular, the relic abundance calculations,

we rely on a code which provides a high-precision, fully-numerical treatment of resonances and coannihilation effects, here necessarily needed to properly include the resonance on the A Higgs boson for the **Funnel** model and chargino coannihilations for the **AMSB** and **NUGM** models (for both pure winos and higgsinos, the lightest chargino is nearly degenerate in mass with the lightest neutralino). Neutralino relic abundances for the three models considered, for a standard cosmological setup and no extra non-thermal sources, are shown in the left-hand side of Fig. 5.12, in the neutralino mass range allowed for each scenario.

In the right panel of Fig. 5.12 we show instead an example of the quintessential enhancement of the thermal neutralino relic abundance at work on the three models within the above described benchmark scenarios, at a common mass $m_\chi = 300$ GeV (see sec 4.3). The upper panel shows the relic abundance of each model as a function of the parameter ξ_ϕ, which, we recall, is defined as the ratio between the quintessential energy density ρ_ϕ to the radiation energy density $\rho_{\rm rad}$ at the neutralino freeze-out temperature taken in the absence of Quintessence. This parameter has been shown to suitably gauge out most of the dependence on the particle physics setup, and to describe the relic density enhancement effect in other cosmological scenarios, as for instance the case of an anisotropic primordial Universe with an effective shear energy density scaling again as a^{-6} [98, 140]. From the figure we deduce that, at a neutralino mass of 300 GeV, the **Funnel** model would require an extra energy density component 10 times larger than that of radiation at neutralino freeze-out, while larger amounts are needed in the **NUGM** and in the **AMSB** cases (respectively around 10^3 and 10^4). The lower panel shows the relative enhancement, defined as in Eq. (4.34). As already mentioned and described in detail in Sec. 4.3, we find a rather small spread in values of $\Delta\Omega$ among the SUSY models considered here and for given values of the parameter ξ_ϕ.

Current exclusion limits

Ruling out a model from antimatter fluxes amounts to evaluating the χ^2 of the expected signal plus background, after taking care of the different solar modulation effects in the relevant period of data-taking. We will show here the *reduced* χ^2, *i.e.* the χ^2 divided by the relevant number of data (respectively 49 for antiprotons and 32 for positrons). The 95% confidence level (C.L.) exclusion limit will lie at a χ^2 around 1.33 for antiprotons and 1.4 for positrons, though $\chi^2 \sim 1$ indicates that the model is around its "*visibility threshold*". We will find models for which reduced χ^2 are above 10 or so, that are excluded with no doubt, and models closer to the quoted confidence levels; for the latter one should keep in mind that we are not taking into account uncertainties in the propagation parameter model and in the halo profile (although in this respect we are taking a rather conservative scenario), hence the limits we will quote should not be intended as sharp cut-offs.

The quality of the data on the local antiproton and positron cosmic ray flux has kept improving in recent years. As regards the antimatter flux data we take into account, we will compare the predicted fluxes to the antiproton data collected with fairly good statistics by the BESS experiment during its flights in 1997, 1998, 1999 and 2000 [128] in the energy range between 180 MeV and 4.2 GeV, and by the CAPRICE experiment during its 1998 flight [129] in the range between 3 and 50 GeV. For the positron fluxes, we consider the data published by the HEAT Collaboration about the 1994-1995 flight [131], by the CAPRICE team in a flight in 1994 [132], and finally the data obtained by MASS-91 in 1991 [130]: the overall energy range covered by these measurements extends from 460 MeV to 34.5 GeV. We have chosen not to include in our analysis any data which have been reported just as antiproton or positron fractions (rather than absolute fluxes) and any datasets such as the one on positrons from the AMS test flight [141], that maps a low energy interval in which a primary neutralino-induced contribution is expected to be rather suppressed.

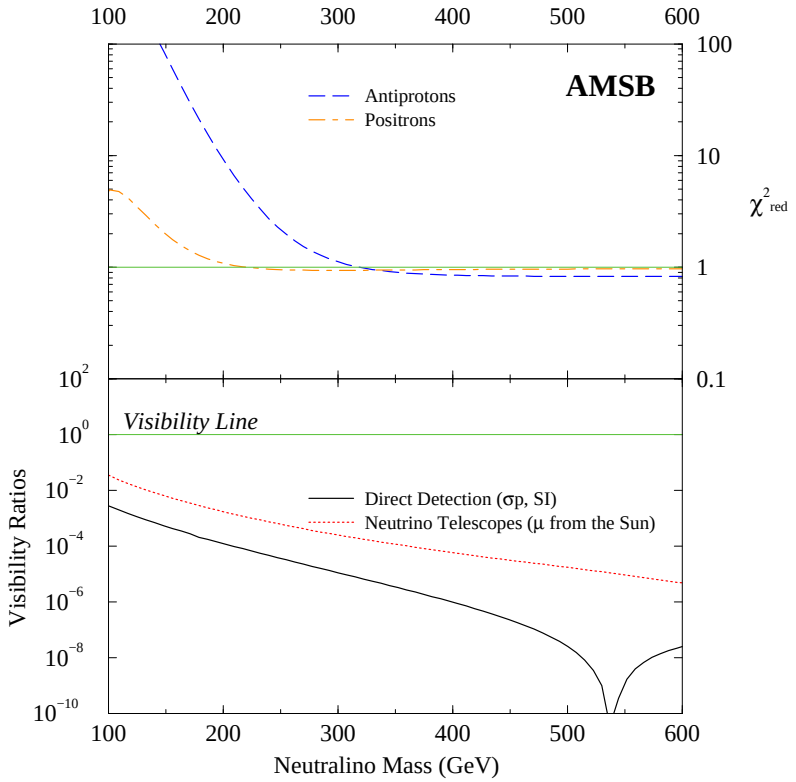

Figure 5.13: *Current exclusion limits on the* **AMSB** *model from direct and indirect Dark Matter searches, as a function of the neutralino mass. In the upper panel we show the reduced* χ^2 *of the background plus SUSY signal, and, as a guideline,* $\chi^2_{\rm red} = 1$*; in the lower panel we show the ratio of the expected signal and of the current exclusion limits (*Visibility Ratio*) for direct Dark Matter detection (neutralino-proton spin-independent scattering cross-section, solid line) and on the neutrino-induced muon flux from neutralino pair-annihilation in the center of the Sun (dotted line). The "*Visibility Line*" corresponds to values of the expected signal equal to the current exclusion limits: models above the Visibility Line would be already ruled out.*

We compare the statistical analysis on antimatter fluxes with the expected signal-to-sensitivity ("*visibility*") ratio for direct, spin-independent searches and for the muon flux at neutrino telescopes, originating from neutralino annihilations in the center of the Sun[4]. The visibility ratio for direct detection refers to the expected neutralino-proton scattering cross section over the current experimental sensitivity level. For definiteness, we will refer to the EDELWEISS 2002 [102] results and estimate the corresponding exclusion limit, rather than to the standard Maxwell-Boltzmann local velocity distribution as usually done, by using the *self-consistently* derived velocity distribution of the halo model under consideration, and taking into account relevant effects, such as target materials, form factors, and threshold. [5]

As far as the muon flux induced by neutrinos from the Sun is concerned, the current best limits are from the SUPER-KAMIOKANDE Collaboration in 2002 [110]. For this detection method too, the signal is computed estimating the capture rates with the appropriate velocity distributions.

[4]We always find that spin-dependent direct detection, and the muon flux from the center of the Earth or from the Galactic center, have visibility ratios by far smaller than those we consider.

[5]An effect compatible with being due to WIMP-nucleon scatterings has been reported by the DAMA Collaboration, see their latest report in Ref. [142]. Unfortunately, none of the models considered here give any effect at the level of such signal.

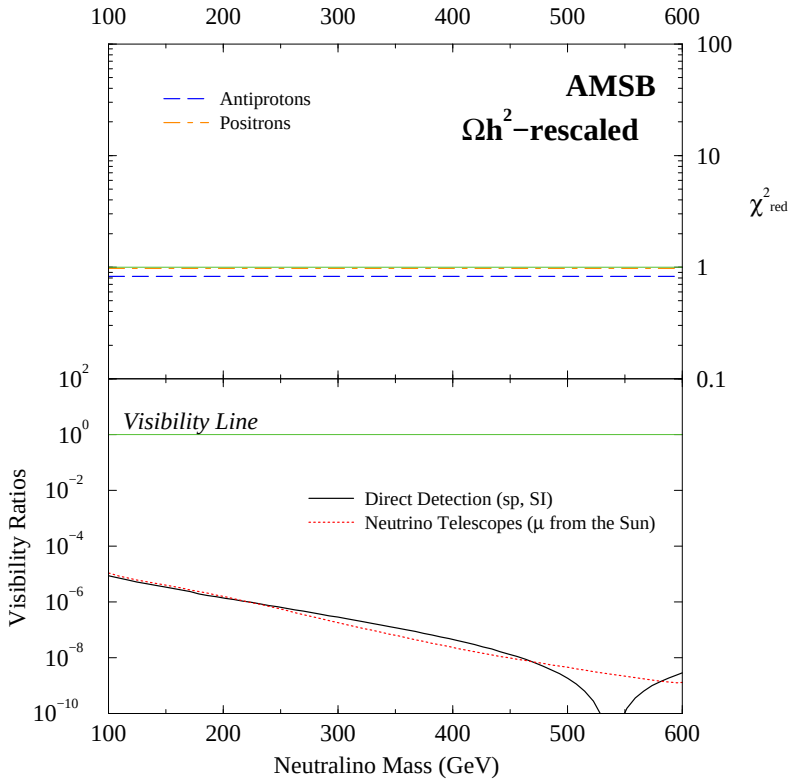

Figure 5.14: *The same as in Fig. 5.13, again in the* **AMSB** *model, but with a rescaled neutralino density profile, according to the formula* $\rho_\chi^{\rm resc} = \rho_{\rm CDM}\ \Omega_{\rm CDM}/{\rm Min}\left(\Omega_\chi, \Omega_{\rm CDM}^{\rm min}\right)$.

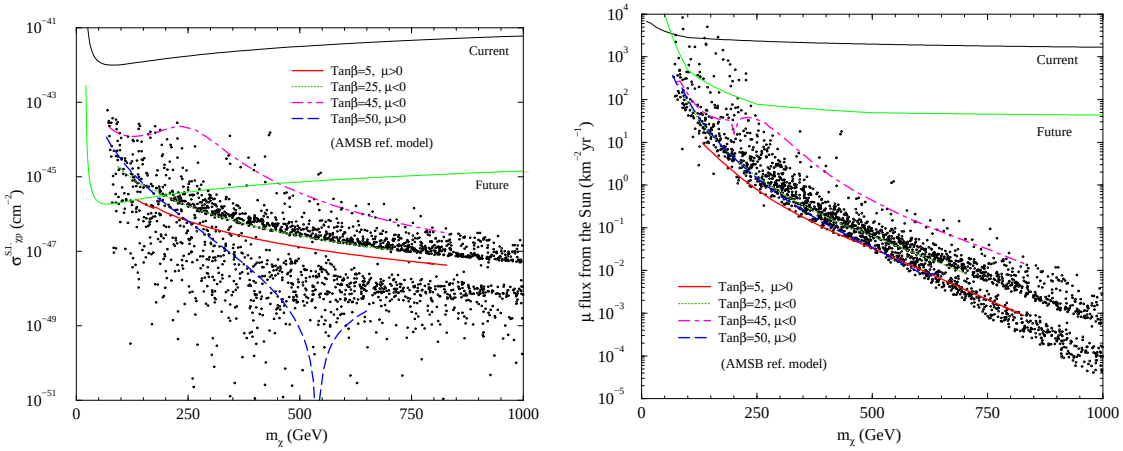

Figure 5.15: *Direct spin independent neutralino-proton scattering cross section (left), and Muon flux induced by neutrinos produced by neutralino annihilations in the center of the Sun (right), for various (around 2500) minimal Anomaly Mediated SUSY breaking models. We linearly scanned* $2 < \tan\beta < 50$, $200 < m_0 < 5000$ *and* $10^4 < m_{3/2} < 4 \cdot 10^5$ *and picked either sign of* μ *with equal probability . Four particular parameter space slices, at* $m_0 = 1500$ *GeV, and at different* $\tan\beta$ *and sign of* μ*, are also shown as guidelines.*

Fig. 5.13 shows the current visibility ratios and exclusion limits for the **AMSB** model.

Remarkably, we find that direct detection, in this particular case, is the less promising search strategy, with expected signals lying more than two orders of magnitudes below the current sensitivity. Neutrino telescopes do little better. On the other hand, within the conservative Burkert halo model we consider, masses below ~ 270 GeV are *ruled out* from the overall fit to antiprotons data, while the expected positron flux is above current sensitivity for masses below approximately 170 GeV. In case we had assumed that the model under scrutiny was describing some *subdominant* component of the full CDM term, and if we had rescaled the neutralino densities according to the thermal relic abundance computed in a standard cosmological scenario, *i.e.* applying the rescaling recipe

$$\rho_{\chi}^{\rm resc} = \rho_{\rm CDM} \, \frac{\Omega_{\rm CDM}}{{\rm Min}\left(\Omega_{\chi}, \Omega_{\rm CDM}^{\rm min}\right)} \, , \tag{5.23}$$

results would have been largely altered, as we show in Fig. 5.14: both direct detection and neutrino telescope visibility ratios would have been five orders of magnitude below one, and antiprotons and positron fluxes would have given rise to a signal completely indistinguishable from the expected background. Relic density enhancement mechanisms are therefore *mandatory* within the minimal AMSB framework to achieve signals compatible with the current and future experimental sensitivity. We find that the same conclusion applies for the other benchmark models we consider here.

As manifest from the shape of the corresponding curve in Fig. 5.13, direct detection rates are particularly low because a cancellation in the contributions from the t-channel exchanges of H_1^0 and H_2^0 takes place in the particular parameter slice we consider here as a *benchmark* scenario. For clarity, we performed a random scan of the full mAMSB parameter space (see the caption in Fig. 5.15 for details on the scan). In the scatter plots of Fig. 5.15 we report our results, together with three parameter space slices as guidelines and with the considered **AMSB** model as well. The left part of the figure refers to direct detection, while on the right we display muon fluxes at neutrino telescopes. Notice that, although larger scattering cross sections may be obtained, all models are far below current sensitivity for direct detection, not altering our conclusions. As regards neutrino telescopes, though very few points lie above the current exclusion limits, we point out that the resulting masses are always smaller than the limits we derived from current data on antimatter searches.

Current exclusion limits for the **Funnel** and for the **NUGM** models are showed in figures 5.16 and 5.17 respectively. In the case of the **Funnel**, where masses are rather large, we do not find any point which is either ruled out by current data on antimatter fluxes or by direct detection and neutrino telescopes. The latter two experimental techniques have so far achieved a sensitivity three orders of magnitude below the expected signals or worse.

Regarding the **NUGM** model, once again we single out a case for which direct Dark Matter detection is the least competitive detection strategy. Neutrino telescopes, though featuring a one-order-of-magnitude better visibility ratios, are also a factor 100 or more below the needed sensitivity. Turning to antimatter, in the **NUGM** scenario positrons do not give any statistical constraint, while antiproton expected fluxes are not compatible with available data for low masses. We remark that this is another example of a SUSY model which is currently constrained by antimatter searches *only*; moreover notice that this is true with the rather conservative Burkert halo profile considered here, and that constraints from antimatter searches within different profiles can be much tighter (see Sec. 5.5.2).

Future search strategies and the role of antimatter

In order to compare the sensitivity of future direct Dark Matter searches and searches with neutrino telescopes with that of antimatter detection, we will hereafter deal with the quantity

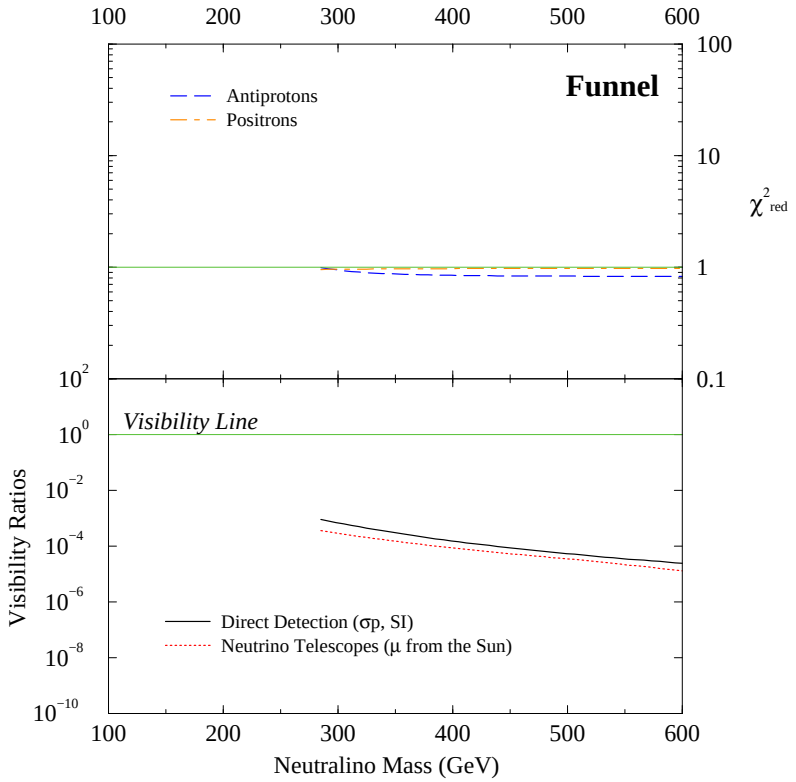

Figure 5.16: *Current exclusions limits on the* **Funnel** *model. Symbols and conventions are the same as in Fig. 5.13.*

I_ϕ, rather than with the χ^2, and plot the experimental discrimination sensitivity of PAMELA at different data taking times. As regards antideuterons, we will keep on, instead, with the visibility ratio; we plot it together with the visibility ratio for direct spin-independent searches, assuming as reference sensitivity for future experiments that of the proposed XENON detector [103]; for the muon-induced flux from the center of the Sun at neutrino telescopes, we implement the projected sensitivity of the km^2-size detector being built by the ICECUBE Collaboration [108].

Fig. 5.18 compares future detection perspectives in the **AMSB** benchmark model. Remarkably, as emerging from the upper panel of the figure, the most promising detection strategies reside in antiproton searches, which in one year of data-taking will probe wino masses up to approximately 370 GeV. For comparison, direct detection at XENON will not be able to detect masses larger than 200 GeV, while this model will not give any signal at Neutrino Telescopes. Let us stress that what we find holds true quite independently from the value of m_0. In turns, this implies that for large values of m_0, where visibility at the LHC is going to be much suppressed, owing to a very heavy squark spectrum, antimatter searches will be the only way to probe this kind of anomaly mediated SUSY breaking models. We point out again that this conclusion holds in case these Dark Matter candidates are providing the bulk of the CDM in the galaxy (*i.e.* in presence of some mechanism to enhance the relic density); otherwise, when fluxes are rescaled, the discrimination capability is washed out.

As regards the **Funnel** benchmark model antideuterons searches give the lion's share in detection perspectives, as previously pointed out. For this model, both antiprotons and positrons will not be able to probe much of the parameter space, since neutralino masses mostly lie above 300 GeV, but searches for low energy antideuterons might be able to reach

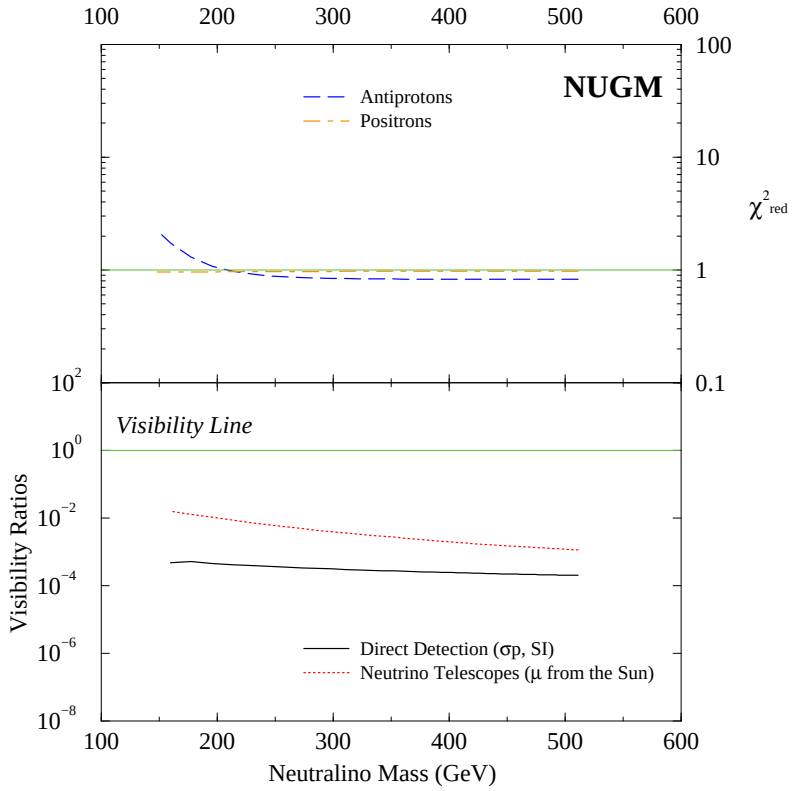

Figure 5.17: *Current exclusions limits on the* **NUGM** *model. Symbols and conventions are the same as in Fig. 5.13.*

significantly heavier masses, up to 450 GeV. A comparison with standard direct detection strategies, whose discrimination capability is going to be less than 350 GeV, shows once again the utmost importance of antimatter searches in the quest for SUSY Dark Matter.

Finally, Fig. 5.20 reproduces our results as far as the **NUGM** benchmark model is concerned. In this case, antiprotons will reach a discrimination sensitivity of 250 GeV, and positrons of 200 GeV, after 3 years of Pamela data taking. For comparison, we see that antideuteron searches will do as good as antiprotons, while direct Dark Matter experiments will probably be marginally able to exclude models up to 400 GeV, though the visibility ratio lies in this case so close to 1 that this does not guarantee that XENON would see any signal, even at very low masses.

5.5.2 The halo model dependence

All the results presented so far are in the context of a rather conservative halo profile. From the point of view of Galactic dynamics, the spherically symmetric Burkert model we have implemented, gives a subdominant term, in a Galaxy embedding a stellar disc close to maximal, *i.e.* a dark term which, in the inner portion of the Galaxy, is hardly providing any dynamical effect at all. From the point of view of structure formation, we have already mentioned that some mechanism has to be invoked to reconcile this final configuration featuring a large core with models with sizable cusps, that, according to numerical simulations, describe the Galaxy before the baryon infall.

Of course, this is not the only consistent picture. In the regime in which the baryons settle in the inner portion of the Galaxy through a smooth and slow process, the back-reaction on

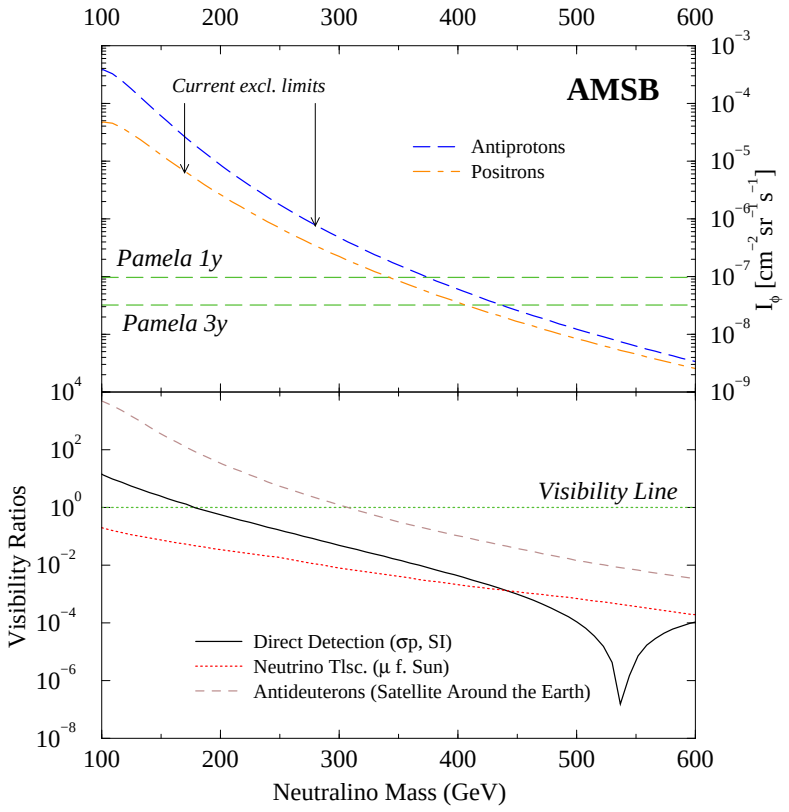

Figure 5.18: *Future exclusions limits on the* **AMSB** *model from direct and indirect Dark Matter searches. In the upper panel we plot the discrimination parameter I_ϕ respectively for antiprotons (long dashed line) and positrons (dot-dashed), as well as the PAMELA experiment projected sensitivity after 1 and 3 years of data taking. The lower panel displays Visibility Ratios (expected signal over projected future exclusion limits) respectively for direct neutralino searches ($\sigma_{\chi-P}$, spin-independent) at XENON-1 ton [103], for indirect neutralino detection through the neutrino-induced muon flux detection from the center of the Sun at ICECUBE [108], and for antideuteron searches with a satellite around the Earth.*

the Dark Matter particle is expected to go in the opposite direction with respect to what we have assumed so far. This is the limit of adiabatic contraction of the system, with no net transfer of angular momentum between baryonic and non-baryonic terms; assuming spherical density profiles and unchanged local velocity distribution, the mass distributions in the initial and final configurations are related by [143]:

$$M_i(r_i) r_i = [M_b(r_f) + M_{CDM}(r_f)]\, r_f \ . \tag{5.24}$$

Here, $M_i(r)$, $M_b(r)$ and $M_{CDM}(r)$ refer, respectively, to the mass profile of the halo before the baryon infall (*i.e.* the form one can infer from N-body simulation results), the baryon component as observed in the Galaxy today, and the cold dark matter component in its nowadays configuration, with the CDM cusp which is preserved or, actually, increased. It is possible to derive models for the Galaxy within this framework and fully consistent with dynamical measurements, see, *e.g.*, [144, 145]. We consider here, as an example, the adiabatically contracted profile derived by implementing the CDM profile found in Ref. [146] through the interpolation of the results from one of the simulations with the highest resolution obtained so far. Since the profile is derived numerically we cannot give its explicit form here; we just mention that it is obtained for a halo with virial mass and concentration parameter

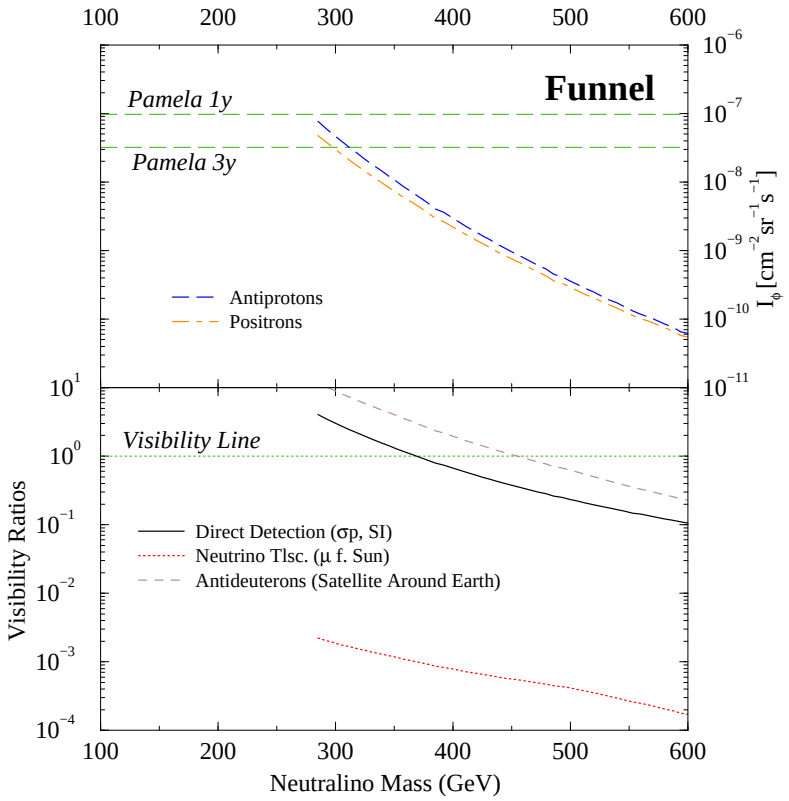

Figure 5.19: *Future exclusions limits on the* **Funnel** *model. Symbols and conventions are the same as in Fig. 5.18.*

respectively $M_{vir} = 1.8 \times 10^{12} \odot$ and $c_{vir} = 12$, and that the local density of the final spherically symmetric dark halo is equal to $\rho_{N03}(r_0) = 0.38$ GeV cm^{-3}. The approximation of adiabatic contraction is assumed to be valid down to the radius of 1 pc, where we suppose that the process which led to the formation of the central black hole in the Galaxy [147] has erased any eventual enhancement (*i.e.* we do not have a spike in the form predicted, *e.g.*, in [148]). As before, this configuration was set up after implementing all available dynamical constraints. The corresponding velocity distribution is derived *self-consistently* as above (for details, see [145]).

Fig. 5.21 shows how the results for the current exclusion limits on the **AMSB** benchmark model are affected when resorting to the two different halo models we have introduced. Direct Dark Matter detection and neutrino telescopes rates are largely unaffected in the adiabatically contracted profile, and the conclusions we drew for the Burkert profile still apply. Antimatter searches are instead largely boosted by the new profile, which features a larger Dark Matter matter density toward the Galactic center: antiproton flux fits *with current data* rule out models with neutralino masses as large as 470 GeV, and positrons up to 370 GeV. Turning to future perspectives, again the picture is not dramatically different for direct detection and neutrino telescopes, as compared with what shown in Fig. 5.18; on the other hand, while antideuterons would probe masses 100 GeV larger than in the Burkert profile, strikingly enough we find that *both antiproton and positron searches will probe, in only 1 year of data taking, the whole parameter space at the PAMELA experiment!*

Since the adiabatically contracted profile is cuspy toward the Galactic center, we expect that another indirect detection channel, namely the observation of gamma rays from the

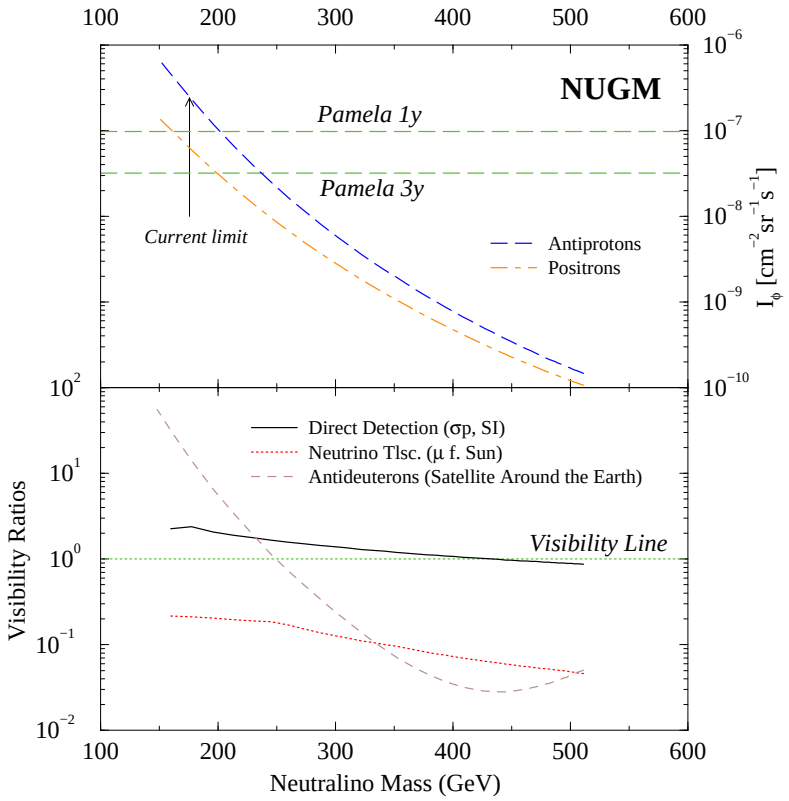

Figure 5.20: *Future exclusions limits on the* **NUGM** *model. Symbols and conventions are the same as in Fig. 5.18.*

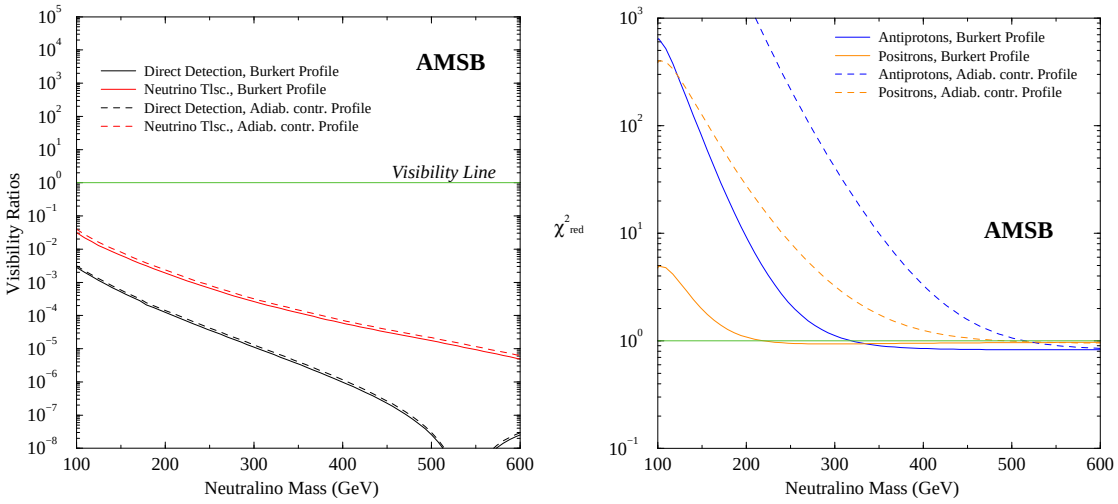

(*a*) (*b*)

Figure 5.21: *A comparison of the* current *Dark Matter exclusion limits, on the* **AMSB** *model, for two different Halo Models, the* **Burkert** *profile (solid lines) and the* **Adiabatically Contracted** *profile (dashed lines). Right: direct ($\sigma_{\chi-P}$, spin independent) and indirect (muons from neutralino annihilations in the center of the Sun) detection Visibility Ratios. Left: the $\chi^2_{\rm red}$ for Antiprotons and Positrons.*

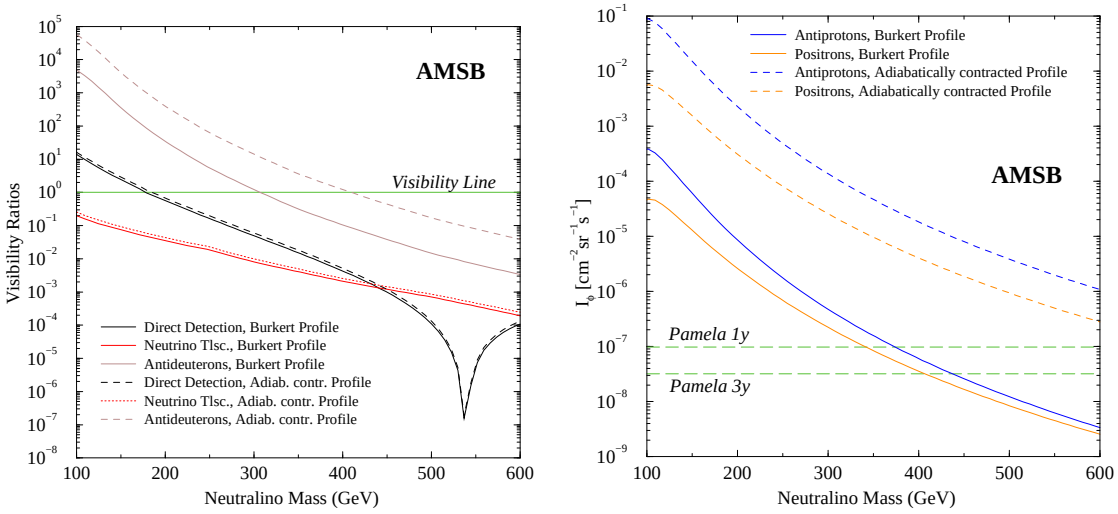

Figure 5.22: *Future Dark Matter discrimination perspectives on the* **AMSB** *model for the* **Burkert** *(solid lines) and for the* **Adiabatically Contracted** *(dashed lines) Halo Model profiles. The left panel shows the Visibility Ratios at XENON-1 ton direct detection and at ICECUBE, as in Fig. 5.21. We also indicate how discrimination perspectives from antideuteron searches on a satellite around Earth vary with the Halo Model. In the right panel we display instead the discrimination parameter I_ϕ for antiprotons and positrons, as well as the putative 1 and 3 years sensitivity of the PAMELA experiment (long dashed lines).*

direction of the center of the Galaxy, could also probe a large fraction of the **AMSB** model parameter space. The EGRET experiment, on the Compton Gamma-Ray Observatory has resolved a γ-ray source toward the GC [149], tentatively extended ($\sim 1.5^\circ$, of the order of the EGRET angular resolution) rather than point-like, and with a spectrum apparently incompatible with that expected for the diffuse γ-ray flux due to the interaction of primary cosmic rays with the interstellar medium, while possibly consistent with a WIMP-induced component [150]. Fluxes expected within our frameworks are compared with the intensity and spectrum of the EGRET γ-ray source; the reader should also keep in mind that alternative explanations have been proposed for this source [151], and that it has been argued that the position of the source should not be identified with the Galactic center [152]. A clearer statement on both these points will be feasible with the upcoming measurements by the next gamma-ray mission in space, the GLAST satellite [153], and, eventually, it will be possible to derive even more stringent bounds.

As shown in Fig. 5.23, it turns out that the adiabatically contracted halo profile is greatly constrained by the current data from gamma rays, which exclude, at the 2-σ level, masses up to 600 GeV within the **AMSB** benchmark model, and puts significant constraints for the other frameworks. It should be noticed however that the signal in gamma-rays is totally dominated by contributions close to the Galactic center rather than evenly distributed along the line of sight, hence the signal is extremely sensitive to what has been assumed on the (essentially unconstrained) distribution of Dark Matter in the Galactic center region; in that respect, note that for the Burkert profile the signal is suppressed by over four orders of magnitude. Antimatter fluxes are much less dependent on this specific feature, and halo model configurations implying an enhancement in the antimatter fluxes without overproducing gamma-rays are certainly viable.

Finally, there are further effects inducing large enhancements of antimatter fluxes and

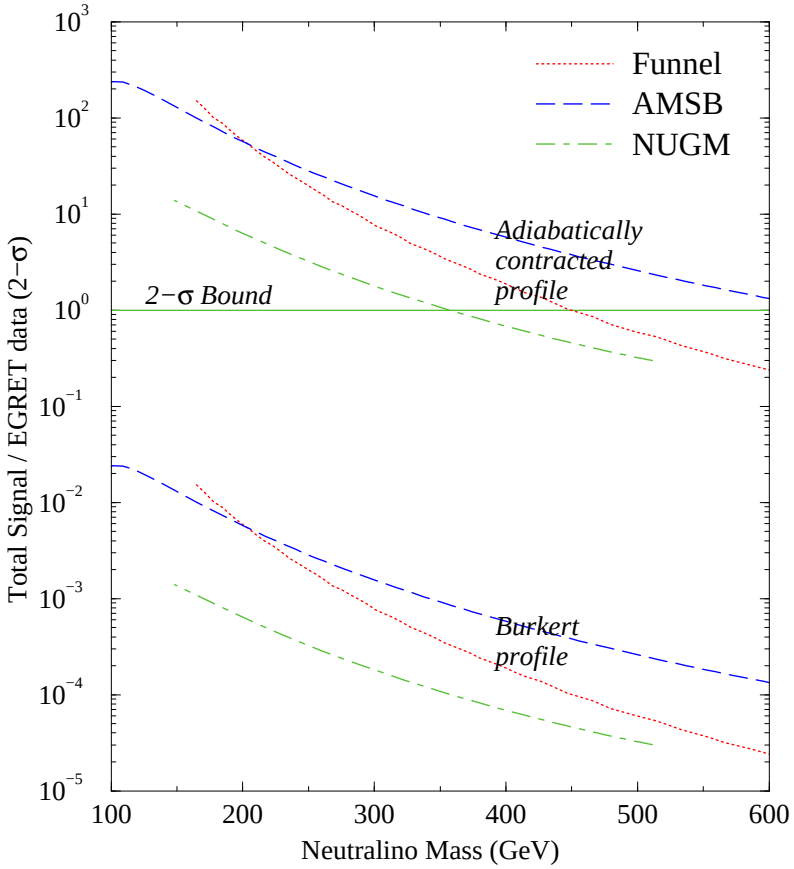

Figure 5.23: *The bound coming from the continuous gamma rays background as measured by EGRET in the bin with the largest sampled energies ($4\,\mathrm{GeV} < E_\gamma < 10\,\mathrm{GeV}$), for the two halo models considered here and for the three benchmark scenarios. As a function of the Neutralino mass, we plot the ratio of the expected signal in the considered energy bin over the 2-σ upper bound from the actual measured datum. Models above the horizontal green line are not consistent with EGRET and the particular considered halo model, and are therefore ruled out. The upper lines represent the results for the adiabatically contracted halo profile, while the three lower lines those for the Burkert profile.*

affecting the other signals less critically. *E.g.*, one can consider halo models which are flattened toward the Galactic plane, rather than being spherical: an increase in the local halo density enters linearly in the direct detection and neutrino telescope rates, while enters quadratically for cosmic ray fluxes (the effect of flattening has been sketched, *e.g.*, in [115]). Moreover, the Dark Matter halo may not be perfectly smooth but have a clumped component, again with possibly large enhancements in antimatter yields, see, *e.g.*, [106].

5.5.3 A statistical overview of SUSY Dark Matter search strategies

In view of the previous considerations, we quantitatively summarize in Tab. 5.3 our results as regards the comparison among different supersymmetric Dark Matter detection strategies within the general MSSM. We made use of the two different benchmark halo models described above: a cuspy profile (*Adiabatically contracted profile*) and a cored profile (*Burkert profile*), as outlined in [145]. Results concerning direct detection and neutrino telescopes are very mildly affected by the halo model under consideration, and we therefore reported our results for the Adiabatically contracted profile only.

In the column *All Models* we include both models whose thermal relic abundance falls

	All Models		WMAP Range	
	Current	**Future**	**Current**	**Future**
Direct SI	$\sim 0\%$	22%	$\sim 0\%$	20%
μ f. Sun	$\sim 0\%$	5%	$\sim 0\%$	3%
$\overline{p}$ – Adiab. P.	38%	80%	$\sim 0\%$	4%
e^+ – Adiab. P.	20%	52%	$\sim 0\%$	$\sim 0\%$
$\overline{p}$ – Burkert P.	10%	41%	$\sim 0\%$	$\sim 0\%$
e^+ – Burkert P.	5%	28%	$\sim 0\%$	$\sim 0\%$

Table 5.3: *A summary of the statistical analysis of the various Dark Matter detection methods. The first two columns refer to all models (WMAP+low relic density), while the last two columns to models with relic abundance within the WMAP range only. For antimatter and gamma rays we indicate the results for both the Adiabatically contracted profile and for the Burkert profile.*

in the WMAP preferred range and models with lower relic densities: we recall that *we do not perform any neutralino density rescaling*, under the hypothesis that some relic density enhancement or non-thermal production mechanism allows models with large annihilation rates to be compatible with the correct required amount of Dark Matter.

First of all, let us stress that, in a statistical sense, *the bulk of the supersymmetric parameter space, compatible with the lower and upper WMAP bounds on the neutralino relic abundance, has still not been probed by Dark Matter searches*, as highlighted by the zeroes appearing in the third column. On the other hand, *taking into account low relic density models, only antimatter searches are currently providing significant constraints on SUSY models*, though with a large dependence on the assumed halo profile. On the other hand, neutrino telescopes and direct detection rule out only marginal portions of the parameter space[6].

As regards future prospects, we find that a significant portion of the viable SUSY parameter space will be probed at large direct detection facilities (approximately 20%, quite independently of the relic abundance of the models). Perspectives at Neutrino Telescopes are less exciting, but we find that about 5% of the parameter space will be accessible at IceCube. Antimatter searches will fail to provide any strong constraint on models with thermal relic abundance in the WMAP range; however, provided some relic density enhancement mechanism is operative, they could become a prominent road to SUSY Dark Matter discovery at future space-based experiments (AMS, PAMELA). In any case, antiprotons are found to be a more promising Dark Matter indirect detection channel than positrons.

[6]This does not mean, of course, that there are no parameter space choices whose detection rates at direct searches and neutrino telescopes fall above current exclusion limits: what we find is that these choices are statistically marginal.

Chapter 6

SUSY Dark Matter and high energy principles

As outlined in Sec. 3, the general MSSM contains a large number of *a priori* free parameters, even in the hypothesis of neglecting inter-generation mixing and CP violating effects. The strategy of analyzing the phenomenology of a theory featuring such a large number of unknown physical entries can be taken only with statistical purposes, as we outlined in Sec. 5. Though the available constraints from the Dark Matter content of the Universe and from the negative search results at accelerator experiments are significantly tight, a major problem of the general MSSM is manifestly that of its apparent *lack of predictivity*. An alternative approach is that of making additional *simplifying assumptions* about symmetries of interactions at energy scales not directly accessible to experiments, or to postulate other physical principles that determine the origin and structure of the soft SUSY breaking terms.

Along this latter line, a privileged setup is that of *Grand Unified Theories* (GUTs), where the strong and electroweak interactions are supposed to *unify* into a larger, unique gauge group (see [154, 155] for an early and a recent review of the topic). A strong motivation for a grand unified setup within the framework of supersymmetric extensions of the Standard Model, completely independent of the above predictivity requirement, is in fact the successful unification of the gauge couplings within SUSY GUTs: as shown in Fig. 6.1, in the Standard Model gauge coupling do not unifiy. The occurrence of SUSY partners at a threshold between 10^2 and 10^4 GeV drives instead the β functions of the gauge coupling in the MSSM to different values, thus yielding a remarkably successful unification at a scale $M_{\rm GUT} \approx 10^{16}$ GeV.

The fact that SUSY particles should appear in the mentioned mass range is suggested by at least two considerations: on the one hand the SUSY solution to the hierarchy problem requires that superpartners feature masses around the electroweak scale; on the other hand, if neutralinos are stable (as it is the case in the MSSM, where R parity is supposed to be a conserved symmetry of the theory) their mass is constrained to be less than a few TeV in order not to overclose the Universe.

Gauge coupling unification is not the only reason why grand unification has been regarded as a good candidate to constrain the patterns of soft SUSY breaking, since GUTs have been shown to successfully address a number of different open issues: to mention few, GUTs provide nice explanations to charge quantization and to the value of the Weinberg angle $\sin\theta_W$; they naturally contain mechanisms of baryogenesis [154]; depending on the GUT unified gauge group, specific relations and predictions concerning the quarks and leptons masses may occur: a well known prediction is that of the bottom-tau Yukawa coupling unification (see Ref. [156–170]); moreover, next-to-minimal GUT groups, like $SO(10)$, provide a natural theoretical framework for the seesaw mechanism of neutrino mass generation. As we will sketch in the final section of the present chapter, this fact entails important phenomenological

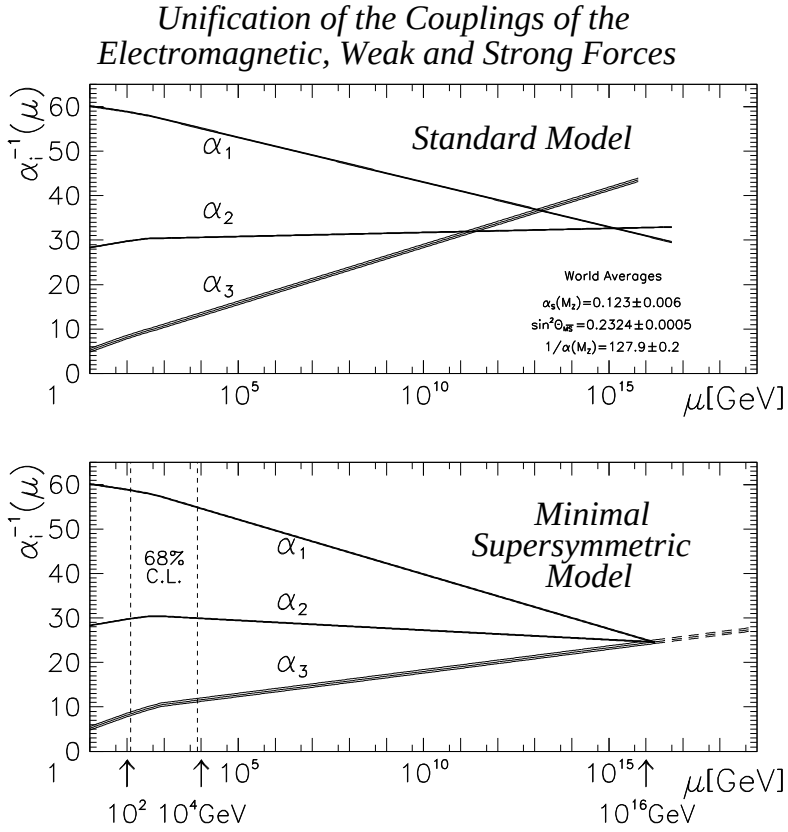

Figure 6.1: *Evolution of the inverse of the three coupling constants in the Standard Model (SM) (top) and in the supersymmetric extension of the SM (MSSM) (bottom). Only in the latter case unification is obtained. The SUSY particles are assumed to contribute only above the effective SUSY scale* $M_{\rm SUSY}$ *of about one TeV, which causes the change in slope in the evolution of the couplings. The 68% C.L. for this scale is indicated by the vertical lines (dashed). The evolution of the couplings was calculated in second order in perturbation theory. The thickness of the lines represents the error in the coupling constants. (Figure from Ref. [154])*

consequences as far as lepton flavor violating processes are concerned.

A generic prediction of grand unification is that of *proton decay* [171–175]: minimal non supersymmetric GUT's have been soon been claimed to be ruled out on the basis of the proton stability (see [171, 172] and [173]). The fact that in SUSY GUTs gauge coupling unification occurs at larger energies compared to typical non-supersymmetric GUT frameworks somehow ameliorates the situation. Nevertheless, the truly minimal SUSY GUT based on the $SU(5)$ gauge group, seems to be ruled out by the SuperKamiolande results on the proton lifetime [174]. In this respect, various mechanisms have been put forward to suppress the relatively fast proton decay predicted in $SU(5)$ SUSY GUTs (see [175] and the discussion in the next section). Nevertheless, in view of the above mentioned possibility of naturally encompassing the seesaw mechanism, and considering that the proton decay issue is by far alleviated within $SO(10)$ GUTs, the latter constitute very appealing alternatives to the minimal gauge group criterion.

As we mentioned above, GUT's are expected to yield, by "conceptual" construction, some kind of prediction for the quark and lepton mass structures and patterns. As well known, an approximate successful Yukawa coupling unification relates the bottom and tau Yukawa

coupling constants, $Y_{b,\tau}$, when considered at some high energy scale (see *e.g.* [156]). It is thus worthwhile to inspect the *theoretical requirement* of the GUT relation $Y_b = Y_\tau$ at $M_{\rm GUT}$ on the SUSY soft breaking masses. We show in Sec. 6.1 a particular, though to some extent general, consequence of such an assumption within a mSUGRA framework: *the Higgs mass parameter μ must be negative.*

The situation is not equally favorable in the case of full Yukawa coupling unification (*i.e.* top-bottom-tau), though some SUSY models may accomplish the task, in highly constrained parameter space areas (see Ref. [176] and References therein). The lack of naturalness in the complete third generation Yukawa coupling unification, together with the fact that it badly *fails* for the two lightest generations, makes this line or research less appealing than that of partial unification; the latter may be regarded as the minimal possible lepto-quark unification, as a consequence of the particles' relevant $SU(2)$ quantum numbers, and is naturally extended to the analogue relation in the neutrinos-up type quarks Yukawa sector in models which include non-null neutrino masses(see next sections, and Ref. [168–170]).

An explicit review on the construction of GUTs lies beyond the scopes of the present work: here we will limit ourselves to consider particular minimal SUSY GUT models, namely $SU(5)$ and $SO(10)$ models. Sec. 6.1 is devoted to the mentioned topic of third generation down-type Yukawa coupling unification: we show that within minimal supergravity the requirement of Yukawa unification forces the sign of μ to negative values and $\tan\beta$ to a definite, limited range. In Sec. 6.2, in order to show the outcome of GUT structures on top of supsersymmetric theories, we resort instead to a class of setups (*no-scale models*). Motivated by GUT arguments or by peculiar space-time geometrical constructions, only gaugino masses are non-vanishing at some high energy boundary conditions scale $M_{\rm bc} > M_{\rm GUT}$, and scalar soft breaking masses are generated through radiative effects (Renormalization Group, RG, running). Finally, the last section deals with a major consequence of lepto-quark unification, inherited by a GUT scenario, namely that of lepton flavor violation. In Sec. 6.3 we adopt Yukawa coupling unification in the up-type lepto-quarks, assuming that one of the neutrino Yukawa coupling is equal to the top Yukawa coupling, and we discuss charged lepton flavor violating rates induced by RG effects between the GUT scale and the seesaw scale, *i.e.* the mass of the heaviest right-handed neutrino. The natural framework for this scenario is an $SO(10)$-like model, though we do not enter into the details on the Higgs sector of the theory which would reproduce the setup we resort to. The scope of the analysis of Sec. 6.3 is instead to outline a complementarity among the search for supersymmetry at next generation accelerators (namely at the Large Hadron Collider, LHC), Dark Matter detection and indirect effects induced by SUSY in charged lepton flavor violating interactions.

6.1 Yukawa coupling unification

The issue of Yukawa Unification (YU) has been extensively studied, see *e.g.* [156–158]. In particular, we address here the YU of the bottom quark and of the tau lepton, which is a prediction of many grand unification setups, including most of the minimal choices, such as various $SU(5)$ GUTs. b-τ YU is a consequence of the fact that the two particles belong to the same $SU(5)$ multiplet, and therefore, at the scale of grand unification M_{GUT} they are predicted to feature the same Yukawa coupling. The experimental difference between m_τ and m_b is then mainly traced back to the combination of two effects. First, the renormalization group (RG) running from M_{GUT} to the electroweak scale naturally drives the two masses to different values. Second, in the minimal supersymmetric standard model, the supersymmetric sparticles affect the values of the masses with different finite radiative corrections, in particular that of the b quark [159].

Previous investigations of b-τ YU include Ref. [160] as regards non supersymmetric GUTs

and Ref. [161–164] and more recently Ref. [165, 166] for the SUSY-GUT case. In particular, in [165] the implications of the recent experimental and theoretical results on the muon anomalous magnetic moment and on the inclusive branching ratio $b \to s\gamma$ were also taken into account, while in [167] the neutralino relic density constrain was examined, in the context of gaugino non-Universality. In Ref. [168–170] the puzzle of neutrino masses and mixing has been tackled in the context of b-τ YU.

A possible approach to b-τ YU is of the "bottom-up" type [164,165]. It consists in defining some parameter which evaluates the *accuracy* of YU, such as

$$\delta_{b\tau} \equiv \frac{h_b(M_{GUT}) - h_\tau(M_{GUT})}{h_\tau(M_{GUT})}.$$

The procedure we take here is instead a "top-down" approach [162, 163, 166]: for a given set of SUSY parameters we fix the value $h_\tau(M_{GUT}) = h_b(M_{GUT})$, requiring the resulting m_τ to be equal to its central experimental value. We then compute $m_b(M_Z)$ through RG running and taking into account the SUSY corrections. A model giving a value of the b-quark mass lying outside the experimental range is ruled out. With this procedure, we perform *exact* b-τ YU at the GUT scale, and directly check whether a given model can, or cannot, be compatible with it, from low energy accelerator data.

It has been already pointed out, see *e.g.* [165, 166], that the requirement of b-τ Yukawa Unification favors negative[1] values of μ. In this section we show that $\mu > 0$ is not compatible with YU, and discuss the $\mu < 0$ case which allows, in a suitable $\tan\beta$ range, the fulfillment of b-τ YU.

The main issue concerning b-τ YU with $\mu > 0$ is that one typically obtains a tree level mass for the b quark which is close to the experimental upper bound, and has to add, on top of it, large *positive* SUSY corrections (see Eq.(6.2) below), that drive $m_b^{\rm corr}$ outside the experimental range (or, the other way round, h_b far away from h_τ). We impose b-τ YU at the GUT scale, we fix $h_\tau(M_{GUT}) = h_b(M_{GUT})$ bottom-up from the properly corrected and RG evolved $m_\tau(M_Z)$, obtaining as outputs the tree level $m_b^{\rm tree}$ and the SUSY-corrected $m_b^{\rm corr}$ masses of the running bottom quark at M_Z. Finally, we compare these numbers with the appropriately evolved b-quark pole mass [178] up to the M_Z scale, with $\alpha_s(M_Z) \simeq 0.1185$, following the procedure of Ref. [179]:

$$m_b(m_b) = 4.25 \pm 0.3 \text{ GeV} \quad \Rightarrow \quad m_b(M_Z) = 2.88 \pm 0.2 \text{ GeV}. \tag{6.1}$$

The largest SUSY corrections arise from sbottom-gluino and stop-chargino loops, frozen at the M_{SUSY} scale [159, 180, 181]. The latter are *non-decoupling effects*, because one gets a finite contribution even in the infinite sparticle mass limit. They can be cast in the following approximate form:

$$\frac{\Delta m_b^{\tilde g}}{m_b} \approx \frac{2\alpha_s}{3\pi} M_3 \mu \; I(m^2_{\tilde b_1}, m^2_{\tilde b_2}, M_3^2) \; \tan\beta, \tag{6.2}$$

$$\frac{\Delta m_b^{\tilde\chi^-}}{m_b} \approx \frac{Y_t^2}{16\pi^2} \mu \; A_t \; I(m^2_{\tilde t_1}, m^2_{\tilde t_2}, \mu^2) \; \tan\beta, \tag{6.3}$$

$$I(x,y,z) \equiv \frac{xy\ln(x/y) + xz\ln(z/x) + yz\ln(y/z)}{(x-y)(y-z)(x-z)}. \tag{6.4}$$

Unless the trilinear coupling A_t is very large, the gluino loop typically dominate (an exception is investigated in Ref. [182]) and the sign of the SUSY contribution is given by the sign of

[1] We use here the standard sign conventions of Ref. [177].

$M_3\mu$. Therefore, since we assume here gaugino mass universality, this implies that b-τ YU is *favored* in the $\mu < 0$ case. We show below that within mSUGRA this actually is the only possibility to achieve successful b-τ YU.

In order to numerically quantify this statement, we study the behavior of $m_b^{\rm tree}$ and $m_b^{\rm corr}$, varying the parameters of the mSUGRA model at positive values of the μ parameter. Our first step is to study the dependence of the b-quark mass on the parameter m_0 (Fig 6.2 (a)). We take here $A_0 = 0$, $\tan\beta = 38.0$ and $M_{1/2} = 1100$ GeV. We point out, as expected, that the size of the corrections decreases with increasing m_0. This is explained on the one hand by the fact that from the radiative EWSB condition the value of μ^2 is slightly decreased by the increase of m_0 [154], and, on the other hand, because an increase in the value of $m_{\tilde{b}_{1,2}}$ leads to a decrease of the function I. In Fig. 6.2 (b) we take instead $A_0 = 0$, $\tan\beta = 38.0$ and $m_0 = 2000$ GeV, and we let $M_{1/2}$ to vary. As can be easily inferred from Eq. (6.2), an increase in $M_{1/2}$ leads to an increase both in M_3 and in μ. In conclusion, the candidate parameter space for b-τ YU lies at low $M_{1/2}$ and large m_0 values. We choose therefore two trial values, $M_{1/2} = 300$ GeV, $m_0 = 2000$ GeV, and we show our results in Fig. 6.3. As readily seen from Eq. (6.2), we find that the SUSY contributions grow with $\tan\beta$. We notice however that the tree level mass strongly decreases with $\tan\beta$, owing to the fact that the positive SUSY contributions to m_τ imply a smaller value for the asymptotic common b-τ Yukawa coupling. The overall conspiracy of these two effects is to maintain the corrected b quark mass well above the experimental upper bound. This conclusion is further confirmed investigating extreme values of $(M_{1/2},\ m_0)$ for high $\tan\beta$, and resorting, moreover, to nonzero values of A_0.

To sum up, we demonstrated that, due to the SUSY corrections to the b-quark mass, top-down b-τ YU is excluded in the case $\mu > 0$. Moreover, in [62] this conclusion has been extended to the framework of minimal non-universal scalar masses.

Regarding the $\mu < 0$ case, the SUSY contributions to the b-quark mass turn to nega-

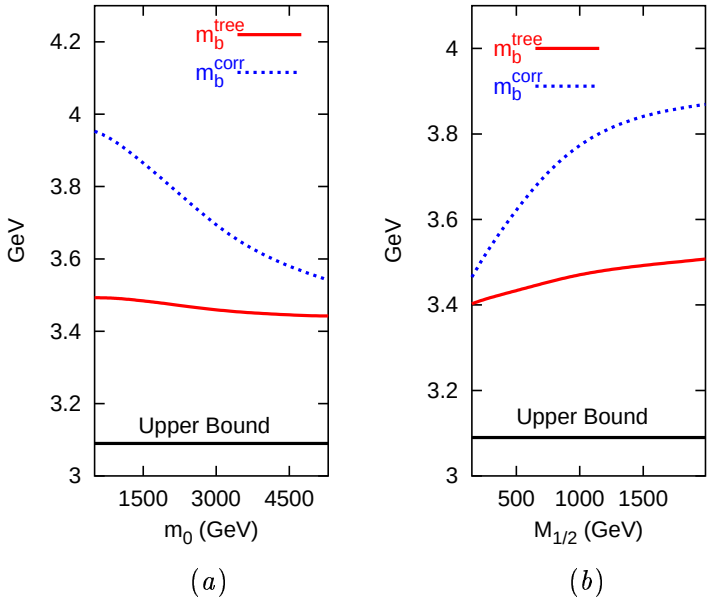

Figure 6.2: *Tree level and SUSY corrected values of the b-quark mass at* $\tan\beta = 38.0$ *and* $A_0 = 0$. *In Panel (a)* m_0 *is varied at fixed* $M_{1/2} = 1100$ GeV *and* $K = 1$. *Finally, in Panel (b) the dependence on* $M_{1/2}$ *is studied at* $m_0 = 2000$ GeV *and* $K = 1$.

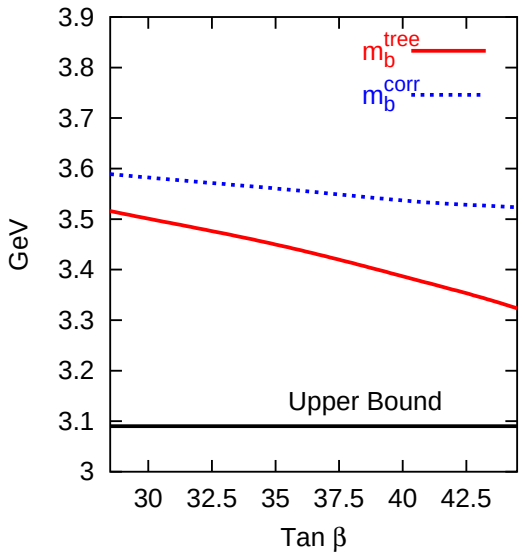

Figure 6.3: *Tree level and SUSY corrected values of the b-quark mass at* $M_{1/2} = 300$ GeV, $m_0 = 2000$ GeV, $A_0 = 0$ *and* $K = 1$.

tive values, and therefore conspire to bring the tree level mass dictated by b-τ YU *within* the experimental range (6.1). The value of $\tan\beta$ directly and critically controls the size of the mentioned SUSY contributions (together with other parameters affecting the details of the particle spectrum), see Eq. (6.2). When $\tan\beta \lesssim 30$, it turns out that the size of the non-decoupling contributions is not sufficient to bring the value of $m_b^{\rm corr}$ within the experimentally allowed range (6.1). On the other hand, at very large $\tan\beta \gtrsim 50$ the corrections are exceedingly large, and often YU is not achieved because $m_b^{\rm corr}$ is found to be below the lowest experimental limit. The precise values of $\tan\beta$ are naturally model- as well as parameter-space-dependent, though, within minimal supergravity-inspired models it is often found that the values for which YU is most naturally achieved lie in the range $\tan\beta \simeq 40 \div 45$. In the next section b-τ YU will be imposed on top of a particular supergravity-motivated GUT theories, namely *no-scale models*, and we will not surprisingly draw conclusions similar to what we obtain here.

6.2 A minimal SUSY GUT setup: no-scale models

A critical issue concerning the supersymmetric extensions of the Standard Model is associated with the mechanism of supersymmetry (SUSY) breaking. The resulting pattern of soft SUSY breaking (SSB) terms, appearing in the effective Lagrangian after integrating over the so-called hidden sector, determines the low energy phenomenology. This pattern is constrained both by theoretical (*e.g.* naturalness in the Higgs sector) and phenomenological (*e.g.* flavor changing neutral interactions, FCNI) requirements. Nevertheless, the number of *a priori* free high energy parameters in generic SUSY breaking scenarios is uncomfortably very large.

There exist, however, particular scenarios where one expects some of these parameters to vanish. In the context of the so called *no-scale models* [183], the scalar soft breaking masses vanish at some high energy input scale where *boundary conditions* are set, $M_{\rm bc}$. Analogous boundary conditions arise in extra dimensional brane models with gauge mediated SUSY breaking [184]. The low energy particle spectrum then depends on the non-vanishing input parameters of the theory, *e.g.* the gaugino masses, through renormalization group (RG)

running.

In Ref. [185] it was shown that requiring $m_0 = 0$ at $M_{\rm GUT} \simeq 2\times 10^{16}$ GeV is not compatible with low energy phenomenology. Nevertheless, if $M_{\rm GUT} < M_{\rm bc} \lesssim M_{\rm Pl} = 2.4 \times 10^{18}$ GeV, GUT interactions running may generate viable particle spectra [186].

In this section we investigate this possibility focusing on two simple GUTs, namely $SU(5)$ and general $SO(10)$ [187]. The requirement of Yukawa coupling unification at the GUT scale, together with all known phenomenological constraints, highly restricts the parameter space of the models under scrutiny, rendering the latter highly predictive. In the minimal setting to which we resort, in fact, once fixed the $M_{\rm bc}$ scale, only two parameters determine the particle spectrum, namely the common gaugino mass at M_{GUT} and the ratio of the two Higgs vevs, $\tan\beta$.

In what follows we show that a portion of the allowed parameter space is compatible with the current data on the cold Dark Matter content of the Universe from the WMAP survey [6]. We also discuss the prospects for neutralino direct detection [188], and argue that a large part of the cosmologically preferred region will be within reach of LHC [189].

No-scale boundary conditions naturally arise in various contexts [183]. In the framework of superstring theories an instance is provided by weakly coupled $E_8 \times E_8$ heterotic string theory compactified on a Calabi-Yau manifold: if the overall modulus field, whose scalar component represents the size of the compactified space, dominates the SUSY breaking, as it is the case when this is triggered by gaugino condensation, the SSB scalar masses, as well as the trilinear scalar couplings, vanish [190]. Analogous high energy structures have been shown to appear also in heterotic M-theory [191]. Furthermore, a no-scale SSB pattern appears with gaugino mediated SUSY breaking in extra dimensional brane models [184]. The visible and hidden sectors live on different 3-branes, and SUSY breaking is communicated through the MSSM gauge superfields propagating in the bulk. Since scalars are separated from the SUSY breaking brane, they get negligible soft breaking masses at $M_{\rm bc}$.

In models with universal gaugino masses, the no-scale SSB scalar mass boundary condition $m_0 = 0$ is not compatible with low energy phenomenology, if the input scale $M_{\rm bc}$ is taken to be the scale of Grand Unification $M_{\rm GUT} \simeq 2 \times 10^{16}$ GeV [185]. If $m_0 = 0$ at the scale where SM gauge couplings unify, in fact, the mass of the lightest stau turns out to be always *smaller* than the mass of the lightest neutralino, regardless of the value of the trilinear scalar coupling A_0. Since the LSP is required to be electrically and color neutral, as indicated by stringent cosmological bounds [192], setting $m_0 = 0$ at $M_{\rm GUT}$ is ruled out [185]. Nevertheless, as pointed out in [185,186], if the SSB input scale is *larger* than $M_{\rm GUT}$, RG evolution driven by GUT-dependent interactions can shift m_0 from zero to some non-vanishing (and possibly non-universal) value at $M_{\rm GUT}$, rendering the model compatible with the above mentioned constraint.

This possibility has been studied in a *minimal* gaugino mediation setting in [186], where the parameter space was taken to be $(M_{\rm bc}, M_{1/2})$ and $B_0 = 0$ at $M_{\rm bc}$, hence fixing $\tan\beta$ by the radiative electroweak symmetry breaking (REWSB) conditions. In [68, 189], instead, in order to fulfill Yukawa coupling unification (YU), the $B_0 = 0$ assumption was relaxed, and the parameter space was taken to be $(\tan\beta, M_{1/2})$ at fixed $M_{\rm bc}$. In this paper we resort to this second possibility, focusing on $SU(5)$ and general $SO(10)$ GUTs [68]. In both cases, consistently with the GUT structure, we require b-τ Yukawa coupling unification (YU). As in the previous section, we resort to a *top-down* approach [62], imposing exact unification at $M_{\rm GUT}$, and setting $h_b(M_{\rm GUT}) = h_\tau(M_{\rm GUT})$ in order to obtain the central experimental value of $m_\tau(M_Z)$ at the weak scale. We then compute the b-quark mass at M_Z including SUSY corrections [180]. We consider the model *compatible* with b-τ YU if the calculated value of $m_b^{\rm corr}(M_Z)$ lies within the 95% C.L. range $m_b(M_Z) = 2.83 \pm 0.22$ [69].

At the scale $M_{\rm bc}$ we set to zero both the soft breaking scalar masses and the trilinear scalar

couplings, while allowing non-vanishing Higgs mixing masses B, supersymmetric higgsino mixing term μ and gaugino masses. The latter are supposed to be universal at $M_{\rm GUT}$. B and μ are traded for M_Z and $\tan\beta$ through REWSB. Therefore we are left with only two parameters, $M_{1/2}$, the universal value of gaugino masses at the GUT scale, and $\tan\beta$. We start with a trial value for $M_{\rm GUT}$, $\alpha_{\rm GUT}$ and for the top and b-τ Yukawas, and run them up to $M_{\rm bc}$, according to the particular chosen GUT model. Evolving the SSB masses and trilinear couplings from $M_{\rm bc}$ to $M_{\rm GUT}$, again depending on the GUT gauge group, we obtain a first approximation of the SSB structure of the model at $M_{\rm GUT}$. Further evolution down to the weak scale, performed with the ISAJET package [139], allows to adjust the value of the Yukawas and to find the values of $M_{\rm GUT}$ and $\alpha_{\rm GUT}$ consistently with the low energy SUSY effective threshold and with the SM gauge coupling running. The whole loop is then repeated until convergence is found. In practice we find that three loops are sufficient to stabilize, for consistency, the SSB pattern as well as the Yukawas and the GUT scale and coupling.

Besides successful b-τ YU, we require the fulfillment of the known phenomenological constraints at the low energy scale. We find that the most stringent bound comes from the inclusive branching ratio $BR(b\to s\gamma)$, which we require to lie in the following range [193]:

$$2.16\times10^{-4} < BR(b\to s\gamma) < 4.34\times10^{-4}. \tag{6.5}$$

Finally, we compute the resulting neutralino relic density $\Omega_\chi h^2$ and the spin independent neutralino-proton cross section $\sigma^{\rm SI}_{\chi p}$, using the latest release of the `DarkSUSY` code [77]. The reference range for the neutralino relic abundance is taken from the WMAP team data analysis; since the lower limit can be evaded under the hypothesis of the existence of another cold Dark Matter component besides neutralinos, or of non-thermal production or cosmological relic abundance enhancement, we take here as a constraint only the 95% C.L. upper bound $\Omega_\chi h^2 \lesssim 0.1287$.

6.2.1 The no-scale $SU(5)$ case

In the minimal $SU(5)$ GUT model [194] the matter content of the MSSM is collected into a $\overline{\mathbf{5}}$ ($\hat{D}^c$, $\hat{L}$) and a $\mathbf{10}$ ($\hat{Q}$, $\hat{U}^c$, $\hat{E}^c$) supermultiplets. The Higgs sector contains three supermultiplets: $\hat{\Sigma}(\mathbf{24})$, responsible for the $SU(5)$ breaking to the SM gauge group, $\hat{H}_1(\mathbf{5})$ and $\hat{H}_2(\mathbf{5})$ containing the MSSM Higgs doublet superfields $\hat{H}_d$ and $\hat{H}_u$. The additional part of the superpotential containing $\hat{\Sigma}(\mathbf{24})$ reads:

$$W_\Sigma = \mu_\Sigma {\rm Tr}\hat{\Sigma}^2 + \frac{1}{6}\lambda' {\rm Tr}\hat{\Sigma}^3 + \lambda \hat{H}_1\hat{\Sigma}\hat{H}_2. \tag{6.6}$$

The boundary conditions at the scale $M_{\rm bc}$ for scalar masses and trilinear couplings are taken to be [189]:

$$m_{10} = m_5 = m_{H_1} = m_{H_2} = m_\Sigma = 0, \text{ and}$$
$$A_t = A_b = A_\lambda = A'_\lambda = 0.$$

The Higgs couplings $\lambda(M_{\rm GUT})$ and $\lambda'(M_{\rm GUT})$ which appear in the superpotential (6.6) are constrained, for the stability of the RGE evolution, in the range

$$|\lambda(M_{\rm GUT})| \lesssim 1.5, \quad |\lambda'(M_{\rm GUT})| \lesssim 3.0\ . \tag{6.7}$$

Moreover, since λ is related to the mass of the colored Higgs triplet responsible for nucleon decay, its value is required to be close to the upper bound of Eq. 6.7. Though the specific choice of $\lambda(M_{\rm GUT})$ and of $\lambda'(M_{\rm GUT})$ affects the SSB parameters at $M_{\rm GUT}$, and hence the low energy spectrum, we checked that the resulting variations at the weak scale are small. Their

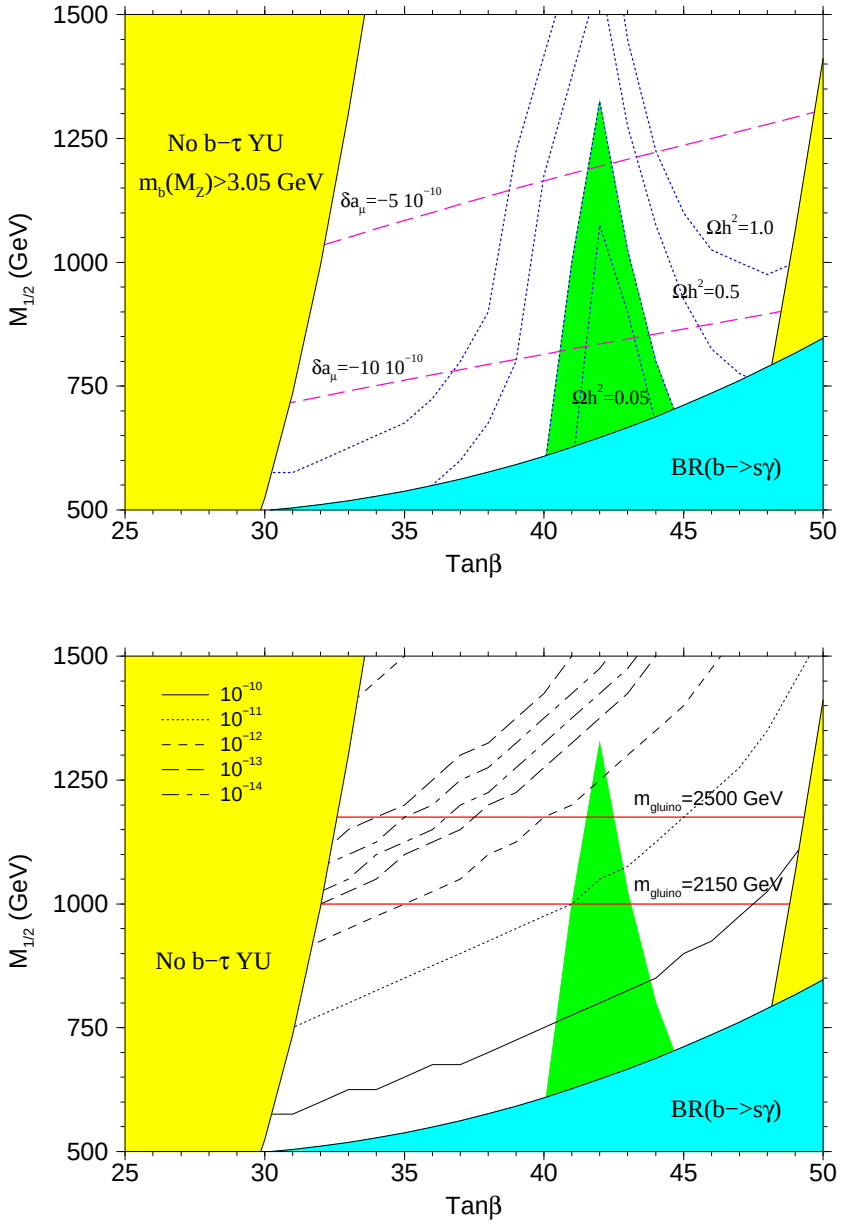

Figure 6.4: *Isolevel curves for the neutralino relic density and muon anomalous magnetic moment (*upper panel*), and for direct WIMP detection and accelerator searches at LHC (*lower panel*) in the case of SU(5) GUT.*

size was in fact found to lie, within few percent, in the range (6.7), as already noticed in [189]. We therefore fixed $\lambda(M_{\rm GUT}) = 1.2$ and $\lambda'(M_{\rm GUT}) = 0.5$ throughout our work.

We start our analysis setting for definiteness $M_{\rm bc} = M_{\rm Pl} = 2.4 \times 10^{18}$ GeV. Top-down b-τ YU constrains the sign of μ to be negative [62], and forces $\tan\beta$ to large values $\gtrsim 28$. We show in the upper panel of Fig. 6.4 the allowed parameter space in the $(\tan\beta, M_{1/2})$ plane and the curves at fixed $\Omega_\chi h^2 = 0.05,\ 0.13,\ 0.5,\ 1.0$. The yellow regions on the left (right) part of the figures do not fulfill b-τ YU, giving rise to $m_b(M_Z) > 3.05$ GeV (resp. $m_b(M_Z) < 2.61$ GeV). Values of $\tan\beta$ larger than 51, besides being excluded by b-τ YU, do not fulfill REWSB. Since the SUSY contributions $\delta m_b \propto (-\tan\beta \cdot f(M_{1/2}))$, with $f(M_{1/2})$ a *decreasing* function of $M_{1/2}$, as we increase $M_{1/2}$ the bounds on $m_b(M_Z)$ are saturated at larger values of $\tan\beta$. The light blue lower part of the figure is ruled out by the $BR(b \to s\gamma)$ constraint (6.5). This bound, for $\mu < 0$, becomes stronger at higher $\tan\beta$ and lower $M_{1/2}$, hence the shape of the excluded region is easily understood. We also plot isolevel lines for the SUSY contributions to the muon anomalous magnetic moment δa_μ. However, due to the current theoretical uncertainties in the evaluation of the SM hadronic contribution, we do not use this quantity as a constraint (see Sec. 3). Finally, we find that in the whole allowed parameter space $m_\chi \simeq 0.44 M_{1/2}$ to within few percent of accuracy.

As regards the cosmologically preferred green region, satisfying (2.22), and the behavior of the Ω_χ isolevel curves, we find $2m_\chi \approx m_A$,in the range $40 \lesssim \tan\beta \lesssim 45$, where m_A indicates the CP-odd neutral Higgs A mass[2]. The line at $2m_\chi = m_A$ lies at $\tan\beta \approx 43$, while at higher (resp. lower) values of $\tan\beta$ $2m_\chi > (<) m_A$. The overall bounds on the parameter space of the model are $40 \lesssim \tan\beta \lesssim 45$ and 590 GeV $\lesssim M_{1/2} \lesssim$ 1330 GeV, which translates into a bound for the lightest neutralino mass of 250 GeV $\lesssim m_\chi \lesssim$ 585 GeV. We also find that for $M_{\rm bc} = M_{\rm Pl}$ the allowed parameter space *excludes* coannihilation effects with the next-to-lightest SUSY particle, the lightest stau, which always lies more than $\approx 25\%$ above the LSP mass.

The lower panel of Fig. 6.4 summarizes the detection perspectives of the model under scrutiny, both at direct WIMP detection experiments [188] (spin-independent $\sigma^{\rm SI}_{\chi p}$ isolevel curves) and at the CERN LHC [189]. Detection rates are beyond reach of *Stage 2* detectors (CDMS2, EDELWEISS2, ZEPLIN2), while the low $M_{1/2}$ and large $\tan\beta$ part of the cosmologically preferred region could be within reach of the so-called *Stage 3* detectors (GENIUS, ZEPLIN4, CRYOARRAY). In the upper-left part of the figure we notice a dip in $\sigma^{\rm SI}_{\chi p}$, due to cancellations among terms stemming from up- and down-type quarks interactions, the largest contributions then coming from t-channel Higgs boson exchanges [101]. As regards SUSY searches at the LHC, following the results of [189] we expect detectability for $m_{\tilde g} \lesssim 2150$ GeV (2500 GeV), at an integrated luminosity of 10 (100) fb^{-1}. In the lower panel of Fig. 6.4 we show the curves at $m_{\tilde g} = 2150,\ 2500$ GeV with red solid lines: in both cases, for $\tan\beta \approx 43$ and $M_{1/2} \gtrsim 1160$ GeV, *i.e.* $m_\chi \gtrsim 500$ GeV, a slice of parameter space compatible with cosmological requirements may be beyond the reach of the CERN LHC.

In Fig. 6.5 we show the constraints on $M_{1/2}$ at various values of the no-scale boundary condition scale $M_{\rm bc}$ for two different values of $\tan\beta = 35.0$ and 47.0, respectively representative of the lower and upper part of the b-τ YU allowed range. The phenomenologically allowed region is in the upper right corner of the plots, where the isolevel curves for the NLSP mass splitting $\Delta_{\tilde\tau} \equiv \dfrac{m_{\tilde\tau_1} - m_\chi}{m_\chi}$ are also depicted at $\Delta_{\tilde\tau} = 0\%,\ 10\%,\ 20\%$. The light blue region is excluded by the $BR(b \to s\gamma)$ constraint (6.5), while in the gray region $m_\chi < m_{\tilde\tau_1}$. Finally, the red region in the lower left corner has $m_{\tilde\tau_1} < 0$. The lowest possible value for $M_{\rm bc}$ is around 5×10^{16} GeV, which is reached at the lowest $\tan\beta$ compatible with b-τ YU,

[2]Funnel regions do not occur, instead, in the models of Ref. [186], since the $B_0 = 0$ condition forces $\tan\beta$ to low values where $2m_\chi \approx m_A$ cannot be fulfilled.

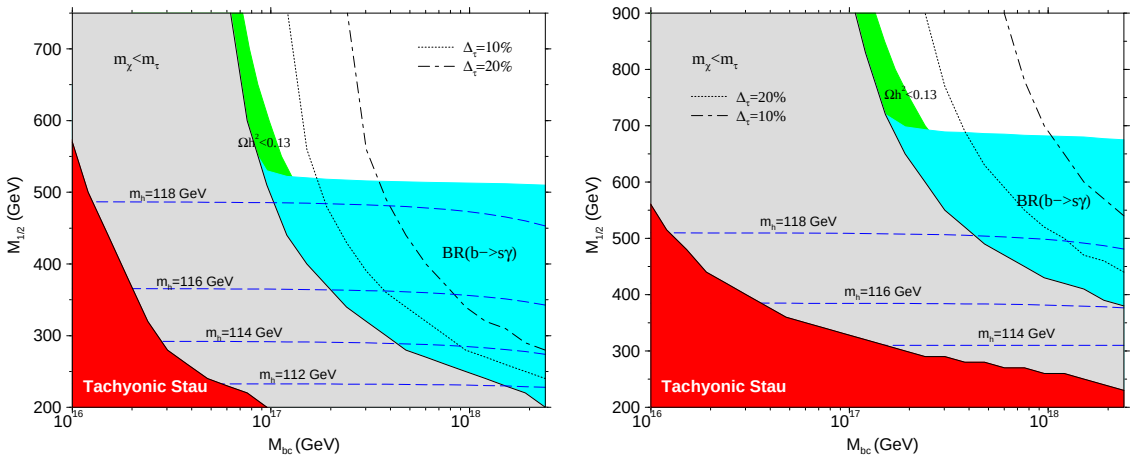

Figure 6.5: *Allowed parameter space at various boundary condition input scale $M_{\rm bc}$, in the case of $SU(5)$ GUT, at* $\tan\beta = 35.0$ *(*left*)* $\tan\beta = 47.0$ *(*right*).*

and, at a given $M_{1/2}$, is always above the corresponding $M_{\rm GUT}$. For completeness, we also include the curves at fixed values of the lightest neutral Higgs m_h, for which the LEP2 bound gives $m_h \gtrsim 114.1$ GeV [195]. We notice that the bound on the Higgs mass, which in the MSSM at large $\tan\beta$ is even milder than the mentioned value, is always weaker than the other considered phenomenological constraints.

As regards the cosmologically viable parameter space, the effect of reducing $M_{\rm bc}$ translates in the appearance of coannihilation regions: we recall that in order to effectively reduce the neutralino relic density, $\Delta_{\tilde\tau}$ must be less than $\approx 10\%$, depending on the absolute value of m_χ, and this is the case for

$$5 \times 10^{16}\ \text{GeV} \lesssim M_{\rm bc} \lesssim 3 \times 10^{17}\ \text{GeV}. \tag{6.8}$$

In Fig. 6.5 we shade in green the actual parameter space regions where $\Omega h^2 < 0.13$. Furthermore, the A-pole condition $2m_\chi \simeq m_A$ is still fulfilled for $M_{\rm bc} < M_{\rm Pl}$, always at $\tan\beta$ close to 43. Therefore, in the range (6.8) an interplay between neutralino-stau coannihilations and direct A-pole annihilations can significantly enlarge the cosmologically preferred parameter space of the models. Outside the funnel region, however, a certain fine-tuning between $\tan\beta$ and $M_{\rm bc}$ is needed in order to enter the coannihilation region (see again Fig. 6.5). Finally, we notice that the isolevel stau mass splitting curves are *steeper* for lower $\tan\beta$. Therefore, at low $\tan\beta$, coannihilations suppress $\Omega_\chi h^2$ to viable values in a *wider range* of $M_{1/2}$ with respect to the high $\tan\beta$ regime: one can clearly understand this statement by imaging vertical lines (*i.e.* lines at fixed $M_{\rm bc}$) intersecting the green regions in the left ($\tan\beta = 35.0$) and right ($\tan\beta = 47.0$) panels of Fig. 6.5.

6.2.2 The no-scale general $SO(10)$ case

In minimal SUSY $SO(10)$ GUT the matter superfields of the MSSM plus an additional gauge singlet right-handed neutrino, are collected in a **16** supermultiplet, while the Higgs superfields belong to a **10**. In the present framework of *universal* gaugino masses[3], a top down-like approach to YU like the one we propose here would lead, at fixed $\tan\beta$, to a large fine-tuning between $M_{1/2}$ and the non-vanishing D-term contribution M_D^2, needed in order to achieve complete YU. We therefore resort to a more *general* $SO(10)$ setting [68], where

[3]See [196] and references therein for the related case of $SO(10)$ with non-universal gaugino masses.

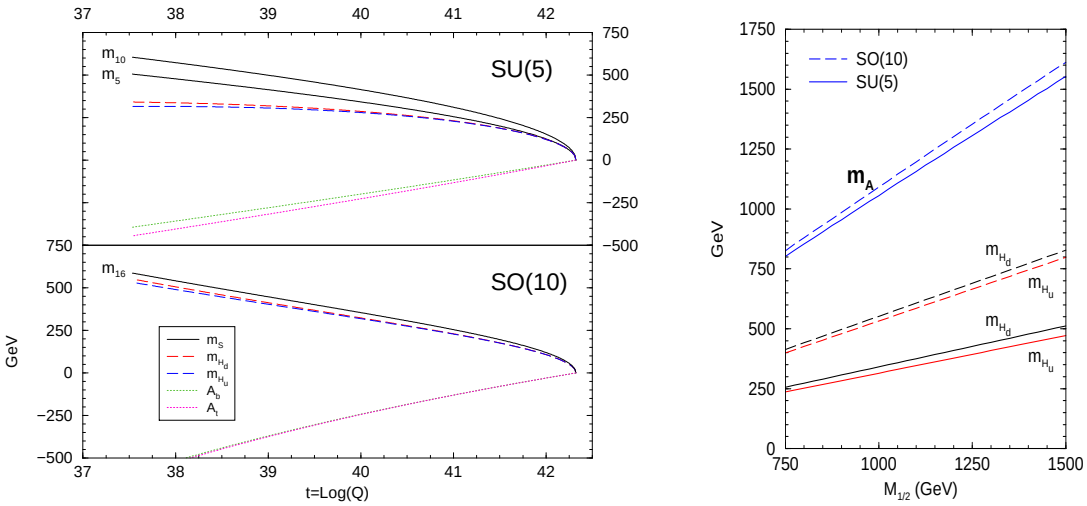

Figure 6.6: *(*Left*): the running of the soft scalar masses and trilinear scalar couplings in $SU(5)$ (upper panel) and $SO(10)$ (lower panel) GUTs for $M_{1/2} = 1$ TeV. (*Right*): the four lower lines represent the m_{H_u} (black) and m_{H_d} (red) soft scalar masses at the GUT scale as a function of $M_{1/2}$; the two upper lines are the resulting values for m_A at the low energy scale. Solid lines indicate the $SU(5)$ case, while dashed lines $SO(10)$. In both figures $M_{\rm bc} = M_{\rm Pl}$ and $\tan\beta = 0.35$.*

the two MSSM Higgs doublets live in two different fundamental representations of the GUT gauge group, and fix $M_D^2 = 0$. In this case the superpotential reads

$$W_{\rm gen} = f_t(\mathbf{16})(\mathbf{16})\hat{H}_2 + f_b(\mathbf{16})(\mathbf{16})\hat{H}_1 \tag{6.9}$$

and only b-τ YU is required. The RGE's depend in general on the Higgs multiplets and on the number of matter generations, namely

$$\frac{{\rm d}g}{{\rm d}t} = \frac{g^3}{16\pi^2}(S-24) \tag{6.10}$$

$$\frac{{\rm d}M}{{\rm d}t} = \frac{2}{16\pi^2}(S-24)g^2 M, \tag{6.11}$$

where S is the sum of the Dynkin indices of the chiral superfields of the model. In the case of two Higgs and 3 generations, $S = 8$.

in the left panel of Fig. 6.6 we begin comparing the effects of the GUT running between $M_{\rm bc}$ (set to $M_{\rm Pl}$ for definiteness) and $M_{\rm GUT}$ for $SU(5)$ and $SO(10)$ GUTs. First, notice that the overall scale at which the soft scalar mass are driven by RG running is comparable in both cases, while the trilinear couplings are evolved towards higher negative values in the $SO(10)$ case. A further remarkable feature is that the Higgs soft SUSY breaking masses are driven to significantly lower values in $SU(5)$ than in $SO(10)$. Last, notice the larger departure from universality which takes place in the scalar sector of $SU(5)$. Being $m_{10}(M_{\rm GUT}) \simeq m_{16}(M_{\rm GUT})$, this translates into a lower soft scalar mass pattern for $SU(5)$.

In the right part of Fig. 6.6 we investigate the effects induced on m_{H_u} and m_{H_d} at the low energy scale by the different GUT running between $M_{\rm bc}$ and $M_{\rm GUT}$. In view of the results of the previous section, we study the mass of the CP-odd Higgs boson A. Notice that, though the differences in the soft scalar Higgs masses are significant, the value of m_A is mainly determined by $M_{1/2}$: the $\approx 50\%$ difference between the $SU(5)$ and $SO(10)$ soft scalar Higgs masses squeezes to a few percent correction in m_A. Henceforth, we expect the same funnel appearing in $SU(5)$ to take place also in the general $SO(10)$ case.

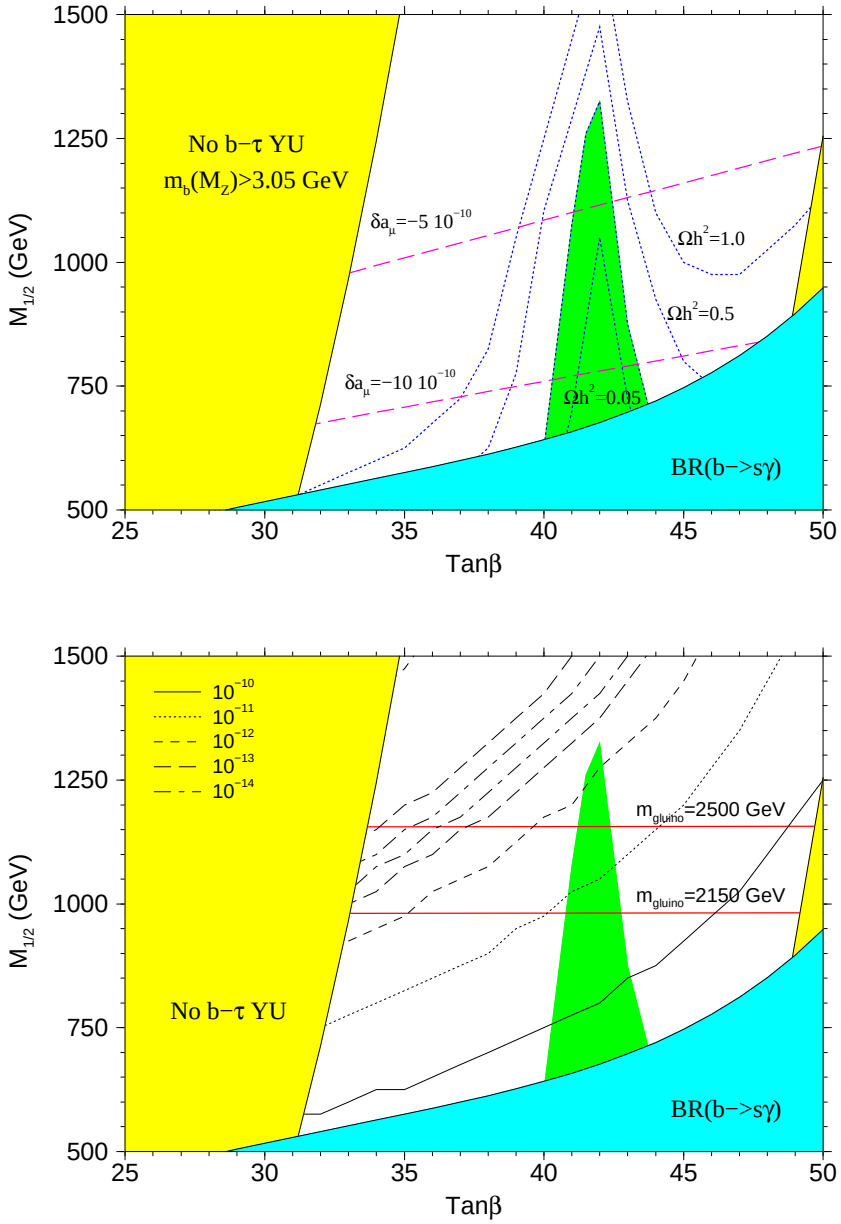

Figure 6.7: *Isolevel curves for the neutralino relic density and muon anomalous magnetic moment (*upper panel*), and for direct WIMP detection and accelerator searches at LHC (*lower panel*) in the case of* general $SO(10)$ *GUT.*

In Fig. 6.7 we show the allowed parameter space in the $SO(10)$ case, with the same notation of Fig. 6.4. As expected, the general features of the $SO(10)$ case are remarkably similar to $SU(5)$, thus confirming that the model-dependence of no-scale scenarios with $M_{\rm bc}$ above $M_{\rm GUT}$ is rather mild, as already pointed out in [186]. This weak dependence on the GUT structure which dictates the running above $M_{\rm GUT}$ is easily understood: the values of the soft masses at $M_{\rm GUT}$ are determined at one loop only by gauge charges through the non-vanishing gaugino masses. All other interactions are one-loop suppressed, and therefore only slightly affect the soft scalar mass pattern at the GUT scale. Moreover, the small splittings in the scalar SSB masses are partly washed out by the common MSSM running between the unification and the weak scales, dominated by gaugino masses. Nevertheless, it is somewhat non trivial that in $SO(10)$ the low energy spectrum allows the fulfillment of the A Higgs resonance condition $2m_\chi \simeq m_A$, in a similar range of $\tan\beta$ as in the $SU(5)$ case.

Concerning the differences between the two considered GUT models, we point out that in the $SO(10)$ case the spectrum at the low energy scale is generically slightly *heavier* than in $SU(5)$, as emphasized before. This amounts to shifting the range of $\tan\beta$ and the lower bound on $M_{1/2}$ towards *larger* values. In the relic density as well we notice that the isolevel curves are closer to each other: this depends on the fact that in the $SO(10)$ case the variations of m_A with $\tan\beta$ are larger than in $SU(5)$, hence the condition $2m_\chi \approx m_A$ is fulfilled in a smaller range of $\tan\beta$, and the funnel is slightly narrowed.

As far as the detectability of the model is concerned (lower panel), we draw the same conclusions as in the previous section: direct detection will be possible only at next to next generation experiments, and only the large m_χ points on top of the A-pole funnel at $\tan\beta \simeq 42$ will be beyond reach of the CERN LHC[4].

As emerging from the pattern shown in the right panel of Fig. 6.6 and from the preceding remarks, lowering $M_{\rm bc}$ would further reduce the differences between $SU(5)$ and $SO(10)$. Therefore, in the framework of $SO(10)$, we expect a scenario very similar to that outlined in Fig. 6.5, in the case $M_{\rm bc} < M_{\rm Pl}$.

6.3 Charged lepton flavor violation in a GUT scenario: SUSY beyond Dark Matter and the LHC

The minimal supersymmetric extension of the standard model, in its original formulation, does not provide a mechanism for the generation of neutrino masses and mixing. A standard approach to the solution of this problem is to resort to the supersymmetric version of the seesaw mechanism, which encompasses a set of three right-handed neutrinos. Though the theory can be assumed to be flavor-diagonal at some high energy input scale, RG flow necessarily involves a certain amount of misalignment in the relevant soft breaking mass matrices at lower energies. Hence the occurrence of lepton flavor violating phenomena is expected, at rates much larger than those which may take place within the standard model of particle physics.

As it is well known, experimental information from neutrino masses and mixing is not sufficient to determine all of the seesaw parameters, and therefore a large degree of uncertainty is involved in the computation of lepton flavor violation rates in a model-independent approach. On the other hand, an alternative attitude consists in resorting to particular Grand Unification frameworks and to constrain the otherwise unknown entries of the relevant combinations of the neutrino Yukawa coupling matrix, through lepto-quark relations.

As a result, in the present section we will carry out an investigation of the different

[4]We are assuming here that the CERN LHC reach for general $SO(10)$ models is comparable to the one for $SU(5)$ models, as suggested by the highlighted strong similarities in the low energy spectra of the two cases.

detection prospects for supersymmetry within the framework of minimal supergravity plus right-handed neutrinos (which will be dubbed *Constrained Minimal SUSY Standard Model with Right-Handed Neutrinos*, CMSSMRN). In particular we will make two GUT-motivated assumptions regarding the Yukawa and flavor structure of the theory, and compare the reach, in the various allowed parameter space regions, in three detection channels: charged lepton flavor violation (*i.e.* the rate for processes of the type $l_i \to l_j \gamma$), the reach of the LHC and of Dark Matter direct or indirect detection.

6.3.1 The setup

The superpotential of the CMSSM incorporating the seesaw mechanism [197] can be written as

$$W = W_{Y_Q} + h^e_{ij} L_i e^c_j H_1 + h^\nu_{ij} L_i \nu^c_j H_2 + M_{R_{ij}} \nu^c_i \nu_j, \tag{6.12}$$

where the leptonic part has been detailed, while the quark Yukawa couplings and the μ parameter are contained in W_{Y_Q}. i, j are generation indices. M_R represents the (heavy) Majorana mass matrix for the right-handed neutrinos. Eq.(6.12) leads to the standard seesaw formula for the (light) neutrino mass matrix

$$\mathcal{M}_\nu = -h^\nu M_R^{-1} h^{\nu\ T} v_2^2, \tag{6.13}$$

where v_2 is the vacuum expectation value (VEV) of the up-type Higgs field, H_2. Under suitable conditions on h^ν and M_R the correct mass splittings and mixing angles in $\mathcal{M}_\nu$ can be obtained.

The amount of lepton flavour violation generated by the SUSY seesaw crucially depends on the flavour structure of h^ν and M_R, the new sources of flavour violation which do not appear in the CMSSM. This dependence can be clearly seen in the Renormalisation Group-induced entries in the slepton mass matrices at the weak scale:

$$(m^2_{\tilde{L}})_{ij} \approx -\frac{3m_0^2 + A_0^2}{8\pi^2} \sum_k (h^\nu_{ik} h^{\nu *}_{jk}) \ln \frac{M_{\rm GUT}}{M_{R_k}}, \qquad i \neq j\,, \tag{6.14}$$

where M_R is the scale of the right-handed neutrinos. From above it is obvious that in case either the neutrino Yukawa couplings or the flavour mixings present in h^ν are very tiny, the strength of LFV will be significantly reduced. Given that there are several possible regions in the seesaw parameter space which may generate the observed mixing in the neutrino sector, one has to resort to some assumptions on h^ν and on M_R to make a quantitative analysis of LFV within this model.

In the present work, we take the view that the presence of non-zero neutrino masses modifies the CMSSM in such a way that the operative seesaw mechanism significantly maximises LFV, leading to another viable discovery road for SUSY in the near future. To this extent, let us make the following assumptions [198–200]:

(a) At least one of the neutrino Yukawa couplings is of $\mathcal{O}(1)$. For definiteness, we choose it to be the third eigenvalue, h^ν_3, setting it equal to the top quark Yukawa, h_t. Assuming neutrino masses are hierarchical, this automatically sets the largest eigenvalue of M_R to be rather close to $M_{\rm GUT}$, around $10^{14} \div 10^{15}$ GeV. The second largest and the smallest eigenvalues $h^\nu_{2,1}$ can be left unspecified as far as the dominant contribution to lepton flavour violation is concerned. However, for a complete neutrino mass model, one needs to specify these eigenvalues too. We mention that this situation naturally occurs within a generic $SO(10)$ GUT model, modulo accidental cancellations.

(b) The matrix which diagonalises the product $h^\nu h^{\nu\,\dagger}$ has either a CKM-like structure with small mixing or a PMNS like structure with large mixing. Notice that the mixing present in $h^\nu h^{\nu\,\dagger}$ determines the amount of LFV, as given by Eq.(6.14). A CKM mixing naturally arise within a $SO(10)$ GUT where the Higgs sector of the theory includes two **10**-plets, respectively coupling to the up and down sector, plus a **126** dimensional Higgs field giving rise to the right-handed neutrinos Majorana mass term. The resulting theory then predicts, with obvious notation

$$h^u = h^\nu, \qquad h^d = h^e. \tag{6.15}$$

Moreover, in the diagonal charged lepton mass matrix basis one has

$$h^\nu = V_{\rm CKM}^T = h^u_{\rm diag} V_{\rm CKM}, \tag{6.16}$$

which fixes the flavor structure of the theory.

On the other hand, a PMNS like mixing in the neutrino Yukawa coupling matrix needs asymmetric textures either in the up- or in the down-sector. This can be accomplished, for instance, coupling the down sector to a combination of symmetric and antisymmetric Higgs representations, again within an $SO(10)$ GUT [199]. In this case one obtains the relation

$$h^\nu = U_{\rm PMNS} h^u_{\rm diag} \tag{6.17}$$

Together with assumption (a), the case with small CKM-like mixing gives a "worst case" scenario, whereas the case with large MNS-like mixing provides a "best case" for LFV.

As far as neutrino masses and mixings are concerned, assumptions (a) and (b) have been extensively studied in the literature, and it has been shown that they may lead to phenomenologically viable models for neutrino masses [199].

Given these hypothesis, the LFV mass-insertions at the weak scale in the CMSSMRN are given, for the worst and best case respectively as:
Worst case:

$$(m^2_{\tilde L})_{21} \approx -\frac{3m_0^2 + A_0^2}{8\pi^2}\, h_t^2 V_{td} V_{ts} \ln\frac{M_{\rm GUT}}{M_{R_3}} + \mathcal{O}(h_2^\nu)^2, \tag{6.18}$$

$$(m^2_{\tilde L})_{32} \approx -\frac{3m_0^2 + A_0^2}{8\pi^2}\, h_t^2 V_{tb} V_{ts} \ln\frac{M_{\rm GUT}}{M_{R_3}} + \mathcal{O}(h_2^\nu)^2, \tag{6.19}$$

$$(m^2_{\tilde L})_{31} \approx -\frac{3m_0^2 + A_0^2}{8\pi^2}\, h_t^2 V_{tb} V_{td} \ln\frac{M_{\rm GUT}}{M_{R_3}} + \mathcal{O}(h_2^\nu)^2. \tag{6.20}$$

Best case:

$$(m^2_{\tilde L})_{21} \approx -\frac{3m_0^2 + A_0^2}{8\pi^2}\, h_t^2 U_{e3} U_{\mu 3} \ln\frac{M_{\rm GUT}}{M_{R_3}} + \mathcal{O}(h_2^\nu)^2, \tag{6.21}$$

$$(m^2_{\tilde L})_{32} \approx -\frac{3m_0^2 + A_0^2}{8\pi^2}\, h_t^2 U_{\mu 3} U_{\tau 3} \ln\frac{M_{\rm GUT}}{M_{R_3}} + \mathcal{O}(h_2^\nu)^2, \tag{6.22}$$

$$(m^2_{\tilde L})_{31} \approx -\frac{3m_0^2 + A_0^2}{8\pi^2}\, h_t^2 U_{e3} U_{\tau 3} \ln\frac{M_{\rm GUT}}{M_{R_3}} + \mathcal{O}(h_2^\nu)^2, \tag{6.23}$$

where V is the CKM matrix and U is the leptonic 'PMNS' mixing matrix. It is now obvious that the seesaw-generated mass insertions above lead to various LFV processes, like rare leptonic radiative decays, $\mu \to e$ conversion in nuclei [201], $\tau \to 3\mu$ [202]. One of the features which stands out is that, in the best case scenario, the amplitude for any LFV process involving $\mu \to e$ transitions *depends* on the neutrino mixing angle, U_{e3}, of which very

little experimental information is available, except for an upper bound (see, *e.g.*, Ref. [203]). The same statement is true for $\tau \to e$ processes too. The $\tau \to \mu$ transitions are instead U_{e3}-independent probes of SUSY, whose importance was first pointed out in Ref. [204]. Otherwise, the leptonic flavour violating transitions are now completely determined in terms of the CMSSMRN soft breaking parameters only.

For definiteness, we list below the present and upcoming experimental limits on the $l_j \to l_i, \gamma$ decays.

Present limits:

$$\begin{array}{rcll} BR(\mu \to e\gamma) & \leq & 1.2 \times 10^{-11} & [205] \\ BR(\tau \to \mu\gamma) & \leq & 3.1 \times 10^{-7} & [206] \\ BR(\tau \to e\gamma) & \leq & 3.7 \times 10^{-7} & [207] \end{array}$$

Upcoming limits:

$$\begin{array}{rcll} BR(\mu \to e\gamma) & \leq & 10^{-13} \div 10^{-14} & [208] \\ BR(\tau \to \mu\gamma) & \leq & 10^{-8} & [207] \\ BR(\tau \to e\gamma) & \leq & 10^{-8} & [207] \end{array}$$

In the next Sections, we will consider the above listed bounds to constrain the CMSSMRN parameter space.

6.3.2 The canonical (m_0 – $M_{1/2}$) plane and LFV

We present our results for the effects of LFV on the CMSSMRN parameter space in the $(m_0 - M_{1/2})$ plane, as customary in CMSSM studies. We then concentrate on the regions of the parameter space which satisfy all the cosmo-phenomenological constraints (see Sec. 3.2).

As a starting point, we present our results for the 'best case' scenario in the plane $(M_{1/2}, m_0)$, for a fixed value of $\tan\beta$ and $A_0 = 0$, and a given sign of μ. In what follows, we will always show both a *small* and a *large* $\tan\beta$ case, respectively setting $\tan\beta = 10$ and 50 (for thourough discussions about the $\tan\beta$-dependence in LFV processes see Ref. [200, 209]).

In Fig. 6.8 we plot the isolevel curves of constant BR($\tau \to \mu\gamma$) for $\tan\beta = 10$ and $\mu > 0$. From the figure, we see that the present experimental limit already starts probing the region of the parameter space at low m_0 and $M_{1/2}$, which is likely to be directly tested at Tevatron. The green patch representing the coannihilation region intersects the isolevels corresponding to BR($\tau \to \mu\gamma$) between 10^{-10} and 10^{-11}, a level of sensitivity likely to be achieved only at dedicated τ-factories. In this low $\tan\beta$ coannihilation region, which will be entirely probed at the LHC, LFV does not significantly impact on the quest for SUSY.

The situation significantly changes, however, for the large $\tan\beta$ region, where one expects a large enhancement in the decay rates (which roughly scale as $\tan^2\beta$). In Fig.6.9, we show BR($\tau \to \mu\gamma$) iso-contours for $\tan\beta = 50$. Notice that we have now chosen $\mu < 0$ so that the A-pole funnel regions (see figure caption) also appear within the allowed parameter space. Here we see that even the present experimental bound on BR($\tau \to \mu\gamma$) can exclude values of m_0 up to 800 GeV and up to 300 GeV in $M_{1/2}$. The intersection of the isolevel curves with the coannihilation region and with the funnel takes place at BR($\tau \to \mu\gamma$) $\approx 10^{-8}$ and extends beyond 10^{-9}, well within the sensitivity reach of present as well as proposed B-factories.

The amplitude of $\mu \to e\gamma$ is U_{e3} dependent, as mentioned earlier. In Fig. 6.10, we plot isolevels corresponding to the present experimental limit on BR($\mu \to e\gamma$) for various values of U_{e3}. Notice that here we take the mixing angle $s_{13} = e^{-i\delta}U_{e3}$ as the relevant variable . We

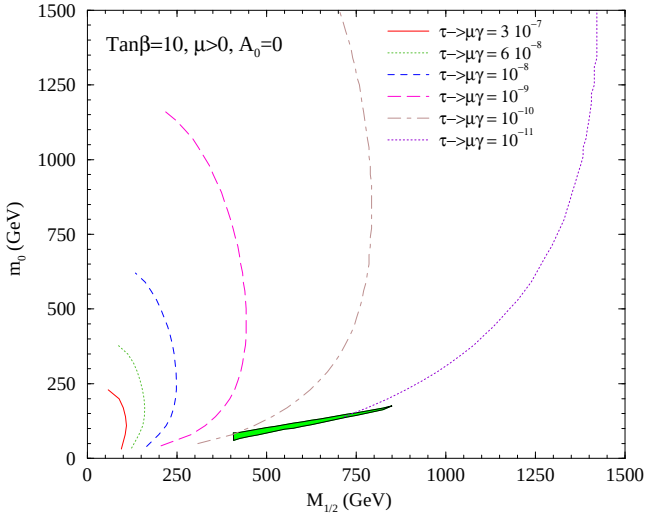

Figure 6.8: *The area shaded in green shows the parameter space, in the* $(M_{1/2}, m_0)$ *plane, allowed by all phenomenological and cosmological constraints, for* $\tan\beta = 10$, $\mu > 0$ *and* $A_0 = 0$. *The lines correspond to various isolevel curves at* $\mathrm{BR}(\tau \to \mu\gamma) = 3\cdot10^{-7}, 6\cdot10^{-8}, 10^{-8}, 10^{-9}, 10^{-10}, 10^{-11}$. *The starting point of each line is dictated by the condition* $m_{\tilde{\chi}_1} = m_{\tilde{\tau}}$, *which fixes the lowest possible value of* m_0. *The isolevel curves terminate where radiative electroweak SUSY breaking (EWSB) conditions cannot be fulfilled, therefore giving the largest possible value of* m_0.

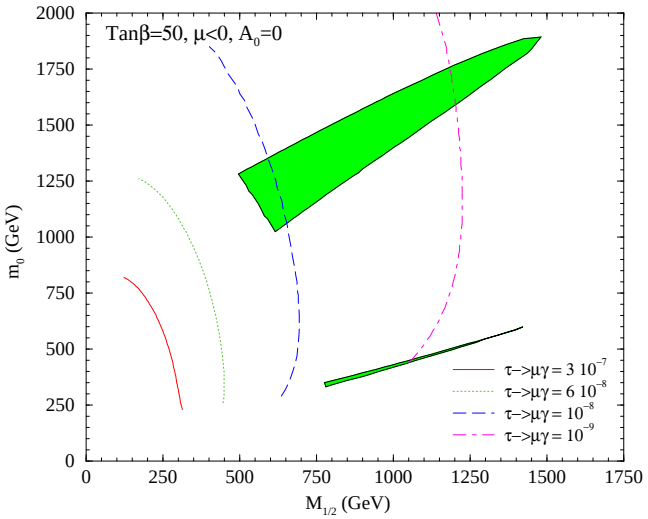

Figure 6.9: *The area shaded in green shows the parameter space, in the* $(M_{1/2}, m_0)$ *plane, allowed by all phenomenological and cosmological constraints, for* $\tan\beta = 50$, $\mu < 0$ *and* $A_0 = 0$. *The upper area at large* m_0 *represents the funnel region. The lines correspond to various isolevel curves at* $\mathrm{BR}(\tau \to \mu\gamma) = 3\cdot10^{-7}, 6\cdot10^{-8}, 10^{-8}, 10^{-9}$. *As in Fig. 6.8, each line starts at* $m_{\tilde{\chi}_1} = m_{\tilde{\tau}}$ *and ends where REWSB conditions are no longer fulfilled.*

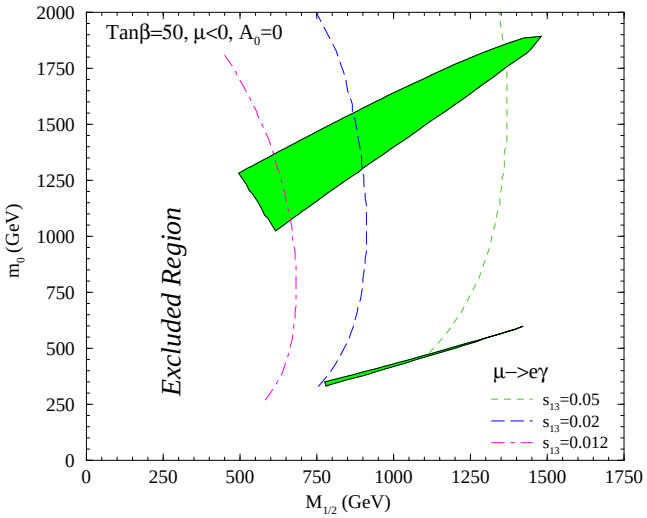

Figure 6.10: *The area shaded in green shows, as in Fig. 6.9, the allowed parameter space, in the* $(M_{1/2}, m_0)$ *plane, for* $\tan\beta = 50$, $\mu < 0$ *and* $A_0 = 0$. *The lines correspond this time to the* exclusion curves *dictated by the current experimental bound on* $\mathrm{BR}(\mu \to e\gamma)$, *for various values of* $s_{13} = 0.05,\ 0.02$ *and* 0.012*: points lying to the left of these curves are henceforth* ruled out *by the current bound* $\mathrm{BR}(\mu \to e\gamma) < 1.2 \cdot 10^{-11}$. *The extreme case* $s_{13} = 0.2$ *would rule out the entire parameter space, and is not shown. Again, as in the preceding figures, each line begins at* $m_{\tilde{\chi}_1} = m_{\tilde{\tau}}$ *and ends where EWSB conditions are no longer fulfilled.*

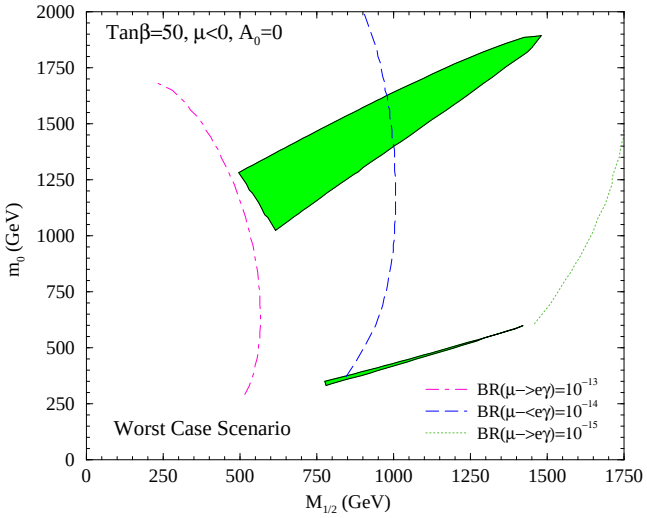

Figure 6.11: *Different isolevel curves of* $\mathrm{BR}(\mu \to e\gamma)$ *for the* worst case scenario, *i.e. corresponding to a CKM-like mixing in the neutrino mixing matrix, on the same parameter space as in Fig. 6.3.2, at* $\tan\beta = 50$, $\mu < 0$ *and* $A_0 = 0$.

choose again $\tan\beta = 50$ and $\mu < 0$. The results are remarkable: taking s_{13}=0.2, close to the present experimental upper bound from CHOOZ, would rule out the *whole parameter space*. This fact can be interpreted as a negative result for either a large U_{e3} or for a large value of $\tan\beta$. In any case, it implies relevant consequences for supersymmetric seesaw models. In the plot, we show values starting from $s_{13} = 0.05$. We see that a value of s_{13} ten times smaller than the present bound ($s_{13} = 0.02$) can still exclude $M_{1/2} < 750\,\text{GeV}$ for any value of m_0.

Finally, in Fig. 6.11 we show the isolevel curves corresponding to various values of $\text{BR}(\mu \to e\gamma)$ in the *worst case scenario*, which, we recall, features a CKM-like mixing in the neutrino Yukawa couplings. Though $\tan\beta$ is fixed to a large value (50), LFV rates are nonetheless rather suppressed: the current experimental bound, for instance, does not give any constraint on the SUSY parameter space. On the other hand, even in this case an improvement in the experimental sensitivity on $\text{BR}(\mu \to e\gamma)$ may lead to access a large part of the cosmo-phenomenologically viable regions. However, from this point on we will consider the *best case scenario* only, because it typically gives more interesting constraints, and it elucidates the possible relevance of U_{e3} for LFV.

6.3.3 Coannihilations, funnels and focus point

LFV processes constitute a meaningful constraint on SUSY models, as the results for the 'best case' scenario presented in the preceding section evidently show. We will demonstrate that sometimes they even *do better* than direct accelerator SUSY searches. Given this situation, we now come back to the issue of the complementarity between the various roads leading to SUSY discovery, directly comparing the LHC reach with the prospects for LFV experiments. We therefore now proceed to detail on the impact of LFV rates for each of the three allowed regions of the CMSSMRN, for benchmark $\tan\beta$ values. Namely, we will concentrate on (a) the coannihilation region, (b) the funnel region and finally (c) the focus point regions

(a) *Coannihilation Region.* The defining condition for this region is $m_{\tilde{\chi}_1} \simeq m_{\tilde{\tau}_1}$, where $\tilde{\tau}_1$ denotes the lighter stau. In the present section, we stick to the points in the $(m_0 - M_{1/2})$ plane which saturate the limiting condition $m_{\tilde{\chi}_1} = m_{\tilde{\tau}_1}$, maximising the extension of the coannihilation strip. We further choose two values for $\tan\beta$, 10 and 50, setting in the first case $\mu > 0$, while in the second $\mu < 0$. The scalar trilinear coupling A_0 is always set to zero.

In Fig. 6.12 we show our predictions for $\text{BR}(\tau \to \mu\gamma)$ and for $\text{BR}(\mu \to e\gamma)$ in the $\tan\beta = 10$, $\mu > 0$ case. The yellow region dictates the lower bound on the neutralino mass, provided by the LEP constraint on the mass of the lightest CP-even Higgs boson m_h [195]. On the other hand, the cyan region gives the upper bound, dictated by the point where $m_{\tilde{\chi}_1} = m_{\tilde{\tau}_1}$ and $\Omega_{\tilde{\chi}_1} h^2 = 0.129$, i.e. the maximal neutralino mass in the coannihilation strip compatible with dark matter constraints [6]. We also show the current and projected experimental sensitivity for $\text{BR}(\mu \to e\gamma)$. We stress that all the parameter space points shown in the plot will be *within the expected sensitivity of the CERN LHC*, since the latter extends, for this value of $\tan\beta$, up to approximately $m_{\tilde{\chi}_1} \simeq 550$ GeV along the coannihilation strip. Clearly, for such a low value of $\tan\beta$, LFV rates are rather suppressed, and at present one can just exclude a narrow region at low neutralino masses, provided s_{13} is close to its present upper bound. Moreover, $\text{BR}(\tau \to \mu\gamma)$ lies at least two orders of magnitudes below the planned experimental sensitivity. Interestingly enough, in case the experimental sensitivity on $\text{BR}(\mu \to e\gamma)$ is lowered down to 10^{-14}, it will be possible to detect, within this scenario, $\mu \to e\gamma$ for s_{13} as low as 10^{-2}.

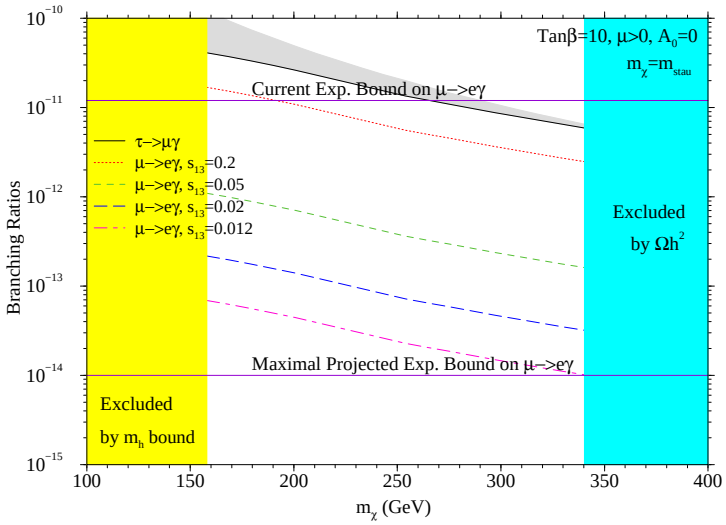

Figure 6.12: BR($\tau \to \mu\gamma$) *and* BR($\mu \to e\gamma$)*, for various values of* $s_{13} = 0.2,\ 0.05,\ 0.02$ *and* 0.012*, along the line, in the* $(M_{1/2}, m_0)$ *plane for* $\tan\beta = 10$*,* $\mu > 0$ *and* $A_0 = 0$*, where* $m_{\tilde{\chi}_1} = m_{\tilde{\tau}_1}$*, i.e. in the lowest part of the coannihilation strip. The yellow shaded area at low neutralino masses is ruled out by the LEP bound on* m_h*, while points within the cyan shaded region at large neutralino masses give an* $\Omega_{\tilde{\chi}_1} h^2$ *value which exceeds the current WMAP constraint on the cold Dark Matter density. The region shaded in gray indicates the possible values for* BR($\tau \to \mu\gamma$) *which one can obtain varying* m_0 *within the parameter space showed in Fig. 6.8. The shape of these shaded regions is analogous for the other lines referring to* BR($\mu \to e\gamma$)*'s. We also show the current and projected sensitivities for* BR($\mu \to e\gamma$)*. We stress that all the points showed in this plot are within the expected CERN LHC reach at an integrated luminosity* $\sim$ 100 fb^{-1}.

The gray shaded band on the BR($\tau \to \mu\gamma$) line is obtained by varying the parameters within the coannihilation region. Although the range of m_0 at a given $M_{1/2}$ (and therefore neutralino mass) is exceedingly tiny, the shaded area is somewhat large, the reason being that the iso-level curves of LFV rates, as shown in Fig. 6.8, are approximately parallel to the coannihilation strip.

As regards the large $\tan\beta$ region, we pick the benchmark value $\tan\beta = 50$, and choose $\mu < 0$ in Fig. 6.13 (a). This time, since the isolevel curves intersect the coannihilation area almost orthogonally, the overall dependence on the m_0 spread is completely negligible, and the gray shaded area is vanishingly small (but depicted over the $\tau \to \mu\gamma$ line). The lower bound on the neutralino mass is dictated by the upper bound on the inclusive BR($b \to s\gamma$), which, for large $\tan\beta$ and negative sign of μ, strongly limits the low mass region of the parameter space. On the other hand, due to stronger couplings in the relevant (co-)annihilation cross sections, the coannihilation strip extends up to rather large neutralino masses. In the present case, the reach of LHC should approximately coincide with the upper bound on the neutralino mass shown in the plot [210]. Noticeably, for such a large value of $\tan\beta$, the current experimental upper bound on BR($\mu \to e\gamma$) happens to put severe constraints on s_{13}: we can for instance qualitatively conclude that if $\tan\beta$ is so large, then s_{13} must be of the order 10^{-2} or less. The $s_{13} = 0.2$ line turns out, for instance, to be *completely excluded* by the present experimental bounds. Concerning future improvements on the experimental sensitivity on BR($\mu \to e\gamma$), we notice that all the lines showed in Fig. 6.13 (a) will certainly be within future reach. On the contrary, the situation for BR($\tau \to \mu\gamma$) is not equally favorable, not even in this large $\tan\beta$ scenario. Yet, BR($\tau \to \mu\gamma$) of $\mathcal{O}(10^{-8})$ would start probing

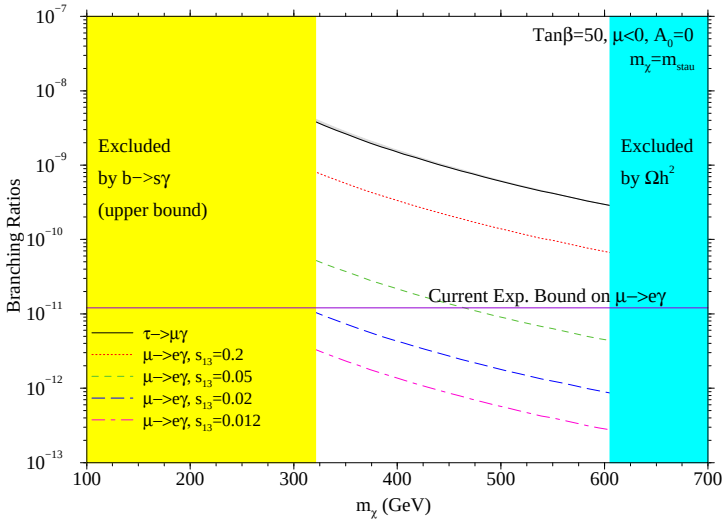

(a)

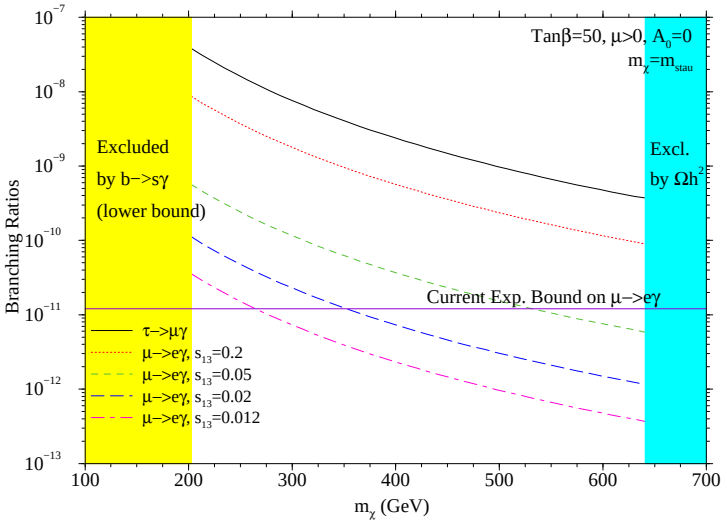

(b)

Figure 6.13: *(a): $\mathrm{BR}(\tau \to \mu\gamma)$ and $\mathrm{BR}(\mu \to e\gamma)$, for various values of $s_{13} = 0.2,\ 0.05,\ 0.02$ and 0.012, along the line, in the $(M_{1/2}, m_0)$ plane for $\tan\beta = 50$, $\mu < 0$ and $A_0 = 0$, where $m_{\tilde{\chi}_1} = m_{\tilde{\tau}_1}$, i.e. in the lowest part of the coannihilation strip. The yellow shaded area at low neutralino masses is ruled out here by the inclusive $BR(b \to s\gamma)$ bound, while points within the cyan shaded region at large neutralino masses give $\Omega_{\tilde{\chi}_1} h^2$ exceeding the current WMAP upper bound on CDM abundance. The current experimental bound on $\mathrm{BR}(\mu \to e\gamma)$ is shown by an horizontal solid violet line. The region shaded in gray indicates the possible values for $\mathrm{BR}(\tau \to \mu\gamma)$ which one can obtain varying m_0 within the coannihilation parameter space showed in the lower green strip of Fig. 6.9. Also here, all the points should be within the expected CERN LHC reach at an integrated luminosity $\sim$ 100 fb^{-1}. (b): The same as in (a), but with positive μ.*

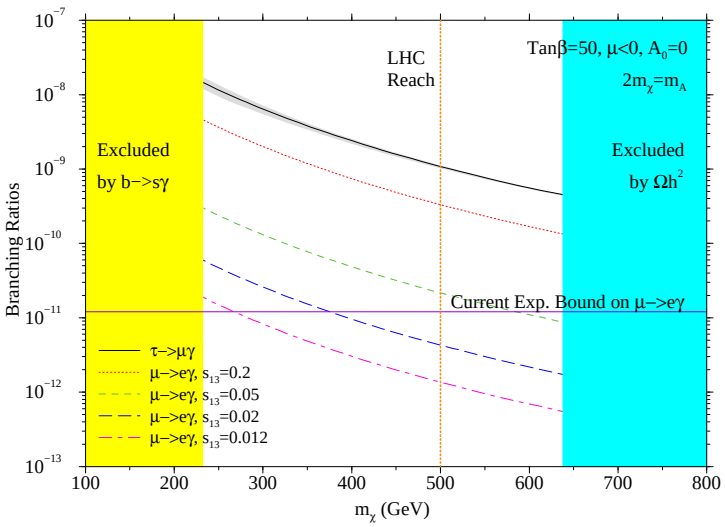

Figure 6.14: $\mathrm{BR}(\tau \to \mu\gamma)$ *and* $\mathrm{BR}(\mu \to e\gamma)$*, for various values of* $s_{13} = 0.2,\ 0.05,\ 0.02$ *and* 0.012*, along the line, in the* $(M_{1/2}, m_0)$ *plane for* $\tan\beta = 50$*,* $\mu < 0$ *and* $A_0 = 0$*, where* $2 \cdot m_{\tilde{\chi}_1} = m_A$*, i.e. in the central part of the funnel region. The yellow shaded area at low neutralino masses is ruled out by the inclusive* $BR(b \to s\gamma)$ *bound, while points within the cyan shaded region at large neutralino masses give an* $\Omega_{\tilde{\chi}_1} h^2$ *exceeding the current WMAP constraint on neutralino relic density. The region shaded in gray indicates the possible values for* $\mathrm{BR}(\tau \to \mu\gamma)$ *which one can obtain varying* m_0 *within the funnel parameter space as showed in the upper large green strip of Fig. 6.9. We also show the current and projected sensitivities to* $\mathrm{BR}(\mu \to e\gamma)$*. The expected CERN LHC reach at an integrated luminosity* $\sim$ $100\ \mathrm{fb}^{-1}$ *is indicated by the vertical orange dotted line: at neutralino masses larger than* $m_{\tilde{\chi}_1} \simeq 500$ GeV *LHC will probably not be able to detect supersymmetry in the present parameter space setting.*

this region.

Lastly, in Fig. 6.13 (b) we show what would happen switching the sign of μ to positive values: the lower limit on $m_{\tilde{\chi}_1}$ is now given by the *lower* bound on $\mathrm{BR}(b \to s\gamma)$, therefore excluding a smaller region, and the coannihilation strip is also slightly enlarged towards larger masses. The predictions for LFV rates are nevertheless not much affected, except for the parameter space which is overall much wider, thus leaving an appealing window at low masses, where LFV processes are particularly large, and even $\mathrm{BR}(\tau \to \mu\gamma)$ may lie within planned experimental sensitivities.

(b) *A-pole funnel Region.* The defining condition for this region is $2m_{\chi_1} \simeq m_A$, and again we show $(m_0, M_{1/2})$ points which saturate the limiting case for which equality holds. In Fig. 6.14 we consider $\tan\beta = 50$ and $\mu < 0$. Also in this case, though the parameter space is by far larger than in the coannihilation strip, as shown in Fig. 6.9, the spread in the LFV rates is again remarkably narrow, as can be inferred from the gray shaded region surrounding the $\mathrm{BR}(\tau \to \mu\gamma)$ line. As before, the lower limit on $m_{\tilde{\chi}_1}$ is set by the upper bound on the inclusive branching ratio $b \to s\gamma$. The projected LHC reach only extends up to $m_{\tilde{\chi}_1} \lesssim 500$ GeV, thus leaving a sizable portion of parameter space outside visibility at the future CERN facility. This is the first instance where LFV experiments actually *compete* with the CERN LHC as an *additional* road to supersymmetry. In fact, values of $s_{13} \lesssim 0.2$ are already ruled out by the current experimental bounds on $\mathrm{BR}(\mu \to e\gamma)$. Should the experimental reach for this branching ratio be lowered down to 10^{-13}, we would be able to detect $\mu \to e\gamma$ signals in the whole funnel region, provided that $s_{13} \gtrsim \mathcal{O}(10^{-2})$. Interestingly, the large mass region lies beyond the expected LHC

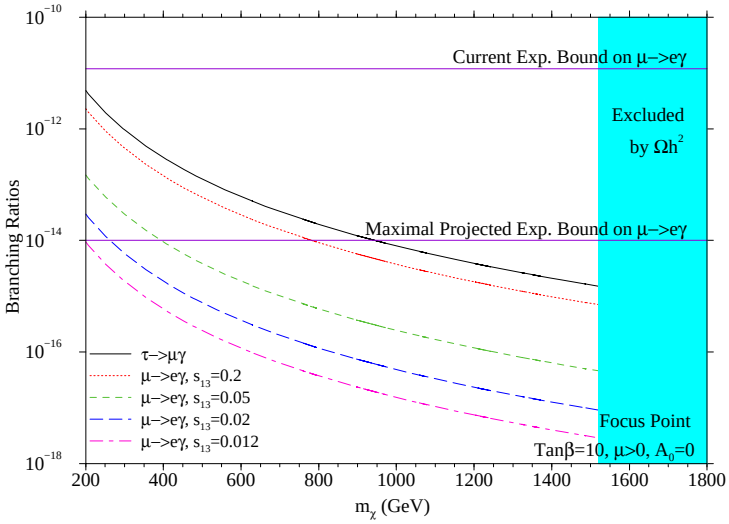

Figure 6.15: BR($\tau \to \mu\gamma$) *and* BR($\mu \to e\gamma$)*, for various values of* $s_{13} = 0.2,\ 0.05,\ 0.02$ *and 0.012, along the extreme focus point region, in the* $(M_{1/2}, m_0)$ *plane for* $\tan\beta = 50$, $\mu < 0$ *and* $A_0 = 0$*. The parameter space points we use here are those such that the higgsino content of the lightest neutralino is maximal. The cyan shaded region at large neutralino masses gives an* $\Omega_{\tilde{\chi}_1} h^2$ *exceeding the current WMAP constraint on CDM density. We also show the current and projected sensitivities to* BR($\mu \to e\gamma$)*. The CERN LHC reach lies at neutralino masses* smaller *than 200 GeV. All the SUSY parameter space points in this plot are therefore* outside *the CERN LHC reach at an integrated luminosity* $\sim$ 100 fb^{-1}.

reach. As in the previous case, we also point out that an experimental sensitivity on BR($\tau \to \mu\gamma$) of $\mathcal{O}(10^{-8})$ would already start probing this region.

(c) *Focus point Region.* In this region, very large values of m_0 lower the Higgs mixing parameter μ, thus entailing the generation of a non-negligible higgsino component in the lightest neutralino[5]. This, in turn, yields an *enhancement* in the annihilation cross section with respect to the pure bino case, together with coannihilation effects with the next to lightest neutralino and, more importantly, with the lightest chargino, owing to the mass matrix structure of neutralinos and charginos. The combination of coannihilation effects and of a larger annihilation cross section forces the neutralino relic density to drop to very low values, which may be nonetheless compatible with the current Dark Matter abundance.

The focus point region poses several computational problems, since it lies very close to parameter space points where REWSB fails, and moreover because it is rather fine-tuned, being very sensitive to the input parameters, especially the top mass, m_t. This is why sometimes this region of parameter space has sometimes not been included in analysis of the CMSSM [64]. Nevertheless, we include it in our discussion. Indeed, we consider it useful to analyze the situation from the LFV rates point of view because it will be very hard to probe most of this region at the LHC.

As before, we once again resort to a low (10) and a large (50) value of $\tan\beta$, and we choose to show the extreme part of the focus point region, i.e. that at the largest possible m_0, and hence where the higgsino content is maximal. Our choice is again

[5]It should be noted that this situation takes naturally place in several other soft SUSY breaking scenarios, for instance with non-universal gaugino masses [211], where the lightest neutralino is mainly a higgsino; relevant consequences for LFV can be found in Ref. [62].

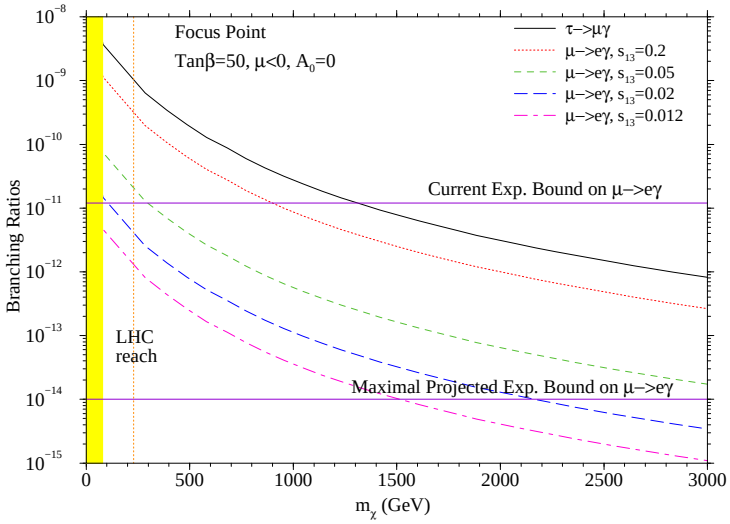

Figure 6.16: BR($\tau \to \mu\gamma$) *and* BR($\mu \to e\gamma$)*, for various values of* $s_{13} = 0.2,\ 0.05,\ 0.02$ *and 0.012, along the extreme focus point region, in the* $(M_{1/2}, m_0)$ *plane for* $\tan\beta = 50$, $\mu < 0$ *and* $A_0 = 0$. *Again, the parameter space points we use here are those such that the higgsino content of the lightest neutralino is maximal. We show neutralino masses up to 3 TeV, which are still allowed by relic density considerations. The expected sensitivity of the CERN LHC is showed by the vertical orange dotted line, while the yellow shaded area on the left indicates the bound stemming from the chargino mass limit set by LEP direct searches.*

motivated by two considerations: first, the region is sufficiently narrow so that LFV rates along the focus point region would appear as single lines in any case; second, by choosing the maximal possible higgsino content we extend the parameter space line up to the largest possible neutralino masses.

Due to the mass vicinity between the lightest neutralino and chargino, the lower neutralino mass bound in the focus point region is typically dictated by the chargino mass constraint from direct searches at LEP. As anticipated, the LHC reach is rather limited in this region: in fact, it lies around a neutralino mass of $\sim$ 200 GeV. The large masses characterizing the sfermion spectrum naturally suppress LFV processes, but nonetheless, even in the less favorable case of $\tan\beta = 10$, LFV can probe SUSY up to neutralino masses around 800 GeV, corresponding to very large values of the soft breaking masses at the GUT scale, namely $M_{1/2} \approx 5.5$ TeV and $m_0 \approx 17.5$ TeV. As regards the large $\tan\beta$ case, BR($\mu \to e\gamma$) may be within future experimental reach for neutralino masses *in the multi-TeV range*, provided s_{13} is of $\mathcal{O}(10^{-1} \div 10^{-2})$. Therefore, the focus point region (as well as the generic case of a higgsino dominated lightest neutralino) typically tends to *favor* BR($\mu \to e\gamma$) with respect to direct accelerator searches in the quest for supersymmetry[6].

6.3.4 The role of U_{e3}

The importance of the parameter U_{e3}, in connection with the neutrino mixing matrix and with LFV in the SUSY seesaw is evident from the discussions we carried out in the previous

[6] In a recent paper [212], it has been pointed out that at future $e^+\,e^-$ Linear Colliders with center of mass energy $\sqrt{s} \approx 0.5 \div 1$ TeV, the accelerator reach in the CMSSM focus point region may be by far larger than that at the CERN LHC

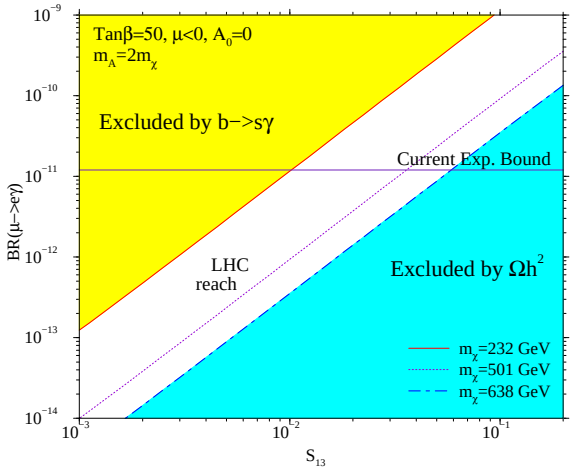

Figure 6.17: *The dependence of* $\mathrm{BR}(\mu \to e\gamma)$ *on* s_{13}*, for* $\tan\beta = 50$*,* $\mu < 0$ *and* $A_0 = 0$ *along the parameter space line, in the* $(M_{1/2}, m_0)$ *plane corresponding to* $2 \cdot m_{\tilde{\chi}_1} = m_A$*, i.e. in the central part of the funnel region. The upper region, shaded in yellow, is ruled out by the* $b \to s\gamma$ *bound, while the lower region, shaded in cyan, is disallowed by the* $\Omega_{\tilde{\chi}_1} h^2$ *bound on the neutralino relic density. The three lines respectively correspond to the lower and the upper neutralino mass limits and to the largest neutralino mass within LHC reach. We also report the current experimental upper bound on* $\mathrm{BR}(\mu \to e\gamma)$*.*

two sections. The precise value of U_{e3} turns out to be of critical importance in at least two contexts in the present analysis:

(i) **LFV versus LHC**
Within the coannihilation regions LFV will play only a "supporting" role with respect to the more powerful LHC searches. The first instance where LFV may reveal itself as a superior tool arises in the heavy mass A-pole funnel region. However, the prominence of LFV searches is crucially dependent on U_{e3}. To make this more precise, in Fig. 6.17 we plot the $\mathrm{BR}(\mu \to e\gamma)$ as a function of s_{13}, showing iso-neutralino mass curves. From the plot it is evident that an experimental sensitivity of 10^{-13} would allow to detect LFV as long as $s_{13} \gtrsim 5 \cdot 10^{-3}$. On the other hand, there is a large band, at heavy SUSY particles masses, lying beyond LHC reach, which will be fully accessible to LFV experiments. The same holds true in the focus point region, where $\mathrm{BR}(\mu \to e\gamma)$ will probe SUSY far more effectively than the LHC, provided U_{e3} is not too small.

(ii) $\mu \to e\gamma$ **versus** $\tau \to \mu\gamma$
We have seen that, if s_{13} is not too small, the constraints coming from $\mu \to e\gamma$ are stronger than those derived from $\tau \to \mu\gamma$. Hence, there should be a *critical value* of s_{13} below which $\tau \to \mu\gamma$ becomes more relevant than $\mu \to e\gamma$. What is exactly this value? To answer this question in Fig. 6.18 we show $\mathrm{BR}(\mu \to e\gamma)$ in units of 10^{-13} as a function of s_{13}, for the particular point at $m_0 = 343$, $M_{1/2} = 500$, $\tan\beta = 50$ and $\mu > 0$. The dashed-dotted line denotes the value of $\mathrm{BR}(\tau \to \mu\gamma)$ in units of 10^{-8}. We observe that the intersection between the $\tau \to \mu\gamma$ line – which is almost independent of s_{13} – and the $\mu \to e\gamma$ line takes place at a value of s_{13} close to 10^{-3}. If $s_{13} \gtrsim 10^{-3}$ then $\mu \to e\gamma$ is more likely to be observed in future experiments than $\tau \to \mu\gamma$. Although these results were obtained for a specific value of m_0 and $M_{1/2}$, changes in these parameters are expected to equally affect both processes so that the critical value $s_{13} \approx 10^{-3}$ does not depend on m_0 or $M_{1/2}$ (We have also checked numerically

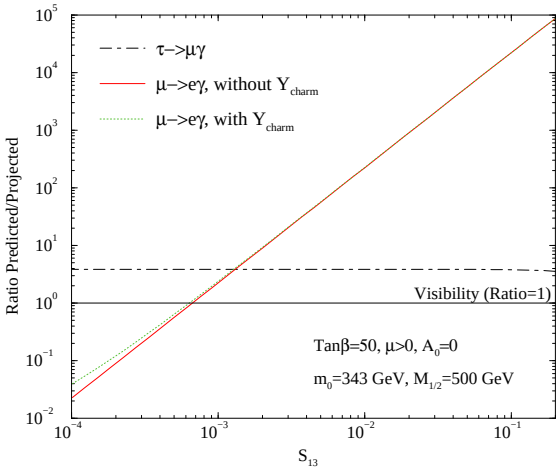

Figure 6.18: *The ratio of the predicted* $\mathrm{BR}(\tau \to \mu\gamma)$ *(respectively* $\mathrm{BR}(\mu \to e\gamma)$*) and the approximate projected maximal sensitivity of* 10^{-8} *(resp.* 10^{-13}*) at a particular parameter space point along the coannihilation strip at* $\tan\beta = 50$*, vanishing* A_0 *and positive* μ*. The green dotted line corresponds to the case where the effect of a second non-zero neutralino Yukawa coupling, set equal to the charm quark Yukawa coupling, is taken into account.*

that this is indeed the case). When s_{13} is very small, the contribution to $\mathrm{BR}(\mu \to e\gamma)$ proportional to the second Yukawa coupling dominates over that proportional to the top Yukawa coupling. In the same figure we show the predictions for $\mathrm{BR}(\mu \to e\gamma)$ *with* and *without* taking into account the effect of the second Yukawa coupling, which we set equal to the charm Yukawa [199]. Notice that such effect is only relevant for $s_{13} \lesssim 7 \times 10^{-4}$.

6.3.5 The complementarity among SUSY searches: summary of the results

We summarise here our results on the complementarity of the three search roads for the three allowed regions of the CMSSMRN, in the 'best case' scenario.

(a) *Coannihilation Regions*: In these regions, which are mostly accessible at LHC, an improvement of two orders of magnitude in the branching ratio sensitivity would make $\mu \to e\gamma$ visible for most of the parameter space as long as $s_{13} \gtrsim 0.02$, even for the low $\tan\beta$ region. For large $\tan\beta$ $\tau \to \mu\gamma$ will start probing this region provided a sensitivity of $\mathcal{O}(10^{-8})$ is reached, independently of s_{13}.

(b) *A-pole funnel Regions*: In these regions the LHC reach is not complete and LFV may be competitive. If $s_{13} \gtrsim 10^{-2}$, the future $\mu \to e\gamma$ experiments will probe most of the parameter space regions. As above, $\tau \to \mu\gamma$ will probe this region once the BR sensitivity reaches $\mathcal{O}(10^{-8})$.

(c) *Focus Point Regions*: Since the LHC reach in this region is rather limited due to the large m_0 and $M_{1/2}$ values, LFV could constitute a privileged road towards SUSY discovery. DM searches will also have partial access to this region in the future (see Sec. 5), thus leading to a new complementarity between LFV and the quest for the cold Dark Matter constituent of the universe.

Chapter 7

Conclusions and Outlook

Are we going to ascertain the existence of low energy Supersymmetry in the next years? Is there any kind of no-go theorem which could guarantee the possibility of directly or indirectly grasp this elusive, and yet unspeakably attractive *last frontier* of the symmetric structure of Nature? Where should our hopes lie on, and what are the most promising among the large plethora of next-generation experimental apparata? What if we are not going to see *anything*?

The length of the list of experimental programs encompassing the quest for Supersymmetry among their scientific goals cannot be overemphasized. The pole position is by all means occupied by the largest experiment mankind has ever initiated, namely the CERN Large Hadron Collider (LHC). The two main scopes of this huge facility, which should be turned on by the end of 2007, are the discovery of the Higgs boson and of Supersymmetry. Remarkably, if the latter is there, then one would be quite confident to put the hands on the former, since the lightest Higgs boson of the MSSM should feature a mass compatible with the LHC reach. The vice-versa is instead unfortunately not guaranteed. Finally, it comes not as a surprise that we are experimenting a *crescendo* of theoretical and phenomenological research papers facing the possibility of higgsless theories or of alternative explanations to the generation of mass in elementary particles: the *no-Higgs and no-SUSY* scenario somehow appears to be an increasingly plausible landscape, at least in the realm of theories [213].

In any case, many dedicated studies have claimed that the LHC is going to "explore most of the viable SUSY parameter space". Even before LEP was turned on, some high-spirited physicist imprudently stated that Supersymmetry was just around the corner. Needless to say, this kind of statements must be read with great care: in principle, the parameter space of Supersymmetry in its full generality may be well beyond *any* conceivable accelerator experiment. The main difference is that now we know that *our Universe is Dark*, and that Supersymmetry provides an excellent particle candidate for the Missing Mass. If the lightest SUSY particle is the main Dark Matter constituent, then its mass *must be* within a couple of orders of magnitude above the LHC reach, at most[1]. On the other hand, if no particular neutralino relic abundance mechanism is operative, one can confidently state that the Dark Matter abundance forces the natural mass range for neutralinos below 2-3 TeV or so. This does not guarantee at all that the LHC will see any trace of Supersymmetry, but at least that its energy range lies "naturally" in the same order of magnitude at which one would expect a SUSY Dark Matter particle.

The detection of SUSY particles at the CERN LHC detectors ATLAS or CMS would be the only unquestionable evidence in favor of Supersymmetry. All other detection techniques could in principle disguise other new physics particles or more exotic Dark Matter candidates.

[1] In the general MSSM, with multiple coannihilation processes, a neutralino mass of the order of 10, and up to 100 TeV, may still be compatible with the required relic abundance, without violating the unitarity bound [214]

Moreover, a systematic particle physics study of Supersymmetry can only be carried out at an accelerator facility, such as the LHC or the Next-Linear-Collider.

The scenery of the multiple experimental pursuit of what somebody dubbed the "Dark side of the Universe" is indeed diversified, and, as we repeatedly pointed out, is not circumscribed to Supersymmetric particle candidates. A very appealing technique seems to be the direct detection of Dark Matter SUSY particles off the nuclei of large sized target detectors. By now, experiments featuring tons of Xenon or other target materials are in deployment phase (XENON, ZEPLINMAX, EDELWEISS II). The information one can in principle extract from the eventual direct detection of a Dark Matter particle consists of the interaction cross section and the mass. The latter may well be in the multi TeV region, hence well beyond the LHC reach. On the other hand, spin-dependent searches (NAIAD) appear to be unable to probe any significant portion of the SUSY parameter space, and are by all means less promising than their scalar counterparts. Let us however stress that, for other particle Dark Matter candidates with different axial and vector couplings, the situation could equally be the other way round.

Indirect detection experiments convey into four categories, according to the final daughter particles generated by neutralino pair annihilations: respectively neutrinos, antiprotons, positrons and gamma rays. As regards the neutrino flux induced by neutralino annihilations, one can expect a sizable signal from the center of the Sun at future km-sized neutrino telescopes (ICECUBE, ANTARES); a SUSY Dark Matter particle can in principle give a visible signal in case its mass is below approximately 0.5 TeV, and provided the strength of spin-dependent neutralino-nucleon interactions is sufficiently large. The neutrino flux from the center of the Earth or of the Galaxy seems, instead, to be by far less promising.

Detection of Dark Matter particles through their antiprotons and positrons yields have been shown to be extremely dependent on the poorly known structure of the galactic dark halo. A careful analysis based on self-consistent halo models has shown that only if the neutralino annihilation rate is very large, and hence if some kind of relic density enhancement mechanism is operative, can these detection channels be of experimental relevance. If the neutralino local density is rescaled according to the standard thermal relic abundance, indirect SUSY Dark Matter detection at antimatter search facilities appears to be hopeless. Moreover, the spectral signatures of these species is often uncomfortably featureless. Last but not least, non-negligible uncertainties are involved in the cosmic rays propagation models. The advent of next generation, space-based experiments PAMELA and AMS could nevertheless provide important constraints both on the SUSY parameter space and on the halo structure.

Finally, gamma rays may well be a promising channel, though highly dependent on the occurrence of high density spikes either in the center of the Galaxy or in other celestial bodies; once again the diffuse gamma ray signal is typically pretty featureless, and the detection of the $\chi\chi \to \gamma\gamma, \gamma Z$ lines appears to be often quite problematic. The GLAST satellite could however shed some light onto intriguing experimental data, leftovers of the EGRET mission, and provide crucial novelties in the field. Ground-based Cerenkov detectors are also attracting a great deal of attention, especially for large mass particle candidates.

The quest for Supersymmetric Dark Matter is naturally tied to that of Supersymmetry. The latter, if it exists, may as well manifest itself through indirect accelerator experiments, which may reveal corrections, induced by new physics, on precision Standard Model quantities or on highly suppressed rare decays. The misalignment between the Standard Model prediction of the experimental results concerning the muon anomalous magnetic moment has been interpreted as a possible evidence towards new physics, and optimistically turned into strong constraints on the SUSY parameter space. Further investigations, both on the experimental and on the theoretical side, are however unanimously recognized as unavoidable and mandatory to clarify the situation. Other high precision quantities could in principle play

the role of *eagle eyes* for Supersymmetry. In the present thesis we discussed the particularly promising case of charged lepton flavor violation (LFV), which may well provide the first clear elementary particle clue for new physics beyond the Standard Model, possibly representing an *hors d'oeuvre* for Supersymmetry in its full glory.

Even though the overall experimental effort in the hunt for Supersymmetry and Supersymmetric Dark Matter seems to be prodigious, it may well be that no signals will emerge in the next years. On the other hand, the intriguing possibility of a cross discovery of the "*Sorcerer's Stone*" of contemporary elementary particle physics will by all means keep lying in the back of many physicists' minds.

Acknowledgements

I am grateful to my supervisors Serguey T. Petcov and Piero Ullio, without whose help and support the present work could not even get started. A great thank to my office mate and collaborator Carlos E. Yaguna, and to all the people I had the opportunity to joyfully work with during these three unforgettable PhD years: Fernando Alday, Federica Bazzocchi, Stefano Bertolini, Lotfi Boubekeur, Michele Cirafici, Sergio Colafrancesco, Michele Frigerio, Carlo Maccaferri, Antonio Masiero, Costantinos Pallis, Valentina Riva, Yasutaka Takanishi, Chiara Tonini, Sudhir K. Vempati and Ettore Vicari.

Stefano Profumo

Bibliography

[1] G. Jungman, M. Kamionkowski and K. Griest, Phys. Rept. **267** (1996) 195 [arXiv:hep-ph/9506380].

[2] L. Bergstrom, Rept. Prog. Phys. **63**, 793 (2000) [arXiv:hep-ph/0002126].

[3] C. Munoz, arXiv:hep-ph/0309346.

[4] G. Bertone, D. Hooper and J. Silk, arXiv:hep-ph/0404175.

[5] **THE EARLY UNIVERSE**. By E.W. Kolb, Michael S. Turner (Fermilab & Chicago U., EFI),. 1990. Redwood City, USA: Addison-Wesley (1990) 547 p. (Frontiers in physics, 69).

[6] D. N. Spergel *et al.*, Astrophys. J. Suppl. **148** (2003) 175 [arXiv:astro-ph/0302209].

[7] J. J. Binney and S. Tremaine, **Galactic Dynamics** (Princeton University Press, Princeton, 1987).

[8] A detailed analysis can be found in M. Persic, P. Salucci and F. Stel, 'The universal rotation curve of spiral galaxies: I. The dark matter connection', *Mon. Not. Roy. Astron. Soc.* **281** (1996) 27 [astro-ph/9506004].

[9] M. Roncadelli, arXiv:astro-ph/0307115.

[10] D. Zaritsky and S. D. M. White, *Astrophys. J.* **435** (1994) 599.

[11] O. Gerhard *et al.*, *Astron. J.* **121** (2001) 1936. M. Capaccioli, N. R. Napolitano and M. Arnaboldi, *astro-ph/0211323* (2002).

[12] T. Treu and L. V. E. Koopmans, *astro-ph/0202342* (2002) .

[13] W. Forman, C. Jones and W. Tucker, *Astrophys. J.* **293** (1985) 102. C. R. Canizares, G. Fabbiano and G. Trinchieri, *Astrophys. J.* **312** (1987) 503. G. Fabbiano, *Annu. Rev. Astron. Astrophys.* **27** (1989) 87.

[14] K. A. Olive, "*TASI lectures on dark matter*" arXiv:astro-ph/0301505.

[15] D. H. Weinberg *et al.*, arXiv:astro-ph/9810142.

[16] G. F. Smoot *et al.*, Astrophys. J. **396** (1992) L1.

[17] A. G. Riess *et al.* [Supernova Search Team Collaboration], Astron. J. **116** (1998) 1009 [arXiv:astro-ph/9805201].

[18] A. G. Riess *et al.* [Supernova Search Team Collaboration], Astrophys. J. **560** (2001) 49 [arXiv:astro-ph/0104455].

[19] W. L. Freedman *et al.*, Astrophys. J. **553** (2001) 47 [arXiv:astro-ph/0012376].

[20] P. J. E. Peebles, **Large-Scale Structure of the Universe** (Princeton University Press, Princeton).

[21] M. Kamionkowski and A. R. Liddle, Phys. Rev. Lett. **84**, 4525 (2000) [arXiv:astro-ph/9911103].

[22] D. N. Spergel and P. J. Steinhardt, Phys. Rev. Lett. **84**, 3760 (2000) [arXiv:astro-ph/9909386].

[23] K. Sigurdson and M. Kamionkowski, Phys. Rev. Lett. **92**, 171302 (2004) [arXiv:astro-ph/0311486].

[24] J. G. Bartlett, A. Blanchard, J. Silk and M. S. Turner, Science **267** (1995) 980 [arXiv:astro-ph/9407061].

[25] W. J. Percival *et al.*, Mon. Not. Roy. Astron. Soc. **327** (2001) 1297 [arXiv:astro-ph/0105252].

[26] R. A. C. Croft, D. H. Weinberg, N. Katz and L. Hernquist, arXiv:astro-ph/9708018.

[27] N. Y. Gnedin and A. J. S. Hamilton, arXiv:astro-ph/0111194.

[28] J. Rich, D. Lloyd Owen and M. Spiro, Phys. Rept. **151** (1987) 239; J. Hemmick et al, Phys. Rev. D **41** (1990) 2074.

[29] H. E. Haber and G. L. Kane, Phys. Rept. **117** (1985) 75.

[30] J. F. Gunion and H. E. Haber, Nucl. Phys. B **272**, 1 (1986) [Erratum-ibid. B **402**, 567 (1993)].

[31] **SUPERSYMMETRY AND SUPERGRAVITY**. By J. Wess (Munich U.), J. Bagger (Johns Hopkins U.),. 1992. 259pp. Princeton, USA: Univ. Pr. (1992) 259 p.

[32] S. P. Martin, arXiv:hep-ph/9709356.

[33] J. Edsjo, arXiv:hep-ph/9704384.

[34] D. J. H. Chung, L. L. Everett, G. L. Kane, S. F. King, J. Lykken and L. T. Wang, arXiv:hep-ph/0312378.

[35] M. Chemtob, arXiv:hep-ph/0406029.

[36] H. Baer, J. K. Mizukoshi and X. Tata, Phys. Lett. B **488**, 367 (2000) [arXiv:hep-ph/0007073].

[37] A. J. Barr, C. G. Lester, M. A. Parker, B. C. Allanach and P. Richardson, JHEP **0303**, 045 (2003) [arXiv:hep-ph/0208214].

[38] K. Hagiwara, A.D. Martin, D. Nomura and T. Teubner, *Phys. Lett.* **B 557** (2003) 69;
M. Davier, S. Eidelman, A. Hocker and Z. Zhang `hep-ph/0208177`.

[39] A. Nyffeler, *Talk given at the XXXVIIIth Rencontres de Moriond on ElectroWeak Interactions and Unified Theories, March 15th to 22nd, 2003.*

[40] G. L. Kane, C. F. Kolda, L. Roszkowski and J. D. Wells, Phys. Rev. D **49** (1994) 6173 [arXiv:hep-ph/9312272].

[41] A.H. Chamseddine, R. Arnowitt and P. Nath, Phys. Rev. Lett. **49** (1982) 970; R. Barbieri, S. Ferrara and C.A. Savoy, Phys. Lett. **B119** (1982) 343; L.J. Hall, J. Lykken and S. Weinberg, Phys. Rev. **D27** (1983) 2359; P. Nath, R. Arnowitt and A.H. Chamseddine, Nucl. Phys. **B227** (1983) 121.

[42] L. Randall and R. Sundrum, Nucl. Phys. B **557** (1999) 79 [arXiv:hep-th/9810155].

[43] G. F. Giudice, M. A. Luty, H. Murayama and R. Rattazzi, JHEP **9812** (1998) 027 [arXiv:hep-ph/9810442].

[44] T. Gherghetta, G. F. Giudice and J. D. Wells, Nucl. Phys. B **559** (1999) 27 [arXiv:hep-ph/9904378].

[45] J. L. Feng and T. Moroi, Phys. Rev. D **61** (2000) 095004 [arXiv:hep-ph/9907319].

[46] S. Profumo and C. E. Yaguna, arXiv:hep-ph/0407036.

[47] H. Baer, A. Belyaev, T. Krupovnickas and A. Mustafayev, JHEP **0406**, 044 (2004) [arXiv:hep-ph/0403214].

[48] T. Falk, K. A. Olive and M. Srednicki, Phys. Lett. B **339** (1994) 248 [arXiv:hep-ph/9409270].

[49] G. Belanger, F. Boudjema, A. Pukhov and A. Semenov, arXiv:hep-ph/0405253.

[50] P. Binetruy, G. Girardi and P. Salati, Nucl. Phys. B **237** (1984) 285;

[51] K. Griest and D. Seckel, Phys. Rev. D **43** (1991) 3191.

[52] J. Edsjo, M. Schelke, P. Ullio and P. Gondolo, JCAP **0304** (2003) 001 [arXiv:hep-ph/0301106].

[53] J. Edsjo and P. Gondolo, Phys. Rev. D **56** (1997) 1879 [arXiv:hep-ph/9704361].

[54] J. R. Ellis, T. Falk and K. A. Olive, Phys. Lett. B **444** (1998) 367 [arXiv:hep-ph/9810360].

[55] J. R. Ellis, T. Falk, K. A. Olive and M. Srednicki, Astropart. Phys. **13** (2000) 181 [Erratum-ibid. **15** (2001) 413] [arXiv:hep-ph/9905481].

[56] T. Nihei, L. Roszkowski and R. Ruiz de Austri, JHEP **0207** (2002) 024 [arXiv:hep-ph/0206266].

[57] J. L. Feng, K. T. Matchev and F. Wilczek, Phys. Lett. B **482** (2000) 388 [arXiv:hep-ph/0004043].

[58] A. Birkedal-Hansen and E. h. Jeong, JHEP **0302**, 047 (2003) [arXiv:hep-ph/0210041].

[59] V. A. Bednyakov, H. V. Klapdor-Kleingrothaus and E. Zaiti, Phys. Rev. D **66** (2002) 015010 [arXiv:hep-ph/0203108].

[60] C. Boehm, A. Djouadi and M. Drees, Phys. Rev. D **62** (2000) 035012 [arXiv:hep-ph/9911496].

[61] J. R. Ellis, K. A. Olive and Y. Santoso, Astropart. Phys. **18** (2003) 395 [arXiv:hep-ph/0112113].

[62] S. Profumo, Phys. Rev. D **68** (2003) 015006 [arXiv:hep-ph/0304071];

[63] S. Profumo, *"Extended coannihilations from non universal sfermion masses"*, arXiv:hep-ph/0305040, *Proceedings of the XXXVIIIth Rencontres de Moriond on ElectroWeak Interactions and Unified Theories, March 15th to 22nd, 2003*

[64] J. R. Ellis, K. A. Olive and Y. Santoso, Phys. Lett. B **539** (2002) 107 [arXiv:hep-ph/0204192].

[65] J. R. Ellis, T. Falk, K. A. Olive and Y. Santoso, Nucl. Phys. B **652** (2003) 259 [arXiv:hep-ph/0210205].

[66] S. Profumo and C. E. Yaguna, Phys. Rev. D **69** (2004) 115009 [arXiv:hep-ph/0402208].

[67] G. Belanger, F. Boudjema, A. Pukhov and A. Semenov, Comput. Phys. Commun. **149** (2002) 103 [arXiv:hep-ph/0112278].

[68] H. Baer, M. A. Diaz, P. Quintana and X. Tata, JHEP **0004** (2000) 016 [arXiv:hep-ph/0002245].

[69] H. Baer, J. Ferrandis, K. Melnikov and X. Tata, Phys. Rev. D **66**, 074007 (2002) [arXiv:hep-ph/0207126].

[70] See U. Chattopadhyay and D. P. Roy, Phys. Rev. D **68** (2003) 033010 [arXiv:hep-ph/0304108] and references therein.

[71] C. H. Chen, M. Drees and J. F. Gunion, Phys. Rev. D **55**, 330 (1997) [Erratum-ibid. D **60**, 039901 (1999)] [arXiv:hep-ph/9607421].

[72] S. Raby, Phys. Lett. B **422**, 158 (1998) [arXiv:hep-ph/9712254]; A. Mafi and S. Raby, Phys. Rev. D **63** (2001) 055010 [arXiv:hep-ph/0009202].

[73] H. Baer, K. m. Cheung and J. F. Gunion, Phys. Rev. D **59** (1999) 075002 [arXiv:hep-ph/9806361].

[74] S. Raby and K. Tobe, Nucl. Phys. B **539** (1999) 3 [arXiv:hep-ph/9807281]; A. Mafi and S. Raby, Phys. Rev. D **62** (2000) 035003 [arXiv:hep-ph/9912436].

[75] G. R. Farrar and A. Masiero, arXiv:hep-ph/9410401.

[76] G. R. Farrar and E. W. Kolb, Phys. Rev. D **53** (1996) 2990 [arXiv:astro-ph/9504081]; D. J. H. Chung, G. R. Farrar and E. W. Kolb, Phys. Rev. D **56** (1997) 6096 [arXiv:astro-ph/9703145].

[77] P. Gondolo, J. Edsjo, P. Ullio, L. Bergstrom, M. Schelke and E. A. Baltz, proceedings of idm2002, York, England, September 2002, astro-ph/0211238; `http://www.physto.se/ edsjo/darksusy/`http://www.physto.se/~edsjo/darksusy/.

[arXiv:astro-ph/0211238].

[78] J. R. Ellis, K. A. Olive, Y. Santoso and V. C. Spanos, Phys. Lett. B **565**, 176 (2003) [arXiv:hep-ph/0303043].

[79] G. D. Starkman, A. Gould, R. Esmailzadeh and S. Dimopoulos, Phys. Rev. D **41**, 3594 (1990).

[80] H. M. Pilkuhn, "Relativistic Particle Physics" (Springer, New York, 1979).

[81] P. Gondolo and G. Gelmini, Nucl. Phys. B **360** (1991) 145.

[82] See e.g. A. B. Lahanas, D. V. Nanopoulos and V. C. Spanos, Phys. Rev. D **62** (2000) 023515 [arXiv:hep-ph/9909497] and

[83] H. Baer and J. O'Farrill, *"Probing neutralino resonance annihilation via indirect detection of dark matter"* arXiv:hep-ph/0312350.

[84] S. Profumo and P. Ullio, JCAP **0311** (2003) 006 [arXiv:hep-ph/0309220].

[85] P. Salati, [arXiv:astro-ph/0207396].

[86] P. Gondolo, J. Edsjo, L. Bergstrom, P. Ullio and E. A. Baltz, [arXiv:astro-ph/0012234].

[87] M. Joyce, Phys. Rev. D **55** (1997) 1875; M. Joyce and T. Prokopec, Phys. Rev. D **57** (1998) 6022.

[88] P. G. Ferreira and M. Joyce, Phys. Rev. D **58** (1998) 023503 [arXiv:astro-ph/9711102].

[89] P. Gondolo and G. Gelmini, Nucl. Phys. B **360** (1991) 145.

[90] B. Spokoiny, Phys. Lett. **B315** (1993) 40.

[91] E.J. Copeland, A.R. Liddle and J.E. Lidsey, (2001) Phys. Rev. D **64** (2001) 023509; G. Huey and J. Lidsey, Phys. Lett. B **514** (2001) 217; V. Sahni, M. Sami and T. Souradeep, Phys. Rev. D **65** (2002) 023518.

[92] B. Ratra and P.J.E. Peebles, Phys. Rev. D **37** (1988) 3406; C. Wetterich, Nucl. Phys. B **302** (1988) 668.

[93] A. Albrecht and C. Skordis, Phys. Rev. Lett. **84** (2000) 2076 [arXiv:astro-ph/9908085].

[94] V. Sahni and L. M. Wang, Phys. Rev. D **62** (2000) 103517 [arXiv:astro-ph/9910097].

[95] F. Rosati, Phys. Lett. B **570** (2003) 5 [arXiv:hep-ph/0302159].

[96] B. Murakami and J. D. Wells, Phys. Rev. D **64**, 015001 (2001); T. Moroi and L. Randall, Nucl. Phys. B **570**, 455 (2000); M. Fujii and K. Hamaguchi, Phys. Lett. B **525**, 143 (2002); M. Fujii and K. Hamaguchi, Phys. Rev. D **66**, 083501 (2002); R. Jeannerot, X. Zhang and R. H. Brandenberger, JHEP **9912**, 003 (1999); W. B. Lin, D. H. Huang, X. Zhang and R. H. Brandenberger, Phys. Rev. Lett. **86**, 954 (2001).

[97] R. Catena, N. Fornengo, A. Masiero, M. Pietroni and F. Rosati, arXiv:astro-ph/0403614.

[98] M. Kamionkowski and M. S. Turner, Phys. Rev. D **42** (1990) 3310.

[99] J. R. Ellis, R. A. Flores and J. D. Lewin, Phys. Lett. B **212** (1988) 375.

[100] G. D. Starkman and D. N. Spergel, Phys. Rev. Lett. **74**, 2623 (1995).

[101] J. R. Ellis, A. Ferstl and K. A. Olive, Phys. Lett. B **481**, 304 (2000) [arXiv:hep-ph/0001005].

[102] A. Benoit et al., The EDELWEISS Collaboration, Phys. Lett. **B545** (2002) 43.

[103] E. Aprile *et al.*, arXiv:astro-ph/0207670.

[104] R. Gaitskell and V. Mandic, *Direct Detection of WIMP Dark Matter, Sensitivity Plots*, `http://dmtools.berkeley.edu/limitplots/`.

[105] N. J. C. Spooner *et al.*, Phys. Lett. B **473** (2000) 330;

[106] L. Bergstrom, J. Edsjo, P. Gondolo and P. Ullio, Phys. Rev. D **59** (1999) 043506 [arXiv:astro-ph/9806072].

[107] F. Halzen, Prog. Part. Nucl. Phys. **40**, 377 (1998).

[108] J. Edsjö, internal Amanda/IceCube report, 2000.

[109] L. Bergstrom, J. Edsjo and P. Gondolo, Phys. Rev. D **55**, 1765 (1997) [arXiv:hep-ph/9607237].

[110] A. Habig et al., *Proceedings of the XVII International Cosmic Ray Conference (ICRC)*, Hamburg, Germany, 2001, p. 1558. Also hep-ex/0106024; S Desai, talk at Identificaiton of Dark Matter, 2002 (idm2002), York, England.

[111] M. Kamionkowski, K. Griest, G. Jungman and B. Sadoulet, Phys. Rev. Lett. **74** (1995) 5174 [arXiv:hep-ph/9412213];

[112] L. Bergstrom, J. Edsjo and P. Gondolo, Phys. Rev. D **58** (1998) 103519 [arXiv:hep-ph/9806293].

[113] J. Silk and M. Srednicki, Phys. Rev. Lett. **50** (1984) 624.

[114] F.W. Stecker, S. Rudaz and T.F. Walsh, Phys. Rev. Lett. **55** (1985) 2622.

[115] A. Bottino, F. Donato, N. Fornengo and P. Salati, Phys. Rev. **D58** (1998) 123503.

[116] L. Bergström, J. Edsjö and P. Ullio, Astrophys. J. **526** (1999) 215.

[117] E.A. Baltz, J. Edsjo, Phys. Rev. **D59** (1999) 023511.

[118] F. Donato, N. Fornengo and P. Salati, Phys. Rev. **D62** (2000) 043003.

[119] F. Donato, N. Fornengo, D. Maurin, P. Salati and R. Taillet, Phys. Rev. **D69** (2004) 063501.

[120] A. Burkert, Astrophys. J. **447** (1995) L25.

[121] P. Salucci and A. Burkert, Astrophys. J. **537** (2000) L9.

[122] A. El-Zant, I. Shlosman and Y. Hoffman, Astrophys. J. **560** (2001) 336.

[123] I.V. Moskalenko, A.W. Strong, J.F. Ormes and M.S. Potgieter, Astrophys. J. **565** (2002) 280.

[124] Galprop numerical package, http://www.mpe.mpg.de/~aws/propagate.html

[125] L.J. Gleeson and W.I. Axford, Astrophys. J. **149** (1967) L115.

[126] L.A. Fisk, J. Geophys. Res. 76 (1971)

[127] JCAP **0407** (2004) 006 [arXiv:hep-ph/0406018].

[128] S. Orito et al., Phys. Rev. Lett. **84** (2000) 1078; Y. Asaoka et al., Phys. Rev. Lett. **88** (2002) 05110.

[129] Boezio et al., Astrophys. J. **561** (2001) 787.

[130] C. Grimani *et al.*, A&A 392, 287-294 (2002)

[131] DuVernois et al., Astrophys. J. **559** (2001) 296.

[132] Boezio et al., Astrophys. J. **532** (2000) 653.

[133] O. Adriani et al. (PAMELA Collaboration), Proc. of the 26th ICRC, Salt Lake City, 1999, OG.4.2.04.

[134] S. Ahlen et al. (AMS Collaboration), Nucl. Instrum. Methods **A350** (1994) 351.

[135] P. Picozza and A. Morselli, J. Phys. **G29** (2003) 903.

[136] LEP2 SUSY Working group, LEPSUYWG/01-03.1.

[137] J. R. Ellis, K. Enqvist, D. V. Nanopoulos and K. Tamvakis, Phys. Lett. B **155** (1985) 381.

[138] M. Drees, Phys. Lett. B **158** (1985) 409.

[139] H. Baer, F.E. Paige, S.D. Protopopescu and X. Tata, hep-ph/0001086.

[140] S. Profumo and P. Ullio, arXiv:astro-ph/0404390.

[141] The AMS Collaboration, Phys. Lett. **B484** (2000) 10.

[142] R. Bernabei et al., The DAMA Collaboration, R. Nuovo Cim. **26** (2003) 1.

[143] G.R. Blumental, S.M. Faber, R. Flores and J.R. Primack,

[144] A. Klypin, H.S. Zhao and R.S. Somerville, Astrophys. J. **573** (2002) 597.

[145] P. Ullio, in preparation

[146] J.F. Navarro et al., MNRAS (2004) in press, astro-ph/0311231.

[147] A.M. Ghez et al, astro-ph/0306130.

[148] P. Gondolo and J. Silk, Phys. Rev. Lett. **83** (1999) 1719.

[149] H.A. Mayer-Hasselwander et al., Astron. Astrophys. **335** (1998) 161.

[150] A. Cesarini et al., Astropart. Phys.(2004), in press.

[151] M. Pohl, Astron. Astrophys. **317** (1997) 441.

[152] D. Hooper and B. Dingus, astro-ph/0212509.

[153] GLAST Proposal to NASA A0-99-055-03 (1999).

[154] Prog. Part. Nucl. Phys. **33** (1994) 201 [arXiv:hep-ph/9402266].

[155] P. Langacker, *Phys. Rep.* **72** (1981) 185.

[156] B. Ananthanarayan, G. Lazarides and Q. Shafi, *Phys. Rev.* **D 44** (1991) 1613 and *Phys. Lett.* **B 300** (1993) 245;
G. Anderson *et al. Phys. Rev.* **D 47** (1993) 3702 and *Phys. Rev.* **D 49** (1994) 3660;
V. Barger, M. Berger and P. Ohmann, *Phys. Rev.* **D 49** (1994) 4908;
B. Ananthanarayan, Q. Shafi and X. Wang, *Phys. Rev.* **D 50** (1994) 5980;
R. Rattazzi and U. Sarid, *Phys. Rev.* **D 53** (1996) 1553.

[157] M. Carena, M. Olechowski, S. Pokorski and C. E. Wagner, *Nucl. Phys.* **B426** (1994) 269.

[158] H. Baer, M.A. Diaz, J. Ferrandis and X. Tata, *Phys. Rev.* **D 61** (2000) 111701;
H. Baer, M. Brhlik, M.A. Diaz, J. Ferrandis, P. Mercadante, P. Quintana and X. Tata, *Phys. Rev.* **D 63** (2001) 015007;
H. Baer and J. Ferrandis, *Phys. Rev. Lett.* **87** (2001) 211803;
D. Auto, H. Baer, C. Balazs, A. Belyaev, J. Ferrandis and X. Tata, `hep-ph/0302155`.

[159] L.J. Hall, R. Rattazzi and U. Sarid, *Phys. Rev.* **D 50** (1994) 7048;
R. Hempfling, *Phys. Rev.* **D 49** (1994) 6168.

[160] M.S. Chanowitz, J. Ellis and M.K. Gaillard, *Nucl. Phys.* **B128** (1977) 506;
A.J. Buras, J. Ellis, M.K. Gaillard and D.V. Nanopolous, *Nucl. Phys.* **B135** (1978) 66.

[161] M. B. Einhorn and D. R. Jones, *Nucl. Phys.* **B196** (1982) 475;
L. E. Ibanez and C. Lopez, *Nucl. Phys.* **B233** (1984) 511;
H. Arason, D. Castano, B. Keszthelyi, S. Mikaelian, E. Piard, P. Ramond and B. Wright, *Phys. Rev. Lett.* **67** (1991) 2933;
A. Giveon, L. J. Hall and U. Sarid, *Phys. Lett.* **B 271** (1991) 138;
S. Kelley, J. L. Lopez and D. V. Nanopoulos, *Phys. Lett.* **B 274** (1992) 387.

[162] P. Langacker and N. Polonsky, *Phys. Rev.* **D 49** (1994) 1454;
W. A. Bardeen, M. Carena, S. Pokorski and C. E. Wagner, *Phys. Lett.* **B 320** (1994) 110.

[163] M. Carena, S. Pokorski and C. E. Wagner,*Nucl. Phys.* **B406** (1993) 59.

[164] N. Polonsky, *Phys. Rev.* **D 54** (1996) 4537.

[165] S. Komine and M. Yamaguchi, *Phys. Rev.* **D 65** (2002) 075013;
U. Chattopadhyay and P. Nath, *Phys. Rev.* **D 65**(2002) 075009.

[166] W. de Boer, M. Huber, A.V. Gladyshev, D.I. Kazakov, *Eur. Phys. J.* **C 20** (2001) 689.

[167] U. Chattopadhyay, A. Corsetti and P. Nath, *Phys. Rev.* **D 66** (2002) 035003.

[168] S.M. Barr and I. Dorsner, *Phys. Lett.* **B 556** (2003) 185.

[169] B. Bajc, G. Senjanovic and F. Vissani, *Phys. Rev. Lett.* **90** (2003) 051802.

[170] A. Masiero, S.K. Vempati and O. Vives, *Nucl. Phys.* **B649** (2003) 189.

[171] P. Nath and R. Arnowitt, Phys. Rev. Lett. **69** (1992) 725, Phys. Rev. Lett. **70** (1993) 3696;
J. Hisano, H. Murayama and T. Yanagida, Nucl. Phys. B **402** (1993) 46.

[172] H. Murayama and A. Pierce, Phys. Rev. **D 65** (2002) 055009.

[173] B. Bajc, P.F. Perez and G. Senjanovic, Phys. Rev. **D 66** (2002) 075005; B. Bajc, P.F. Perez and G. Senjanovic, talk given by B.B. at Beyond the Desert 02, Oulu, Finland, 2-7 June 2002, `hep-ph/0210374`.

[174] **Super-Kamiokande** Collaboration, Y. Hayato et al., Phys. Rev. Lett. **83** (1999) 1529.

[175] D. Emmanuel-Costa and S. Wiesenfeldt, Nucl. Phys. B **661** (2003) 62.

[176] D. Auto, H. Baer, A. Belyaev and T. Krupovnickas, arXiv:hep-ph/0407165.

[177] V. Barger, C.E.M. Wagner, et al, hep-ph/0003154.

[178] K. Hagiwara et al.,*Phys. Rev.* **D 66** (2002) 010001;
C.T. Sachrajda, *Nucl. Instrum. Meth.* **A 462** (2001) 23.

[179] H. Baer, J. Ferrandis, K. Melnikov, X. Tata, *Phys. Rev.* **D 66** (2002) 074007.

[180] D.M. Pierce, J.A. Bagger, K.T. Matchev and R.J. Zhang, *Nucl. Phys.* **B491** (1997) 3.

[181] M. Carena, D. Garcia, U. Nierste, C.E.M. Wagner, *Nucl. Phys.* **B577** (2000) 88.

[182] T. Blazek, R. Dermisek, S. Raby, *Phys. Rev. Lett.* **88** (2002) 111804; *Phys. Rev.* **D 65** (2002) 115004.

[183] For a review see A. B. Lahanas and D. V. Nanopoulos, Phys. Rept. **145** (1987) 1.

[184] D. E. Kaplan, G. D. Kribs and M. Schmaltz, Phys. Rev. D **62** (2000) 035010; Z. Chacko, M. Luty, A. E. Nelson and E. Pontón, JHEP **0001** (2000) 003.

[185] J. Ellis, D. V. Nanopoulos and K. A. Olive, Phys. Lett. B **525** (2002) 308.

[186] M. Schmaltz and W. Skiba, Phys. Rev. D **62** (2000) 095005.

[187] S. Profumo, JHEP **0306**, 052 (2003) [arXiv:hep-ph/0306119].

[188] H. Baer, C. Balazs, A. Belyaev and J. O'Farrill, JCAP **0309** (2003) 007 [arXiv:hep-ph/0305191].

[189] H. Baer, A. Belyaev, T. Krupovnickas and X. Tata, Phys. Rev. D **65** (2002) 075024.

[190] E. Witten, Phys. Lett. B **155** (1985) 151.

[191] H. P. Nilles, M. Olechowski and M. Yamaguchi, Phys. Lett. B **415** (1997) 24; Nucl. Phys. B **530** (1998) 43.

[192] J. Rich, M. Spiro and J. Lloyd-Owen, *Phys. Rep.* **151** (1987) 239.

[193] H. Baer, C. Balazs, A. Belyaev, J. Mizukoshi, X. Tata and Y. Wang, hep-ph/0210441.

[194] N. Polonsky and A. Pomarol, Phys. Rev. D **51** (1995) 6532.

[195] **ALEPH**, **DELPHI**, **L3** and **OPAL** Collaborations, hep-ex/0107029, LHWG Note/2001-03.

[196] S. Komine, M. Yamaguchi, Phys. Rev. D **63** (2001) 035005; H. Baer, C. Balazs, A. Belyaev, R. Dermisek, A. Mafi and A. Mustafayev, JHEP **0205** (2002) 061; C. Balazs and R. Dermisek, hep-ph/0303161.

[197] T. Yanagida in *Proc. Workshop on Unified Theories &c.,* eds. O. Sawada and A. Sugamoto (Tsukuba, 1979); M. Gell-Mann, P. Ramond, and R. Slansky, in *Supergravity,* eds. D. Freedman *et al.,* (North Holland 1980 Amsterdam); S.L. Glashow, in *Quarks and Leptons, Cargèse 1979,* eds. M. Lévy, *et al.,* (Plenum 1980 New York), p. 707; R. N. Mohapatra and G. Senjanovic, Phys. Rev. Lett. **44**, 912 (1980).

[198] T. Moroi, JHEP **0003**, 019 (2000) [arXiv:hep-ph/0002208]; T. Moroi, Phys. Lett. B **493**, 366 (2000) [arXiv:hep-ph/0007328]; N. Akama, Y. Kiyo, S. Komine and T. Moroi, Phys. Rev. D **64**, 095012 (2001) [arXiv:hep-ph/0104263]; D. Chang, A. Masiero and H. Murayama, Phys. Rev. D **67**, 075013 (2003) [arXiv:hep-ph/0205111].

[199] A. Masiero, S. K. Vempati and O. Vives, Nucl. Phys. B **649**, 189 (2003) [arXiv:hep-ph/0209303].

[200] J. Hisano, T. Moroi, K. Tobe, M. Yamaguchi and T. Yanagida, Phys. Lett. B **357** (1995) 579 [arXiv:hep-ph/9501407]; J. Hisano and D. Nomura, Phys. Rev. D **59**, 116005 (1999) [arXiv:hep-ph/9810479]. See also: I. Masina and C. A. Savoy, Nucl. Phys. B **661**, 365 (2003) [arXiv:hep-ph/0211283].

[201] See for example, R. Kitano, M. Koike and Y. Okada, Phys. Rev. D **66**, 096002 (2002) [arXiv:hep-ph/0203110]; R. Kitano, M. Koike, S. Komine and Y. Okada, Phys. Lett. B **575**, 300 (2003) [arXiv:hep-ph/0308021] and references there in.

[202] K. S. Babu and C. Kolda, Phys. Rev. Lett. **89**, 241802 (2002) [arXiv:hep-ph/0206310]; A. Dedes, J. R. Ellis and M. Raidal, Phys. Lett. B **549**, 159 (2002) [arXiv:hep-ph/0209207]; A. Brignole and A. Rossi, Phys. Lett. B **566**, 217 (2003) [arXiv:hep-ph/0304081].

[203] J. Sato, K. Tobe and T. Yanagida, Phys. Lett. B **498**, 189 (2001) [arXiv:hep-ph/0010348].

[204] T. Blazek and S. F. King, Phys. Lett. B **518**, 109 (2001) [arXiv:hep-ph/0105005].

[205] M. L. Brooks *et al.* [MEGA Collaboration], Phys. Rev. Lett. **83** (1999) 1521 [arXiv:hep-ex/9905013].

[206] K. Abe *et al.* [Belle Collaboration], arXiv:hep-ex/0310029.

[207] K. Inami, for the Belle Colloboration, Talk presented at the 19th International Workshop on Weak Interactions and Neutrinos (WIN-03) October 6th to 11th, 2003, Lake Geneva, Wisconsin, USA.

[208] Web page: `http://meg.psi.ch`

[209] See, *e.g.* J. Hisano, D. Nomura and T. Yanagida, Phys. Lett. B **437**, 351 (1998) [arXiv:hep-ph/9711348]; S. F. King and M. Oliveira, Phys. Rev. D **60**, 035003 (1999) [arXiv:hep-ph/9804283]; J. R. Ellis, M. E. Gomez, G. K. Leontaris, S. Lola and D. V. Nanopoulos, Eur. Phys. J. C **14**, 319 (2000) [arXiv:hep-ph/9911459]; S. Baek, T. Goto, Y. Okada and K. i. Okumura, Phys. Rev. D **63**, 051701 (2001) [arXiv:hep-ph/0002141].

[210] H. Baer, C. Balazs, A. Belyaev, T. Krupovnickas and X. Tata, JHEP **0306** (2003) 054 [arXiv:hep-ph/0304303].

[211] C. T. Hill, Phys. Lett. B **135** (1984) 47; J. R. Ellis, K. Enqvist, D. V. Nanopoulos and K. Tamvakis, Phys. Lett. B **155** (1985) 381; M. Drees, Phys. Lett. B **158** (1985) 409.

[212] H. Baer, A. Belyaev, T. Krupovnickas and X. Tata, arXiv:hep-ph/0311351.

[213] R. Barbieri, arXiv:hep-ph/0312253.

[214] K. Griest and M. Kamionkowski, Phys. Rev. Lett. **64** (1990) 615.